

Electronic Thesis and Dissertation Repository

8-20-2014 12:00 AM

Response of Transmission Line Conductors Under Downburst Wind

Haitham Aboshosha
The University of Western Ontario

Supervisor
Ashraf El Damatty
The University of Western Ontario

Graduate Program in Civil and Environmental Engineering
A thesis submitted in partial fulfillment of the requirements for the degree in Doctor of Philosophy
© Haitham Aboshosha 2014

Follow this and additional works at: <https://ir.lib.uwo.ca/etd>



Part of the [Aerodynamics and Fluid Mechanics Commons](#), [Civil Engineering Commons](#), [Computational Engineering Commons](#), and the [Structural Engineering Commons](#)

Recommended Citation

Aboshosha, Haitham, "Response of Transmission Line Conductors Under Downburst Wind" (2014). *Electronic Thesis and Dissertation Repository*. 2237.
<https://ir.lib.uwo.ca/etd/2237>

This Dissertation/Thesis is brought to you for free and open access by Scholarship@Western. It has been accepted for inclusion in Electronic Thesis and Dissertation Repository by an authorized administrator of Scholarship@Western. For more information, please contact wlsadmin@uwo.ca.

RESPONSE OF TRANSMISSION LINE CONDUCTORS UNDER DOWNBURST WIND

(Thesis format: Integrated Article)

by

Haitham Aboshosha

Graduate Program in Engineering Science

Department of Civil and Environmental Engineering

A thesis submitted in partial fulfillment
of the requirements for the degree of
Doctor of Philosophy

The School of Graduate and Postdoctoral Studies
The University of Western Ontario
London, Ontario, Canada

© Haitham Aboshosha 2014

Abstract

Electricity is transmitted by Transmission Lines (TLs) from the source of production to the distribution system and then to the end consumers. Failure of a TL can lead to significant economic losses and to negative social consequences resulting from the interruption of power. High Intensity Winds (HIW), in the form of downbursts and tornadoes, are believed to be responsible for more than 80% of the weather-related failure of TLs around the world. The studies reported in this thesis are part of an ongoing extensive research program at Western University focusing on the response of TLs under HIW. Previous investigations conducted to study the behavior and to assess the failure of TLs under downburst wind indicated the importance of accounting for the forces transmitted from the conductors to the towers. The current thesis focuses on the response of TL conductors subjected to downburst wind while considering various terrain exposures. The thesis is written using the "Integrated Article" format and includes various complementary studies. First, an effective numerical technique to analyze transmission line (TL) conductors subjected to HIW events is developed. This is followed by a derivation of a simplified closed form solution to estimate the forces transmitted from the conductors to the towers due to downburst winds. Then, an expression for the conductor aerodynamic damping, which is a main parameter affecting the conductors' dynamic behavior, corresponding to downburst wind, is derived and validated. Afterwards, dynamic behaviour of TL conductors under downburst and synoptic winds corresponding to open terrain exposure is investigated. In order to account for other terrain exposures, a new roughness model adequate for Large Eddy Simulation (LES) of moderate-rough to rough terrain exposures typically encountered by TLs is developed and validated. Then this model is used in conducting LES of downbursts for various terrain exposures in order to: (i) characterize the downburst turbulence, (ii) investigate the dynamic behavior of TL conductors under downburst wind corresponding to different exposures. The research accomplished in this thesis, in terms of development of efficient structural analysis tools and characterization of the wind field, provides an advancement in knowledge about the behavior of transmission lines in general and conductors in particular during downburst events.

Keywords

High Intensity Wind (HIW), downburst, tornado, synoptic winds, transmission lines, conductors, cable, finite element, numerical technique, closed form, practitioner engineers, aerodynamic damping, Computational Fluid Dynamics (CFD), turbulence, Large Eddy Simulation (LES), ground roughness, atmospheric boundary layer (ABL), aerodynamic roughness z_0 , wind spectra, wind profile, turbulent intensity, length scales, correlation, coherence, peak factor, gust factor, gust front factor, dynamic response.

Co-Authorship

This thesis has been prepared in accordance with the regulations for an Integrated-Article format thesis stipulated by the Faculty of Graduate Studies at Western University and has been co-authored as:

Chapter 2: Effective Technique to Analyze Transmission Line Conductors under High Intensity Winds.

An effective numerical technique to analyze transmission line conductors has been developed by H. Aboshosha under the close supervision of Dr. A. El Damatty. A paper co-authored by H. Aboshosha A. El Damatty has been published in *Wind and Structures an International Journal*.

Chapter 3: Closed Form Solution for the Reactions of Transmission Line Conductors under Downburst Winds.

A closed form solution to evaluate the reactions of transmission line conductors under downburst wind has been developed by H. Aboshosha under the close supervision of Dr. A. El Damatty. A version of this work co-authored by H. Aboshosha A. El Damatty will be submitted to the *International Journal for Numerical Methods in Engineering, UK*.

Chapter 4: Aerodynamic Damping of Transmission Line Conductors under Downburst Winds

An expression for the aerodynamic damping of transmission line conductors subjected to downburst wind has been developed and validated by H. Aboshosha under the close supervision of Dr. G. Bituamlak and Dr. A. El Damatty. A version of this work co-authored by H. Aboshosha G. Bituamlak A. El Damatty will be submitted to *Wind and Structures an International Journal*.

Chapter 5: Assessment of Dynamic Effect for Transmission Line Conductors under Downburst and Synoptic Winds

Analyses of transmission line conductors under downburst and synoptic wind have been conducted by H. Aboshosha under the close supervision of Dr. A. El Damatty. A version of this work co-authored by H. Aboshosha A. El Damatty will be submitted to the journal of *Engineering Structures*.

Chapter 6: LES of Wind Flow over Various Upwind Exposures

A new roughness model that allows for modeling moderate rough to rough terrains using Large Eddy Simulation (LES) has been developed by H. Aboshosha under the close supervision of Dr. G. Bitsuamlak and Dr. A. El Damatty. A version of this work co-authored by H. Aboshosha A. El Damatty G. Bitsuamlak was submitted to *Wind and Structures an International Journal*.

Chapter 7: Turbulent Downburst Wind Field and Corresponding Dynamic Behavior of Transmission Line Conductors

Large Eddy Simulations of downburst events occurring above various terrain exposures have been conducted by H. Aboshosha under the close supervision of Dr. G. Bitsuamlak and Dr. A. El Damatty. A version of this work co-authored by H. Aboshosha G. Bitsuamlak A. El Damatty was submitted to the *Journal of Wind Engineering and Industrial Aerodynamics*.

Acknowledgments

Foremost, I would like to express my sincere gratitude to my advisors Prof. Ashraf El Damatty and Prof. Girma Bitsuamlak for their continuous support in my Ph.D, for their patience, motivation, enthusiasm, kind funding, and immense knowledge. Their guidance helped me in all time of research and writing of this thesis.

I would like to thank the National Science and Engineering Research Centre (NSERC) for the kind funding through the Industrial Post Graduate Scholarship with the Boundary Layer Wind Tunnel Laboratory (BLWTL). I would like also to thank the team of Alan G. Davenport Wind Engineering Group at the BLWTL, especially Dr. J. Peter C. King, Dr. Eric Ho, Dr. Lingzhe Kong and Karen Norman, for the internship opportunity I had during my PhD. This opportunity allowed me to work on diverse exciting projects in the field of wind engineering which significantly solidified my background and enhanced the quality of my research.

I would like to thank Hydro One company and Ontario Centre of Excellence (OCE) for their kind funding. I would like also to thank Dr. Ayman Alansary who helped me in editing this final version of the thesis.

Special thanks shall go to the SHARCNET for providing access to their high performance computation facility.

Many thanks to my research group (A. Hamada, A. Ansary, A. Musa, A. Eladawy, A. Ibrahim, M. Hamada, Z. Nassir, A. El shaer, A. Awol) for the time we spent together sharing ideas and learning from each others. I also would like to thank all my friends who shared with me the journey of this PhD. Without them I couldn't have been able to make it.

Last but not the least; I would like to thank my sincere wife: Maryam for her patience, encouragement and support during all stages of this PhD and for her valuable technical and non-technical advices. I would like to thank my young kids: Malik and Yusuf for filling my life with great happiness. Also, special thanks shall go to my parents, for supporting me throughout my life.

Table of Contents

Abstract.....	ii
Co-Authorship.....	iv
Acknowledgments.....	vi
Table of Contents.....	vii
List of Tables.....	xii
List of Figures.....	xiv
List of Appendices.....	xxi
List of Symbols.....	xxii
Chapter 1.....	1
1 Introduction.....	1
1.1 Background.....	1
1.2 Downburst Wind Field.....	4
1.3 Studies on the Effect of Downbursts on TLs.....	8
1.3.1 Modeling of Conductors.....	11
1.3.2 Dynamic Analysis of TL Conductors.....	11
1.4 Objectives of the Study.....	13
1.5 Organization of the Thesis.....	14
1.6 References.....	18
Chapter 2.....	24
2 Effective Technique to Analyze Transmission Line Conductors under High Intensity Winds.....	24
2.1 Introduction.....	24
2.2 Formulation.....	26
2.2.1 Conductor Transverse and Vertical Reactions (R_y and R_z).....	28
2.2.2 Insulator Equilibrium.....	33

2.3	Solution Technique	35
2.4	Validating the Technique	36
2.4.1	Results of the Analysis.....	39
2.5	Conclusions.....	43
2.6	References.....	44
Chapter 3	47
3	Closed Form Solution for the Reactions of Transmission Line Conductors under Downburst Winds	47
3.1	Introduction.....	47
3.2	Formulation.....	51
3.2.1	The Transverse Reaction R_y	54
3.2.2	The Longitudinal Reaction R_x	55
3.3	Factors f_{yi} , f_{LL} , f_L , f_R , and f_{RR} and the Wind Intensity g_{py}	63
3.4	Maximum Longitudinal Reaction, R_{x3max}	69
3.5	Accuracy of the Proposed Solution.....	71
3.6	Conclusions.....	73
3.7	References.....	74
Chapter 4	77
4	Aerodynamic Damping of Transmission Line Conductors under Downburst Winds .	77
4.1	Introduction.....	77
4.2	Analytical Expression for the Conductor Aerodynamic Damping	79
4.2.1	Aerodynamic Damping under Downburst Winds.....	79
4.2.2	Conductor Tension and Natural Frequencies under Downburst Winds ...	82
4.2.3	Conductor Aerodynamic Damping under Downbursts.....	90
4.3	Evaluation of the Aerodynamic Damping by CFD.....	93
4.3.1	CFD Technique to Obtain the Aerodynamic Damping	94

4.3.2	Simulating the Conductor under a Steady Uniform Winds	99
4.3.3	Simulating the Conductor under Downburst Winds	102
4.4	Conclusions.....	106
4.5	References.....	107
Chapter 5.....		111
5	Assessment of Dynamic Effect for Transmission Line Conductors under Downburst and Synoptic Winds	111
5.1	Introduction.....	111
5.2	Description of Different Cases Considered in the Analysis	114
5.3	Mean Wind Velocities	116
5.4	Fluctuating Wind Velocities	117
5.5	Technique Used to Analyze Conductor Systems.....	119
5.5.1	Step 1: Non-linear Quasi-Static Analysis under the Mean Wind	120
5.5.2	Step 2: Linear Dynamic Analysis under the Fluctuating Wind Load.....	128
5.5.3	Step 3: Quasi-Static Linear Analysis under the Fluctuating Wind	133
5.6	Results of the Dynamic Analyses	134
5.7	Conclusions.....	138
5.8	Acknowledgment	140
5.9	References.....	140
Chapter 6.....		144
6	LES of Wind Flow over Various Upwind Exposures	144
6.1	Introduction.....	144
6.2	Modified Surface Gradient Drag (MSGD) model	148
6.2.1	Calculation of the Drag Coefficient C_d^*	152
6.3	Synthesizing Fractal Surfaces with a Targeted z_0	154
6.3.1	Generating Unscaled Fractal Surfaces using RFM.....	154

6.3.2	Scaling of the Fractal Surfaces	155
6.4	LES Model	158
6.4.1	Grid Sensitivity Study	165
6.4.2	Results of the ABL Simulation	166
6.4.3	Application for Inflow Boundary Condition Generation	171
6.5	Conclusions	172
6.6	Acknowledgments	173
6.7	References	173
Chapter 7	179
7	Turbulent Downburst Wind Field and Corresponding Dynamic Behavior of Transmission Line Conductors	179
7.1	Introduction	179
7.2	LES Model Setup	183
7.2.1	Modeling of Terrain Roughness	186
7.3	Running Mean and Turbulent Wind Decomposition	190
7.4	LES Results and Discussion	192
7.4.1	Grid Independence	192
7.4.2	Evolution of the Wind Field with Time	195
7.4.3	Mean Wind Field	195
7.4.4	Turbulent Wind Field	198
7.5	Assessing the Dynamic Effect on Transmission Line Conductors	210
7.6	Application of the Gust Front Factor (GFF) Approach to Obtain the Peak Responses of Transmission Line Conductors	216
7.7	Conclusions	218
7.8	References	221
Chapter 8	227
8	Conclusions and Recommendations	227

8.1.1	Effective Technique to Analyze Transmission Line Conductors under High Intensity Winds	228
8.1.2	A Closed Form Solution for the Reactions of a Transmission Line Conductor under Downburst Winds	229
8.1.3	Aerodynamic Damping of Transmission Line Conductors under Downburst Winds	229
8.1.4	Assessment of Dynamic Effects for Transmission Line Conductors under Downburst and Synoptic Winds	230
8.1.5	LES of Wind in the Built-Environment: Inflow and Roughness Induced by Fractal Surfaces.....	232
8.1.6	Turbulence Characterization of Stationary Downbursts using LES	233
8.2	Recommendation for Future Research.....	236
Appendix A: Parameters of the Numerical Technique Used to Analyze TL Conductors under HIW		238
Appendix B: Parameters of the Numerical Technique Used to Analyze TL Conductors under Downburst Wind		240
Appendix C: Figures for the reaction time responses		242
Appendix D: Results of the Dynamic Analyses under Various Terrain Exposures		248
Curriculum Vitae		254

List of Tables

Table 2.1 loading parameters	38
Table 2.2 Properties of the Conductor	39
Table 2.3 Nodal reactions and displacement results for the Downburst Case	42
Table 2.4 Nodal reactions and displacement results for the Tornado Case	43
Table 3.1 Summary of the parametric study	64
Table 3.2 Properties of the considered conductor system.....	71
Table 3.3 Comparison between the reaction calculated by the current method and those using FEA.....	72
Table 3.4 Reactions calculated for the case of ($L_x/D_j=0.5$, $R/D_j=1.60$ and $\Theta=30^\circ$)	73
Table 4.1 Summary of the parametric study	88
Table 4.2 Properties of the studied conductor	94
Table 4.3 Discretization schemes and solution technique for the CFD simulations	97
Table 4.4 the mean and RMS drag coefficient of a stationary square cylinder	100
Table 5.1 Properties of the conductor systems	114
Table 5.2 Studied cases.....	115
Table 5.3 Gust factors for the different wind cases	135
Table 6.1 Steps involved in simulating roughness associated with the fractal surfaces	157
Table 6.2 Generated exposure conditions.....	161
Table 6.3 Averaging lengths l_x , l_y , l_{xy}	162
Table 6.4 Discretization schemes and solution technique for the CFD simulations	165

Table 7.1 Discretization schemes and solution technique	184
Table 7.2 Properties of the employed grids	186
Table 7.3 Studied cases.....	210

List of Figures

Figure 1.1 Guyed transmission tower (Source: Wikipedia: http://operationcircuitbreaker.wordpress.com/chapter-4-transmission-line-vulnerabilities)....	2
Figure 1.2 Self-supported transmission tower (Source: Wikipedia: http://operationcircuitbreaker.wordpress.com/chapter-4-transmission-line-vulnerabilities)....	3
Figure 1.3 Comparison between vertical velocity profile for downbursts. Reproduced from Kim and Hangan (2007).....	5
Figure 1.4 Critical downburst case (Shehata and El Damatty 2008)	10
Figure 2.1 the system layout	27
Figure 2.2 Equilibrium at point N.....	27
Figure 2.3 Analysis of a conductor span (n+1).....	28
Figure 2.4 Conductor Segment	32
Figure 2.5 equilibrium of the insulator	34
Figure 2.6 Flow chart of the proposed solution approach	36
Figure 2.7 Downburst loading Case.....	37
Figure 2.8 Tornado Loading Case	38
Figure 2.9 Load distribution induced from the Downburst Loading	38
Figure 2.10 Load distribution induced from the Tornado Loading	39
Figure 2.11 deflected shape under downburst loading	41
Figure 2.12 deflected shape under tornado loading	41
Figure 3.1 Downburst Parameters.....	48

Figure 3.2 Idealization of the multi-spanned conductor system: a) Aboshosha and El Damatty (2014) b) the current study, Distribution of the tensile forces: c) Aboshosha and El Damatty (2014) d) the current study.....	50
Figure 3.3 Distribution of the downburst load for $L_x/D_j=0.5$, $R/D_j=1.60$ and $\Theta=30^\circ$	54
Figure 3.4 Horizontal view of conductor span i	54
Figure 3.5 Conductor Segment	56
Figure 3.6 Equilibrium of the longitudinal forces (a) at point no. 2 (b) at point no. 3	59
Figure 3.7 Variation of the factor f_{y_i} under different DPs	65
Figure 3.8 Variation of the factor f_R under different DPs.....	65
Figure 3.9 Variation of the factor f_L under different DPs.....	66
Figure 3.10 Variation of the factor f_{LL} under different DPs	66
Figure 3.11 Variation of the factor f_{RR} under different DPs.....	67
Figure 3.12 Ratio between V_{pmax}/V_j for different locations (R/D_j , Z/D_j)	67
Figure 3.13 Steps to calculate the reactions at the tower of interest.....	68
Figure 3.14 f_{3max} for the case of the maximum longitudinal reaction.....	70
Figure 4.1 Decomposition of the mean velocity.....	80
Figure 4.2 Conductor Layout.....	85
Figure 4.3 First two vibration modes for different vibration types.....	85
Figure 4.4 the stable location of the conductor.....	88
Figure 4.5 Downburst Parameters.....	89
Figure 4.6 Variation of the load shape factor, f_y , with the Downburst Parameters	89

Figure 4.7 Variation of the Integral I_1 for first out of plane mode with the Downburst Parameters where $N=1$	91
Figure 4.8 Variation of the Integral I_N with the Downburst Parameters for the in plane anti-symmetric modes where $N=1,2,\dots$ and for the out of plane modes where $N=2,3,\dots$	92
Figure 4.9 Variation of the Integral I_N with the Downburst Parameters for the in plane symmetric modes where $N=1,2,\dots$	92
Figure 4.10 Schematic of the utilized technique to perform the FSI	98
Figure 4.11 the CFD Domain and its Meshing	98
Figure 4.12 Results of the stationary conductor a-time history of the Drag Coefficient C_d b-instantaneous velocity contours c-instantaneous vorticity contours	101
Figure 4.13 Fitting the peaks of the response with the logarithmic decrement of damping.	102
Figure 4.14 Time history of the non-stationary mean velocity component at the conductor midpoint	104
Figure 4.15 Variation of the 1st natural frequency with time	104
Figure 4.16 Mean, turbulent and total wind velocity at the conductor midpoint.....	105
Figure 4.17 Total and resonant displacement responses resulted from the CFD and from employing the recent damping formula	105
Figure 4.18 variation of the aerodynamic damping of the first mode with the time	105
Figure 5.1 Insulator used in different systems: (a)-single spanned, Wikipedia: http://en.wikipedia.org/wiki/Baltic_Cable (b)-six spanned, http://www.electrotechnik.net/2010/01/back-flashovers-introduction.html	113
Figure 5.2 Downburst parameters D_j , R and Θ	115
Figure 5.3 Velocity time history at point p for: (a) downburst case no. 1 (Dbx , $L_x=300$, $V_{refp}=40$ m/s) (b) synoptic wind case no. 9 (Sy , $L_x=300$, $V_{refp}=40$ m/s).....	118

Figure 5.4 Steps of the conductor analysis	119
Figure 5.5 Schematic illustration of the conductor-system	121
Figure 5.6 Flow chart of the employed technique (iterate until convergence)	122
Figure 5.7 Time variation of the wind intensity, the tension force for the single-spanned and six-spanned systems.....	124
Figure 5.8 Time variation of the mean transverse displacement dy and vertical displacement dz at point r	125
Figure 5.9 Distribution of the wind load g_y along the conductor spans at the time instance t_{max}	126
Figure 5.10 Conductor profile at the time instance t_{max} for the single-spanned system	126
Figure 5.11 Conductor deformed configuration at the time instance t_{max} for the six-spanned system	127
Figure 5.12 Employed two-nodded cable element	128
Figure 5.13 Drag force at node i due to incoming wind	130
Figure 5.14 Comparison between the results of the in-house program and FEA (a) time history of R_x (b) time history of R_y (c) running R_y components (d) running R_x components	133
Figure 5.15 Contribution of different components in the peak responses	137
Figure 5.16 Normalized peak reactions	138
Figure 6.1 Schematic of driver and test domains.....	147
Figure 6.2 SGD models: (a) Anderson and Meneveau (2010) and (b) Modified.....	149
Figure 6.3 Computational domain, the employed grids and boundary conditions	159
Figure 6.4 Generated fractal surfaces corresponding to $z_0=0.1, 0.3$ and $0.7m$ respectively .	160

Figure 6.5 Generated surface grid points with positive $\frac{\partial h}{\partial x}$ (dark).....	161
Figure 6.6 Balance between the imposed pressure gradient force and the drag forces (a) the modified SGD model with lamped pressure gradient force (b) original SGD model with uniform pressure gradient force	164
Figure 6.7 Time history of the calculated shear stress.....	164
Figure 6.8 Mean velocity in the longitudinal direction $u_m(z)$: a) normal scale, b) logarithmic scale and c) difference percentile.....	165
Figure 6.9 Mean velocity profile for the three generated surfaces using normal scale	166
Figure 6.10 Mean velocity profile for the three generated surfaces using logarithmic scale	167
Figure 6.11 Normalized shear stress τ_{xz}	167
Figure 6.12 longitudinal r.m.s fluctuations.....	169
Figure 6.13 Velocity time history at two different elevations and three different roughness conditions.....	170
Figure 6.14 PSD of the velocities at two different elevations and three different roughness conditions.....	170
Figure 7.1 Comparison between the vertical velocity profile of downbursts using IJ and CS methods.....	180
Figure 7.2 Computational domain and boundary conditions.....	184
Figure 7.3 Employed Grids.....	185
Figure 7.4 Illustration of the modified SGD model by Aboshosha et al. (2014).....	189
Figure 7.5 Roughness produced by using fractal surfaces for four different exposures.....	190
Figure 7.6 Spatial averaging of the instantaneous velocities	190

Figure 7.7 Spatial and temporal averaging of the instantaneous radial velocity at $R=1.25 D_j$ and $Z=0.05 D_j$	191
Figure 7.8 Maximum averaged radial and vertical velocity profiles obtained from Grid 1 (G1) and Grid 2 (G2).....	192
Figure 7.9 Evolution of the (a) normalized vorticity and (b) radial velocity for the open terrain condition with the time: (1) $T_n=8$, (2) $T_n=10$, (3) $T_n=12$, (4) $T_n=14$, (5) $T_n=16$; Where $T_n=T.D_j/V_j$	194
Figure 7.10 Radial averaged velocity at $R/D_j=0.5, 1.0, 1.5$ and 2.0 at $T_n=7.9, 8.8, 9.5$ and 12.8 ; Where $T_n=T.D_j/V_j$	195
Figure 7.11 Radial velocity profile comparisons for the open exposure	196
Figure 7.12 Instantaneous and envelope peak radial velocity	197
Figure 7.13 Maximum mean radial velocity $/V_j$	198
Figure 7.14 Turbulent intensity I_{ur} measured at the time instance of the maximum mean radial velocity.....	198
Figure 7.15 Procedure of obtaining the length scales from the fluctuating velocities (a) fluctuating radial velocities (b) fitting the circumferential correlation function $R(dz)$ (c) fitting the vertical correlation function $R(\Theta)$ and (d) averaging the autocorrelation function	201
Figure 7.16 Circumferential length scale of turbulence L_θ	202
Figure 7.17 Vertical length scales of turbulence L_w	203
Figure 7.18 Radial turbulence length scale L_r	203
Figure 7.19 Turbulent spectra	205
Figure 7.20 Peak factor g_v	206
Figure 7.21 Fitting the root coherence function.....	207

Figure 7.22 Coherency decay constant in the vertical direction C_w	209
Figure 7.23 Coherency decay constant in the circumferential direction C_θ	209
Figure 7.24 Velocity time history at point p for downburst case no. 1 (Dbx, $L_x=300$, $V_{refp}=40$ m/s)	211
Figure 7.25 Mean, background and resonant contributions to the peak response - open terrain ($z_0=0.03$ m)	213
Figure 7.26 Mean, background and resonant contribution to the peak response- country side terrain ($z_0=0.1$ m).....	213
Figure 7.27 Mean, background and resonant contribution to the peak response- suburban terrain ($z_0=0.3$ m).....	214
Figure 7.28 Mean, background and resonant contribution to the peak response - urban terrain ($z_0=0.7$ m)	214
Figure 7.29 Peak response normalized by $g_{py} \cdot L_x$ for the different terrain exposures	215

List of Appendices

Appendix A: Parameters of the Numerical Technique Used to Analyze TL Conductors under HIW.....	238
Appendix B: Parameters of the Numerical Technique Used to Analyze TL Conductors under Downburst Wind.....	240
Appendix C: Figures for the reaction time responses	242
Appendix D: Results of the Dynamic Analyses under Various Terrain Exposures	248

List of Symbols

Symbol	Units	Description
a	--	Scaling factor for the randomly generated fractal surfaces
A	m^2	Conductor cross section area
a_i	--	Polynomial constant for span i.
b_i	--	Polynomial constant for span i.
c_i	--	Polynomial constant for span i.
C_d	--	Drag coefficient of the conductor
C_s	--	Smagorinsky constant
$\overline{C_d}, \widetilde{C_d}$	--	Mean and r.m.s. drag coefficient
$[C(t)]$	N/(m/s)	Time dependent damping matrix
$[C_{ai}]$	N/(m/s)	Damping matrix for node i
$c_{ai}(t)$	N/(m/s)	Damping coefficient at node i
$Cont_M$	--	Contribution of the mean component to the peak response
$Cont_{BG}$	--	Contribution of the background component to the peak response
$Cont_R$	--	Contribution of the resonant component to the peak response
C_d^*	--	Drag coefficient used in the modified SGD model
C_{z_p}	--	Drag coefficient at the level of z_p
CFL	--	Courant Fredric Levy number

Symbol	Units	Description
C_w, C_θ	--	Coherency decay constants in vertical and circumferential directions
D	m	facing area per unit length
Db_x	--	Downburst case for the maximum longitudinal reaction R_x ($D=2.0 L_x$, $R=1.60 D_j$ and $\Theta=30^\circ$)
Db_y	--	Downburst case for the maximum transverse reaction R_y ($D=2.0 L_x$, $R=1.20 D_j$ and $\Theta=0^\circ$)
d_{xN}, d_{yN}, d_{zN}	m	displacement of the conductor at node N in the longitudinal, transverse, and vertical directions, respectively
$\{d_x\}_{Nd \times 1}^{i+1}$	m	Vector of longitudinal displacement obtained at iteration i+1
D_j	m	Jet diameter of the downburst
d	m	displacement height used to shift the logarithmic flow region above the canopy
$d\theta$	rad	magnitude of the angular separations
dz	m	magnitude of the vertical separations
E	N/m^2	Modulus of elasticity
Err_{av}	--	Average error
$F_w(t)$	N	Fluctuating wind force
$\{F_w(t)\}$	N	Load vector of the fluctuating forces
F_{mi}	N	drag force applied on the segment due to the incoming mean wind velocity

Symbol	Units	Description
$F_{idair}(t)$	N	Aerodynamic damping force
$\{F_w(t)\}$	N	Fluctuating load vector due to the wind load
f_{cut}	hz	Cut off frequency
f_{shedd}	hz	Shedding frequency of the vortices formed by Helmholtz instability
f_s	hz	Sampling frequency
f_{ij}	N	Drag force in the i -direction at layer no. j
FAI	--	Frontal area index
f_y	--	Load shape factor that accounts for downburst sizes and locations
f_N	hz	Frequency of mode no N
f	hz	modal frequency
$\{f_x\}_{Ndx1}$	m	Unbalanced load vector in the longitudinal direction
$f_{yb}, f_{LL}, f_L, f_R,$ f_{RR}	--	Factors accounting for downburst sizes and locations
$G1$ and $G2$	--	Subscripts G1 and G2 reffers to grids G1 and G2, respectively
g_v	--	Peak velocity factor
GF_{QS}	--	Gust facto calculated using the peak response obtained from the quasi-static analysis
GF	--	Gust facto calculated using the peak response obtained from the dynamic analysis
GFF	--	Gust Front Factor

Symbol	Units	Description
g_{0y}	N/m	Load intensity at node 0
$g_{Py_{max}}$	N/m	Maximum intensity of the transverse load at point p
g_{Py}	N/m	Intensity of the transverse load at point p
g_y, g_z	N/m	Transverse and vertical load acting on the conductor
$g_{yi}(s, t)$	N/m	Transverse load acting on span i at a spatial location s and time t
$h_{scaled}(r, \theta)$	m	Heights of the scaled fractal surfaces generated using polar coordinates
$h(r, \Theta)$	m	Heights of the fractal surfaces generated using polar coordinates
H_{pG}	m	height of the layer where the pressure gradient is lumped, and it is taken as 20% of the domain height H.
$h_{scaled}(x, y)$	m	Heights of a scaled fractal surface
H_d	m	Height of the region where the drag forces are introduced, which is taken in the current study in the order of 60 times the aerodynamic roughness of the surface z_0
$h(x, y)$	m	height of the topography at x, y location
I	--	Turbulent intensity
I_{ur}	--	Turbulent intensity of the radial velocities
i_R	()	Influence line of the response
i_{Ry1}	N	Influence line of the transverse reaction of the single-spanned system
i_{Ry6}	N	Influence line of the transverse reaction of the six-spanned system

Symbol	Units	Description
I_0	()	modified Bessel function of first kind
$K_1(t)$	N/m	modal stiffness for the first mode
$[k_{eG}]$	N/m	Element stiffness matrix in the global coordinates
$[K(t)]$	N/m	Time dependent stiffness matrix obtained using the conductor tension force and the location resulting from the quasi-static analysis under the mean loads
k_s	m	Ground roughness
K_{insi}	N/m	Longitudinal stiffness of the insulator located at point i
$[K_x]_{Nd \times Nd}^i$	N/m	Tangential stiffness matrix in the longitudinal direction at iteration i
k	m	Wave length
l_x, l_y	m	Average wave length in the x and y-directions
l_{xy}	m	Resultant average wave length
\tilde{k}_y	--	Gaussian random numbers with zero mean and 0.5 standard deviation
\tilde{k}_θ	--	Gaussian random numbers with zero mean and 0.5 standard deviation
k_0	()	modified Bessel function of second kind
$[k_{e1}]$	N/m	Element stiffness matrix in the local coordinates 1, 2 and 3
$[K]_{Nd \times Nd}, [K_{yz}]$	N/m	Equivalent stiffness matrix to account for the effect of the end displacement on the reactions
L_0	m	Conductor length before the application wind loading under its own weight, which can be calculated as $L_0 = L_x \cdot (1 + 8/3 \cdot (S/L_x)^2)$

Symbol	Units	Description
L_{θ}	m	Circumferential length scale of turbulence
L_w	m	Vertical length scales of turbulence
L_r	m	Radial length scales of turbulence
L_e	m	Element length
L_u	m	Longitudinal length scale of turbulence
L_{uv}	m	Transverse turbulent length scale of the longitudinal velocities
L_{seg}	m	Length of a conductor segment
L_F	M	Length scale which relates the 1 st out of plane conductor natural frequency to the wind velocity at the origin, $V_{ns0}(t)$
L_{zn}	m	The vertical projection of the insulator after the deformation = $v + d_{zn}$, where d_{zn} is the displacement in the Z direction, which is usually negative
L_x	m	Conductor span length
$[M_i]$,	kg	Mass matrix for node i
M_1	kg	modal mass for the first mode
m^*	kg	modal mass of the system
N_d	--	Number of conductor-insulator connecting points = number of spans+1
M_{zgyA}	N.m	Moment induced by the transverse external load g_y around z at end A
M_{ygzA}	N.m	Moment induced by the vertical external load g_z around y at end A

Symbol	Units	Description
M_{zgyB}	N.m	Moment induced by the transverse external load g_y around z at end B
M_{ygzB}	N.m	Moment induced by the vertical external load g_z around y at end B
$[M]$	kg	Mass matrix
\hat{n}_k	--	Unit vector of the velocity direction
P	N/m ²	pressure
$Q_y(s)^*$	N	First order shearing force in the transverse direction
$Q_z(s)^*$	N	First order shearing force in the vertical direction
R_{y3}, R_{x3}	N	Transverse and longitudinal reactions at tower no. 3, respectively
R_{3xmax}	N	Maximum longitudinal reaction at tower no. 3 (the tower of interest)
R_{xSol}, R_{ySol}	N	Longitudinal and transverse reactions resulting from the closed form solution
R_{xFEA}, R_{yFEA}	N	Longitudinal and transverse reactions resulting from the finite element analysis
R_{y1}^*, R_{x1}^*	N	Maximum mean transverse and longitudinal reactions for the single-spanned system, respectively
R_{y6}^*, R_{x6}^*	N	Maximum mean transverse and longitudinal reactions for the six-spanned, respectively
R_{y1}, R_{x1}	N	Transverse and longitudinal reactions for the single-spanned system, respectively
R_{y6}, R_{x6}	N	Transverse and longitudinal reactions for the six-spanned, respectively

Symbol	Units	Description
r_p	()	Peak response
\bar{r}_{\max}	()	Maximum mean response for the downburst winds or mean response for the synoptic winds
R_{y1p}, R_{x1p}	N	Peak transverse and longitudinal reactions for the single-spanned system, respectively
R_{y6p}, R_{x6p}	N	Peak transverse and longitudinal reactions for the six-spanned system, respectively
$R(xx)$	()	Ramp function $R(xx)=(xx/2+ xx /2)$
$R(dz)$	--	Vertical spatial correlation
$R(\Theta)$	--	Circumferential spatial correlation
$R(\tau)$	sec	Autocorrelation function
\hat{R}, \bar{R}	()	Peak and mean responses, respectively
$[R]$	--	Directional cosine matrix
R	m	Radius from the downburst centre
R_{resN}	N	Resultant force at node N, $R_{resN} = \sqrt{R_{xN}^2 + R_{yN}^2 + R_{zN}^2}$
R_{xN}, R_{yN}, R_{zN}	N	Reactions of the conductor at node N in the longitudinal, transverse, and vertical directions, respectively
$(R_x)_{n+1}$	N	Longitudinal reaction of conductor span no. n+1
$(RAy)_{n+1}$	N	Transverse reaction of conductor span no. n+1 at the end A
$(RAz)_{n+1}$	N	Vertical reaction of conductor span no. n+1 at the end A

Symbol	Units	Description
$(RBy)_{n+1}$	N	Transverse reaction of conductor span no. n+1 at the end B
$(RBz)_{n+1}$	N	Vertical reaction of conductor span no. n+1 at the end B
$\{R_y\}_{Ndx1}$	N	Vector of the transverse reactions
$\{R_z\}_{Ndx1}$	N	Vector of the transverse reactions
$\{R_y^F\}_{Ndx1}$		Vectors of transverse reactions considering no end displacements
$\{R_z^F\}_{Ndx1}$		Vectors of vertical reactions considering no end displacements
R_{x0}	N	Conductor longitudinal reaction under its own weight $R_{x0} = W.L_x^2 / (8S)$
S	m	Conductor sag
s	--	Local axis in the longitudinal direction. It equals to 0 and 1 at the start and end of each span, respectively
$S_u(f)$	$m^2/s^2 / (hz)$	Spectra of the radial velocity
S_y	--	Synoptic winds
$S_{uu}(f)$	$M^2/s^2 / (hz)$	Spectra of the longitudinal fluctuations
$S(k)$	$m^2/(m)$	spectra of the roughness
S_{ij}	N/m^2	strain rate tensor
$[T_e]$	--	Transformation matrix
τ_{turb}	sec	Time scale of turbulence

Symbol	Units	Description
$T_{0-cross}$	sec	Time corresponding to the first zero crossing of the autocorrelation function
T	sec	Averaging time which is equal to $1/f_{cut}$.
T_n	--	Non dimensional time where $T_n = \text{Time} \cdot V_j / D_j$
T_{LO}	N	Tension in the left span to the tower of interest considering zero end displacements
T_{RO}	N	Tension in the right span to the tower of interest considering zero end displacements
T_{LLO}	N	Tension in the far left span to the tower of interest considering zero end displacements
T_{RRO}	N	Tension in the far right span to the tower of interest considering zero end displacements
T_{LL}	N	Tension developed in the far left conductor span to the tower of interest
T_L	N	Tension developed in the left conductor span to the tower of interest
T_R	N	Tension developed in the right conductor span to the tower of interest
T_{RR}	N	Tension developed in the far right conductor span to the tower of interest
T_i	N	Tension developed in conductor span i
U_r	m/s	Radial velocity

Symbol	Units	Description
U_{rpeak}	m/s	Peak radial velocity
U_{rmax}	m/s	Maximum radial velocity obtained using grid G1
U_{wmax}	m/s	Maximum vertical velocity obtained using grid G1
\tilde{u}_i	m/s	resolved velocity at the reference height in the direction i
U_m	m/s	Mean velocity
$U^{m\Delta}$	m/s	magnitude of the velocity at the reference height filtered using filtering width $m.\Delta$
U_n	m/s	Velocity at the upper layer (no. n)
u_i	m/s	fluid velocity in the i direction
u_{gi}	m/s	grid velocity in the i direction
u_*	m/s	friction velocity
$u_m(z)$	m/s	Mean velocity at z elevation
$u_{mG1}(z)$	m/s	Mean velocity obtained using grid G1
$u_{mG2}(z)$	m/s	Mean velocity obtained using grid G2
$\bar{u}_{Log}(z),$	m/s	Logarithmic mean velocity profile
$\bar{u}_{CFD}(z)$	m/s	Mean velocity profile obtained from the CFD
v	m	Insulator length
V_{mi}	m/s	incoming mean velocity

Symbol	Units	Description
V_{ref}	(m/s)	Reference velocity taken as the maximum "running mean" velocity at point p
y_p	m	Distance to the conductor from the first grid
V_p	m/s	Velocity at the first grid point
$V_{ns}(n, t)$	m/s	Non stationary mean component at a location n and time t
$v(n, t)$	m/s	Fluctuating component
$V_{ns0}(t)$	m/s	Non-stationary mean velocity at a reference point 0 at time t
V_c	m/s	Conductor speed
V_{pmax}	m/s	Maximum velocity at point p
V_j	m/s	Jet velocity
W	N/m	Conductor weight per unit length
X_0, X_{mean}	m	Displacement amplitude and the mean displacement, respectively
X	m	distance from the jet centre to the point of interest
z_p	m	Height of the reference velocity
z_0	m	Aerodynamic roughness
Z_p	m	Elevation of point p
$\langle \dots \rangle$	--	Horizontal plane averaging
β	--	Spectral slope
		Ratio between the conductor span length to the projected length

Symbol	Units	Description
δ_{ij}	--	represents Kronecker delta
Δ_z	m	Height of the first grid layer above the ground
Δ_{zn}	m	Height of the upper grid layer (no. n)
Δ	m	grid size
Δ_{xy} :	m	Grid length in x - and y -directions
φ_k	Rad.	phase angles
ϕ	--	Mode shape
$\phi_o, \phi_{ios}, \phi_{ias}$	--	Out of plane, in-plane symmetric and in-plane asymmetric mode shapes
ϕ_y	--	Mode shape in the transverse direction
φ_u	--	normalized mean velocities
Π	N/m ³	imposed pressure gradient to enforce the flow
ρ	kg/m ³	Air density (1.25 kg/m ³)
$\sigma_{ur max}$	m/s	R.m.s of the fluctuating velocity
θ_{ij}	rad	Angle between axes i and j
Θ	°	Angle from the tower of interest to the downburst centre
τ_{i3}	N/m ²	Shear stress in the direction of i acting on the horizontal direction
τ_{ij}	N/m ²	the SGS Reynolds stress

Symbol	Units	Description
$\tau_{13calc}, \tau_{13tar}$	N/m ²	Calculated and targeted shear stress in the
ν	m ² /s	molecular viscosity
ν	Hz	Rate of zero crossing
ν_e	m ² /s	eddy viscosity
ζ_{air}	--	Aerodynamic damping

To my beloved parents,
to my beloved wife, Maryam
to my dear kids, Malik and Yusuf
for patiently enduring and sharing these years of hard work

To my supervisor, Dr. A El Damatty
for his support, encouragement, kind funding, ethics and guidance during these years of study
period

To my supervisor, Dr. G. Bitsuamlak
for his support, encouragement, high moralities and the technical and personal guidance
during these years of hard work

Chapter 1

1 Introduction

1.1 Background

Transmission Lines (TLs) are considered one of the essential components of the urban infrastructure system. Their role is to transmit electricity from sources of production to the distribution system and then to consumers. Figure 1.1 shows a photo of a typical TL system. As shown in the figure, the main components of a typical TL are: the conductors that transmit the electricity, the tower that supports the conductors through insulators, and the ground wires that transmit undesired electrical charges to the ground in the case of lightning. The tower shown in Figure 1.1 is called "guyed tower" where the tower stability is provided by a number of guys connected to the tower and anchored to the ground, and by a pin support located at the tower base. Figure 1.2 shows another system where the tower is self-supported. The towers shown in Figure 1.1 and 1.2 are steel lattice structures that are commonly used in high voltage lines. Other tower systems include steel poles, and H-frame concrete or wood structures that are typically used with relatively low voltage lines. TLs need to resist the applied environmental loads including wind and ice loads. Among the different wind events that can lead to strong loads on TLs are downbursts and tornadoes. Downbursts and tornadoes are commonly referred to as the High Intensity Winds (HIW). Both are localized events that have different characteristics compared to other large scale events (hurricanes and cyclones). A downburst is a strong downdraft that induces an outburst of damaging winds near the ground as described by Fujita (1999). A tornado, on the other hand, is a short-lived localized set of surface vortex flows extending from the clouds to the earth and associated with strong uplift.

In the past decades, it became evident that HIW can have devastating effects on TLs. Dempsey and White (1996) reported that more than 80 % of weather-related failures of TLs around the world are due to HIW events. Li (2000) stated that in Australia downbursts lead to more than 90% of the weather-related failures.

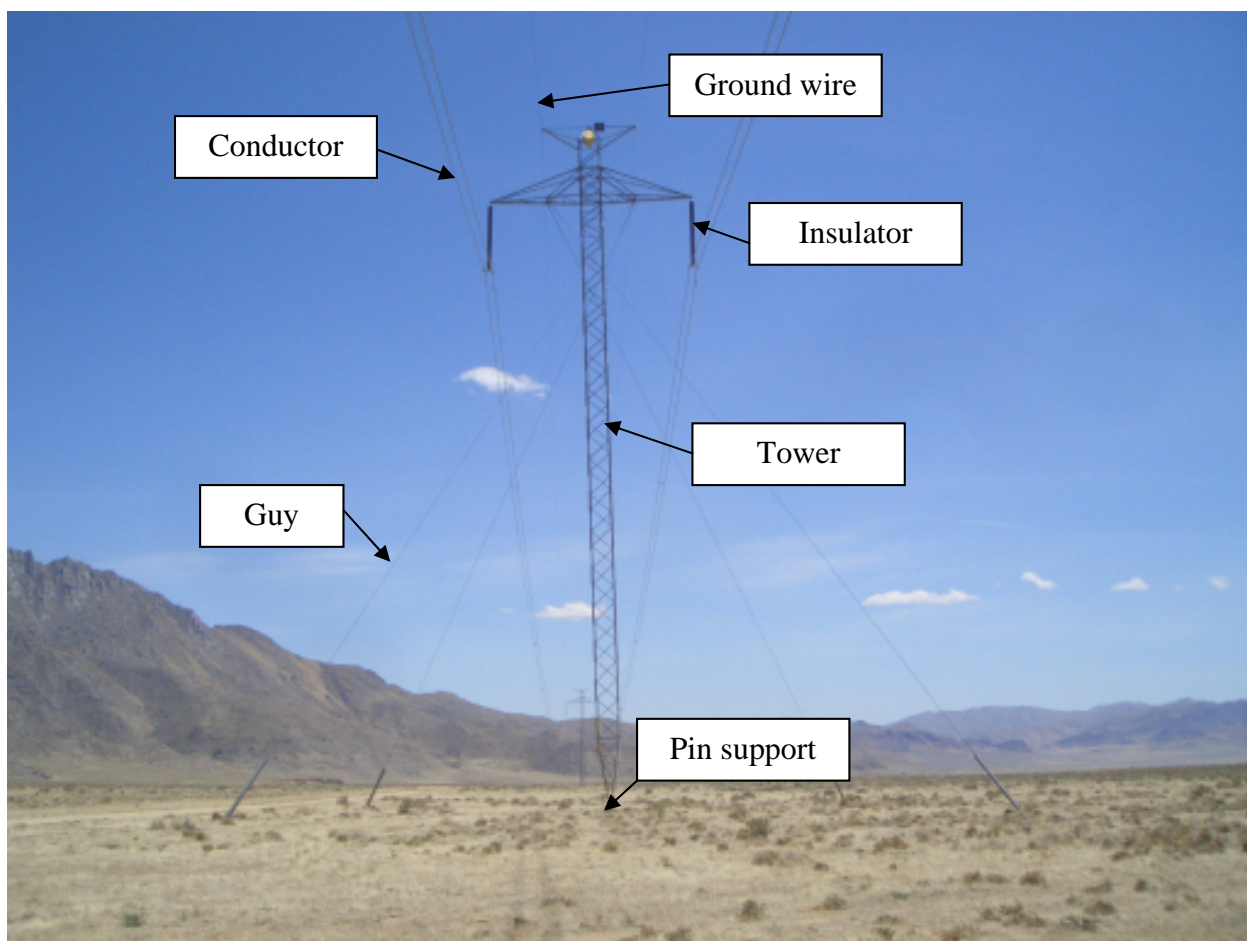


**Figure 1.1 Guyed transmission tower (Source: Wikipedia:
<http://operationcircuitbreaker.wordpress.com/chapter-4-transmission-line-vulnerabilities>)**

This thesis is part of an ongoing intensive research program that was initiated about a decade ago at Western University focusing on various aspects of this problem. The current study focuses on the behavior of conductors under downburst loading. This is an important topic due to a number of reasons:

1. Research conducted on this topic is limited, and there is insufficient information about the characteristics of downburst loads acting on the conductors as well as the conductors' response under these loads.
2. Conductors are the components that are most susceptible to the dynamic effects in a TL system.

3. Conductors are the most challenging components of a TL system in terms of their structural analysis because of their extreme flexibility.
4. Due to the localized nature of HIW events, loads acting on conductors can lead to completely different conductor behavior than that associated with large scale events.



**Figure 1.2 Self-supported transmission tower (Source: Wikipedia:
<http://operationcircuitbreaker.wordpress.com/chapter-4-transmission-line-vulnerabilities>)**

A literature review covering various aspects related to this research is provided in this introduction chapter. The review includes research previously conducted to characterize the downburst wind field in addition to the research conducted on the response of TLs under downbursts. Also, a general review of the previous research conducted on the structural modeling of the conductors as well as their dynamic response under wind loads is provided. The objectives and the thesis organization are then outlined in this chapter.

1.2 Downburst Wind Field

Downbursts are localized events that have a wind field significantly different than the fields associated with synoptic wind systems. According to Wilson et al. (1984), a typical downburst event may have a diameter in the range of 1000 to 6000 m. Hjelmfelt (1988) reported a range for downburst sizes between 1500 and 3000 m based on 11 downburst events. Downbursts can lead to very high velocities near the ground. Previous field studies, such as the Federal Aviation Administration Lincoln Laboratory Operational Weather Studies (FLOWS; Fujita, 1985), showed that the maximum downburst wind velocities occur at the first 50 m above the ground, as indicated by Fujita and Wakimoto (1981), Wilson et al. (1984), and Hjelmfelt (1988). Savory et al. (2001) indicated that the maximum recorded wind speed during downburst events is equal to 67 m/s which is within the range of velocities corresponding to F2 tornado defined by Fujita and Pearson (1973). Fujita (1990) and Boss (2010) indicated that the probability of structural damage due to downbursts is higher than tornadoes because of their high frequency of occurrence. Various studies were conducted to characterize the downburst wind field. In general, these studies can be classified into field studies, experimental studies, and numerical simulations using the Computational Fluid Dynamics (CFD) tools. Although field measurements can provide accurate information regarding the velocity field, it is a challenging task to conduct site measurements for downbursts due to the unpredictability of the event occurrence in terms of time and space. This motivated many researchers to study downbursts either experimentally (Osegura and Bowles 1988, Lundgren et al. 1992, Alahyari and Longmire 1994, Yao and Lundgren 1996, Wood et al. 2001 and Chay and Letchford 2002) or numerically (Kim and Hangan 2007, Sengupta and Sarkar 2008, Mason et al. 2009, Mason et al. 2010a,b). Most of experimental and numerical studies on downbursts are based on the impinging jet (IJ) model suggested by Fujita (1985) and the cooling source (CS) model developed by Anderson et al. (1992). The IJ model, as inferred from its name, is based on the analogy between a strong downdraft that touches the ground during downburst event and a jet that impinges to a wall. The CS model is based on simulating the density perturbation happening in the cloud base by the cooling process. This continuously increases the density of the air inside the cloud base until it becomes heavier than the adjacent air and falls down forming the downburst. This can be

modeled numerically using a negative energy source located in the computational domain at the level of the cloud base, and it can be modeled experimentally by releasing a fluid parcel in a slightly denser ambient fluid.

There are some advantages of numerical simulations over physical experiments. Numerical simulations allow for simulating the actual size of downbursts, and thus, avoiding potential scaling effects, which is not the case for physical experiments. Also, numerical simulations allow for generating detailed information of the flow field in both time and space compared with physical experiments. The following discussion focuses on the numerical studies of downbursts.

Kim and Hangan (2007) employed the IJ model to simulate a laboratory-scale downburst with a diameter of 0.038 m and a jet velocity of 7.5 m/s. They solved the Unsteady Reynolds Averaged Navier Stokes (URANS) equations to obtain the time-dependent mean downburst velocities. These time-dependent mean velocities are typically referred to as the "running mean" velocities. Kim and Hangan (2007) extracted the maximum "running mean" velocity profile and compared it with the profiles obtained from previous experiments conducted by Donaldson (1971) and Didden Ho (1985) as illustrated in Figure 1.3.

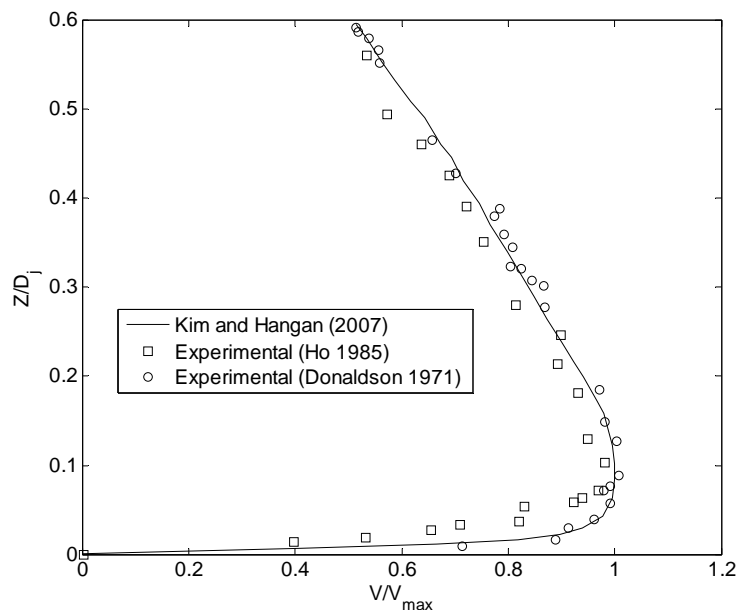


Figure 1.3 Comparison between vertical velocity profile for downbursts.

Reproduced from Kim and Hangan (2007)

Sengupta and Sarkar (2008) used the IJ model to simulate downbursts. They employed K-epsilon, K-omega, Shear Stress Transport (SST) and Large Eddy Simulation (LES) turbulence models, and compared the resulting profiles with those obtained from experiments. The comparison showed a very good agreement between the profile obtained from LES and the profile obtained from the tests. Studies conducted by Hadz'iabdic' (2005), Chay et al. (2006) and Gant (2009) also recommend using LES to simulate downburst wind fields.

Mason et al. (2009) employed the CS model to simulate downbursts in two-dimensional domain generated over various terrain roughness. Their study indicated that the increase in the ground roughness tends to decrease the maximum horizontal velocity and to increase the elevation where it happens. Later, Mason et al. (2010) studied the flow field of a translating downburst using a three-dimensional domain. For the two simulations mentioned above, the Shear Adaptive Simulation (SAS) method introduced by Menter and Egerov (2005) was utilized to account for turbulence while the neutral wall function was used to model terrain roughness. According to Teske and Lewellen (1977), the usage of neutral wall function in modeling terrain roughness is acceptable when the grid employed in discretizing the domain has a small height for the first layer above the ground. Mason et al. (2009, 2010) used a 1.0 m high first grid layer, which justifies the employment of the neutral wall function. However, the usage of that 1.0 m high layer shades doubt on their results for terrain aerodynamic roughness, z_0 , greater than 0.016 m, which include typical terrain exposures encountered by TLs (ESDU 2001). That is because of the following reasons; according to Richards and Hoxey (1993), Franke et al. (2004), Fluent Inc. (2005), Ansys Ltd., (2005), and Blocken et al. (2007), the height of the first grid layer, Δ_z , limits the ground roughness, k_s , and the aerodynamic roughness, z_0 , as $k_s \sim 30 z_0$, that can be modeled. Maximum roughness that can be modeled cannot exceed the mid height of the first grid layer, $(k_s \text{ or } 30 z_0) \leq 0.5 \Delta_z$. This leads to a 0.016 m maximum allowable aerodynamic roughness z_0 in the simulations conducted by Masons et al. (2009 and 2010).

Masons et al. (2009) compared the downburst profiles obtained using CS model with those using IJ model. The comparison revealed that the profiles obtained using CS model

are narrower and have a lower elevation for the maximum horizontal velocities than the profiles obtained from IJ method. This could be a result of employing a ramp function to enforce the flow in the simulations conducted using the CS model, compared with an instantaneous enforcing in the simulations conducted using the IJ model.

Vermeire et al. (2011a) simulated downbursts occurring over various terrains, with z_0 equals to 0.001-0.1 m, using the CS model and employing LES to resolve for turbulence. Similar to Mason et al. (2009), they utilized the neutral wall function using a 1.0 m high first grid layer which shades doubt on their findings for terrain roughness z_0 greater than 0.016 m. Later, Vermeire et al. (2011b) used the CS model to study the interaction between multiple downburst events and reported a 55% increase in the velocity magnitude compared to that of a single event.

All of the above simulations provide good insights on downburst wind field. However, none of these studies discussed the turbulent characteristics (such as turbulent intensities, length scales, spectra, and peak factors) of the flow near the ground. These characteristics are essential to quantify peak loads on structures including TLs and their responses as indicated by Chen and Letchford (2004a, b), Chay and Albermani (2005), Chay et al. (2006), Holmes et al. (2008) and Kwon and Kareem (2009). Holmes et al. (2008) analyzed the velocities of a downburst event recorded at the Wind Science and Engineering Research Center at Texas Tech University (Gast-Orwig and Schroeder 2005) and obtained the turbulent characteristics of the event. Unfortunately, these characteristics are for open terrain exposure only and limited to the locations where the velocities were measured. Detailed turbulent characteristics of downburst events happening over various terrain exposures typically encountered by TLs are still missing and this is one of the aspects covered in this thesis.

Obtaining the turbulent characteristics can be achieved using a high resolution LES with a careful modeling of terrain roughness. As mentioned earlier, terrain roughness was commonly modeled using wall functions which provide a constraint on the maximum roughness that can be modeled. This constraint has a significant effect especially when detailed flow characteristics close to the ground is needed. Methods such as terrain

following coordinates, immersed boundary methods (IBM) and canopy models do not have limitation on the roughness that can be modeled. However, they do not allow for modeling a terrain exposure with a prescribed aerodynamic roughness z_0 , which is needed for obtaining the turbulent characteristics of downbursts acting on different exposures. There is a need for a new method capable of modeling a prescribed aerodynamic roughness in LES without imposing a constraint on the roughness that can be modeled, and this is one of the topics covered in the thesis.

1.3 Studies on the Effect of Downbursts on TLs

Many studies have been conducted over the last two decades to investigate the effect of downbursts on TLs. Savory et al. (2001) studied the susceptibility of a transmission tower failure under downburst and tornado cases. They considered a downburst with 80 m/s maximum radial velocity and a tornado with a 90 m/s maximum tangential velocity. Their study predicted no potential failure under the downburst and predicted a failure to occur under the tornado. It should be mentioned that this conclusion is reached while neglecting the forces transmitted from the conductors to the tower.

Kanak et al. (2007) studied a downburst event that occurred in South-Western Slovakia in 2003 where at least 18 electric self-supported transmission line towers were destroyed. Seven of the fallen towers collapsed in a 1.2 km line, where the line was perpendicular to the trajectory of the thunderstorm. Observations of the failed towers showed that members in the middle third were damaged while others in the upper and lower zones remained straight. Kanak et al. (2007) attributed the failure to a localized high velocity that appeared at the location of the failed zone in the towers.

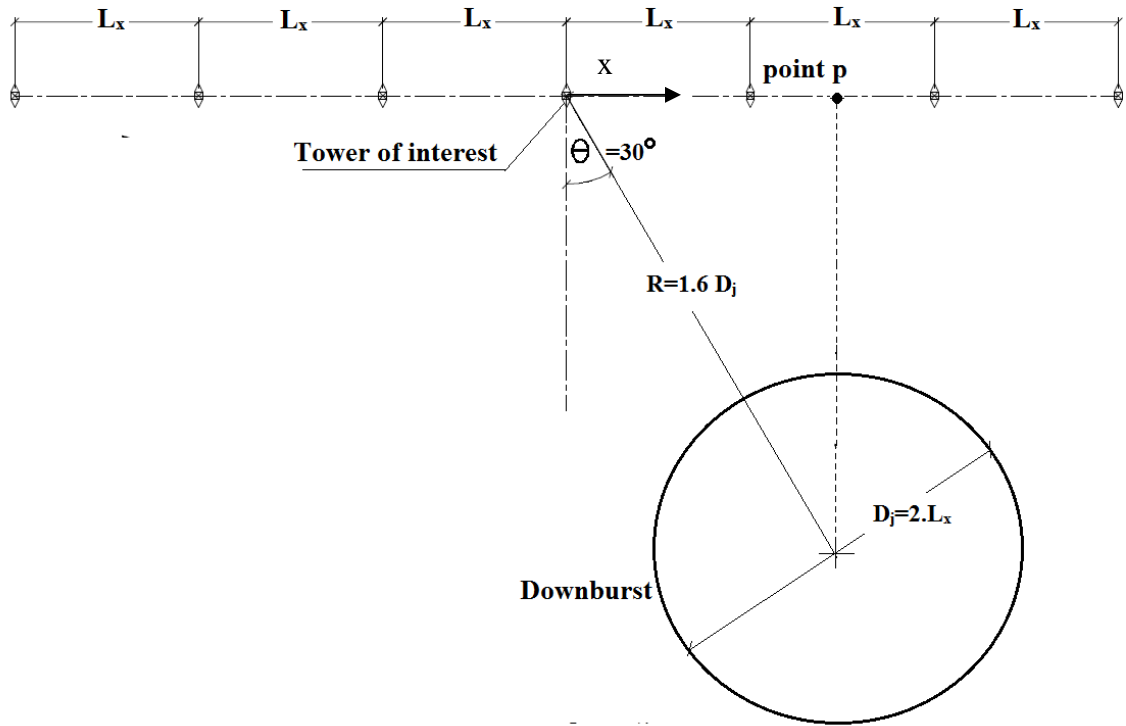
Shehata et al. (2005) emphasized the importance of including loads acting on the conductors. They developed a Finite Element Model to analyze the different components of the line under downburst wind. They carried out their study using a downburst wind field resulting from the CFD simulation conducted by Kim and Hangan (2007). Since the downburst wind field was simulated for a laboratory-scale using a CFD model (with a jet diameter of 0.038 m), Shehata et al. (2005) proposed a method to scale up the resulting laboratory-scale wind field. Shehata conducted a sensitivity analysis to assess the number

of spans that needs to be considered in order to accurately estimate the forces transferred from a conductor to the towers. The analysis showed that modeling six spans, three at each side of the tower, is enough to obtain accurate estimation of the transferred forces. Shehata and El Damatty (2007) studied the effect of different downburst configurations on the member forces of a guyed transmission tower using FEM developed in their earlier study. Since downbursts are localized events with a size comparable to the span of the line, Shehata and El Damatty (2007) conducted a parametric study by varying the event size, through changing the jet diameter, D_j , and its location relative to the tower of interest represented by the polar coordinates R and Θ . Their study indicated that maximum forces that develop in the tower members are caused by different combinations of the event jet diameter, D_j , and the its relative location to the tower (R and Θ).

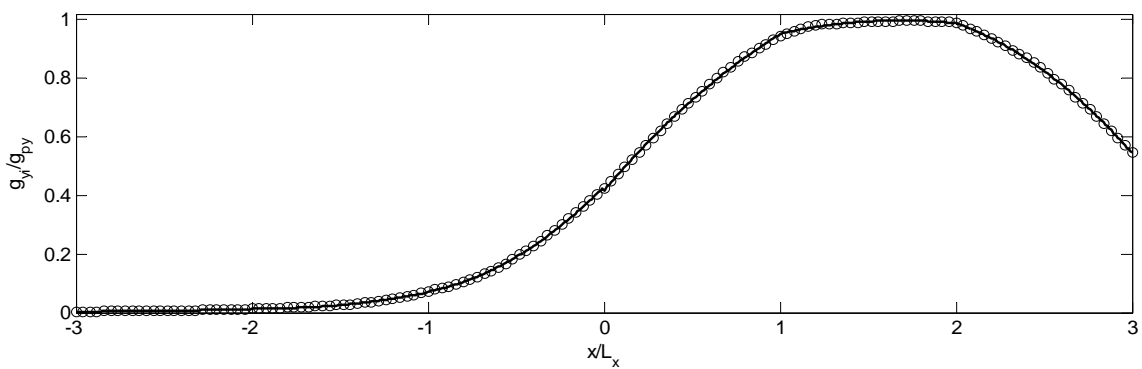
Later, Shehata and El Damatty (2008) performed a failure analysis on a tower that belongs to Mantioba Hydro Company, Canada which physically failed in 1996 during a downburst event. First, they conducted a parametric study to identify the critical downburst configurations, in terms of event size and location, leading to peak forces in the tower members. Then, they determined the loads corresponding to those critical downburst configurations. Those loads were applied incrementally in the finite element model until failure occurred. Their study indicated that the most critical failure mode happens when a downburst with a jet diameter, D_j , that is equal to twice the span length hits the ground at a radial distance of $1.6 D_j$ and an angle Θ of 30° measured from the tower of interest, as shown in Figure 1.4. The corresponding downburst loads on the conductor are also shown in the figure. The variation of loading between the spans adjacent to the tower led to a change in the tension force developing in different spans. This effect resulted in a net force acting on the tower cross arm in the longitudinal direction of the line. Darwish and El Damatty (2011) studied the behaviour of a self-supporting tower under downbursts and, similar to Shehata and El Damatty (2007), identified the critical downburst configurations for the tower.

All of the above mentioned studies employed the quasi-static Finite Element Method (FEM) to calculate the line response including the conductors. Complexities associated

with modeling of conductors using the FEM and the requirement to conduct dynamic analysis are discussed in the following subsections.



A) Downburst configuration



B) Load applied on the conductor normalized by the load at point p

Figure 1.4 Critical downburst case (Shehata and El Damatty 2008)

1.3.1 Modeling of Conductors

Analysis of TL conductors under downburst wind using finite element model is very challenging. That is because conductors are very flexible structural elements that behave highly non-linear, which makes their analysis very time consuming. In addition, evaluating the maximum downburst forces in the members of a transmission tower require a long parametric study covering different potential sizes and locations of the event. Those reasons emphasize the need for development of procedures that are efficient and accurate for the evaluation of the response of the conductors under downburst loading.

Irvine (1981) derived a closed-form solution for the reactions of a single-spanned conductor when the loading can be fitted with a third degree polynomial. Yu et al. (1995) derived a solution to calculate the reactions for a single-spanned conductor subjected to concentrated loads. These two solutions do not account for the flexibility of the insulators, which affect the values of the conductor reactions significantly (Darwish et al. 2010). The flexibility of the insulators can be accounted for using the concept of the "rolling span" developed by Winkelman (1959). However, this concept is based on neglecting the differences between the tension developing in the conductors' adjacent spans. Consequently, it cannot predict the longitudinal reactions transmitted from the conductor to the supporting towers, which can be significant (Shehata and El Damatty 2008). Based on the analytical solution of elastic catenary, Ahmadi-Kashani and Bell (1988) and Wie et al. (1999) developed cable elements able to simulate an entire span. Although those elements have the advantage of reducing the computational time as a result of reducing the number of degrees of freedom, they are applicable only under uniform loading, which is not the case for downburst wind.

1.3.2 Dynamic Analysis of TL Conductors

Most of the previous attempts to analyze the behaviour and/or study the failure of transmission lines under downburst (Shehata and El Damatty 2007, Darwish and El Damatty 2011, Savory et al. 2001, Shehata et al. 2005) were performed using quasi-static analysis, i.e. assuming no dynamic effects between the line components and the wind.

Although this assumption is justifiable for the towers because of their high fundamental frequencies (Holmes 2008), it might not be always valid for the conductors. Conductors are typically more vulnerable to be dynamically excited because their natural frequencies are more closer to the frequencies of the turbulent wind. Although the aerodynamic damping of the conductors can attenuate a large portion of their dynamic excitation, it might not be always enough for neglecting the dynamic effects. For example, Loredou-Souza and Davenport (1998) studied the response of a single spanned conductor system subjected to normal winds. Their study showed that, depending on the amount of aerodynamic damping, the resonant response can be as important as the background response. Researchers such as Battista et al. (2003) and Gani and Legeron (2010) also emphasized the importance of including the dynamic effects while evaluating TL responses under normal wind.

On the other hand, Darwish et al. (2010) showed a negligible dynamic effect on the conductor response due to downburst fluctuating loads. Two reasons might be behind this conclusion. The first reason is that in their study the turbulent component of the downburst was extracted from a real event and was assumed to be fully correlated along the conductor spans. This assumption tends to magnify the background responses compared to the resonant responses. The second reason is related to the aerodynamic damping. Darwish et al. (2010) utilized the expression for aerodynamic damping provided by Davenport (1962), which is suitable for normal winds. This expression requires additional modification to account for the increase of the conductor's tensile force and the resulting increase in the conductor's natural frequencies when subjected to a downburst. Neglecting this effect exaggerates the aerodynamic damping and tends to attenuate the dynamic excitation. Lin et al. (2012) studied a single span conductor subjected to 57 simulated downbursts. Although most of their results were in the favor of neglecting the dynamic effects, some of their results had reverse findings and, therefore, the authors recommended the need for further research. The two above mentioned studies (Darwish et al. 2010, Lin et al. 2012) have focused on the dynamic response of TL under downburst wind while considering only an open terrain type of exposure. To the best of the author knowledge, no other studies are available in the literature that considered other types of terrain exposure.

Conducting dynamic analyses of TL conductor under downburst wind is more challenging than under normal wind. That is because, as mentioned earlier, downburst is a non-stationary event having mean velocities that are time-dependent. This leads to changing the mean forces applied on the conductors and consequently changing the conductor tension forces and frequencies. This is not the case under normal wind with a time independent mean velocities. Although, finite element non-linear dynamic analysis can be used to obtain the dynamic response of the conductors under fluctuating downburst wind, it is expected to be computationally very demanding.

Based on the above mentioned investigations, studying the dynamic excitation of TL conductors subjected to downbursts requires further research in order to: (1) develop an expression for the conductor aerodynamic damping that accounts for the changes in the conductor frequency under downburst wind. (2) develop a robust technique capable of analyzing TL conductors under downburst events taking into the account the change in their mean characteristics. (3) assess the dynamic effect of the conductors while accounting for different terrain exposures.

The above-mentioned three topics of research are covered in this thesis.

1.4 Objectives of the Study

This thesis focuses on the response of TL conductors under downburst wind. The objectives of the thesis can be summarized as follows:

1. Develop new efficient and yet accurate methods that can be used to predict the structural response of TL conductors under HIW loads.
2. Develop an expression for the evaluation of aerodynamic damping under time-varying downburst loading.
3. Assess the importance of performing dynamic analyses for TL conductors when subjected to downburst and synoptic wind corresponding to open terrain exposure.
4. Develop a new CFD LES model that accounts for different terrain exposures encountered by TLs.

5. Characterize downburst turbulence and assess the importance of performing dynamic analyses for TL conductors under downburst wind considering various terrain exposures encountered by TLs.

1.5 Organization of the Thesis

This thesis has been prepared using the “Integrated-Article” format. In Chapter 1, the present chapter, a review of the studies and approaches related to downburst wind field and transmission line response under downbursts is provided. This is followed by presenting the main objectives of the current study. These objectives are addressed in detail in the following six chapters.

Chapter 2: Effective Technique to Analyze Transmission Line Conductors under High Intensity Winds

In this chapter, an effective numerical technique to calculate the reactions of a multi-spanned transmission line conductor system, under arbitrary loads varying along the spans, is developed. These variable loads are generated by High Intensity Wind (HIW) events in the form of tornadoes and downbursts. The chapter starts by showing a derivation of a semi-closed form solution to obtain the displacements and the reactions at the ends of each conductor span. This solution accounts for the nonlinearity of the system and the flexibility of the insulators. The solution leads to a set of nonlinear simultaneous equations, which need to be solved numerically to obtain the conductor response. A numerical scheme is suggested and employed to solve the equation set resulting from the technique. The technique is employed to analyze two conductor systems under loads resulting from HIW events. The two conductors are reanalyzed using Non-linear Finite Element Analyses (FEA) to assess the accuracy of the proposed technique.

Chapter 3: Closed Form Solution for the Reactions of a Transmission Line Conductor under Downburst Winds

In this chapter, a closed form solution, suitable for structural practitioner engineers, to calculate the reactions of a transmission line conductor subjected to downbursts loads is derived. A simplified multi-spanned conductor-insulator is considered in the derivation.

The considered system allows for the interaction between the spans without the need of solving coupled non-linear equations. The solution is derived to cover downbursts with arbitrary parameters, including different downburst sizes and relative locations to the tower of interest. A set of critical downburst cases that was previously recommended for the design of the line has been also considered. The accuracy of the derived closed-form solution is assessed and confirmed under both downburst with arbitrary size and location, and downburst corresponding to the critical cases. The assessment is carried out by comparing the conductor reactions obtained using the proposed closed-form solution with those predicted by FEM.

Chapter 4 Aerodynamic Damping of Transmission Line Conductors under Downburst Winds

This chapter proposes a new analytical expression for the conductor aerodynamic damping under downburst wind. The developed expression accounts for the localized effect of downbursts which is characterized by the event size and its relative location to the conductor. In order to assess the accuracy of this analytical expression, a CFD technique, that considers the Fluid Structure Interaction (FSI) between the conductor and the wind load is developed. This CFD technique is utilized to predict the conductor response under downburst wind which is then compared with the response obtained from dynamic analysis using damping calculated by the developed analytical expression.

Chapter 5 Assessment of Dynamic Effect for Transmission Line Conductors under Downburst and Synoptic Winds

In this chapter, the dynamic response of single and multiple spanned transmission line conductor systems subjected to fluctuating downburst and synoptic winds is studied considering different wind velocities and different length spans. Two critical downburst configurations, recommended in the literature and expected to cause the maximum conductor reactions, are considered in the analyses. The considered downburst wind field is generated by adding the running mean velocity component obtained from the CFD simulation conducted by Kim and Hanagan (2007) to the turbulent component. The turbulent component is generated numerically using the technique described by Chen and

Letchford (2004a) and Chay *et al.* (2006) while properly modeling the turbulent intensity and the spectra. The objective of this chapter is to assess the importance of including the dynamic effect when predicting the conductor's reactions on the towers. This is achieved by calculating the mean, the background, and the resonant reaction components using the following steps: (i) Conduct a non-linear static analysis of the conductor systems to obtain the conductor's tension forces and displacements under the mean wind velocities. These tension forces and displacements are used to calculate the stiffness of the conductor to be used in the dynamic analysis. (ii) Conduct a linear dynamic analysis under the wind turbulence to calculate the peak dynamic responses including resonant and background components using stiffness obtained in step (i). (iii) Conduct a linear quasi-static analysis under the wind turbulence to calculate the background component of the responses. The contribution of each component to the peak responses is calculated. Importance of the dynamic effect is assessed by investigating the contribution values of the resonant component to the peak responses.

Chapter 6 LES of Wind Flow over Various Upwind Exposures

In the previous chapters, analysis of the TL is conducted using the downburst wind field conducted by Kim and Hangan (2007), which is based on the Reynolds Averaged Navier-Stokes (RANS) equations. This allows for obtaining the mean component of downburst wind field but not for the turbulent component. Large Eddy Simulation (LES) can be considered as the most commonly used practical approach which provides the turbulent component of a wind field. In the case of downburst, turbulent wind field especially near the ground, is strongly affected by the ground roughness. The existing models for considering the roughness effect in LES have a practical limitation on the maximum roughness that can be simulated as a function of the grid size. This is found to be very influential for the case of moderately rough to rough surfaces, and alters the accuracy of the LES for those surfaces and alters the feasibility of obtaining the turbulent characteristics of downburst above these surfaces. Therefore, in this chapter, a new model of simulating terrain roughness which is based on the usage of fractal surfaces is developed. The model allows for conducting LES of rough terrains with a prescribed aerodynamic roughness. To successfully develop this model, a previous model called the

surface gradient drag-based (SGD) model (Anderson and Meneveau 2010) is first modified. The modification involves assigning drag forces from the ground surface into multiple layers. This modification allows for simulating rougher terrains. In the LES, terrain roughness is described through the usage of randomly generated fractal surfaces. Typically, previous knowledge of the aerodynamic roughness, z_0 , of a fractal surface is not feasible before conducting the simulation, which alters the main goal of the study represented in modeling rough terrains with prescribed roughness. Therefore, a new technique is developed to scale the generated fractal surfaces in order to have aerodynamic roughness as prescribed. Three different fractal surfaces representing countryside, suburban, and urban terrains, are generated and modeled using LES.

Chapter 7 Turbulent Downburst Wind Field and Corresponding Dynamic Behavior of Transmission Line Conductors

The roughness model developed in Chapter 6 is employed in this chapter to characterize the turbulence associated with downbursts. Four different terrain conditions are considered in the simulations. The flow field resulting from the simulations contains both mean and turbulent components. Therefore, the resulting field is averaged spatially and temporally to extract the mean component. Then by subtracting the mean component from the flow field, the turbulent component is evaluated.

The turbulent wind field is extensively analyzed to obtain the turbulence characteristics. Turbulent intensity, length scales, spectra, peak factors, and coherency decay coefficients are calculated at different radii from the downburst centre and at different elevations from the ground. These turbulent characteristics are very important to calculate the dynamic excitation of structures in general and TL conductor in particular. Dynamic analyses of the conductors considered previously in chapter (5) are conducted using the wind field resulting from the LESs.

Chapter 8 presents summary and conclusions of the entire thesis together with recommendations for further research work.

1.6 References

- Ahmadi-Kashani, K., Bell, A.J. 1988. The analysis of cables subject to uniformly distributed loads. *Engineering Structures*. 10(3), 174-184.
- Anderson W., Meneveau C., 2010. A Large-Eddy Simulation Model for Boundary-Layer Flow Over Surfaces with Horizontally Resolved but Vertically Unresolved Roughness Elements. *Boundary-Layer Meteorol* 137:397–415
- Anderson, J.R., Orf, L.G., Straka, J.M., 1992. A 3-D model system for simulating thunderstorm microburst outflows. *Meteorology and Atmospheric Physics* 49, 125–131.
- Ansys Ltd., 2005. Ansys CFX-solver, Release 10.0: Theory. Canonsburg.
- Alahyari, A., Longmire, E.K., 1994. Particle image velocimetry in a variable density flow: application to a dynamically evolving downburst. *Experiments in Fluids* 17, 434–440.
- Battista, R.C., Rodrigues, R.S. and Pfeil, M.S. 2003. Dynamic behavior and stability of transmission line tower under wind forces. *J. Wind Eng. Ind. Aerod.*, 91(8), 1051-1067.
- Blocken, B., Stathopoulos, T., and Carmeliet, J. 2007. CFD simulation of the atmospheric boundary layer: wall function problems, *Atmospheric Environment*, 41, 38-252.
- Boss. 2010. Downbursts, Tornadoes cause different damage, *Spokesman, Review*.
- Chay, M.T., Letchford, C.W. 2002. Pressure distributions on a cube in a simulated thunderstorm downburst - part a: stationary downburst observations. *Journal of Wind Engineering and Industrial Aerodynamics* 90, 711–732.
- Chay, M., and Albermani, F., 2005. Dynamic response of a SDOF system subjected to simulated downburst winds. *Proc., Asia-Pacific Conf. on Wind Engineering (APCWE-VI)*, 1562–1584.
- Chay, M., Albermani, F., and Wilson, R., 2006. Numerical and analytical simulation of downburst wind loads. *Eng. Struct.*, 28(2), 240–254.

- Chen, L., and Letchford, C. W. 2004a. A deterministic-stochastic hybrid model of downbursts and its impact on a cantilevered structure. *Eng. Struct.*, 26(5), 619–629.
- Chen, L., and Letchford, C. W., 2004b. Parametric study on the alongwind response of the CAARC building to downbursts in the time domain. *J. Wind. Eng. Ind. Aerodyn.*, 92(9), 703–724.
- Choi, E.C.C. and Hidayat, F.A., 2002. Dynamic response of structures to thunderstorm winds. *Prog. Struct. Eng. Mech.*, 4, 408-416.
- Darwish M., El Damatty A., and Hangan, H. 2010. Dynamic characteristics of transmission line conductors and behaviour under turbulent downburst loading", *Wind and Structures, An International Journal*, 13(4), 327-346.
- Darwish, M.M. and El Damatty, A.A. 2011. Behavior of self supported transmission line towers under stationary downburst loading", *Wind and Structures, An International Journal*, 14(5) 481-498.
- Davenport, A.G. 1962. Buffeting of a suspension bridge by storm winds", *J. ASCE Struct. Div.*, 88 (3), 233-264.
- Didden, N., Ho, C.M. 1985. Unsteady separation in a boundary layer produced by an impinging jet. *J. Fluid Mech.* 160, 235–256.
- Engineering Sciences Data Unit (ESDU) 85020. 2001. Characteristics of atmospheric turbulence near the ground. Part II: single point data for strong winds.
- Fluent Inc., 2005. *Fluent 6.2 User's Guide*, Fluent Inc., Lebanon.
- Franke, J., Hirsch, C., Jensen, A.G., Krüs, H.W., Schatzmann, M., Westbury, P.S., Miles, S.D., Wisse, J.A., Wright, N.G. 2004. Recommendations on the use of CFD in wind engineering. Proceedings of the International Conference on Urban Wind Engineering and Building Aerodynamics, in: van Beeck JPAJ (Ed.), COST Action C14, Impact of Wind and Storm on City Life Built Environment, von Karman Institute, Sint-Genesius-Rode, Belgium, 5 - 7 May 2004.
- Fujita TT, Pearson AD. 1973. Results of FPP classification of 1971 and 1972 tornadoes, 8th conference on severe local storms (abstracts only). *Bull Am Meteorol Soc* 54:609.

- Fujita, T.T., Wakimoto, R.M. 1981. Five scales of airflow associated with a series of downbursts on 16 July 1981. *Monthly Weather Review* 109, 1438–1456.
- Fujita, T.T., 1985. The downburst microburst and macroburst. University of Chicago, Department of Geophysical Sciences 128 pp
- Fujita, T.T. 1990. Downbursts: meteorological features and wind field characteristics", *Journal of Wind Engineering & Industrial Aerodynamics*, 36(1), 75-86.
- Gani, F. and Legeron, F. 2010. Dynamic response of transmission lines guyed towers under wind loading. *Can. J. Civ. Eng.*, 37(3), 450-465.
- Gant, S.E. 2009. Reliability issues of LES-related approaches in an industrial context. *Flow, Turbulence and Combustion* 84, 325–335.
- Hadz'iabdic', M. 2005. LES, RANS and Combined Simulation of Impinging Flows and Heat Transfer Ph.D Thesis. University of Sarajevo 185pp.
- Hjelmfelt, M.R. 1988. Structure and life cycle of microburst outflows observed in Colorado. *Journal of Applied Meteorology* 27, 900–927.
- Holmes, J.D. 1999, Modeling of extreme thunderstorm winds for wind loading and risk assessment, *Proceedings, of the 10th International Conference on Wind Engineering*, Copenhagen 1999, Balkema Press, Amsterdam, 1999, pp. 1409-1455.
- Holmes, J.D. 2008. Recent Developments in the Specification of wind loads on Transmission Lines. *Journal of Wind & Engineering*, Vol. 5, No. 1, Jan 2008, pp. 8-18
- Holmes, J., Hangan, H., Schroeder, J., Letchford, C., Orwig, K. 2008. A forensic study of the Lubbock-Reese downdraft of 2002. *Wind and Structures*, Vol. 11, 2, 137-152
- Irvine, H.M. 1981. *Cable Structures*, MIT Press, Cambridge.
- Kanak, J., Benko, M., Simon, A. and Sokol, A. 2007. Case study of the 9 May 2003 windstorm in southwestern Slovakia, *Atmos. Res.*, 83,162-175.
- Kim, J., Hangan, H. 2007. Numerical simulations of impinging jets with application to downbursts, *J. Wind Eng. Ind. Aerodyn.*, 95(4), 279-298.
- Kwon, D. and Kareem, A. 2009. Gust-Front Factor: New Framework for Wind Load Effects on Structures, *J. Struct. Eng.* 135(6), 717-732.

- Li, C.Q. 2000. A stochastic model of severe thunderstorms for transmission line design, *Probab. Eng. Mech.*, 15, 359-364.
- Lin, E.W., Orf, L.G., Savory, E., Novacco, C. 2007. Proposed large-scale modelling of the transient features of a downburst outflow. *Wind and Structures* 10, 315–346.
- Lin, W.E., Savory, E., McIntyre, R.P., Vandelaar, C.S., King, J.P.C. 2012. The response of an overhead electrical power transmission line to two types of wind forcing. *J. Wind Eng. Ind. Aerodyn.* 100 58–69
- Lundgren, T.S., Yao, J., Mansour, N.N., 1992. Microburst modelling and scaling. *Journal of Fluids Mechanics* 239, 461–488.
- Mason, M., Wood, G., Fletcher, D. 2009. Numerical simulation of downburst winds. *Journal of Wind Engineering and Industrial Aerodynamics* 97, 523–539.
- Mason, M., Fletcher, D., Wood, G. 2010a. Numerical simulation of idealised three-dimensional downburst wind fields. *Engineering Structures* 32, 3558–3570.
- Mason, M. Wood, G., Fletcher, D. 2010b. Numerical investigation of the influence of topography on simulated downburst wind fields. *J. Wind Eng. Ind. Aerodyn.* 98 (2010) 21–33
- Menter, F.R., Egorov, Y. 2005. A scale adaptive simulation model using two- equation models. In: 43rd AIAA Aerospace Sciences Meeting and Exhibit, American Institute of Aeronautics and Astronautics.
- McCarthy, P. and Melsness, M. 1996. Severe weather elements associated with September 5, 1996 hydro tower failures near Grosse Isle, Manitoba, Canada”, *Manitoba Environmental Service Centre, Environment Canada*, 21 pp.
- Osegura, R.M., Bowles, R.L. 1988. A simple, analytic 3-dimensional downburst model based on boundary layer stagnation flow. NASA Technical Memorandum, 100632 National Aeronautics and Space Administration.
- Richards, P.J., Hoxey, R.P. 1993. Appropriate boundary conditions for computational wind engineering models using the k- ϵ turbulence model. *Journal of Wind Engineering and Industrial Aerodynamics* 46&47, 145-153.
- Savory, E., Parke, G., Zeinoddini, M., Toy, N. and Disney, P. 2001. Modelling of tornado and microburst-induced wind loading and failure of a lattice transmission tower", *Eng. Struct.*, 23, 365-375.

- Selvam, R., Holmes, J.D. 1992. Numerical simulations of thunderstorm down-bursts. *Journal of Wind Engineering and Industrial Aerodynamics* 44, 2817–2825.
- Sengupta, A., Sarkar, P.P. 2008. Experimental measurement and numerical simulation of an impinging jet with application to thunderstorm microburst winds. *Journal of Wind Engineering and Industrial Aerodynamics* 96, 345–365.
- Shehata, A.Y., El Damatty, A.A. and Savory, E. 2005. Finite element modeling of transmission line under downburst wind loading", *Finite Elements Anal. Des.*, 42(1), 71-89.
- Shehata, A.Y. and El Damatty, A.A. 2007. Behaviour of guyed transmission line structures under downburst wind loading", *Wind and Structures, An International Journal*, 10(3) 249-268, 98.
- Shehata, A.Y. and El Damatty, A.A. 2008. Failure analysis of a transmission tower during a microburst", *Wind and Structures*, 11(3) 193-208.
- Sparling, B., Wegner, L. 2007. Estimating peak wind load effects in guyed masts", *Wind and Structures*, 10(4), 347-366.
- Teske, M.E., Lewellen, W.S. 1977. Turbulent transport model of a thunderstorm gust front. In: *Proceedings of the 10th Conference on Severe Local Storms*, American Meteorological Society, Omaha.
- Vermeire, B., Orf, L. Savory, E. 2011a. Improved modelling of downburst outflows for wind engineering applications using a cooling source approach. *J. Wind Eng. Ind. Aerodyn.* 99, 801–814
- Vickery, D., 1992. Assessment of microburst models for downdraft estimation." *J. Aircr.*, 29(6), 1043–1048.
- Wei, P., Bingnan, S., Jinchun T. 1999. A catenary element for the analysis of cable structures", *Applied Mathematics and Mechanics (English Edition)*, 20(5), 0253-4827
- Wilson, J.W., Roberts, R.D., Kessinger, C., McCarthy, J., 1984. Microburst wind structure and evaluation of Doppler radar for airport wind shear detection. *Journal of Climate and Applied Meteorology* 23, 898–915.
- Whittingham, H., 1964. *Extreme Wind Gust in Australia*. Bureau of Meteorology (Melbourne), Department of Science, Bulletin 46.

- Yao, J., Lundgren, T.S. 1996. Experimental investigation of microbursts. Experiments in Fluids 21, 17–25.
- Yu, P., Wong, P. and Kaempffer, F. 1995. Tension of conductor under concentrated loads", J. Appl. Mech. -Trans. ASME, 62(3), 802-809.

Chapter 2

2 Effective Technique to Analyze Transmission Line Conductors under High Intensity Winds

2.1 Introduction

Transmission lines are used to carry electricity from the source of production to the consumers. They consist of towers, conductors, insulators and ground wires. Conductors, which are responsible for transmitting the electricity, are supported by the towers using insulators. Ground wires, which are usually smaller than the conductors, transmit the electrical charges in the case of lightening to the ground. Because they are usually located in rural areas, a failure in transmission lines requires a long time to repair. Such failures may cause consumer long outage time, which can lead to substantial economical losses in addition to the repairing costs. By reviewing many cases of weather-related transmission line failures around the world, it is evident that most of the failures are results of High Intensity Winds (HIW) in the form of downburst or tornados. For example, Manitoba Hydro (1996) company, Canada, reported a failure of 19 transmission towers due to a downburst. Li (2000) reported that more than 90% of transmission line failures in Australia resulted from downburst events that are usually associated with thunderstorms. A downburst is a strong downdraft that induces an outburst of damaging winds near the ground as described by Fujita (1999). A tornado, by contrast, is a short-lived localized set of surface vortex flows extending from the clouds to the earth and associated with strong uplift.

Savory et al. (2001) studied the failure of a transmission tower under both downburst and tornado wind fields. By neglecting the forces acting on the conductors, failures were only predicted in the case of tornadoes, while no failure was shown to be associated with downbursts. The failure study performed by Shehata et al. (2008) predicted three different failure modes for the towers while being subjected to downbursts. Due to the localized nature of a downburst, wind forces acting on the conductor spans on either sides of a tower can be significantly different. This can lead to a variation in the longitudinal tensile forces acting on the two spans. The difference between those two forces can lead

to a large longitudinal load transmitted to the tower cross arms, causing out-of-plane bending in this region. The study conducted by Shehata et al. (2008) revealed that the most critical failure mode resulted from this longitudinal load transmitted from the conductors to the towers. The recent failure study performed by El Damatty and Aboshosha (2012) indicated a similar failure. Aboshosha and El Damatty (2013) conducted a parametric study to calculate the transmitted longitudinal and transverse loads from the conductor to the towers when conductors are subjected to different downbursts. The study showed that the longitudinal load can exceed 60% of the transverse load, and therefore, cannot be ignored. The above studies emphasize the importance of designing transmission towers to withstand the downburst loads acting on the conductors.

In previous studies aiming to describe the behaviour and/or the failure modes of transmission line structures under HIW, Finite Element Analysis (FEA) was utilized to calculate the conductor reactions. In the work done by Shehata and El Damatty (2007), conductors and ground wires were modeled using 2D-Non-linear Consistent Beam Element developed by Koziey and Mirza (1994). The analysis was performed in two directions separately: horizontally to obtain the response under the radial downburst velocities, and vertically to account for the vertical downburst velocities and the conductor's own weight. The two-dimensional element was acceptable for downbursts as their associated velocities in the horizontal direction are much higher than those in the vertical direction, and thus decoupling between the two directions can be justified. On the other hand, tornadoes have comparable velocities in all three directions. As such, Hamada and El Damatty (2011) used a three-dimensional non-linear Cable Element to model the conductors. Due to the conductors' high level of flexibility and significant nonlinear behaviour, their analysis using FEA is a time-consuming exercise. Due to the localized nature of HIW, the analysis of TL under such events needs to be repeated many times by considering different sizes and various locations for the events, as reported by Shehata and El Damatty, Hamada and El Damatty (2011) and Darwish et al. (2010). As such, it is important to develop a time-efficient technique to analyze multi-span conductors under both transverse and vertical loads that vary along the conductor spans.

Irvine (1981) derived a closed-form solution for the reactions of a single-spanned conductor when the loading can be fitted with a 3rd degree polynomial. Also, Yu et al. (1995) derived an exact solution to calculate the reactions for a single-spanned conductor subjected to high concentrated loads. The flexibility of the insulators was neglected in both solutions. As indicated by Darwish et al. (2010), the insulator flexibility is important in quantifying the amount of forces carried by the towers. Winkelman (1959) developed the concept of rolling span, which accounts for the insulator flexibility. However, it is based on neglecting the differences between the conductors' tensile forces in the adjacent spans, and therefore, no longitudinal reactions are transmitted from the conductors to the supporting towers. That is not true for the case of HIW which causes unbalanced loading on the conductor spans adjacent to a tower. Ahmadi-Kashani and Bell (1988) and Wie et al. (1999) developed cable elements able to simulate a whole span based on the analytical solution of elastic catenary. Such elements have the big advantage of reducing the degrees of freedom, and consequently, the computational time. However, such elements can be used for uniform wind loads only, which is not the case for HIW.

2.2 Formulation

In this study, the multi-spanned conductor system illustrated in Figure 2.1 is considered for analysis. The system has spans with length, L_x , and sag, S , under the conductor's own weight. Each span is supported by two insulators with a length, v . The insulators are assumed to be axially rigid. The system is subjected to loads in the transverse direction Y defined as $g_y(x)$ and in the vertical Z direction defined as $g_z(x)$. As a result, the conductor system will have displacements and reactions in the X , Y and Z directions. The analysis is performed by dividing the system in to a number of elements at the conductor-insulator connecting points, which are named, $N-1$, N and $N+1$, as shown in Figure 2.1. A cut on a typical conductor-insulator point ($\#N$), given by Figure 2.2, shows three unknown displacement components, dx_N , dy_N and dz_N and three unknown reaction components, R_{xN} , R_{yN} and R_{zN} , in x , y and z directions, respectively. At all the connections, six unknowns exist: three reaction components and three displacement components.

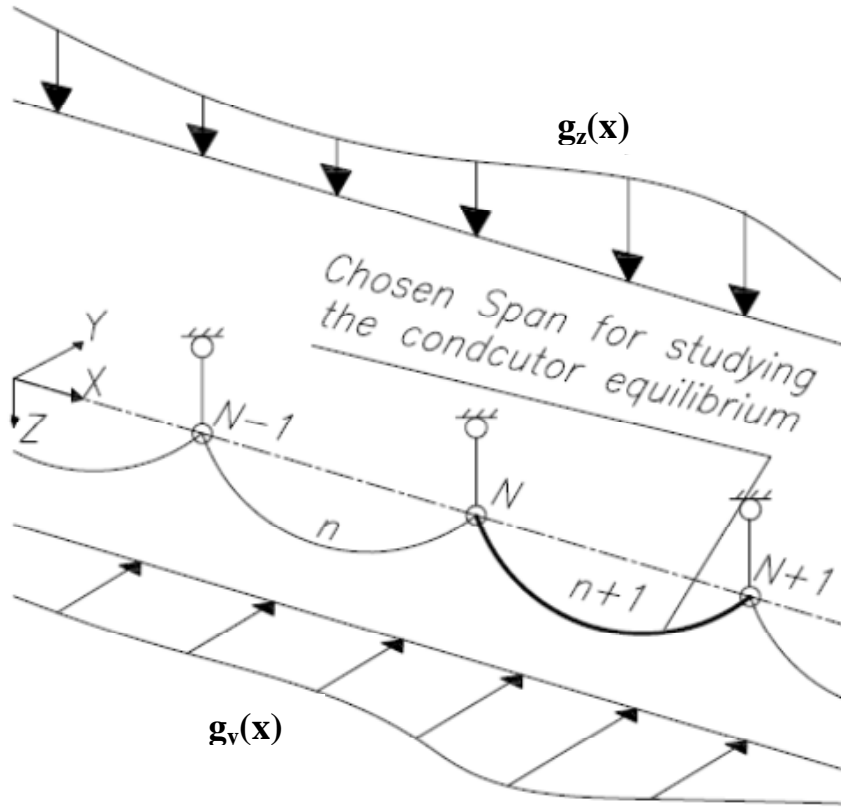


Figure 2.1 the system layout

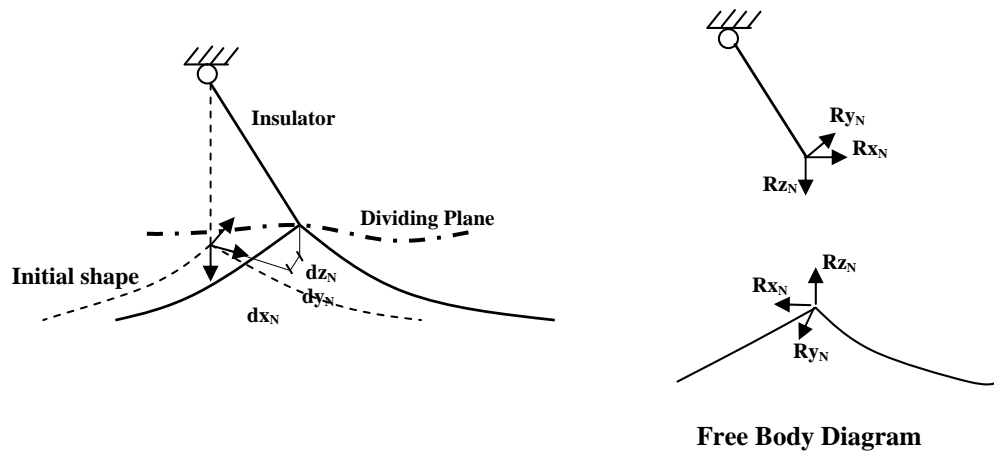


Figure 2.2 Equilibrium at point N

Therefore in order to solve for those unknowns, six equations are required at each connecting point. Three equations are derived by studying the moment equilibrium of the conductors and by equating the conductor length using two different approaches, as will be illustrated by subsections 2.1 and 2.2. The remaining three equations are derived by satisfying the equilibrium of the insulator as will be illustrated by subsection 2.2.3.

2.2.1 Conductor Transverse and Vertical Reactions (R_y and R_z)

Conductor equilibrium is utilized to obtain expressions for the reactions in Y and Z directions. Conductor span, $n+1$, which spans between the connecting points, N and $N+1$, and illustrated in bold in Figure 2.1, is considered in the derivation below. Such a span has six end displacements $dx_N, dy_N, dz_N, dx_{N+1}, dy_{N+1}$ and dz_{N+1} and five end reactions, $(R_x)_{n+1}, (R_A)_y, (R_A)_z, (R_B)_y$ and $(R_B)_z$, as illustrated in Figure 2.3. It should be noted that since no longitudinal forces act on the conductor, the reaction, $(R_x)_{n+1}$, at the end A and that at the end B are set to be equal.

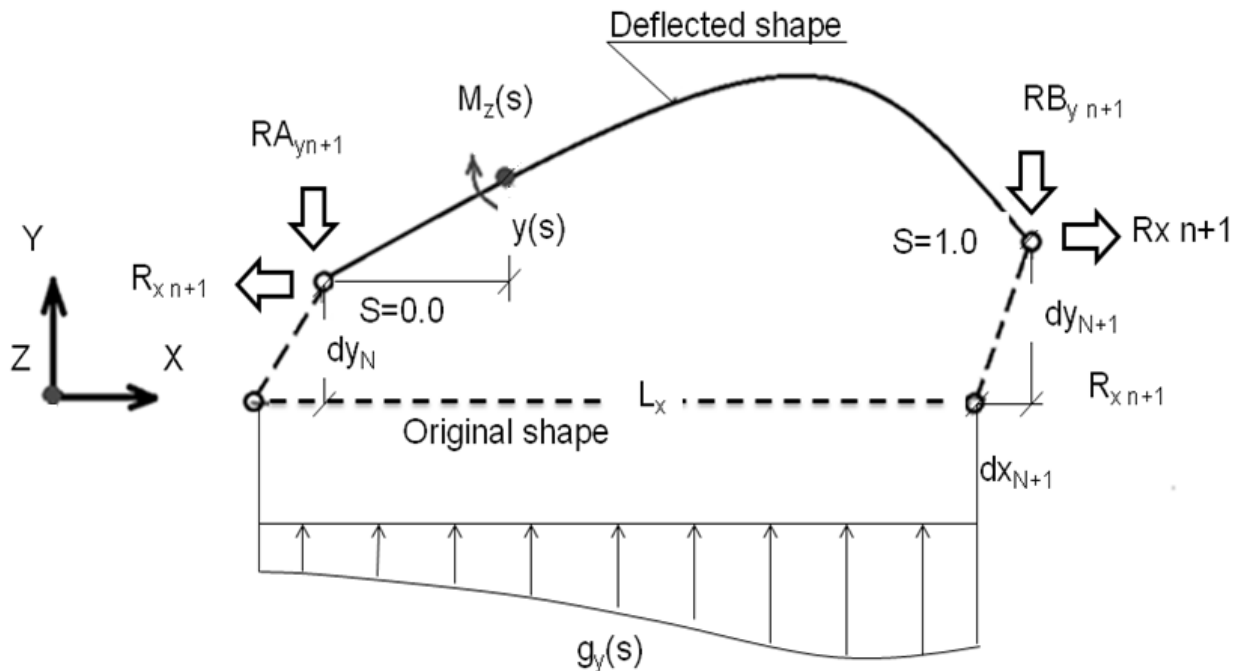


Figure 2.3 Analysis of a conductor span (n+1)

By applying the moment equilibrium at the end points, B and A, around Z and Y directions, expressions for the reactions in y direction, at the end A $(RA_y)_{n+1}$ and at the end B $(RB_y)_{n+1}$, and in z direction, at the end A $(RA_z)_{n+1}$ and at the end B $(RB_z)_{n+1}$, can be derived as indicated by Eqs. (2.1)-(2.4), respectively. Such equations depend on the first order moment induced by the external loads at point A, M_{zgyA} and M_{ygzA} , and at point B, M_{zgyB} and M_{ygzB} , which are defined by Eq. (2.5).

$$(RA_y)_{n+1} = \frac{M_{zgyB} + (R_x)_{n+1}(dy_{n+1} - dy_n)}{L_x} \quad \text{Equation 2.1}$$

$$(RB_y)_{n+1} = \frac{M_{zgyA} - (R_x)_{n+1}(dy_{n+1} - dy_n)}{L_x} \quad \text{Equation 2.2}$$

$$(RA_z)_{n+1} = \frac{M_{ygzB} + (R_x)_{n+1}(dz_{n+1} - dz_n)}{L_x} \quad \text{Equation 2.3}$$

$$(RB_z)_{n+1} = \frac{M_{ygzA} - (R_x)_{n+1}(dz_{n+1} - dz_n)}{L_x} \quad \text{Equation 2.4}$$

$$\begin{aligned} M_{zgyB} &= L_x^2 \cdot \int_{s=0}^{s=1} g_y(s) \cdot (1-s) \cdot ds & M_{zgyA} &= L_x^2 \cdot \int_{s=0}^{s=1} g_y(s) \cdot (s) \cdot ds \\ M_{ygzB} &= L_x^2 \cdot \int_{s=0}^{s=1} g_z(s) \cdot (1-s) \cdot ds & M_{ygzA} &= L_x^2 \cdot \int_{s=0}^{s=1} g_z(s) \cdot (s) \cdot ds \end{aligned} \quad \text{Equation 2.5}$$

Where:

M_{igK} : The first order moment around axis i at point K induced by a loading $g_j(s)$

s: Local coordinate in the longitudinal direction =0.0 and 1.0 at the conductor start and end points

$g_y(s)$, $g_z(s)$: Load intensity at the location s, in y and z directions, respectively.

For a connecting point, N, the reactions in Y and Z directions, R_{yN} and R_{zN} , are equal to the summation of the reactions, $(RB_y)_n$ and $(RB_z)_n$, from the end B in span N and the reactions, $(RA_y)_{n+1}$ and $(RA_z)_{n+1}$, from the end A at span N+1, as indicated by Eqs. (2.6) and (2.7), respectively. Eqs. (2.6) and (2.7) can be rewritten in a matrix notation to express the reaction vectors in y and z directions, $\{R_y\}_{Nd \times 1}$ and $\{R_z\}_{Nd \times 1}$, for Nd number of connecting points, as illustrated by Eqs. (2.8) and (2.9), respectively. Reaction vectors, $\{R_y\}_{Nd \times 1}$ and $\{R_z\}_{Nd \times 1}$, given by Eqs. (2.8) and (2.9) are the total reaction due to first and second order analyses. First order analysis assumes no displacements exist at the span ends and is represented in the reaction vectors, $\{R_y^F\}_{Nd \times 1}$ and $\{R_z^F\}_{Nd \times 1}$, which are only functions of the applied loads, g_y and g_z , respectively and defined in Appendix A. Second order analysis accounts for displacements and their effect on the reactions. Such effect is considered by the multiplication of the stiffness matrix, $[K]_{Nd \times Nd}$ with the displacement vectors $\{dy\}$ or $\{dz\}$, as shown by Eqs. (2.8) and (2.9), respectively.

So far, transverse and vertical reactions at a general conductor-insulator node N can be calculated according to Eqs. (2.6) and (2.7). In the next subsection, 2.2, an expression for the longitudinal reaction is to be derived.

$$R_{yN} = RA_{yn+1} + RB_{yn} = \frac{M_{zgyBn} + M_{zgyA_{n+1}}}{L_x} - \frac{R_{x,n}}{L_x} \cdot dy_{N-1} + \left(\frac{R_{x,n}}{L_x} + \frac{R_{x,n+1}}{L_x} \right) \cdot dy_N - \frac{R_{x,n+1}}{L_x} \cdot dy_{N+1} \quad \text{Equation 2.6}$$

$$R_{zN} = RA_{zn+1} + RB_{zn} = \frac{M_{ygzBn} + M_{ygzA_{n+1}}}{L_x} - \frac{R_{x,n}}{L_x} \cdot dz_{N-1} + \left(\frac{R_{x,n}}{L_x} + \frac{R_{x,n+1}}{L_x} \right) \cdot dz_N - \frac{R_{x,n+1}}{L_x} \cdot dz_{N+1} \quad \text{Equation 2.7}$$

$$\{R_y\}_{Nd \times 1} = \{R_y^F\}_{Nd \times 1} + [K]_{Nd \times Nd} \cdot \{dy\}_{Nd \times 1} \quad \text{Equation 2.8}$$

$$\{R_z\}_{Nd \times 1} = \{R_z^F\}_{Nd \times 1} + [K]_{Nd \times Nd} \cdot \{dz\}_{Nd \times 1} \quad \text{Equation 2.9}$$

Where:

Nd: Number of conductor-insulator connecting points = number of spans+1

$\{R_y^F\}_{Ndx1}$, $\{R_z^F\}_{Ndx1}$: Vectors of y and z reactions considering no end displacements, which are defined in Appendix A.

$[K]_{NdxNd}$: Equivalent stiffness matrix to account for the effect of the end displacement on the reactions, which is defined in Appendix A.

2.2.1.1 Conductor Longitudinal Reaction (R_x)

An expression for the longitudinal reaction component, R_x , is derived by evaluating the length of the deformed conductor using two approaches. The first approach is based on the axial strain of the member, as indicated by Eq. (2.10). The second approach is based on the length of the transverse-vertical elastic profile of the conductor. The length of an infinitesimal segment, dL , shown in Figure 2.4, can be calculated as a function of the transverse slope dy/dx and the vertical slope dz/dx as indicated by Eq. (2.11), which can be simplified to Eq. (2.12). The derivatives dy/dx and dz/dx are required in the simplified integral and can be calculated by the expressions given in Eqs. (2.13) and (2.14), respectively. Such expressions are based on the assumption that no bending moment can be resisted by the conductor, and therefore, external bending moments along the deformed conductor are equal to zero. The derivatives dy/dx and dz/dx depend on the first order shearing forces, $Q_y(s)^*$ and $Q_z(s)^*$, expressed by Eqs. (2.15) and (2.16), respectively. By substituting the shearing forces in the integral presented by Eq. (2.12), an expression for the conductor longitudinal reaction can be derived as indicated by Eq. (2.17). At the conductor-insulator connecting point, N, the reaction in X direction, R_{xN} , can be calculated by subtracting the longitudinal reaction of the left span, R_{xn} , from the reaction of the right span, R_{xn+1} , as indicated by Eq. (2.18).

$$L = L_0 \cdot \left(1 + \frac{R_x - R_{x0}}{E \cdot A}\right) \quad \text{Equation 2.10}$$

Where:

R_{x0} : Conductor longitudinal reaction under its own weight $R_{x0} = W.L_x^2 / (8S)$

E: Modulus of elasticity, A: Conductor cross section area, W: Conductor weight, S: Conductor sag

L_0 : Conductor length before the application wind loading under its own weight, which can be calculated as $L_0 = L_x \cdot \left(1 + 8/3 \cdot (S/L_x)^2\right)$ according to Irvine (1981).

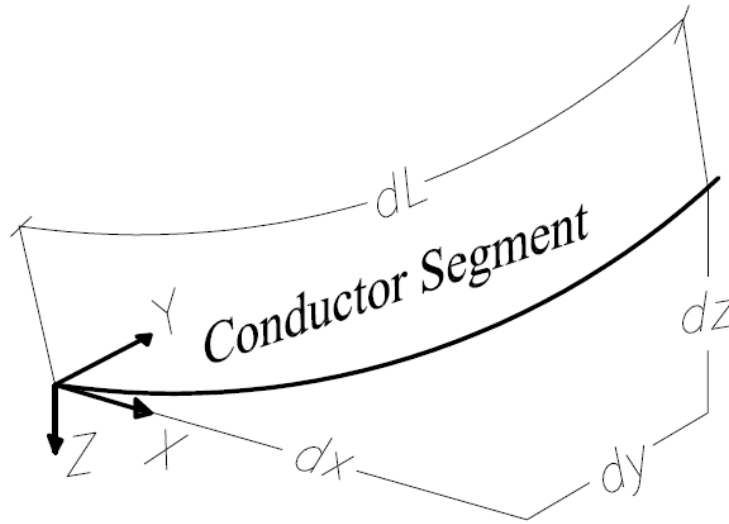


Figure 2.4 Conductor Segment

$$L_{n+1} = \int dL_{n+1} = \int \sqrt{1 + \left(\frac{dy}{dx}\right)_{n+1}^2 + \left(\frac{dz}{dx}\right)_{n+1}^2} \cdot L_x \cdot ds \quad \text{Equation 2.11}$$

$$L_{n+1} = L_x \cdot \int_0^1 \left(1 + \frac{1}{2} \left(\frac{dy}{dx}\right)_{n+1}^2 + \frac{1}{2} \left(\frac{dz}{dx}\right)_{n+1}^2\right) \cdot ds \quad \text{Equation 2.12}$$

$$\left(\frac{dy}{dx}(s)\right)_{n+1} = \frac{Q_{yn+1}(s)^*}{R_{xn+1}} + \frac{(dy_{N+1} - dy_N)}{L_x} \quad \text{Equation 2.13}$$

$$\left(\frac{dz}{dx}(s)\right)_{n+1} = \frac{Q_{zn+1}(s)^*}{R_{xn+1}} + \frac{(dy_{N+1} - dy_N)}{L_x} \quad \text{Equation 2.14}$$

$$Q_y(s)^* = \frac{M_{zgyB}}{L_x} - L_x \cdot \int_0^s g_y(s_1) \cdot ds_1 \quad \text{Equation 2.15}$$

$$Q_z(s)^* = \frac{M_{ygzB}}{L_x} - L_x \cdot \int_0^s g_z(s_1) \cdot ds_1 \quad \text{Equation 2.16}$$

$$R_{xn+1} = \sqrt{\frac{\int_0^1 Q_{yn+1}(s)^{*2} ds + \int_0^1 Q_{zn+1}(s)^{*2} ds + 2 \cdot \frac{R_{xn+1}}{Lx} \left((dy_{N+1} - dy_N) \int_0^1 Q_{yn+1}(s)^* ds + (dz_{N+1} - dz_N) \int_0^1 Q_{zn+1}(s)^* ds \right)}{2 \left(\frac{L_0}{L_x + dx_{N+1} - dx_N} \left(\frac{R_{xn+1} - R_{x0}}{EA} + 1 \right) - 1 \right)}} \quad \text{Equation 2.17}$$

$$R_{xn} = R_{xn+1} - R_{xn} = \sqrt{\frac{a_n}{\left(\frac{L_0 \cdot b_n}{L_x + dx_{N+1} - dx_N} - 1 \right)}} - \sqrt{\frac{a_{n-1}}{\left(\frac{L_0 \cdot b_{n-1}}{L_x + dx_N - dx_{N-1}} - 1 \right)}} \quad \text{Equation 2.18}$$

Where:-

$$a_n = \frac{1}{\sqrt{2}} \sqrt{\int_0^1 Q_{yn}(s)^{*2} ds + \int_0^1 Q_{zn}(s)^{*2} ds + 2 \cdot \frac{R_{xn}}{Lx} \left((dy_{N+1} - dy_N) \int_0^1 Q_{yn}(s)^* ds + (dz_{N+1} - dz_N) \int_0^1 Q_{zn}(s)^* ds \right)} \quad b_n = 1 + \frac{R_{xn} - R_{x0}}{EA}$$

2.2.2 Insulator Equilibrium

Insulators are modeled as rigid pendulums with length, v , which is constant before and after the application of the loading. Considering an insulator, N , as shown in Figure 2.5, and applying the equilibrium of the moment at the nagging point, 0 , around x , y and z axes, a relationship between the nodal displacements (d_{xN} , d_{yN} and d_{zN}) and the nodal reactions (R_{xN} , R_{yN} and R_{zN}) is obtained as given by Eqs. (2.19)-(2.21). Eqs. (2.19)-(2.21), which describe the insulator response, have six unknowns: three displacement components, d_{xN} , d_{yN} and d_{zN} , and three reaction components, R_{xN} , R_{yN} and R_{zN} . Eqs. (2.8), (2.9) and (18) share the same six unknowns and describe the conductor response.

Therefore, a combination of these Eqs. ((2.8),(2.9),(2.18) and (2.19)-(2.21)) can be used to solve the entire system as will be illustrated by Section 2.3.

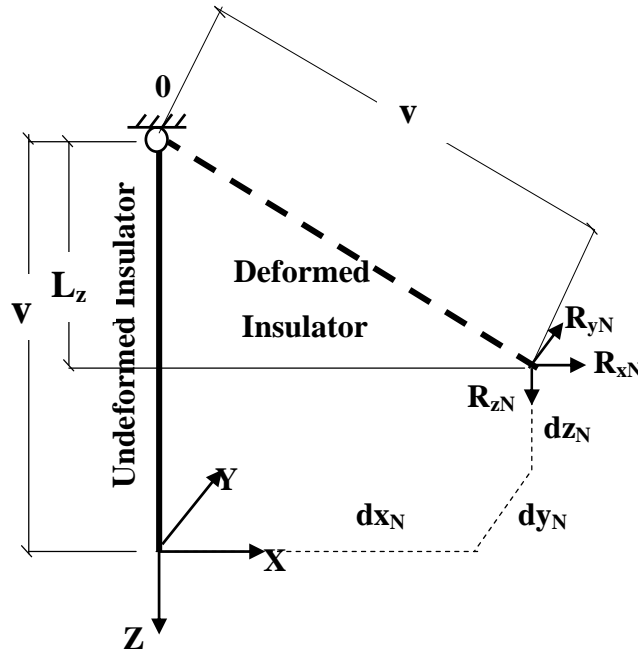


Figure 2.5 equilibrium of the insulator

$$d_{xN} = v \cdot \frac{R_{xN}}{R_{resN}} \quad \text{Equation 2.19}$$

$$d_{yN} = v \cdot \frac{R_{yN}}{R_{resN}} \quad \text{Equation 2.20}$$

$$L_{zN} = v \cdot \frac{R_{zN}}{R_{resN}} \quad \text{Equation 2.21}$$

Where:

R_{resN} : The resultant force at node N, $R_{resN} = \sqrt{R_{xN}^2 + R_{yN}^2 + R_{zN}^2}$

L_{zN} : The vertical projection of the insulator after the deformation = $v + d_{zn}$, where d_{zn} is the displacement in the Z direction, which is usually negative.

2.3 Solution Technique

At each conductor-insulator connecting point, six non-linear equations exist, which are Eqs. (2.8), (2.9), (2.18), (2.19), (2.20) and (2.21), and six unknowns also exist, which are the displacement components and three reaction components. Since the number of equations equals the number of unknowns, the problem can be solved. However, such a system of equations needs to be solved iteratively. The easiest approach to solve those equations is by iterating in a sequential manner, where only one equation is solved at a time. First, initial displacements are to be assumed. Then, the reactions are to be updated using Eqs. (2.8), (2.9) and (2.18) to satisfy the conductor equilibrium, and then the nodal displacements are to be updated using Eqs. (2.19)-(2.21) to satisfy the insulator equilibrium until convergence takes place. It is found that such sequential techniques can be easily unstable. The instability may happen in Eq. (2.18), while attempting to update the reactions in x direction, R_x , assuming constant displacements in x-direction, dx . This instability is due to the high level of coupling between displacements and reactions in the x-direction. Consequently, a more stable approach, illustrated by the flow chart shown in Figure 2.6, is proposed. As indicated by the flow chart, Newton Raphson's iterative method is utilized to solve Eq. (2.18) with Eq. (2.19) simultaneously in dx and R_x while assuming the other variables as constants. The displacement vector in x direction at iteration number $i+1$, $\{d_x\}_{Ndx1}^{i+1}$, is calculated using Eq. (2.22) as a function of the displacement vector at the previous iteration i , $\{d_x\}_{Ndx1}^i$. After convergence takes place, the reaction vector, R_x , is calculated from the displacement vector using Eq. (2.23).

$$\{d_x\}_{Ndx1}^{i+1} = \{d_x\}_{Ndx1}^i + [K_x]_{NdxNd}^i \cdot \{f_x\}_{Ndx1}^i \quad \text{Equation 2.22}$$

Where:

i : Iteration number

$\{f_x\}_{Ndx1}$: Unbalanced load vector in, which is defined in Appendix A

$[K_x]_{NdxNd}$: Tangential stiffness matrix that is given in Appendix A,

whose the (N, J) element equals to $-\frac{\partial f(N)}{\partial x(J)}$, where N and J are the

row and the column numbers

$$R_x(N) = d_x(N) \cdot \frac{R_{res}(N)}{V}$$

Equation 2.23

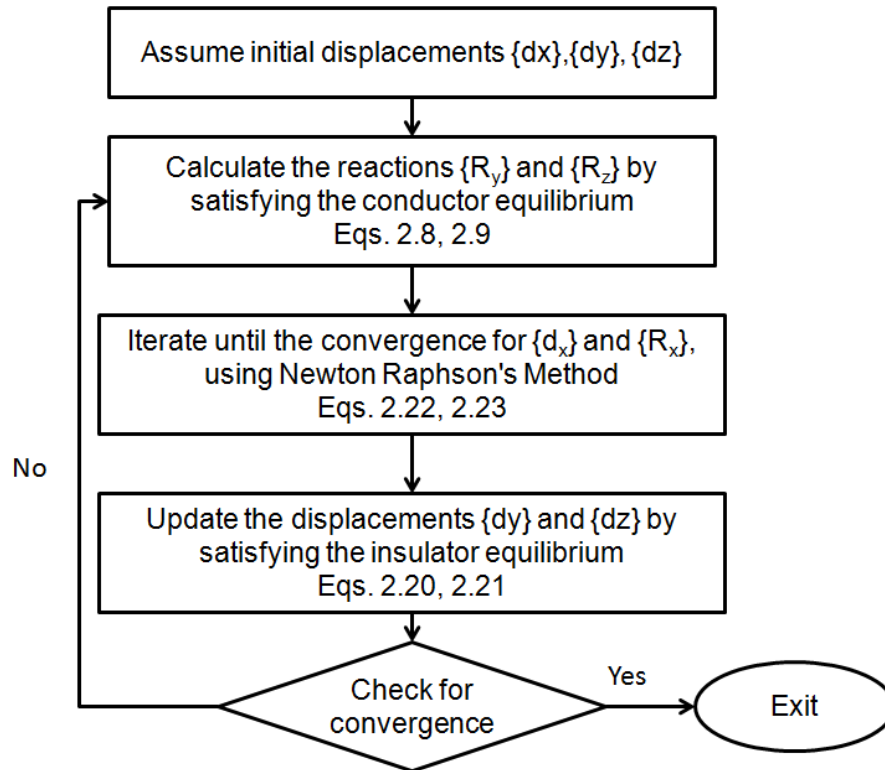


Figure 2.6 Flow chart of the proposed solution approach

2.4 Validating the Technique

Two cases of loading are selected in order to validate the developed technique. The first case of loading represents a downburst, while the second represents a tornado. Downburst and tornado wind fields resulting from the CFD simulation performed by Hangan and Kim (2007) and Hangan and Kim (2008) are utilized. The technique illustrated by Shehata et al. (2005) is employed to scale up the CFD results and to calculate wind forces on the conductors. According to Shehata and El Damatty (2007) and Hamada and El Damatty (2011), the behaviour of a Transmission Line (TL) under HIW is strongly

dependent on the event size, D , and the relative location between the event and the towers, defined by the polar coordinates, R and Θ . Values of those parameters for the considered cases of downburst and tornado are given by Figure 2.7 and Figure 2.8, respectively. According to El Damatty and Aboshosha (2012), Aboshosha and El Damatty (2013) and El Damatty and Hamada (2012), those parameters are found to be critical for the considered lines and can lead to the failure of the intermediate tower. Those downburst and tornado configurations induce unequal wind loads acting on the conductors located on either sides of the middle tower. The HIW parameters of the chosen events are summarized in Table 2.1, while the corresponding distribution of wind loads is given in Figure 2.9 and 2.10, respectively. As shown in Figures 2.9 and 2.10, only six conductor spans adjacent to the intermediate tower are chosen in the analysis, similar to the number used by Shehata et al. (2005). Shehata et al. (2005) showed that analyzing six spans is enough to obtain accurate prediction of the transmitted forces from the conductors to the intermediate tower. The first and last nodes of the considered six-spanned system are assumed to be restrained in the three directions, similar to the system analyzed by Shehata et al. (2005). The properties of the chosen conductor are summarized in Table 2.2.

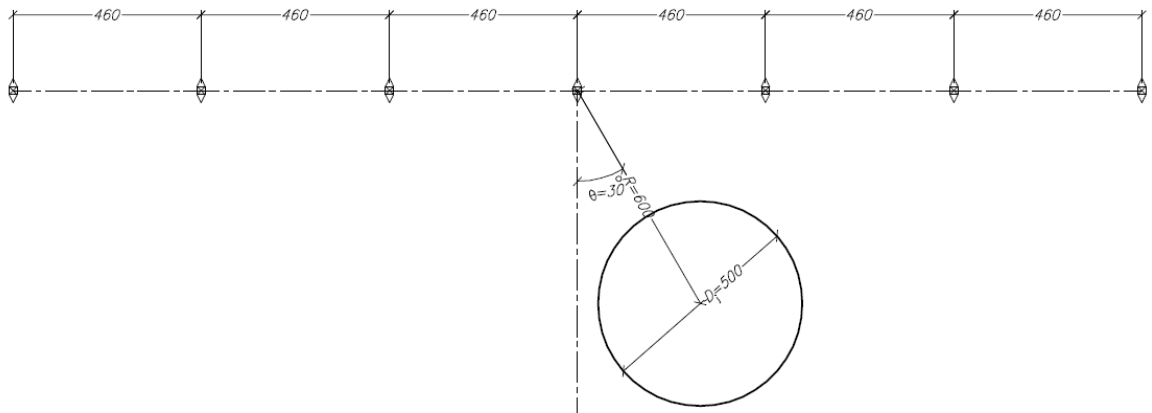


Figure 2.7 Downburst loading Case

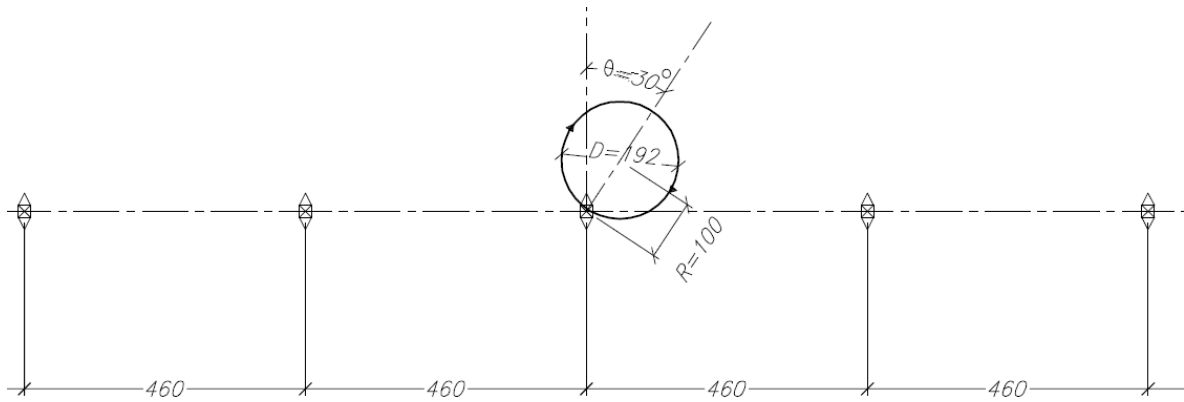


Figure 2.8 Tornado Loading Case

Table 2.1 loading parameters

Downburst Loading Parameters	Tornado Loading Parameters
$D=500.0$ m	$D=192.0$ m
$R_j=600.0$ m	$R=100.0$ m
$\Theta=30^\circ$	$\Theta=-30^\circ$
Jet Velocity, $V_j=40.0$ m/s	Tornado F2 on Fujita Scale, with maximum tangential velocity =78 m/s happens at 96.0 m from the tornado eye

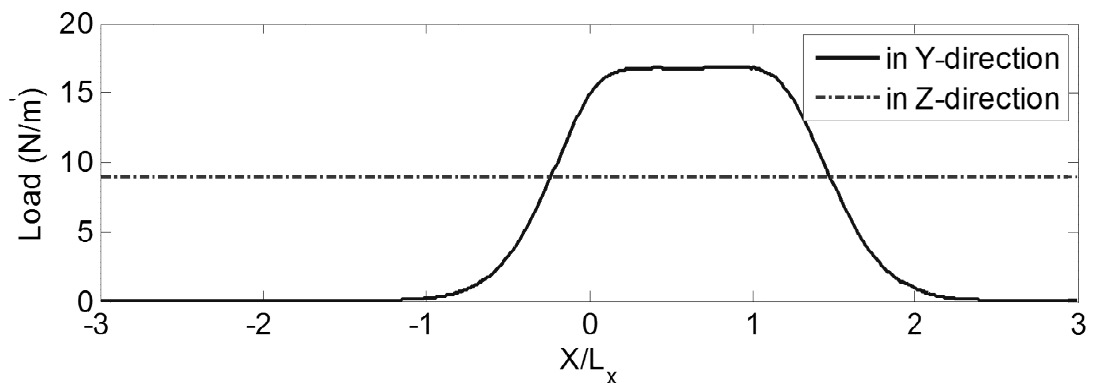


Figure 2.9 Load distribution induced from the Downburst Loading

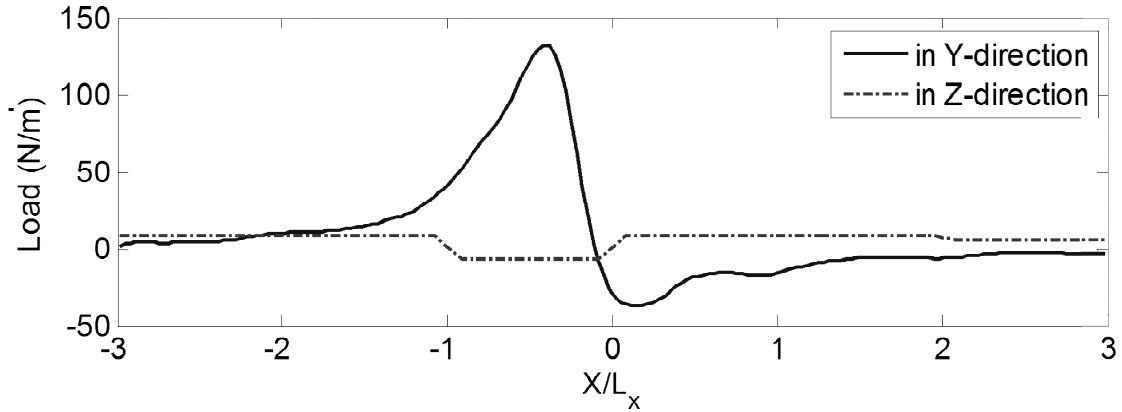


Figure 2.10 Load distribution induced from the Tornado Loading

Table 2.2 Properties of the Conductor

Property	Value
Span Length L_x (m)	460.0
Sag Length S (m)	16.0
Elasticity Modulus E (N/m ²)	5.2E10
Weight W (N/m)	8.96
Facing Area from the wind (m ² /m)	0.022
Drag coefficient C_d	1.0
Cross sectional Area (m ²)	3.80E-04
Insulator Length v (m)	4.0
Insulator Axial Stiffness	Rigid
Elevation for the hanging point (m)	40.0

2.4.1 Results of the Analysis

The results are obtained in terms of the nodal displacements and nodal reactions as summarized in Table 2.3 for the downburst case and in Table 2.4 for the tornado case. A deformed shape can be obtained using the expressions provided by the following equations.

$$dy_{n+1}(s) = dy_n + \frac{(RA_y)_{n+1} \cdot L_x \cdot s - L_x^2 \cdot \int_{s_1=0}^{s_1=s} g_y(s_1) \cdot (s - s_1) \cdot ds_1}{Rx_{n+1}} \quad \text{Equation 2.24}$$

$$dz_{n+1}(s) = dz_n + \frac{(RA_z)_{n+1} \cdot L_x \cdot s - L_x^2 \cdot \int_{s_1=0}^{s_1=s} g_z(s_1) \cdot (s - s_1) \cdot ds_1}{Rx_{n+1}} \quad \text{Equation 2.25}$$

Such expressions are based on equating the bending moments at a general location, s , inside a span, $n+1$, to zero. The obtained deformed shape is plotted in Figures 2.11 and 12 for the downburst and tornado cases, respectively. In order to assess the accuracy and the efficiency of the proposed technique, the same conductor system is reanalyzed using Finite Element Analysis (FEA). The commercial software package SAP 2000 is utilized to perform the FEA, using a 3D cable element to simulate the conductors, a technique similar to what was done by Hamada and El Damatty (2011). In the SAP program, each conductor span is divided into 30 elements to account for the load variation along the length. The resulting deformed shape obtained using the FEA is plotted and compared with that from the proposed technique as shown in Figures 2.11 and 12 for the downburst and the tornado cases, respectively. It is clear from the figures that the two responses are in good agreement. Nodal displacements and reactions obtained from the FEA are summarized in Tables 3 and 4 for the downburst and the tornado cases, respectively. Differences between the responses predicted using the proposed technique and those by employing the FEA are also summarized in the two tables. The maximum differences in the displacements are 3% and 5% for the downburst and the tornado cases, respectively. In the meanwhile, the maximum differences in the reactions are 4% and 6% for the downburst and the tornado cases, respectively. Such an agreement between the analytical and FEA results provides a validation for the developed technique. In terms of efficiency, the proposed technique shows a significant reduction in the computational time required to perform the analysis, when compared with the FEA. The technique required only 0.35 seconds to solve the six-spanned problem, while FEA takes 65 seconds to solve the same problem. This means that the proposed technique is about 186 and 185 times faster than the FEA. It is important to mention that a large parametric study is often required by varying the event size and location in order to obtain the maximum forces acting on a tower due to HIW event. As such the saving in the computational time of one analysis makes a large difference in the overall time required to conduct a parametric study. For

example, the parametric study conducted by Shehata and El Damatty (2007), which involved 308 load cases took 44.6 hours using FEA, while it has taken only 18 minutes using the developed technique in this study.

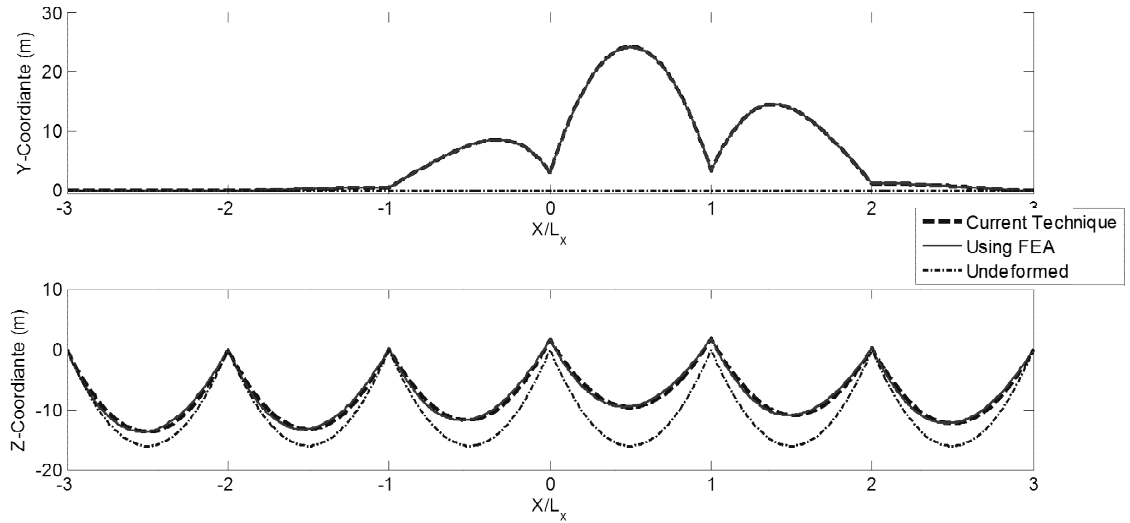


Figure 2.11 deflected shape under downburst loading

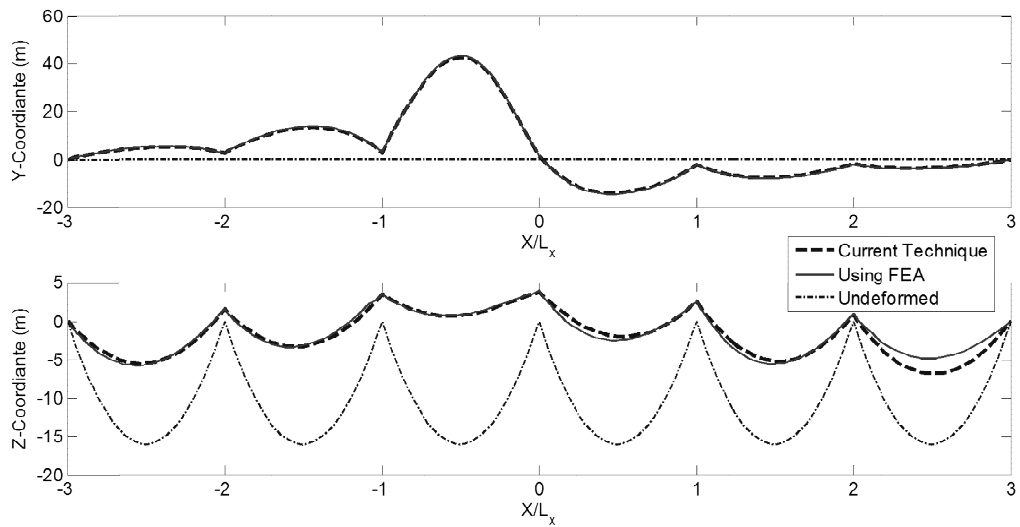


Figure 2.12 deflected shape under tornado loading

Table 2.3 Nodal reactions and displacement results for the Downburst Case

Joint	FEA			Current Technique			Difference %		
	d _x (m)	d _y (m)	d _z (m)	d _x (m)	d _y (m)	d _z (m)	d _x	d _y	d _z (m)
2	0.412	0.027	-0.022	0.422	0.027	-0.022	2%	1%	-3%
3	0.886	0.618	-0.148	0.909	0.613	-0.153	3%	1%	-3%
4	1.210	3.021	-1.67	1.235	3.018	-1.683	2%	0%	0%
5	-0.533	3.335	-1.85	-0.548	3.333	-1.858	-3%	0%	0%
6	-0.648	1.275	-0.26	-0.668	1.268	-0.265	-3%	1%	0%

Joint	FEA			Current Technique			Difference %		
	R _x (N)	R _y (N)	R _z (N)	R _x (N)	R _y (N)	R _z (N)	R _x (N)	R _y (N)	R _z (N)
1	17356	1	2065	17313	1	2081	0%	1%	1%
2	428	28	4127	441	28	4159	3%	1%	1%
3	937	653	4074	970	654	4106	4%	0%	1%
4	2178	5438	4186	2247	5491	4217	3%	1%	1%
5	-1045	6538	4209	-1085	6596	4240	-4%	1%	1%
6	-706	1390	4073	-734	1394	4105	-4%	0%	1%
7	-19178	69	2055	-19152	69	2070	0%	0%	1%

Table 2.4 Nodal reactions and displacement results for the Tornado Case

Joint	FEA			Current Technique			Difference %		
	d_x (m)	d_y (m)	d_z (m)	d_x	d_y	d_z (m)	d_x	d_y	d_z (m)
2	1.641	2.690	-1.541	1.668	2.684	-1.542	2%	0%	0%
3	2.732	2.881	-3.502	2.721	2.890	-3.502	0%	0%	0%
4	-3.66	1.522	-3.604	-3.710	1.444	-3.631	-1%	5%	-1%
5	-2.951	-2.263	-2.509	-2.970	-2.244	-2.534	-1%	-1%	-1%
6	-1.512	-1.831	-0.778	-1.508	-1.838	-0.791	0%	0%	2%

Joint	FEA			Current Technique			Difference %		
	R_x (N)	R_y (N)	R_z (N)	R_x (N)	R_y (N)	R_z (N)	R_x (N)	R_y (N)	R_z (N)
1	36448	1265	1928	37935	1324	1968	4%	5%	2%
2	2720	4459	4085	2864	4595	4213	5%	3%	3%
3	22163	23404	4036	22582	24000	4165	2%	3%	3%
4	-19530	8309	2121	-20205	7856	2004	-3%	-5%	6%
5	-8100	-6196	4085	-8524	-6416	4216	-5%	-4%	3%
6	-1895	-2303	4058	-1972	-2393	4184	-4%	-4%	3%
7	-31805	-926	1995	-32681	-974	2039	-3%	-5%	2%

2.5 Conclusions

A new technique is developed to analyze multi-spanned transmission line conductor systems under HIW. The technique divides the system at the conductor-insulator connecting points, where six unknowns appear: three reaction components and three displacement components. Six equations are required to solve for those unknowns. Three equations are derived by satisfying the moment equilibrium of the conductors and by equating the conductor length using two different approaches. The remaining three equations are derived by satisfying the moment equilibrium of the insulators. The resulting six equations are nonlinear and coupled. As such, an iterative technique is suggested to solve the governing equations. In this technique, equations that govern the longitudinal responses are solved in a coupled way while the rest of the equations are

solved sequentially. The proposed technique is the first that is based on a semi-closed form solution and is able to solve for a multi-spanned conductor systems subjected to varying loads in the transverse and vertical directions, while accounting for the insulator flexibility. Accuracy and efficiency of the technique are tested under two different cases of HIW. The technique showed good agreement in terms of the predicted reactions and displacements, when compared with FEA. The maximum difference in the displacement between the two methods is 4% for the downburst and 5% for the tornado cases. In terms of the reactions, a maximum difference of 5% for the downburst case and of 6% for the tornado case is found. The method shows a significant reduction in the computational time compared to FEA. The technique is shown to be 185 times faster than the FEA, for the considered cases. Analysis of transmission lines under HIW requires conducting a large number of analyses to capture the potential sizes and locations of these localized events. As such, a reduction in the computational time for each analysis becomes very important and useful for this type of application.

2.6 References

- Aboshosha, H., El Damatty, A., (2013)," Downburst Induced Forces on the Conductors of Electric Transmission Lines and the Corresponding Vulnerability of Towers Failure", *Proceedings of the Canadian Society of Civil Engineers CSCE 2013, Montreal, Québec, Canada-GEN-164*.
- Ahmadi-Kashani, K., Bell, A.J. (1988),"The analysis of cables subject to uniformly distributed loads", *Engineering Structures*, 10(3), 174-184.
- C.Q. Li (2000), "A stochastic model of severe thunderstorms for transmission line design", *Probab. Eng. Mech.*, 15, 359-364.
- Darwish M., El Damatty A., and Hangan, H. (2010), "Dynamic characteristics of transmission line conductors and behaviour under turbulent downburst loading", *Wind and Structures, An International Journal*, 13(4), 327-346.
- El Damatty, A., A. Hamada (2012), "Behaviour of Guyed Transmission Line Structures under Tornado Wind Loads – Case Studies", *ASCE -Structural Engineering Institute – Electrical Transmission and Substation Structures Conference, Columbus, Ohio, USA, November 2012*

- El Damatty, A., Aboshosha, H., (2012), "Capacity of Electrical Transmission Towers under Downburst Loading", *Proceedings of the First Australasia and South-East Asia Structural Engineering and Construction Conference, Perth, Australia*, St-117-0354.
- Fujita, T.T. (1990), "Downbursts: meteorological features and wind field characteristics", *Journal of Wind Engineering & Industrial Aerodynamics*, **36**(1), 75-86.
- Hangan, H. and Kim, J. (2007), "Numerical simulations of impinging jets with application to downbursts", *J. Wind Eng. Ind. Aerodyn.*, **95**(4), 279-298.
- Hangan, H. and Kim, J. (2008), "Swirl ratio effects on tornado vortices in relation to the Fujita scale", *Wind and Structures, An International Journal*, **11**(4), 291-302.
- Hamada, A. and El Damatty, A.A. (2011), "Behaviour of guyed transmission line structures under tornado wind loading", *Comput. Struct.*, **89**(11-12), 986-1003.
- Irvine, H.M. (1981), *Cable Structures*, MIT Press, Cambridge.
- Koziey, B. and Mirza, F. (1994), "Consistent Curved Beam Element", *Comput. Struct.*, **51**(6), 643-654.
- Manitoba Hydro Transmission and Civil Design Department (1999), "Bipole 1 & 2 HVDC transmission line wind storm failure on September 5, 1996 review of emergency response, restoration and design of these lines", Manitoba Hydro, 98-L1/1-37010-06000, 54.
- Savory, E., Parke, G.A.R., Zeinoddini, M., Toy, N. and Disney, P. (2001), "Modeling of tornado and microburst-induced wind loading and failure of a lattice transmission tower", *Eng. Struct.*, **23**(4), 365-375
- Shehata, A.Y., El Damatty, A.A. and Savory, E. (2005), "Finite element modeling of transmission line under downburst wind loading", *Finite Elements Anal. Des.*, **42**(1), 71-89.
- Shehata, A.Y. and El Damatty, A.A. (2007), "Behaviour of guyed transmission line structures under downburst wind loading", *Wind and Structures, An International Journal*, **10**(3), 249-268.
- Shehata, A.Y. and El Damatty, A.A. (2008), "Failure analysis of a transmission tower during a microburst", *Wind and Structures*, **11**(3), 193-208.

- Wei, P., Bingnan, S., Jinchun T. (1999), "A catenary element for the analysis of cable structures", *Applied Mathematics and Mechanics (English Edition)*, 20(5), 0253-4827
- Winkelman, P.F., (1959) "Sag-Tension Computations and Field Measurements of Bonneville Power Administration", *AIEE Paper*, 59-900
- Yu, P., Wong, P. and Kaempffer, F. (1995), "Tension of conductor under concentrated loads", *J. Appl. Mech. -Trans. ASME*, **62**(3), 802-809.

Chapter 3

3 Closed Form Solution for the Reactions of Transmission Line Conductors under Downburst Winds

3.1 Introduction

Electricity is carried by Transmission Lines (TL) from sources of production to end customers. Transmission Lines (TLs) consist mainly of towers, conductors and insulators. Conductors, which are supported by the towers through the insulators, are responsible for transmitting the electricity. The economic losses associated with the failure of a TL do not only result from the repairing costs but also from the interruption of power, which can extend for few months. It is reported that High Intensity Winds (HIW), in the forms of downburst or tornadoes, are responsible for more than 80% of the weather-related failures of TLs worldwide (Dempsey and White 1996). A downburst is a strong downdraft that induces an outburst of damaging winds near the ground as described by Fujita (1990). In September 1996, Manitoba Hydro Company, Canada, reported a failure of 19 transmission towers due to a downburst event (McCarthy and Melsness 1996). In Australia, Li (2000) stated that downbursts are responsible for more than 90% of the weather-related failures. Shehata et al. (2008) conducted a failure study on a guyed transmission line subjected to downbursts. They utilized the downburst wind field obtained by Kim and Hangan (2007) using a Computational Fluid Dynamics (CFD) simulation, in which the downburst was treated as an impinging jet. Their study showed that the most critical failure mode happens due to a downburst with a jet diameter, D_j , equals to twice the conductor span length, L_x , which is located at a radial distance, $R=1.60 D_j$, and an angle $\Theta=30^\circ$ measured from the tower of interest, as shown in Fig. 3.1. This leads to a large differential tension between the conductor spans on the sides of the tower of interest which leads to a large longitudinal forces transmitted from the conductors to the tower. Design standards are now at an early stage of including HIW in the design of TLs. For example, the AS/NZS (2010) provides a map showing the areas where downbursts have to be included in the design.

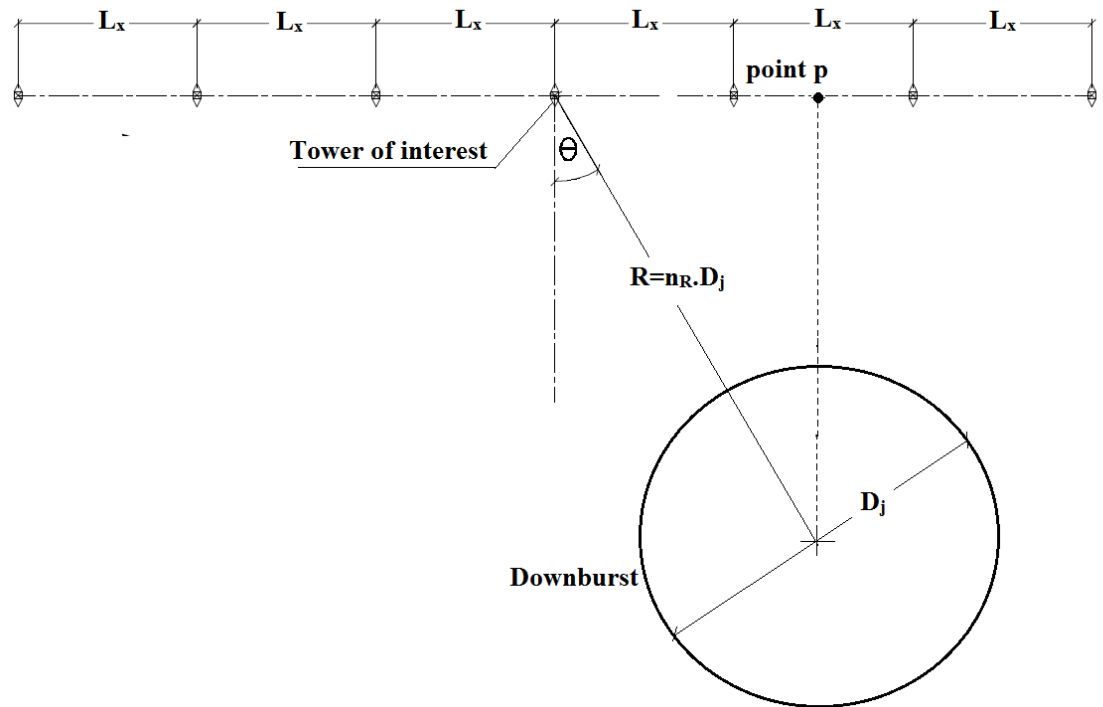


Figure 3.1 Downburst Parameters

The standard uses a uniform load to model the downburst effect on the conductor spans. Although, this can be used to reasonably obtain the transverse reactions, it does not allow for the prediction of the differential conductor tension between the spans, which was found to be important. The studies performed by El Damatty and Aboshosha (2012), Aboshosha and El Damatty (2013) and El Damatty et al. (2013) manifested the importance of accounting for the differential conductor tension while studying the downburst effect on the TLs.

Finite Element Analysis (FEA) was utilized in most of the previous studies to predict the behavior or the failure of transmission lines under downbursts (Shehata et al. 2005, Shehata and El Damatty 2007, Darwish et al. 2010). Their studies showed that analyzing the conductors using FEA and predicting the critical longitudinal forces transmitted to the towers due to downburst loading is a time consuming task. This is due to the following: (1) Conductors are highly flexible structure elements. Therefore, their behavior under transverse loading associated with downbursts is highly non-linear due to the large deformations and the P-delta effect. (2) Since downbursts are localized events, their size

and location can vary, which lead to altering the loads acting on the conductors and consequently the transmitted forces from the conductors to the towers. As such, the determination of the maximum forces transmitted requires a long parametric study that involves altering the downburst size and location.

Other than FEA, Irvine (1981) proposed a closed-form solution to obtain the reaction for a single spanned conductor, which is subjected to loads that can be fitted by a 3rd degree polynomial. Yu et al. (1995), also proposed a closed-form solution for a single spanned conductor subjected to high concentrated loads. However, both solutions do not consider the flexibility of the insulators, which has a significant effect on the forces transmitted to the towers (Darwish et al. 2010). The method of the rolling span, proposed by Winkelman (1959), accounts for the insulator flexibility. However, it neglects the differences between the conductors' tensile forces in the adjacent spans and, consequently, fails to predict the longitudinal forces transmitted to the towers. Ahmadi-Kashani and Bell (1988) and Wie et al. (1999) developed cable elements that are able to simulate a whole span based on the analytical solution of elastic catenary. Modeling a whole span using those elements reduces the number of degrees of freedom significantly compared with discretizing the span using multiple regular cable elements. However, those elements were developed for uniform wind loads only, which is not the case for downburst winds. This motivated Aboshosha and El Damatty (2014) to develop a semi-analytical technique to solve for the conductor reactions under a general non-uniform distribution of loading. Aboshosha and El Damatty (2014) showed that this technique is quite efficient and accurate in predicting the conductor's response under downburst loading. The drawback of this technique is that it involves solving simultaneous nonlinear equations with a relatively large number of unknowns, and this requires an iterative technique. This might not be easy to handle by practitioner engineers. The first objective of the current study is to simplify this technique in order to reach a closed form solution that can be used to calculate the forces transmitted from the conductors to the towers due to a downburst with a general size and location in space. The second objective is to focus the solution to calculate the longitudinal forces for the critical downburst case recommended for the line design by El Damatty et al. (2013). The margin of error resulting from the assumptions incorporated in the developed closed form solution is

quantified. The paper starts by laying down the mathematical formulations describing the problem and deriving the closed form solution step by step for both the transverse and the longitudinal reactions due to a general downburst configuration as shown in section 3.2. The closed form solution obtained in section 3.2 requires some factors that depend on the downburst size and location.

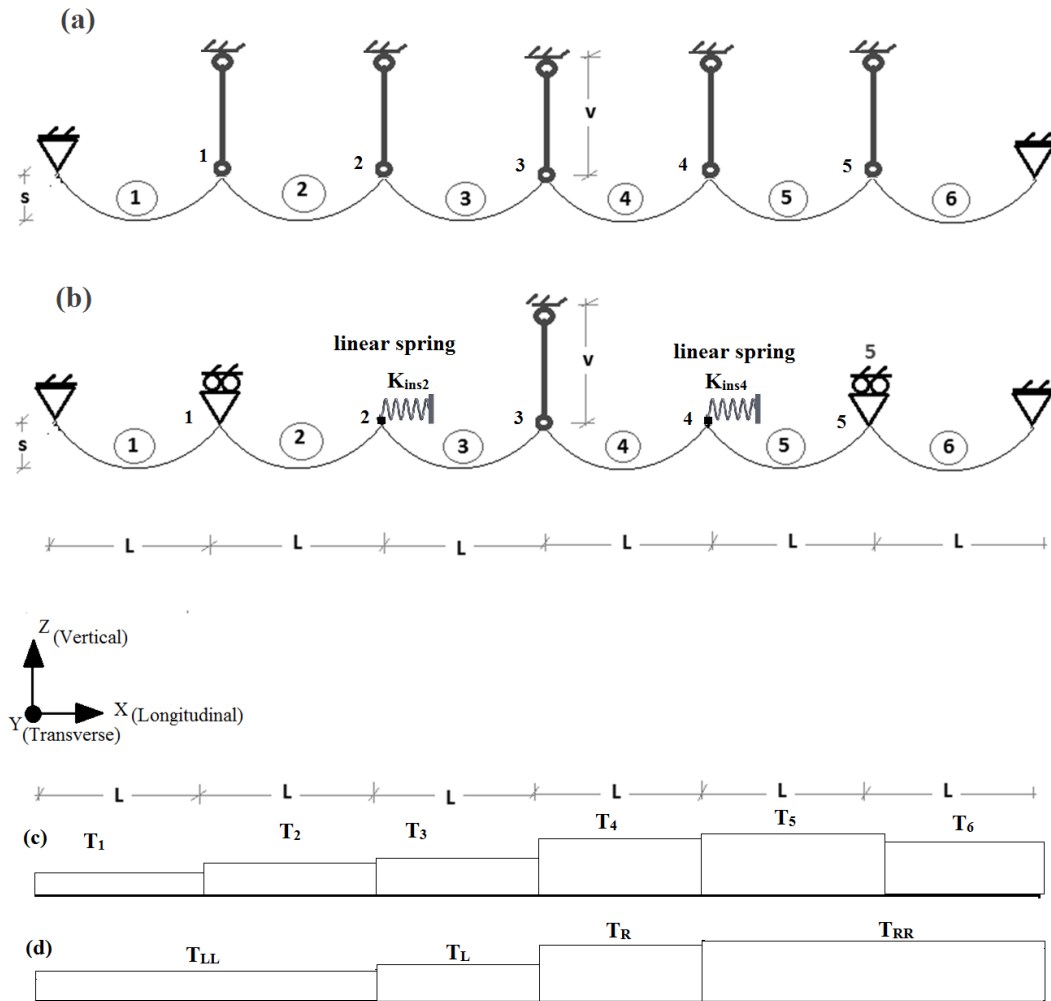


Figure 3.2 Idealization of the multi-spanned conductor system: a) Aboshosha and El Damatty (2014) b) the current study, Distribution of the tensile forces: c) Aboshosha and El Damatty (2014) d) the current study

These factors are obtained in section 3.3. In section 3.4, the formulation focuses on the critical downburst case that is responsible for inducing the maximum longitudinal conductor reaction and previously recommended for the line design. A parametric study is then conducted in section 3.5 to assess the accuracy of the closed form solution. Accuracy is estimated by comparing the reactions obtained from the closed form solution with the reactions obtained from non-linear finite element analyses.

3.2 Formulation

Based on how the conductors are supported, transmission towers can be classified into three categories: supporting towers, tension towers and end towers. For the supporting towers, conductors at both sides of the tower are supported by a single insulator to balance most of the tension forces between the two sides. This category of towers is used in the straight portion of the line and represents the majority of the towers. Tension towers are typically used when there is a change in the inclination of the line direction. Different than the supporting towers, conductors at both sides of the tension towers are supported by individual insulators. This arrangement leads to a resultant tension that needs to be resisted by the tower. Therefore, tension towers are typically stiffer than supporting towers. A tension tower can also serve as a stop-breaking tower resisting the tension force in the case of broken wires preventing the progressive collapse of supporting towers. End towers are used at the end of the TLs, which makes them subjected to a single-sided conductor tension. Similar to tension towers, end towers are stiffer than supporting towers due to the requirement of resisting the large unbalanced tension forces. In the current study, a closed form solution for the forces transmitted from the conductors to the towers is obtained for supporting and tension towers.

Fig. 3.2(a) shows the idealization of a conductor system presented by Aboshosha and El Damatty (2014). The purpose of this model was to evaluate the transverse and longitudinal forces transmitted from the conductors to the intermediate tower under downburst loading (located at point no. 3 shown in the figure). As shown in the figure, three spans on both sides of the tower are modeled in order to estimate the conductor forces transmitted to the tower. This selection of the number of spans follows the recommendation of Shehata et al. (2005), which was proposed after conducting a

parametric study by varying the number of considered spans. They found no variation in the results in terms of reactions at the intermediate tower (at point no. 3) when further spans are considered. In the model shown in the Fig. 3.2(a), the insulators are represented using link elements and the pretension conductor forces are considered in the analysis. External loads applied to the model consist of the own weight of the conductors acting in the vertical plane together with the downburst loading acting in a transverse direction relative to the line (along y-axis shown in Fig. 3.2). The conductor's tension forces vary along the six considered spans, as shown in Fig. 3.2(c), as well as the displacements (along x) of the five insulators (points 1-5). Therefore, there is a large number of unknowns in the system of equations describing the model. This system of equations is coupled and highly non-linear because of the significant flexibility of both the conductors and the insulators. Although Aboshosha and El Damatty (2014) proposed a technique for solving this system of multi-variable non-linear equations, the author believes that further simplifications are needed to come up with an analytical model that is simpler to solve and, hence, can be used by practitioner engineers. This requires developing a system that has less number of unknowns and can be decoupled without compromising the accuracy of the solution. To do so, two assumptions are made. The first assumption is in the idealization of the conductor system using the model shown in Fig. 3.2(b). Compared to the model shown in Fig. 3.2(a), insulators at nodes 1 and 5 are replaced by roller supports (instead of link members), while insulators as nodes 2 and 4 are replaced by linear springs. As noticed in Fig. 1(b), at the tower of interest (point 3), the exact stiffness of the insulator is still accounted for through the simulation of the insulator as a link member. Such an assumption will reduce the number of unknown tension forces to four (T_{LL} , T_L , T_R and T_{RR}) instead of six (T_i where $i=1:6$) as illustrated by Figs. 3.2(c, d). It also allows for decoupling of the tension forces in the left spans (T_{LL} and T_L) and in the right spans (T_{RR} and T_R), as will be discussed later in section 3.2.2. The second assumption is related to the downburst wind field. The field resulting from the CFD simulation conducted by Kim and Hangan (2007) is employed in the current study. This wind field has components in the transverse, y, and the vertical, z, directions. Shehata and El Damatty (2005), Darwish et al (2010) and Aboshosha and El Damatty (2013a) indicated that the vertical component is usually minor and, hence, can be neglected. Therefore, downburst

loads in the transverse y-direction are only considered in the current study. Due to the localized nature of downbursts, their wind field and consequently their associated loads vary in time and space. In the current study, a separation of variables between space and time is assumed for the downburst loading using Equation 3.1.

$$g_{yi}(s,t) = g_{py}(t).f(s) = g_{py}(t).(a_i + b_i s + c_i s^2) \quad \text{Equation 3.1}$$

where g_{py} : load intensity at point p which is the nearest point on the line to the downburst centre as illustrated in Figure 3.1, s: is the local axis that is equal to 0.0 and 1.0 at the beginning and at the end of the conductor span i, respectively. a_i, b_i, c_i : Polynomial constants for span i.

A similar approach was adopted by Chen and Letchford (2004a,b), Chay and Albermani (2005) and Chay et al. (2006) and Kwon and Kareem (2009). The time dependent function, $g_{py}(t)$, represents the load intensity at point p illustrated in Fig. 2, which is the nearest point on the line to the downburst centre. This point is typically subjected to the maximum load intensity from the downburst compared to other points on the line.

As indicated by Equation 3.1, a second order polynomial is assumed for the spatial variation of the downburst loading along each conductor span. Fig. 3 shows a comparison between the downburst load acting on the conductor and extracted from a previous CFD data (Kim and Hangan 2007) for a downburst with jet diameter $D_j=2.L_x$ located at $R=1.6 D_j$ and $\Theta=30^\circ$, compared with the load fitted using a second degree polynomial. The maximum difference between the two loads is found to be equal to 0.4%, which indicates that using a second order polynomial to represent the spatial variation of the loads is suitable. Expressions for the transverse reaction in the y direction, R_{y3} , and the longitudinal reaction in the x direction, R_{x3} , at the tower of interest are derived in the following subsections.

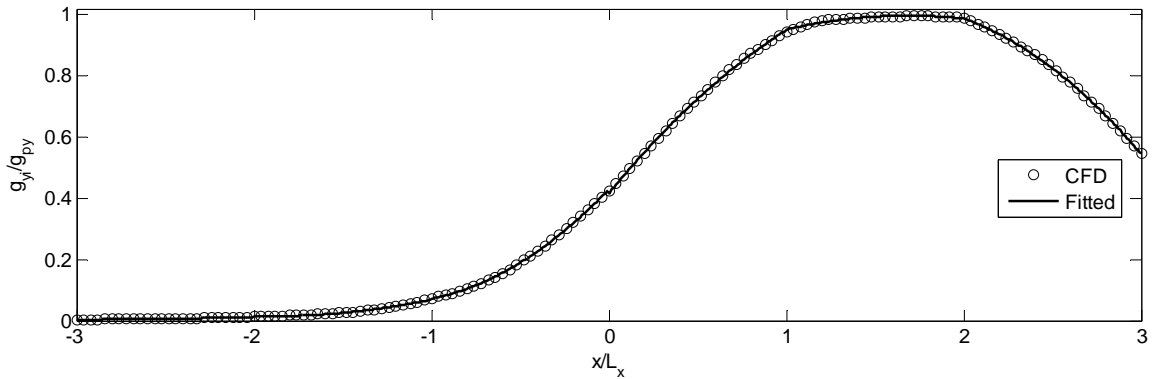


Figure 3.3 Distribution of the downburst load for $L_x/D_j=0.5$, $R/D_j=1.60$ and $\Theta=30^\circ$

3.2.1 The Transverse Reaction R_y

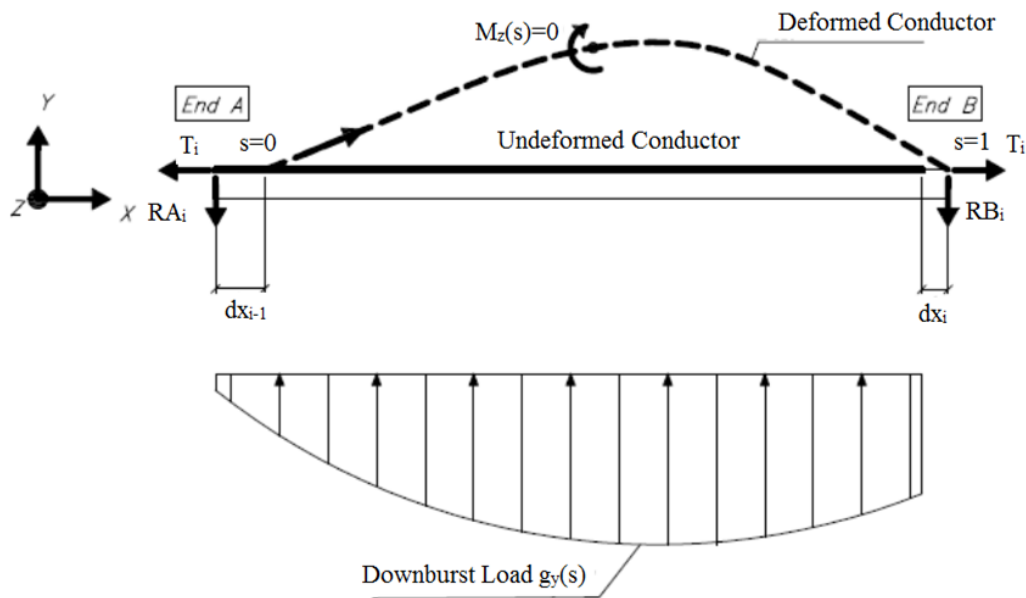


Figure 3.4 Horizontal view of conductor span i

The typical conductor span, i , illustrated in Fig. 3.4 is considered in the analysis. Displacements at the supporting points, $s=0$ and $s=1.0$, in the longitudinal x -direction, dx_{i-1} and dx_i , are allowed. By applying the moment equilibrium around z -axis at the end points "B" and "A", transverse reactions in the y direction at those points, $R_{A_{yi}}$, $R_{B_{yi}}$, can be calculated as expressed by Equations 3.2 and 3.3, respectively.

$$RA_{yi} = L_x \cdot \int_{s=0}^{s=1} g_{yi}(s) \cdot (1-s) \cdot ds = g_{y3} \cdot L_x \cdot \left(\frac{a_i}{2} + \frac{b_i}{6} + \frac{c_i}{12} \right) \quad \text{Equation 3.2}$$

$$RB_{yi} = L_x \cdot \int_{s=0}^{s=1} g_{yi}(s) \cdot (s) \cdot ds = g_{y3} \cdot L_x \cdot \left(\frac{a_i}{2} + \frac{b_i}{3} + \frac{c_i}{4} \right) \quad \text{Equation 3.3}$$

The transverse reaction in the y direction at the tower of interest, R_{y3} , can be calculated by summing the reactions from the adjacent spans, RB_{y3} and RA_{y4} , as indicated by Equation 3.4. The transverse reaction, R_{y3} , is expressed by the factor f_{y3} . This factor depends on the distribution of the downburst load along the spans adjacent to the tower of interest (no. 3 and 4 in Fig. 2) and is expressed by Equation 3.5.

$$R_{y3} = RA_{y4} + RB_{y3} = f_{y3} \cdot g_{py} \cdot L_x \quad \text{Equation 3.4}$$

$$f_{y3} = \frac{a_4}{2} + \frac{b_4}{6} + \frac{c_4}{12} + \frac{a_3}{2} + \frac{b_3}{3} + \frac{c_3}{4} \quad \text{Equation 3.5}$$

3.2.2 The Longitudinal Reaction R_x

Expression for the longitudinal reaction at the tower of interest is obtained by conducting 3 steps: (1) An expression for the tension force that developed inside a general span i , T_i , is obtained in terms of the span's end displacements. This is achieved by equating the conductor length with the length calculated from the integral of the transverse-vertical profile.

(2) Expressions for the tension in the left and right spans to the tower of interest, T_L and T_R , respectively, are derived by satisfying the equilibrium of the forces at nodes no. 2 and 4, while employing the expression obtained in step 1 for the tension T_i .

(3) Expression for the longitudinal reaction, R_{x3} , at the tower of interest is obtained by using the equilibrium of the forces at the tower of interest (node no. 3). Details about the steps involved to obtain the longitudinal reaction are discussed below.

3.2.2.1 Expression for the Tension Inside a Typical Span T_i

Expression for the conductor tension, T_i , is obtained by equating the conductor length, L_i , given by Equation 3.6 as a function of the span length L_x and the sag S , with the length obtained by integrating the transverse-vertical deformed profile of the conductor.

$$L_i = L_x \cdot \beta \quad \text{Equation 3.6}$$

$$\text{where } \beta = \left(1 + \frac{8.S^2}{3.L_x^2} \right)$$

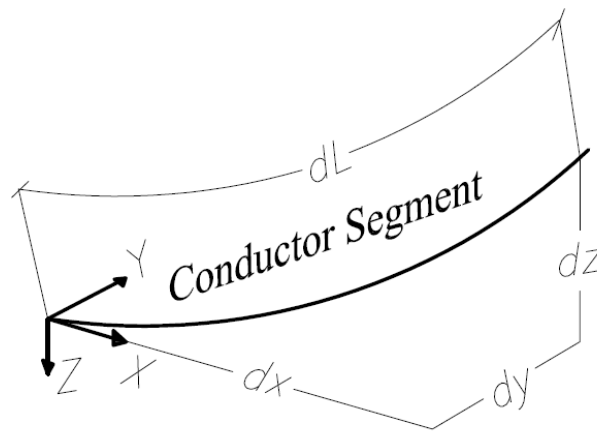


Figure 3.5 Conductor Segment

The length of an infinitesimal segment, dL , shown in Fig. 5, can be calculated as a function of the transverse slope dy/dx and the vertical slope dz/dx as indicated by Equation 3.7, which can be simplified as in Equation 3.8.

$$L_i = \int dL_i = \int \sqrt{1 + \left(\frac{dy}{dx} \right)_i^2 + \left(\frac{dz}{dx} \right)_i^2} \cdot L_x \cdot ds \quad \text{Equation 3.7}$$

$$L_i = L_x \cdot \int_0^1 \left(1 + \frac{1}{2} \left(\frac{dy}{dx} \right)_i^2 + \frac{1}{2} \left(\frac{dz}{dx} \right)_i^2 \right) \cdot ds \quad \text{Equation 3.8}$$

The derivatives dy/dx and dz/dx are required in the simplified integral and can be calculated by Equations 3.9.

$$\left(\frac{dy}{dx}(s)\right)_i = \frac{Q_{yi}(s)}{R_{xi}}, \left(\frac{dz}{dx}(s)\right)_i = \frac{Q_{zi}(s)}{R_{xi}} \quad \text{Equation 3.9}$$

Such expressions are based on the assumption that no bending moment can be resisted by the conductor and, therefore, external bending moments along the deformed conductor are equal to zero. The derivatives dy/dx and dz/dx depend on the shearing forces, $Q_{yi}(s)$ and $Q_{zi}(s)$, which are expressed by Equations 3.10.

$$Q_{yi}(s) = RA_y - g_{py} \cdot L_x \cdot \left(a_i \cdot s + \frac{b_i s^2}{2} + \frac{c_i s^3}{3}\right) \quad \text{Equation 3.10}$$

$$Q_{zi}(s) = W \cdot L_x \cdot (0.5 - s)$$

where w : the conductor weight

By substituting the shearing forces, Q_{yi} and Q_{zi} , and the derivatives, dy/dx and dz/dx , as from Equations 3.10 and 3.9, respectively, into the integral represented by Equation 3.8, the conductor tension, T_i , can be expressed by Equation 3.11.

$$T_i = \sqrt{\frac{I_i}{2(\beta - 1 - \frac{dx_i}{L_x} + \frac{dx_{i-1}}{L_x})}} \quad \text{Equation 3.11}$$

where: $I_i = \int_0^1 Q_{yi}(s)^2 ds + \int_0^1 Q_{zi}(s)^2 ds$, which equals to

$$I_i = \frac{g_{py}^2 \cdot L_x^2}{12} \cdot \left(a_i^2 + \frac{4}{15} b_i^2 + \frac{16}{189} c_i^2 + a_i \cdot b_i + \frac{3}{5} a_i \cdot c_i + \frac{1}{3} b_i \cdot c_i\right) + \frac{W^2 \cdot L_x^2}{12}$$

3.2.2.2 Tension in the Left and Right Spans of the Tower of Interest, T_L and T_R

Longitudinal reaction at the tower of interest, R_{x3} , can be calculated as the difference between the conductor tensions in the left span (no. 3), T_L , and the right span (no. 4), T_R ,

relative to the tower of interest. By using the expression for the tension force given by Equation 3.11, tension in the left span, T_L , can be expressed by Equation 3.12 as a function of the displacements dx_2 and dx_3 , where T_{L0} is the tension in the left span considering zero end displacements ($dx_2=dx_3=0$) and can be calculated using Equation 3.13. The tension, T_{L0} , expressed by Equation 3.13 is a function of the factor, f_L , which depends on the distribution of the downburst load applied to the left span and is expressed by Equation 3.14.

$$T_L = T_{L0} \cdot \frac{1}{\sqrt{1 - \frac{dx_3 - dx_2}{L_x(\beta - 1)}}} \quad \text{Equation 3.12}$$

$$T_{L0} = L_x \cdot \sqrt{\frac{W^2 + f_L \cdot g_{0y}^2}{24(\beta - 1)}} \quad \text{Equation 3.13}$$

$$f_L = a_3^2 + \frac{4}{15}b_3^2 + \frac{16}{189}c_3^2 + a_3 \cdot b_3 + \frac{3}{5}a_3 \cdot c_3 + \frac{1}{3}b_3 \cdot c_3 \quad \text{Equation 3.14}$$

By expanding the tension T_L expressed by Equation 3.12 using Taylor series, while considering the first two terms, tension in the left spans, T_L , can be expressed by Equation 3.15.

$$T_L = T_{L0} \cdot \left[1 + \frac{dx_3 - dx_2}{2L_x(\beta - 1)} \right] \quad \text{Equation 3.15}$$

The expression given for the tension in the left span to the tower of interest, T_L , (Equation 3.15), includes the displacement at the towers no. 2 and 3, dx_2 and dx_3 , respectively. The displacement dx_2 can be replaced in the equation using information regarding the tension force developed in the far left spans to the tower of interest, T_{LL} , and the spring stiffness at node 2, K_{ins2} . This is achieved by conducting the following 4 steps:

(1) Insulator at point no. 2 is modeled using a linear spring. This allows expressing the displacement dx_2 , by Equation 3.16 as a function of the force resisted by the spring, R_{x2} . It should be mentioned that modeling the insulator by a linear spring neglects the

contribution of the longitudinal reaction, R_{x2} , in the resultant force, R_{res2} . The effect of such approximation on the solution accuracy is discussed in section 3.5.

$$dx_2 = \frac{R_{x2}}{K_{ins2}} = \frac{R_{x2}}{R_{res2} / v} = \frac{R_{x2}}{L_x \sqrt{W^2 + f_{y2}^2 g_{py}^2} / v} \quad \text{Equation 3.16}$$

$$f_{y2} = \frac{a_3}{2} + \frac{b_3}{6} + \frac{c_3}{12} + \frac{a_2}{2} + \frac{b_2}{3} + \frac{c_2}{4}$$

where K_{ins2} : insulator stiffness which is equal to the R_{res2} / v , v : insulator length, R_{res2} : resultant force in the insulator which is considered equal to R_{yz2} , R_{yz2} : resultant force in the insulator considering the vertical, R_{z2} and the transverse components, R_{y2}

$$R_{yz2} = \sqrt{R_{z2}^2 + R_{y2}^2}, \quad R_{z2} = W \cdot L_x, \quad R_{y2} = f_{y2} \cdot g_{py} \cdot L_x.$$

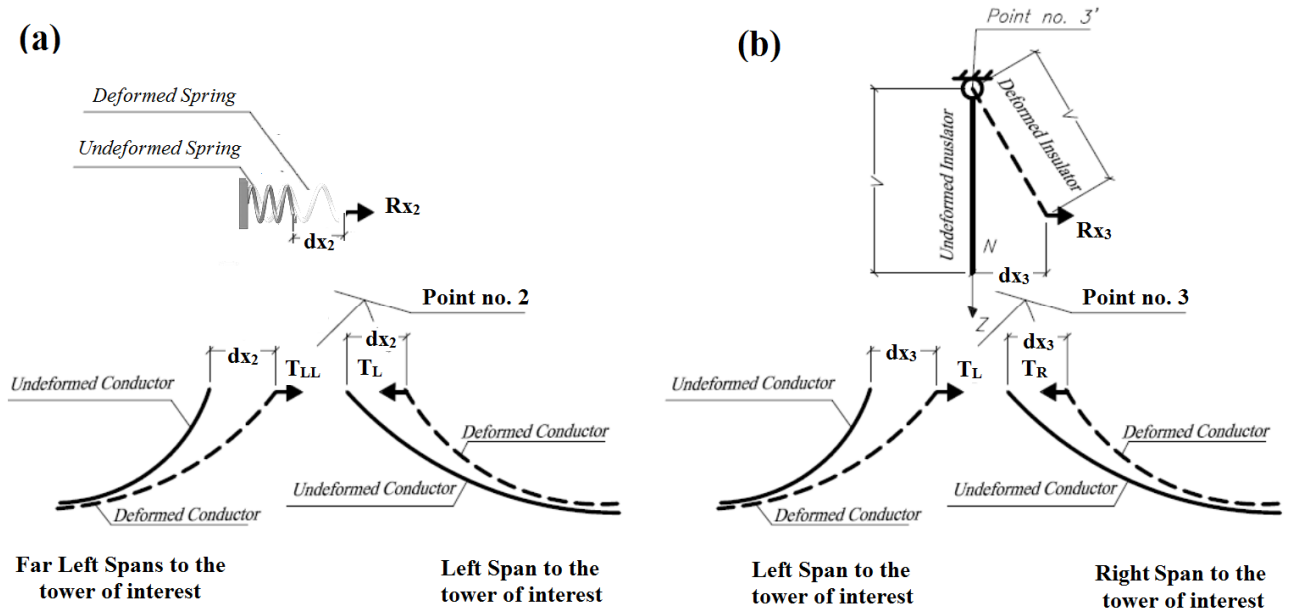


Figure 3.6 Equilibrium of the longitudinal forces (a) at point no. 2 (b) at point no. 3

(2) By applying the equilibrium of the longitudinal forces as shown in Fig. 3.6(a), the resisted force, R_{x2} , is expressed by Equation 3.17 as a function of the tension in the far left spans to the tower of interest (1st and 2nd spans), T_{LL} , and the tension in the left span to the tower of interest (3rd span), T_L ,

$$R_{x2} = T_L - T_{LL} \quad \text{Equation 3.17}$$

(3) Tension in the far left spans to the tower of interest (1st and 2nd span), T_{LL} , can be calculated using Equation 3.11, where $i = 1$ or 2 . By using the advantage that tension in the first two spans is constant, $T_1 = T_2 = T_{LL}$, the term C , defined by Equation 3.18 will be also constant for the first two spans.

$$C = \frac{1}{2T_{LL}^2} = \frac{\beta - 1 - \frac{dx_i}{L_x} + \frac{dx_{i-1}}{L_x}}{I_i} \quad i=1,2} = \frac{\sum_{i=1}^2 (\beta - 1 - \frac{dx_i}{L_x} + \frac{dx_{i-1}}{L_x})}{\sum_{i=1}^2 I_i} \quad \text{Equation 3.18}$$

The numerator in Equation 3.18 can be reduced as shown in Equation 3.19 as a function of the displacement dx_2 , only.

$$\sum_{i=1}^2 (\beta - 1 - \frac{dx_i}{L_x} + \frac{dx_{i-1}}{L_x}) = 2(\beta - 1) - \frac{dx_2}{L_x} \quad \text{Equation 3.19}$$

By substituting Equation 3.19 into Equation 3.18, tension in the far left spans to the tower of interest (1st and 2nd spans), T_{LL} , is expressed by Equation 3.20, where T_{LL0} , is the tension in the far left spans assuming no displacement at the point no.2 ($dx_2=0$) and is expressed by Equation 3.21. The tension, T_{LL} , expressed by Equation 3.21 is a function of the factor f_L , which depends on the distribution of the downburst load acting on the left spans and expressed by Equation 3.22.

$$T_{LL} = T_{LL0} \cdot [1 + \frac{dx_2}{4L_x(\beta - 1)}] \quad \text{Equation 3.20}$$

$$T_{LL0} = L_x \cdot \sqrt{\frac{W^2 + f_{LL} \cdot g_{0y}^2}{24(\beta - 1)}} \quad \text{Equation 3.21}$$

$$f_L = \frac{1}{2} \sum_{i=1}^2 a_i^2 + \frac{4}{15} b_i^2 + \frac{16}{189} c_i^2 + a_i \cdot b_i + \frac{3}{5} a_i \cdot c_i + \frac{1}{3} b_i \cdot c_i \quad \text{Equation 3.22}$$

(4) By substituting Equations 3.20, 3.17 and 3.16 into Equation 3.15, tension in the left span to the tower of interest (3rd span), T_L , can be expressed by Equations 3.23 as a function of the displacement at the tower of interest, dx_3 , only.

$$T_L = T_{L0} (\alpha_L + \gamma_L \cdot d_{x3}) \quad \text{Equation 3.23}$$

$$\alpha_L = \frac{K_L + T_{LL0}}{K_L + T_{L0}}, \quad \gamma_L = \left(2L_x (\beta - 1) \left(1 + \frac{T_{L0}}{K_L} \right) \right)^{-1}$$

$$K_L = 2L_x (\beta - 1) \left(K_{ins2} + \frac{T_{LL0}}{4 \cdot L_x (\beta - 1)} \right)$$

Similarly, tension in the right span of the tower of interest (4th span), T_R , can be expressed as a function of the displacement dx_3 only using Equations 3.24. In these equations, K_{ins4} , is the stiffness of the insulator at node no. 4 and is expressed by Equation 3.25, while T_{R0} and T_{RR0} are the tensions in the right span (4th span) and in the far right spans (5th and 6th spans) to the tower of interest considering zero displacements dx_4 and dx_5 , and are expressed by Equations 3.26 and 27, respectively. The tensions T_{R0} and T_{RR0} , are functions of the factors f_R and f_{RR} , which are expressed by Equations 3.28 ad 3.29.

$$T_R = T_{R0} (\alpha_R - \gamma_R \cdot d_{x3}) \quad \text{Equation 3.24}$$

$$\alpha_R = \frac{K_R + T_{RR0}}{K_R + T_{R0}}, \quad \gamma_R = \left(2L_x (\beta - 1) \left(1 + \frac{T_{R0}}{K_R} \right) \right)^{-1}$$

$$K_R = 2L_x (\beta - 1) \left(K_{ins4} + \frac{T_{RR0}}{4 \cdot L_x (\beta - 1)} \right)$$

$$K_{ins4} = R_{yz4} / v = \sqrt{W^2 + f_{y4}^2 g_{py}^2} \cdot L_x / v \quad \text{Equation 3.25}$$

$$f_{y4} = \frac{a_5}{2} + \frac{b_5}{6} + \frac{c_5}{12} + \frac{a_3}{2} + \frac{b_3}{3} + \frac{c_3}{4} \quad ,$$

where R_{yz4} : resultant force in insulator no. 4 considering the vertical, R_{z4} and the transverse components, R_{y4} , $R_{yz4} = \sqrt{R_{z4}^2 + R_{y4}^2}$, $R_{z4} = W.L_x$, $R_{y4} = f_{y4} \cdot g_{py} \cdot L_x$, where the factor f_{y4} , is defined in the equation and is a function of the DPs.

$$T_{R0} = L_x \cdot \sqrt{\frac{W^2 + f_R \cdot g_{0y}^2}{24(\beta - 1)}} \quad \text{Equation 3.26}$$

$$T_{RR0} = L_x \cdot \sqrt{\frac{W^2 + f_{RR} \cdot g_{0y}^2}{24(\beta - 1)}} \quad \text{Equation 3.27}$$

$$f_R = a_4^2 + \frac{4}{15} b_4^2 + \frac{16}{189} c_4^2 + a_4 \cdot b_4 + \frac{3}{5} a_4 \cdot c_4 + \frac{1}{3} b_4 \cdot c_4 \quad \text{Equation 3.28}$$

$$f_{RR} = \frac{1}{2} \sum_{i=5}^6 a_i^2 + \frac{4}{15} b_i^2 + \frac{16}{189} c_i^2 + a_i \cdot b_i + \frac{3}{5} a_i \cdot c_i + \frac{1}{3} b_i \cdot c_i \quad \text{Equation 3.29}$$

3.2.2.3 Equilibrium of the Forces at the Tower of Interest (Node no. 3)

The longitudinal reaction at the tower of interest, R_{x3} , can be calculated as a function of the displacement dx_3 , using Equation 3.30, by applying the equilibrium of the forces as shown in Fig. 6(b).

$$R_{x3} = T_R(dx_3) - T_L(dx_3) \quad \text{Equation 3.30}$$

By considering the moment equilibrium of the insulator around y-axis at point 3', shown in Fig. 6(b), displacement dx_3 can be expressed by Equation 3.31 as a function of the longitudinal reaction, R_{x3} .

$$dx_3 = \frac{v \cdot R_{x3}}{R_{res}} = \frac{v \cdot R_{x3}}{R_{yz3} \cdot \sqrt{1 + \left(\frac{R_{x3}}{R_{yz3}} \right)^2}} \quad \text{Equation 3.31}$$

By substituting the displacement, dx_3 , from Equation 3.31, into Equation 3.30, the longitudinal reaction, R_{x3} , can be expressed by Equation 3.32.

$$R_{x3} = \frac{\alpha_R T_{R0} - \alpha_L T_{L0}}{1 + \frac{v \cdot (\gamma_R T_{R0} + \gamma_L T_{L0})}{R_{yz3} \sqrt{1 + \left(\frac{R_{x3}}{R_{yz3}}\right)^2}}} \quad \text{Equation 3.32}$$

The longitudinal reaction, R_{x3} , given by Equation 3.32 contains the reaction, R_{x3} , in both sides of the equation. This is a result of P-delta effect associated with the link member used to model the insulator at the tower of interest. For the cases of relatively small wind loads, longitudinal reaction, R_{x3} , given by Equation 3.32, is found to converge using a single cycle starting from a zero value of R_{x3} . On the other hand, for the cases of higher wind loads, a small number of iterations may be required. In general it is found that 3-4 iterations are enough to obtain a converged reaction solution.

So far, expressions for the transverse, R_{y3} , and the longitudinal, R_{x3} , reactions at the tower are derived for an arbitrary downburst using Equations 3.4 and 3.32, respectively. In these equations, the effect of changing the downburst size and location are accounted for using the factors f_{yi} , f_{LL} , f_L , f_R and f_{RR} . Those factors are calculated in the following section considering a wide range of downburst sizes and locations.

3.3 Factors f_{yi} , f_{LL} , f_L , f_R , and f_{RR} and the Wind Intensity g_{py}

Due to the localized nature of downbursts, downburst parameters (DPs) illustrated in Fig. 2 and represented by the event size, D_j and its relative location to the tower of interest, given by the polar coordinates (R and Θ), define the distribution of the forces along the conductor spans (Shehata and El Damatty 2007 and Aboshosha and El Damatty 2013a).

Such DPs affect the factor f_{y3} defined by Equation 3.5 and required to obtain the transverse reaction at the tower of interest, R_{y3} , using Equation 3.4. Downburst parameters also affect the factors f_{y2} and f_{y4} defined by Equations 3.16 and 3.25 and are needed to obtain the stiffness of the linear springs, K_{ins2} and K_{ins4} , at points no. 2 and 4, respectively. A general expression for the three factors, (f_{y2} , f_{y3} and f_{y4}), satisfying

Equations 3.5, 3.16 and 3.25 can be rewritten as indicated by Equation 3.33, where $i=2, 3$ and 4. This indicates that a single graph can be generated and used to obtain the three factors using the DPs relative to the three towers 2, 3 and 4, as will be illustrated later in this section.

$$f_{yi} = \frac{a_{i+1}}{2} + \frac{b_{i+1}}{6} + \frac{c_{i+1}}{12} + \frac{a_i}{2} + \frac{b_i}{3} + \frac{c_i}{4} \quad \text{Equation 3.33}$$

In addition to the factors characterizing the transverse reactions, DPs also affect the factors f_{LL} , f_L , f_R and f_{RR} , which are required in Equations 3.21, 3.13, 3.26 and 3.27 to calculate the tension in the far left spans, T_{LL} , left span, T_L , right span, T_R , and the far right spans, T_{RR} , of the tower of interest, respectively. A parametric study, summarized in Table 3.1, is performed to obtain the variation of such factors under different DPs. In the parametric study, a conductor averaged height of 0.025-0.075 D_j is considered. This represents a range of 25 to 75 meter for a typical downburst with 1000 m diameter. According to Hangan and Kim (2007), downburst peak velocity profile is fairly constant along the height of 0.025-0.15 D_j . The downburst wind field resulting from the Computational Fluid Dynamics (CFD) simulations performed by Kim and Hangan (2007) is utilized and scaled up by the technique described by Shehata et al. (2005) to obtain the forces acting on the conductor.

The factors f_{yi} , f_{LL} , f_L , f_R and f_{RR} are calculated using Equations 3.33, 3.22, 3.14, 3.28 and 3.29 and plotted as functions of the DPs as shown in Figs. 3.7-3.11, respectively. From the figures, for the cases of a zero downburst inclination, Θ , when the span length-to-downburst diameter ratio, n_L , approaches zero, the distribution of the loads becomes uniform along the entire spans and the five factors approach unity.

Table 3.1 Summary of the parametric study

Chosen Downburst Parameters (DPs)	Value
Span lengths $L_x = n_L \cdot D_j$	$n_L = 0.0, 0.2, 0.4, 0.6, 0.8$ and 1.0
Radii $R = n_R \cdot D_j$	$n_R = 0.75, 1.0, 1.25, 1.5$ and 2.0
Angles Θ	$0^\circ, 15^\circ, 30^\circ$ and 45°

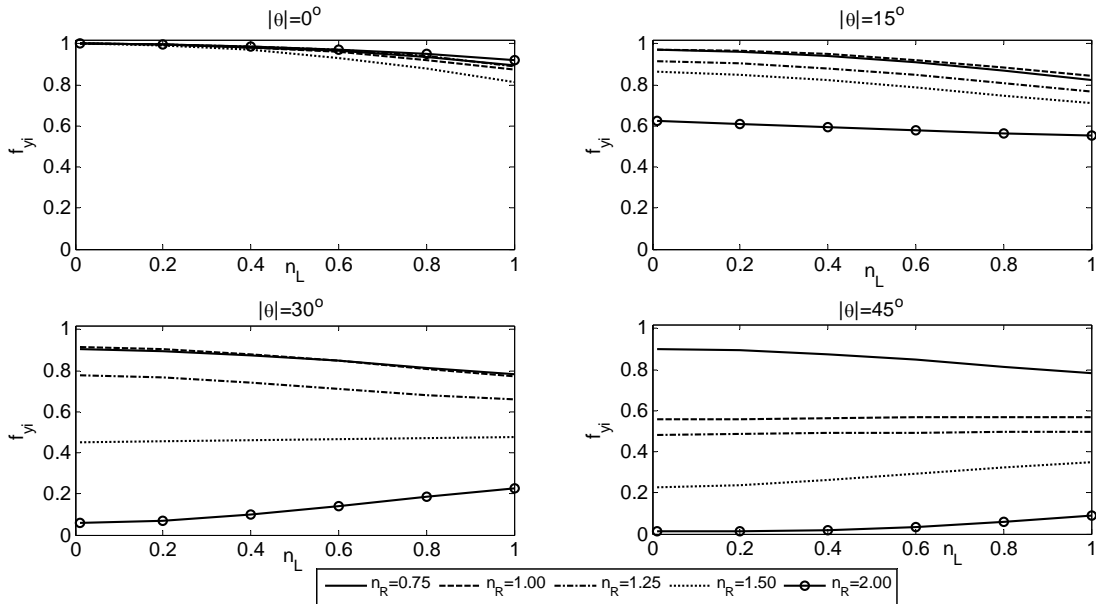


Figure 3.7 Variation of the factor f_{yi} under different DPs

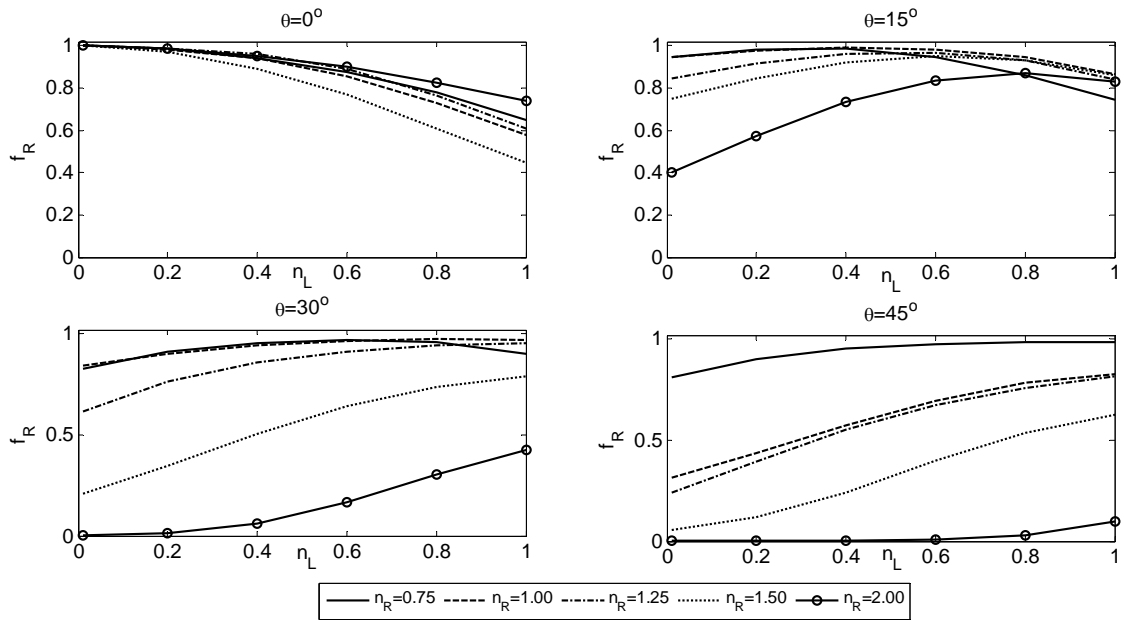


Figure 3.8 Variation of the factor f_R under different DPs

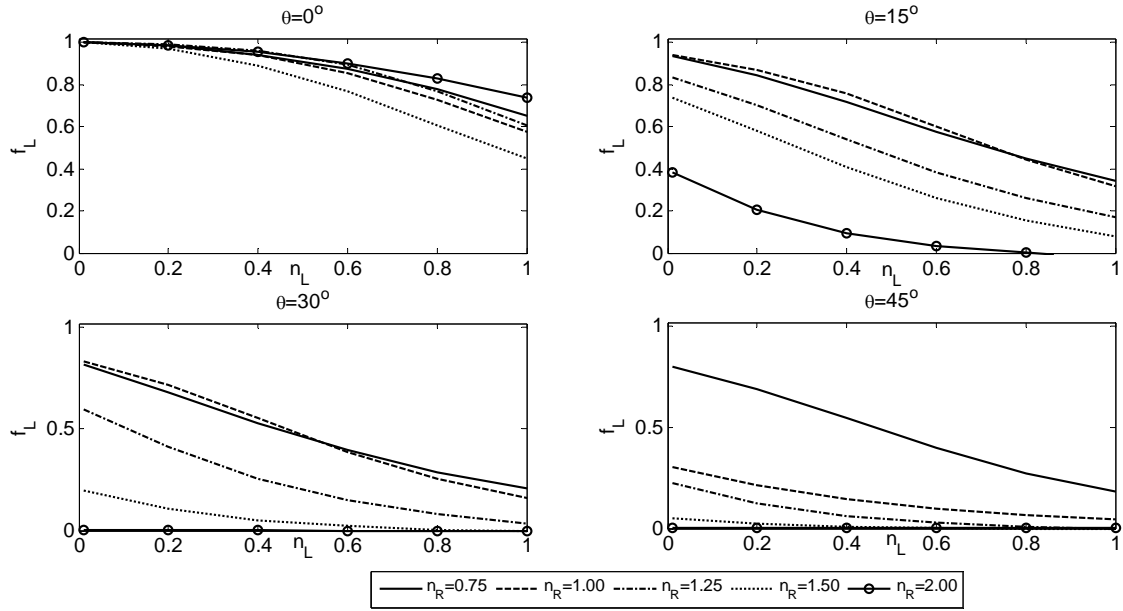


Figure 3.9 Variation of the factor f_L under different DPs

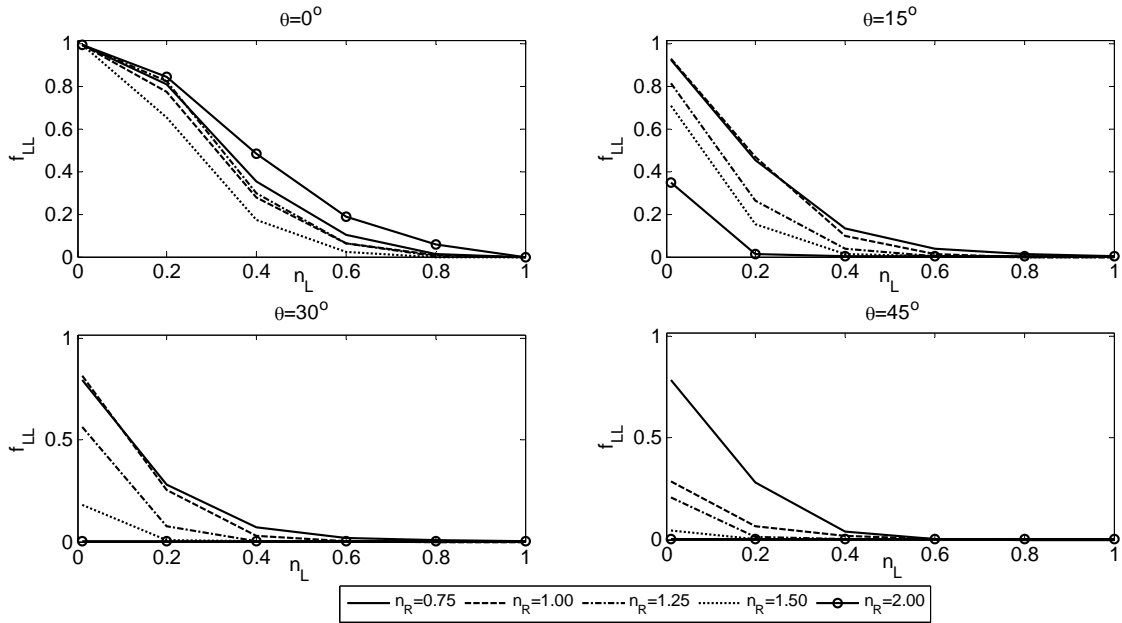


Figure 3.10 Variation of the factor f_{LL} under different DPs

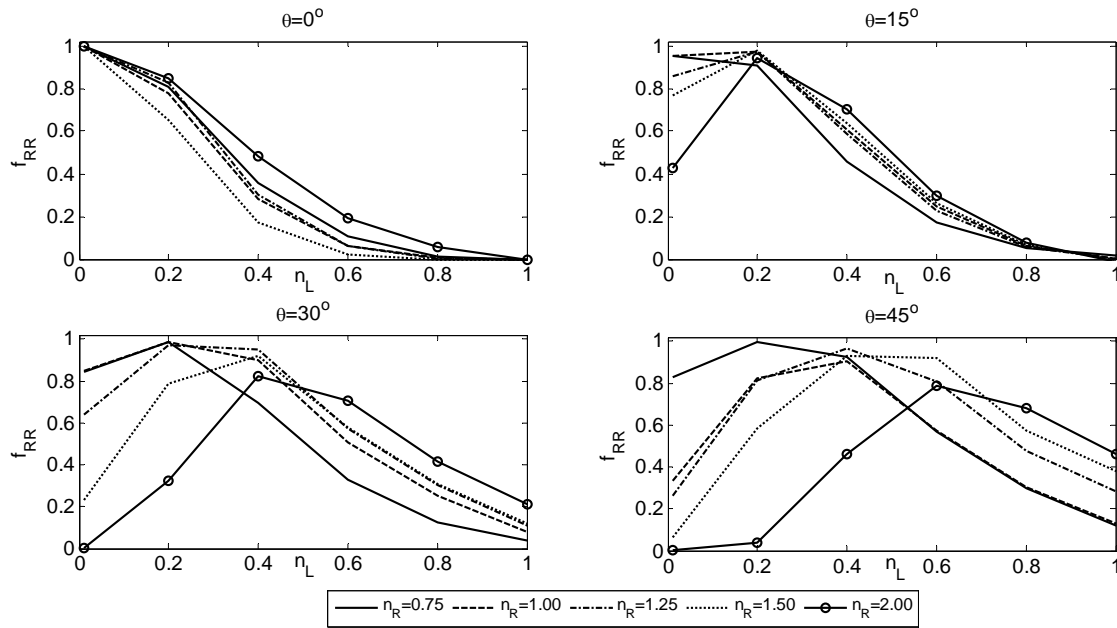


Figure 3.11 Variation of the factor f_{RR} under different DPs

That is similar to the case of normal wind, where the transverse reaction R_{y3} is simply $g_{py} \cdot L_x$ and the longitudinal reaction R_{x3} is zero. Also the figures show that as the angle Θ increases, the factors f_{RR} and f_R increase and the factors f_{LL} and f_L decrease, which induces more longitudinal Reaction, R_{x3} , as indicated by Equations 3.13, 3.21, 3.23, 3.24, 3.26, 3.27 and 3.32.

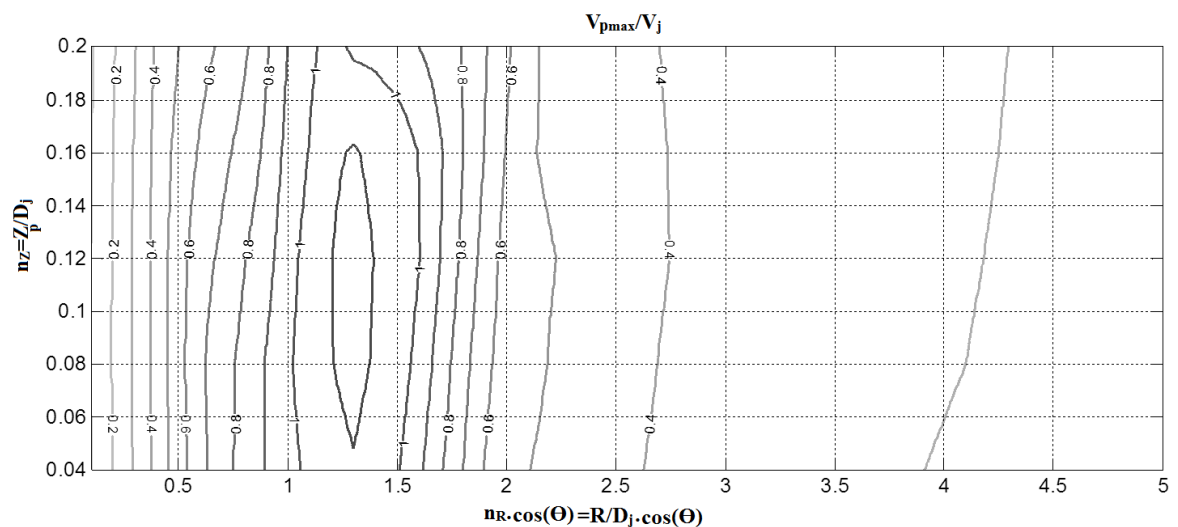


Figure 3.12 Ratio between V_{pmax}/V_j for different locations (R/D_j , Z/D_j)

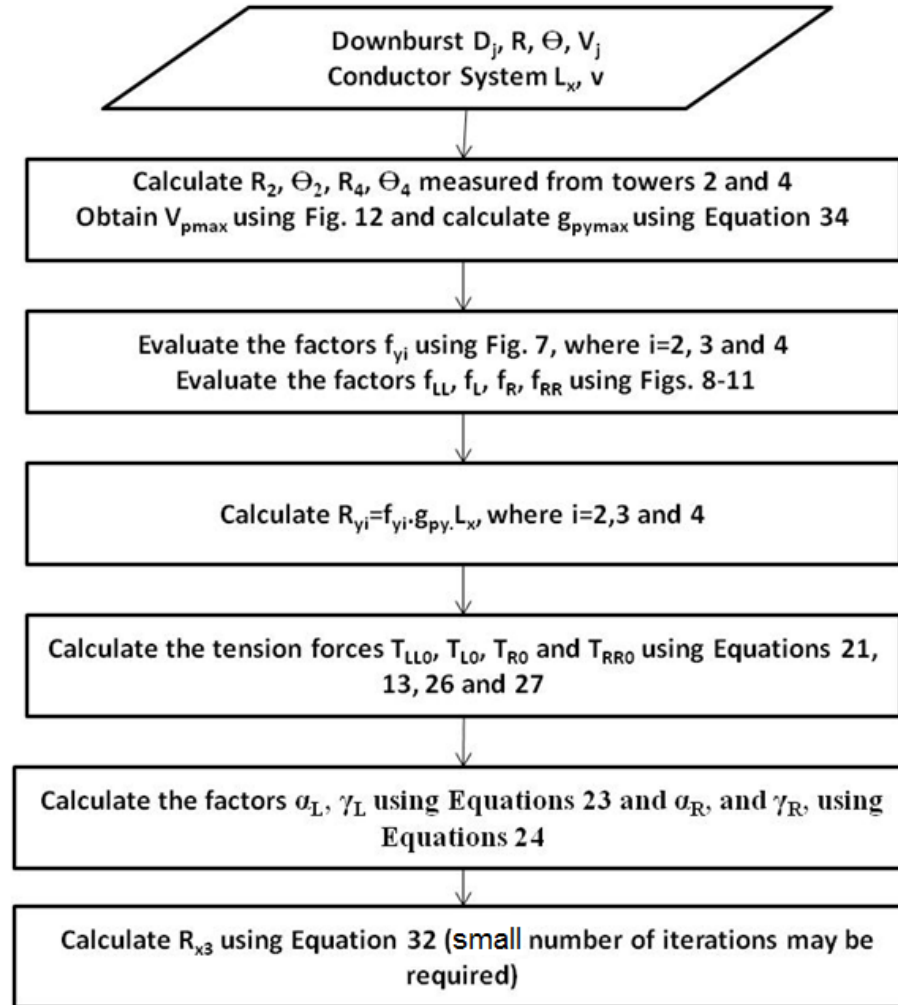


Figure 3.13 Steps to calculate the reactions at the tower of interest

The expressions given by Equations 3.4 and 3.32 together with the graphs in Figs. 3.7-3.11, can be used to calculate the temporal reactions at the tower of interest at a time t . If the maximum temporal reactions are required, temporal wind intensity at the point p , $g_{py}(t)$, can be replaced by the maximum intensity, g_{pymax} . This maximum temporal intensity is a function of the maximum temporal velocity measured at point p , V_{pmax} , as expressed by Equation 3.34. The maximum temporal velocity, V_{pmax} , is a function of the jet velocity, V_j , the horizontal distance, $R \cdot \cos(\Theta)$, from the point p to the downburst centre and the vertical elevation of point p above the ground, Z_p . In the current study, relationship between the velocity V_{pmax} and the jet velocity, V_j , is obtained from the CFD simulation by Kim and Hangan (2007) and plotted in Fig 12. This contour plot together

with Equation 34 can be used to calculate the maximum temporal intensity, $g_{Py_{max}}$, as a function of the jet velocity, V_j .

$$g_{Py_{max}} = \frac{1}{2} \rho \cdot C_d \cdot D \cdot V_{p_{max}}^2 = \frac{1}{2} \rho \cdot C_d \cdot D \cdot V_j^2 \cdot \left(V_{p_{max}} / V_j \right)^2 \quad \text{Equation 3.34}$$

where C_d : Drag coefficient of the conductor; D : facing area per unit length

Consequently, the calculation of the maximum transmitted forces at the tower of interest for an arbitrary downburst, can be conducted using the contour plot given in Fig. 12 in addition to the graphs for the factors f_y , f_{LL} , f_L , f_R and f_{RR} , given by Figs. 3.7-3.11. A summary of the steps required to predict those maximum forces is given in the flowchart presented in Figure 3.13.

As mentioned earlier, the study conducted by El Damatty et al. (2013) recommended a critical case to be considered in the line design, with DPs ($L_x/D_j=0.5$, $R/D_j=1.60$ and $\Theta=30^\circ$). This case is responsible for the maximum longitudinal reaction and, hence, is investigated in the next section.

3.4 Maximum Longitudinal Reaction, R_{x3max}

In Figure 3.13, the steps required to calculate the reactions due to a downburst having arbitrary size and location are given. These steps can be simplified by focusing on a downburst with specific parameters ($L_x/D_j=0.5$, $R/D_j=1.60$ and $\Theta=30^\circ$) leading to maximum values of the longitudinal reaction. Under these parameters, the factors f_{y3} , f_{LL} , f_L , f_R , f_{RR} , f_{y2} and f_{y4} are equal to 0.446, 0.000, 0.042, 0.517, 0.823, 0.096 and 0.890, respectively. By substituting those values into Equations 3.13, 3.21, 3.23, 3.24, 3.26, 3.27 and 3.32, the maximum longitudinal reaction, R_{x3max} , can be calculated by Equation 3.35, where f_{3max} is a parameter that depends on the sag to the span length (S/L_x), the conductor weight to the wind intensity ($W/g_{py_{max}}$) and the span to the insulator length (L_x/v), and can be obtained from Fig. 3.14. It should be mentioned that the parameter, f_{3max} , is calculated by conducting a parametric study while varying the sag to the span length (S/L_x) from 2-5%, the conductor weight to the wind intensity ($W/g_{py_{max}}$) from 25 to 400 % and the span to the insulator length (L_x/v) from 60- ∞ . These ranges are chosen

to cover most possible cases of conductors subjected to downburst wind. The case of L_x/v equal to ∞ , represents the case of conductors supported by tension towers, where the insulator length is set to zero to prevent the interaction between the spans.

$$R_{3x\max} = f_{3\max} \cdot g_{py\max} \cdot L_x \quad \text{Equation 3.35}$$

Equation 3.35 and Fig. 3.14 can be used to calculate the maximum longitudinal reaction at the tower of interest for the critical case recommended by El Damatty et al. (2013). Equations 3.4 and 3.32 together with Figs. 3.7-3.11 can be employed to calculate the reactions under a downburst with arbitrary size and location. The accuracy of the reactions estimated under the case of a downburst with an arbitrary size and location and the specific case of maximum longitudinal reaction is investigated in the next section.

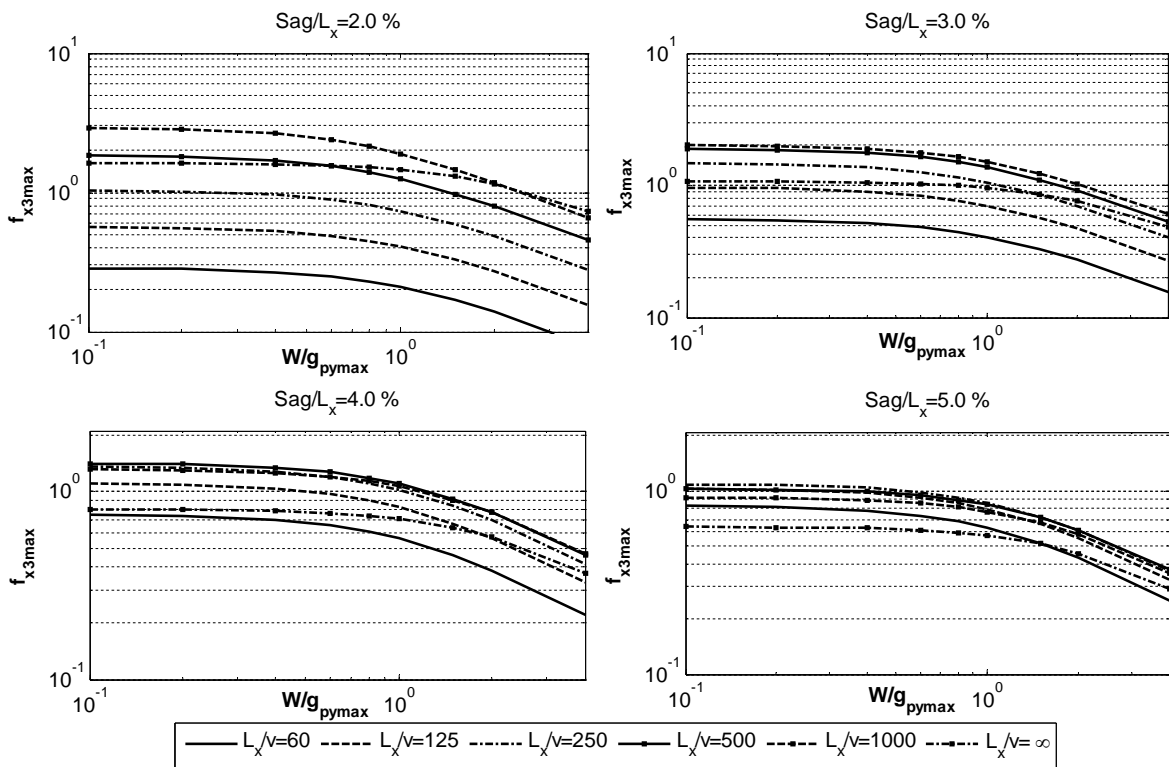


Figure 3.14 $f_{3\max}$ for the case of the maximum longitudinal reaction

3.5 Accuracy of the Proposed Solution

The conductor system, whose properties are summarized in Table 3.2, is considered for assessing the accuracy of the proposed technique under both: (1) Downburst with arbitrary size and location (2) Downburst with size and location causing maximum longitudinal reaction. The reactions of this system are predicted employing the proposed method and also employing Finite Element Analysis (FEA) using the commercial program SAP 2000 (CSI 2008). Thirty two cases, summarized in Table 3.3, are used to investigate the accuracy of the solution under downburst with arbitrary size and location. For the critical downburst case causing maximum longitudinal reaction, eighteen cases, summarized in Table 3.4, are used. Conductor reactions obtained from the proposed closed form solution in both the transverse and the longitudinal directions, (R_{3ysol} and R_{3xsol}), are compared with those obtained from the FEA, (R_{3yFEA} and R_{3xFEA}), respectively.

Table 3.2 Properties of the considered conductor system

Property	Value
Elasticity Modulus $E(N/m^2)$	6.6 E10
Weight $W(N/m)$	8.96
Facing Area from the wind $D (m^2/m)$	0.022
Drag coefficient C_d	1.0
Cross sectional Area (m^2)	3.8E-04
Insulator Length $v(m)$	3.0
Average Height (m)	40.0
Insulator length $v (m)$	1, 3 and 5
Sag/Lx	2.0-5.0 %

Generally, the results provided in Tables 3.3 and 3.4 indicate that the reactions obtained from the developed method are in a very good agreement with those calculated by FEA. As shown in the tables, the differences in the longitudinal reactions can be positive or

negative with no specific trend, but generally, the absolute differences increase with the decrease in the weight to wind load ratio, $W/g_{py\max}$.

Table 3.3 Comparison between the reaction calculated by the current method and those using FEA

Case	L_x/D_j	R/D_j	Θ	$W/g_{3\max}$	S/L	R_{ySol} (kN)	R_{yFEA} (kN)	R_{yDiff} %	R_{xSol} (kN)	R_{xFEA} (kN)	R_{xDiff} %
1	0.5	1.2	30	0.25	2.5%	9.32	9.68	-3.7%	7.765	7.421	4.6%
2	0.5	1.2	30	0.25	5.0%	9.39	9.66	-2.8%	13.420	11.686	14.8%
3	0.5	1.2	30	4	2.5%	0.58	0.60	-2.4%	0.052	0.049	5.0%
4	0.5	1.2	30	4	5.0%	0.59	0.60	-1.8%	0.111	0.107	3.9%
5	0.5	1.2	45	0.25	2.5%	4.66	4.76	-2.1%	8.087	8.585	-5.8%
6	0.5	1.2	45	0.25	5.0%	5.81	5.94	-2.1%	18.560	16.557	12.1%
7	0.5	1.2	45	4	2.5%	0.29	0.30	-3.0%	0.064	0.061	5.3%
8	0.5	1.2	45	4	5.0%	0.36	0.37	-1.7%	0.155	0.145	6.6%
9	0.5	1.6	30	0.25	2.5%	6.20	6.35	-2.2%	5.002	5.325	-6.1%
10	0.5	1.6	30	0.25	5.0%	6.18	6.32	-2.2%	13.389	12.747	5.0%
11	0.5	1.6	30	4	2.5%	0.39	0.40	-3.9%	0.044	0.042	4.8%
12	0.5	1.6	30	4	5.0%	0.39	0.40	-2.4%	0.093	0.090	3.5%
13	0.5	1.6	45	0.25	2.5%	2.73	2.77	-1.8%	3.929	4.168	-5.7%
14	0.5	1.6	45	0.25	5.0%	2.73	2.77	-1.4%	11.520	10.001	15.2%
15	0.5	1.6	45	4	2.5%	0.17	0.19	-7.4%	0.048	0.046	5.1%
16	0.5	1.6	45	4	5.0%	0.17	0.18	-4.4%	0.090	0.083	8.2%
17	1	1.2	30	0.25	2.5%	9.11	9.69	-6.0%	5.320	6.258	-15.0%
18	1	1.2	30	0.25	5.0%	9.19	9.60	-4.3%	11.100	13.140	-15.5%
19	1	1.2	30	4	2.5%	0.57	0.61	-6.3%	0.028	0.028	1.2%
20	1	1.2	30	4	5.0%	0.57	0.60	-4.3%	0.087	0.089	-2.5%
21	1	1.2	45	0.25	2.5%	6.34	6.84	-7.3%	6.430	7.534	-14.6%
22	1	1.2	45	0.25	5.0%	6.42	6.79	-5.5%	18.820	20.940	-10.1%
23	1	1.2	45	4	2.5%	0.40	0.43	-7.0%	0.040	0.039	2.3%
24	1	1.2	45	4	5.0%	0.40	0.43	-5.7%	0.145	0.151	-4.0%
25	1	1.6	30	0.25	2.5%	8.22	8.87	-7.3%	4.100	4.803	-14.6%
26	1	1.6	30	0.25	5.0%	7.88	8.36	-5.7%	12.310	14.498	-15.1%
27	1	1.6	30	4	2.5%	0.52	0.56	-7.4%	0.025	0.025	1.7%
28	1	1.6	30	4	5.0%	0.49	0.52	-5.9%	0.079	0.081	-2.1%
29	1	1.6	45	0.25	2.5%	4.23	4.24	-0.2%	4.395	4.835	-9.1%
30	1	1.6	45	0.25	5.0%	4.27	4.34	-1.6%	13.887	15.225	-8.8%
31	1	1.6	45	4	2.5%	0.26	0.28	-4.4%	0.036	0.035	2.8%
32	1	1.6	45	4	5.0%	0.27	0.27	-2.4%	0.090	0.095	-4.6%

It reaches around 15% for the case of $W/g_{py\max}=0.25$, which is a considerably small ratio. The longitudinal reactions calculated by the current method are slightly less than the reactions calculated by the FEA, with a maximum difference in the order of 7%. The differences in the transverse and in the longitudinal reactions are results of the assumptions employed in deriving the closed form solution.

Given the uncertainty in the downburst wind field, the level of accuracy of this proposed technique is believed to be acceptable. The simplicity of this method in solving a complicated non-linear structure under a complex wind field is considered to be a significant advantage in the analysis and design of the lines to resist downbursts.

Table 3.4 Reactions calculated for the case of ($L_x/D_j=0.5$, $R/D_j=1.60$ and $\Theta=30^\circ$)

Case	$W/g_{p\max}$	S/L	v (m)	R_{ySol} (kN)	R_{yFEA} (kN)	R_{yDiff} %	R_{xSol} (kN)	R_{xFEA} (kN)	R_{xDiff} %
1	0.25	2.0%	1.0	6.20	6.25	-0.9%	20.01	17.37	15.1%
2	0.25	2.0%	3.0	6.20	6.33	-2.1%	5.00	5.33	-6.1%
3	0.25	2.0%	5.0	6.20	6.75	-6.7%	2.95	3.16	-6.8%
4	0.25	3.5%	1.0	6.20	6.26	-0.9%	22.49	19.83	13.4%
5	0.25	3.5%	3.0	6.20	6.35	-2.3%	12.52	11.72	6.8%
6	0.25	3.5%	5.0	6.20	6.37	-2.6%	7.87	7.43	5.9%
7	0.25	5.0%	1.0	6.18	6.23	-0.9%	17.36	16.58	4.7%
8	0.25	5.0%	3.0	6.18	6.30	-1.9%	13.39	12.75	5.0%
9	0.25	5.0%	5.0	6.18	6.33	-2.5%	10.51	10.14	3.7%
10	4	2.0%	1.0	0.39	0.39	-0.9%	0.103	0.094	10.1%
11	4	2.0%	3.0	0.39	0.40	-3.4%	0.044	0.042	4.8%
12	4	2.0%	5.0	0.39	0.41	-5.9%	0.028	0.028	2.2%
13	4	3.5%	1.0	0.39	0.39	-0.9%	0.134	0.128	4.8%
14	4	3.5%	3.0	0.39	0.40	-2.3%	0.084	0.079	5.9%
15	4	3.5%	5.0	0.39	0.40	-3.8%	0.062	0.059	5.1%
16	4	5.0%	1.0	0.39	0.39	-0.9%	0.124	0.123	0.9%
17	4	5.0%	3.0	0.39	0.39	-1.9%	0.093	0.090	3.5%
18	4	5.0%	5.0	0.39	0.40	-2.9%	0.077	0.073	4.6%

3.6 Conclusions

A closed form solution, which can be used to calculate the forces transmitted from transmission line conductors to the towers under downburst loads, is developed in the current study. It is based on simulating the insulators to the right and to the left of the

tower of interest by a combination of roller supports and linear springs. The solution can predict the transmitted forces for a downburst with a generic size and location using a set of equations and charts. The solution is then focused on the downburst configuration causing maximum longitudinal reaction, which is recommended for the line design. The maximum longitudinal reactions are found to be dependent on three dimensionless parameters: the conductor sag-to-length ratio, the conductor weight-to-wind intensity ratio, and the span-to-insulator length ratio. Knowing these parameters, the maximum longitudinal reactions can be easily calculated using the developed technique.

The accuracy of the technique is assessed by conducting a comparison to the results obtained using non-linear finite element analyses. Thirty two cases of downburst with a generic size and location and eighteen critical downburst cases corresponding to maximum longitudinal reactions are considered.

The differences in the longitudinal reactions are found to be less than 15%, while it is less than 7% for the transverse reactions. The maximum differences occur for very light-weight conductors subjected to strong wind with a weight to wind intensity ratio, W/g_{pymax} , in the order of 0.25.

The proposed solution is simple and reasonably accurate given the complexity of both the downburst wind field and the structural behaviour of the conductor system. The authors believe that it represents a practical and useful tool for practitioners involved in the design of transmission lines, particularly under downburst loads.

3.7 References

- Aboshosha H., El Damatty A. 2013. Downburst Induced Forces on the Conductors of Electric Transmission Lines and the Corresponding Vulnerability of Towers Failure. Proceedings of the Canadian Society of Civil Engineers Conference (CSCE 2013), Montreal, QC, Canada, May 29: June 1, 2013.
- Aboshosha H., El Damatty A., 2014. Effective Technique for the Reactions of Transmission Line Conductors under High Intensity Winds. *Wind and Structures, an International Journal*. 18(3) 235-252.

- Ahmadi-Kashani, K., Bell, A.J. 1988. The analysis of cables subject to uniformly distributed loads. *Engineering Structures*, 10(3), 174-184.
- Australian Standard / New Zealand Standard AS/NZS: 7000. 2010. Overhead line design - Detailed procedures. Standards Australia Limited / Standards New Zealand, North Sydney, Australia.
- Chay, M., Albermani, F. 2005. Dynamic response of a SDOF system subjected to simulated downburst winds. *Proc., Asia-Pacific Conf. on Wind Engineering (APCWE-VI)*, 1562–1584.
- Chay, M., Albermani, F., Wilson, R. 2006. Numerical and analytical simulation of downburst wind loads. *Eng. Struct.*, 28, 240–254.
- Chen, L., Letchford, C.W. 2004a. A deterministic-stochastic hybrid model of downburst and its impact on a cantilevered structure. *Eng. Struct.*, 26(5), 619-629.
- Chen, L., Letchford, C. W. 2004b. Parametric study on the along wind response of the CAARC building to downbursts in the time domain. *J. Wind. Eng. Ind. Aerodyn.*, 92(9), 703-724.
- Computer and Structures, Inc. CSI 2008. SAP2000 V.12, CSI Analysis Reference Manual, Berkeley, California, USA.
- Darwish, M., El Damatty, A., Hangan, H. 2010. Dynamic characteristics of transmission line conductors and behaviour under turbulent downburst loading. *Wind and Structures, An International Journal*. 13(4), 327-346.
- Dempsey, D., White, H.B. 1996. Wind wreak havoc on lines. *T&D World Mag.* 48 (6), 32-42
- El Damatty, A., Aboshosha, H. 2012. Capacity of Electrical Transmission Towers under Downburst Loading. *First Australasia and South-East Asia Structural Engineering and Construction Conference*, Perth, Australia November 28th-December 02nd, 2012
- El Damatty, A., Hamada, A., Alawady, A. 2013. Development of critical load cases simulating the effect of downbursts and tornados on transmission line structures. Key note lecture on the 8th Asia-Pacific Conference on Wind Engineering, APCWE8, Chennai, India. December 10th-14th, 2013.

- Fujita, T.T. 1990. Downbursts: meteorological features and wind field characteristics, *Journal of Wind Engineering & Industrial Aerodynamics*. 36(1), 75-86.
- Irvine, H.M. 1981. *Cable Structures*, MIT Press, Cambridge.
- Kim, J., Hangan, H. 2007. Numerical simulations of impinging jets with application to downbursts. *J. Wind Eng. Ind. Aerodyn.*, 95(4), 279-298.
- Kwon, D., Kareem, A. 2009. Gust-Front Factor: New Framework for Wind Load Effects on Structures. *J. Struct. Eng.*, 135(6), 717-732.
- Li C. Q. 2000. A stochastic model of severe thunderstorms for transmission line design. *Probab. Eng. Mech.* 15, 359-364.
- McCarthy, P., Melsness, M. 1996. Severe weather elements associated with September 5, 1996 hydro tower failures near Grosse Isle, Manitoba, Canada. Manitoba Environmental Service Centre, Environment Canada. 21 pp.
- Shehata, A.Y., El Damatty, A.A., Savory, E. 2005. Finite element modeling of transmission line under downburst wind loading. *Finite Elements Anal. Des.* 42(1), 71-89.
- Shehata, A.Y., El Damatty, A.A. 2007. Behaviour of guyed transmission line structures under downburst wind loading. *Wind and Structures, An International Journal*. 10(3), 249-268.
- Shehata, A.Y., El Damatty, A.A. 2008. Failure analysis of a transmission tower during a microburst. *Wind and Structures*. 11(3), 193-208.
- Wei, P., Bingnan, S., Jinchun T. 1999. A catenary element for the analysis of cable structures. *Applied Mathematics and Mechanics (English Edition)*. 20(5), 0253-4827
- Winkelman, P.F. 1959. Sag-Tension Computations and Field Measurements of Bonneville Power Administration. AIEE Paper, 59-900
- Yu, P., Wong, P. and Kaempffer, F. 1995. Tension of conductor under concentrated loads. *J. Appl. Mech. -Trans. ASME*. 62(3), 802-809.

Chapter 4

4 Aerodynamic Damping of Transmission Line Conductors under Downburst Winds

4.1 Introduction

Electricity is carried from the source of production to the consumers by transmission lines. Transmission lines consist of towers, conductors, insulators and ground wires. Conductors, which are supported by the towers through insulators, transmit the electricity. Ground wires are used as protection elements to transmit the electric charges to the ground in the case of lightning. Transmission lines usually travel long distances and pass through rural areas and covers a wide area hard to be missed by any local wind events. A failure in a transmission lines may require a long time to repair which can cause significant economic losses on top of the repairing costs. By reviewing many cases of transmission line failures around the world, it is revealed that most of the failures are related to High Intensity Winds (HIW) in the form of downburst or tornados. Li (2000) reported that more than 90% of transmission line failures in Australia resulted from downburst events that are usually associated with thunderstorms. In September 1996, Manitoba Hydro Company, Canada, reported a failure of 19 transmission towers due to downburst as reported by McCarthy and Melsness (1996). A downburst is a strong downdraft that induces an outburst of damaging winds near the ground as indicated by Fujita (1990). Many researchers studied the behaviour and the failure of transmission towers under downbursts. However, most of those studies were performed using static analysis. Those include the studies performed by Shehata and El Damatty (2007), Darwish and El Damatty (2011), Savory et al. (2001) and Shehata et al. (2005). Only, few studies were performed using dynamic analysis. Wang et al. (2009) studied the dynamic response of a high-rise transmission tower under a moving downburst. Wind fluctuating velocities associated with the downburst were generated numerically. Wind tunnel tests were performed to obtain the drag coefficient for different tower sections. The study showed only a minor dynamic effect of the downburst on the tower, owing to the relatively high natural frequency of the tower compared with the dominant frequency of

the event. This may not be the case for the conductors, which have lower natural frequencies. Loredo-Souza and Davenport (1998) performed wind tunnel tests of two single spanned conductors subjected to turbulent normal winds. Their study showed that depending on the amount of the aerodynamic damping, the resonant response can be as important as the background response. Battista et al. (2003) and Gani and Legeron (2010) also emphasized the importance of including the dynamic effects.

On the contrary, the study conducted by Darwish et al. (2010) showed that the dynamic response is mainly due to the background component and the resonant component is minor. Two reasons might have led to such conclusions. First, wind velocity associated with downbursts can be decomposed into a non-stationary mean component and a fluctuating component. In the work done by Darwish et al. (2010), turbulent component was extracted from a real event and was assumed to be fully correlated along the conductor spans. Assuming a fully correlated turbulent component magnifies the background responses compared to the resonant responses. The second reason is related to the aerodynamic damping. Darwish et al. (2010) utilized the expression for the aerodynamic damping given by Davenport (1962) which is suitable for Normal Winds (NWs). This analytical expression does not account for the effect of increase in the conductor tensile forces and the conductor natural frequencies when subjected to a downburst. Neglecting these two parameters can exaggerate the aerodynamic damping and, consequently, unrealistically dissipate the dynamic excitation. Lin et al. (2012) studied a single span conductor subjected to 57 simulated downbursts. Although, most of their results were in the favor of neglecting the dynamic effects, some of their results had different trends, and therefore, the authors mentioned the need for further research.

The present study focuses on developing an analytical expression for the aerodynamic damping under downburst winds. The study is divided into two main parts: In the first part (provided in section 4.2), analytical expression for the aerodynamic damping is derived considering the mean velocities associated with downbursts. The expression accounts for the damping variation with the change of the Downburst Parameters (DPs), including the downburst size and relative location to the conductor. It also accounts for the change in the conductor natural frequencies due to the change in the wind speeds. In

the second part (provided in section 4.3), a Computational Fluid Dynamics (CFD) technique is developed to model the Fluid Structure Interaction (FSI) between the wind and the conductor. Such a technique is utilized to assess the accuracy of the derived expression. The CFD technique was first validated by evaluating the aerodynamic damping of a conductor under Normal Wind (NW) and comparing the results with well established and widely accepted theoretical estimation. Then, the validated CFD technique is utilized in the 3rd part (provided in section 4.4) to assess the accuracy of the aerodynamic damping under downburst.

4.2 Analytical Expression for the Conductor Aerodynamic Damping

4.2.1 Aerodynamic Damping under Downburst Winds

In this section, a derivation is performed to obtain the conductor aerodynamic damping under downburst wind. Wind velocities at a location "n" associated with a downburst can be decomposed into a non-stationary mean component, $V_{ns}(n,t)$, and a fluctuating component, $v(n,t)$, as indicated by Equation 4.1. Only the mean component is considered in this study as it is the main responsible for the aerodynamic damping (Davenport 1962). This mean component is decomposed into the multiplication of two functions, as indicated by Equation 4.2. The first function, $\phi_v(n)$, depends on the location while the second, $V_{ns0}(t)$, depends on time, similar to what was suggested by Chay et al. (2006) and Kwon and Kareem (2009). The time dependent function, $V_{ns0}(t)$, is defined as the velocity at the reference point 0, shown in Figure 4.1. Mean drag wind force, dF , applied on a small conductor length, dL , is a function of the mean wind velocity, $V_{ns}(n,t)$, and the conductor speed, V_c , as expressed by Equation 4.3. By expressing the event mean velocity, $V_{ns}(n,t)$, as the multiplication of the two functions and by eliminating the quadrature of the conductor velocity, wind drag force, dF , can be calculated using Equation 4.4. First term in Equation 4.4 represents the drag force due to mean velocity, $V_{ns}(n,t)$, while the second term is the force due to the aerodynamic damping, dF_{air} , which can be expressed by Equation 4.5. The aerodynamic damping force, dF_{air} , is a function of the conductor velocity, $V_c(n,t)$, which is equal to the modal velocity, V_{cmod} , multiplied with the value of the mode shape at the location "n", $\phi(n)$. By summing the force, dF ,

along the whole conductor span, the total damping force due to the wind, F_{airmod} , can be calculated using Equation 4.6, where $\phi_y(n)$ is the mode shape component in the direction of wind. By equating the total damping force due to wind, F_{airmod} , with the damping force for a viscous damper, F_{viscous} , expressed by Equation 4.7, an expression for the aerodynamic damping, ζ_{air} , under downbursts is obtained and is given by Equation 4.8. This expression shows a dependency of the aerodynamic damping on the mean velocities characterized by the velocity at point 0, $V_{\text{ns0}}(t)$, and the velocity distribution function, $\phi_v(n)$. The expression also shows a dependency of the damping on the natural frequencies, $f(t)$, which is a function of time in the case of downbursts. This is due to the change in conductor tension with the change of the downburst velocities. In the next subsection, an expression for the conductor tension is derived under different downburst sizes and locations. Such an expression is used to describe the change in the natural frequencies, $f(t)$, with time. It is worth mentioning that, for the horizontal conductor modes, $\phi_y=\phi$, and under Normal Winds (NWs), mean wind speed and natural frequencies become time independent ($V_{\text{ns0}}(t)=V_{\text{ns0}}$, $f(t)=f$) and the velocity profile can be assumed uniform ($\phi_v(n)=1.0$). As such, the expression for the aerodynamic damping under downburst winds, given by Equation 4.8, converges to the original expression under normal winds proposed by Davenport (1962) and given by Equation 4.9.

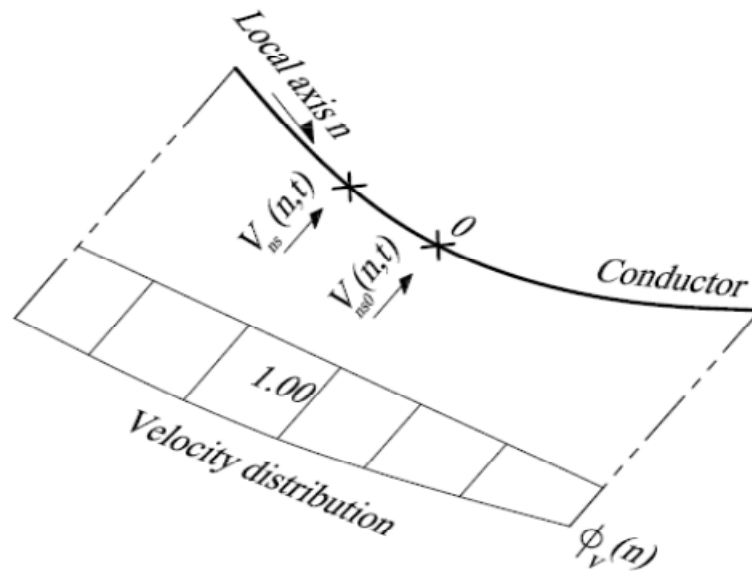


Figure 4.1 Decomposition of the mean velocity

$$V(n, t) = V_{ns}(n, t) + v(n, t) \quad \text{Equation 4.1}$$

where: n: Local coordinate attached to the conductor which varies between 0 at beginning of the conductor span to 1 at the end of the span and t is time

$V_{ns}(n, t)$: Non stationary mean component

$v(n, t)$: Fluctuating component

$$V_{ns}(n, t) = V_{ns0}(t) \cdot \phi_v(n) \quad \text{Equation 4.2}$$

$$dF = \frac{1}{2} \rho \cdot C_d \cdot D \cdot (V_{ns}(n, t) - V_c(n, t))^2 \quad \text{Equation 4.3}$$

Where:

$V_{ns0}(t)$: Non-stationary mean velocity at a reference point 0 at time t

V_c : Conductor speed

C_d : Drag coefficient of the conductor

D : Conductor projected area for the wind per unit length m^2/m

ρ : Air density

$$dF = \frac{1}{2} \rho \cdot C_d \cdot D \cdot V_{ns}(n, t)^2 + \rho \cdot C_d \cdot D \cdot V_c(n, t) \cdot V_{ns}(n, t) \quad \text{Equation 4.4}$$

$$dF_{air} = \rho \cdot C_d \cdot D \cdot V_c(n, t) \cdot V_{ns0}(t) \cdot \phi_v(n) \quad \text{Equation 4.5}$$

$$F_{airmod} = \int_0^1 dF_{air} \cdot L \cdot \phi_y(n) \cdot dn = \rho \cdot C_d \cdot D \cdot L \cdot V_{ns0}(t) \cdot V_{cmod} \int_0^1 \phi_v(n) \cdot \phi_y^2(n) \cdot dn \quad \text{Equation 4.6}$$

$$F_{viscous} = 4\pi \cdot f \cdot \zeta_{airDb} \cdot V_{cmod} \cdot m^* \quad \text{Equation 4.7}$$

Where:

f: modal frequency

ζ_{airDb} :damping ratio for the downburst wind

m^* : modal mass of the system which equals to $m.L. \int_0^1 \phi^2(n).dn$,

where m and L are the mass per unit length and the conductor length, respectively.

$\phi_y(n)$: Component of the mode shape in the direction of the wind

$$\zeta_{airDb} = \frac{C_d \rho D^2 V_{ns0}(t)}{4\pi m f(t).D} \frac{\int_0^1 \phi_v(n) \cdot \phi_y^2(n) \cdot dn}{\int_0^1 \phi^2(n) \cdot dn} \quad \text{Equation 4.8}$$

$$\zeta_{airNW} = \frac{C_d \rho D^2 V_{ns0}}{4\pi m f.D} \quad \text{Equation 4.9}$$

where

ζ_{airNW} : damping ratio under normal wind

4.2.2 Conductor Tension and Natural Frequencies under Downburst Winds

As mentioned earlier, downbursts are non stationary events associated with time-dependent mean velocities. Those time-dependent velocities lead to changing the tension force developed in the conductor with time and, consequently, altering both the conductor natural frequencies and the aerodynamic damping as implied from Equation 4.8. Therefore, this section focuses on developing expressions for the conductor tension force and the conductor natural frequencies when subjected to downbursts. Previous studies on the response of TLs subjected to downbursts (Shehata and El Damatty 2008, Darwish et al. 2010, Aboshosha and El Damatty 2013) indicated the importance of considering various potential downburst sizes and locations when studying the responses of the line. These studies also indicated that critical downburst size and location leading to maximum forces in the line are caused by high downburst radial velocities and not by vertical velocities. Conductor forces caused by the vertical velocities are usually minor and can be neglected when added to the conductor weight. As such, the effect of the vertical

velocities is neglected in the current study. Figure 4.2 shows a span of the conductor considered for the evaluation of the tension force. The span is assumed to be subjected to transverse load associated with the radial component of the downburst, g_y , and a vertical load due to conductor weight, W . As shown in Equation 4.10, the transverse load g_y is expressed by a second degree polynomial.

$$g_y(n) = g_{0y} \cdot (a + bn + cn^2) \quad \text{Equation 4.10}$$

where g_{0y} : load intensity at node 0, which is calculated by

$$g_{0y} = \frac{1}{2} \rho \cdot C_d \cdot V_{ns0}(t)^2 \cdot D \cdot \cos(\theta_0)^2$$

where θ_0 : Inclination angle between the radial component at point 0 with the perpendicular on the conductor

An expression for the tension force developed in the conductor span illustrated in Figure 4.2 is conducted by equating the span length L , expressed by Equation 4.11, with the length calculated by integrating the transverse-vertical conductor profile using Equation 4.12. Expression for the length using Equation 4.12 requires information about the derivatives of the deformed shape, dy/dx , and dz/dx . Such derivatives can be expressed as functions of the shear forces as indicated by Equation 4.13. Relationships presented in Equation 4.13 imply that no bending moment can be resisted by the conductor along its length. Shear forces along the conductor can be calculated using Equation 4.14. By substituting such shear forces from Equation 4.14 into Equation 4.12 and equating the two conductor lengths (from Equation 4.11 and from Equation 4.12), expression for the tension force, R_x , is obtained as indicated by Equation 4.15. Tension force, R_x , expressed by Equation 4.15 is valid for any arbitrary downburst where its associated loads can be fitted with a second degree polynomial. The parameter, f_y , utilized in Equation 4.15 and defined by Equation 4.16, accounts for the distribution of the downburst loads.

$$L = L_x \cdot \beta = L_x \left(1 + \frac{8}{3} \frac{s^2}{L_x^2} \right) \quad \text{Equation 4.11}$$

where

L_x : Span horizontal projected length

β : the ratio between the cable length L over the cable projected length L_x

s : Sag length under its own weight

$$L = \int dL = L_x \int_0^1 \left(1 + \frac{1}{2} \frac{dy^2}{dx^2} + \frac{1}{2} \frac{dz^2}{dx^2} \right) .dn \quad \text{Equation 4.12}$$

$$\frac{dy}{dx}(n) = \frac{Q_y(n)}{R_x}, \quad \frac{dz}{dx}(n) = \frac{Q_z(n)}{R_x} \quad \text{Equation 4.13}$$

where

$Q_y(n)$, $Q_z(n)$: Shear force at n in y and z directions

$$Q_y(n) = RA_y - g_{0y} \int_0^n (a + bn + cn^2) dn = RA_y - g_{0y} \cdot \left(a \cdot n + \frac{bn^2}{2} + \frac{cn^3}{3} \right) \quad \text{Equation 4.14}$$

$$Q_z(n) = W \cdot L_x \cdot \left(\frac{1}{2} - n \right)$$

where: RA_y : The y -reaction at point A as illustrated by Figure 4.2

$$RA_y = \frac{M_{zgyB}}{L_x} = L_x \cdot \int_0^1 g_y(n) \cdot (1-n) \cdot dn = g_{y0} \cdot L_x \cdot \left(\frac{a}{2} + \frac{b}{6} + \frac{c}{12} \right)$$

M_{zgyB} : The moment around z induced by the load g_y at point B.

$$R_x = \frac{f_y}{\sqrt{24}} \cdot L_x \cdot g_{0y} \frac{\sqrt{1 + \left(\frac{W}{f_y \cdot g_{0y}} \right)^2}}{\sqrt{\beta - 1}} \quad \text{Equation 4.15}$$

$$f_y = a^2 + b^2 \frac{4}{15} + \frac{16}{189} c^2 + a \cdot b + \frac{3}{5} a \cdot c + \frac{1}{3} b \cdot c \quad \text{Equation 4.16}$$

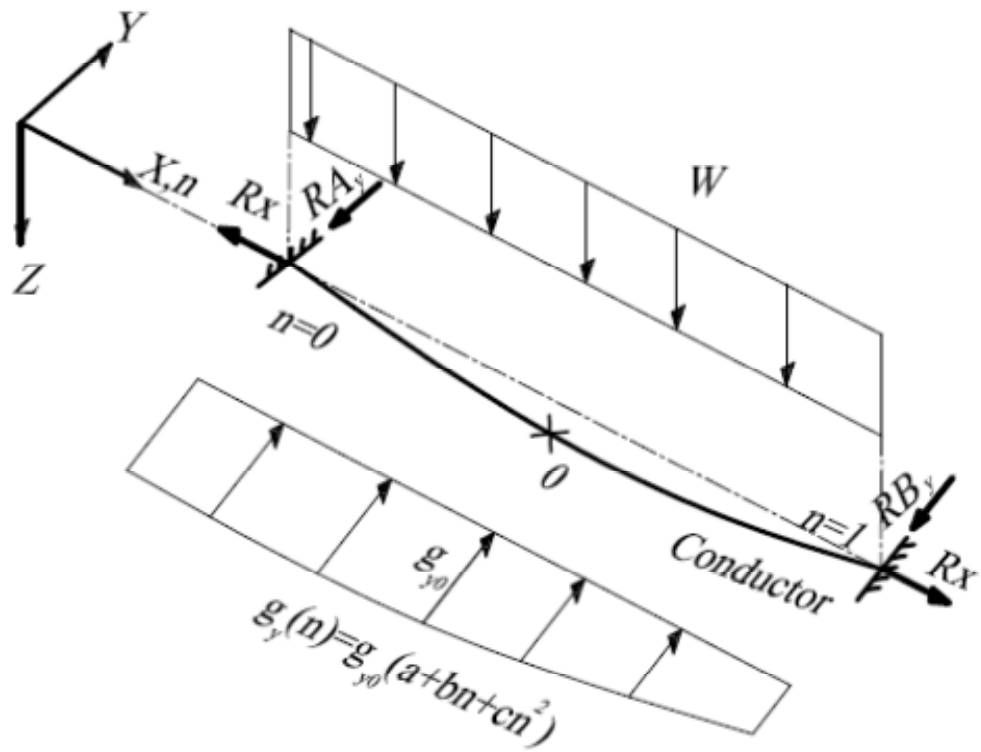


Figure 4.2 Conductor Layout

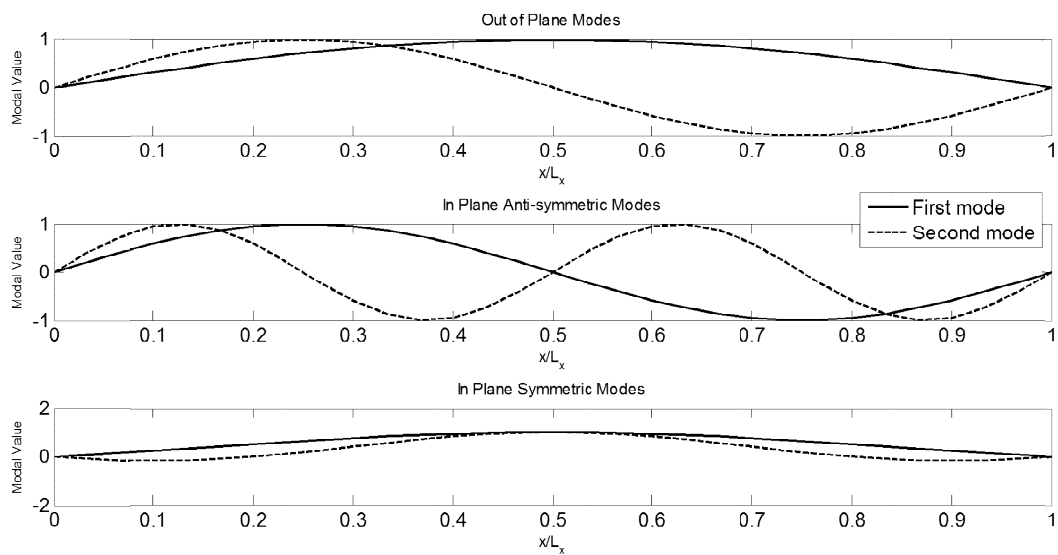


Figure 4.3 First two vibration modes for different vibration types

Irvine (1974) employed the linear theory to derive expressions for the natural frequencies and mode shapes of a sagged cable subjected to different tensile forces, and validated these expressions by experiments. Based on his findings, cable vibration modes can be classified into three types: out of plane modes, in-plane antisymmetric modes and in-plane symmetric modes. Figure 4.3 illustrates the first two modes of each type. Expressions for such modes, $\phi(n)$, are given by Equation 4.17. Irvine (1974) indicated that the cable frequencies are related to the cable axial stiffness. However, for transmission line conductors, this dependency becomes weak and natural frequencies can be expressed independently of their axial stiffness, as indicated by Equation 4.18. Expressions for the natural frequencies, given by Equation 4.18, are utilized in the current study to relate the natural frequency to the conductor tension. By substituting the conductor tension, R_x , from Equation 4.15 into Equation 4.18, natural frequencies can be estimated as a function of the mean wind velocity at node 0, as indicated by Equation 4.19. The length, L_F , required in this equation is defined in Equation 4.20, and represents the length which relates the 1st out of plane conductor natural frequency to the mean wind velocity at node 0, $V_{ns0}(t)$. The factor $C_w(t)$ also required in Equation 4.19, is defined by Equation 4.21, and inclination angle of the average plane that contains the deformed conductor, α , as illustrated in Figure 4.4. Such a factor approaches unity when the wind loads are much higher than the conductor weight. Expression for the natural frequencies, given by Equation 4.19, requires the factor f_y to be known. Such a factor is affected by the distribution of the wind loads along the conductor. As mentioned earlier, studies conducted by Shehata and El Damatty (2007a), Darwish and El Damatty (2011), El Damatty and Aboshosha (2012) indicated that the distribution of the downburst load on the conductor depends on the Downburst Parameters (DP). Those DPs, illustrated in Figure 3.1, represent the event size and relative location to the conductor defined by the polar coordinates R and Θ . Therefore, a parametric study, summarized in Table 4.1, is performed to obtain the load distributions and consequently the factor f_y . Downburst wind field resulting from the Computational Fluid Dynamics (CFD) simulation developed by Kim and Hangan (2007) is utilized. The technique illustrated by Shehata et al. (2005) is used to scale-up the velocities obtained from the CFD simulation and to obtain the forces on the conductors.

Figure 4.6 shows the parameter, f_y , for different DPs. The figure indicates that when the span length to downburst diameter ratio, n_L , decreases, the factor, f_y , approaches unity. This represents the case of uniform loading. The parameter, f_y , can be obtained from Figure 4.6 and can be employed to calculate the natural frequency, $f_N(t)$, using Equation 4.19.

$$\begin{aligned}\phi_o(n) &= (N.\pi n) \\ \phi_{ias}(n) &= \text{Sin}(2N.\pi n) \\ \phi_{is}(n) &= 0.4355(1+(-1)^{N-1} \sin((2N+1).\pi n) - \cos((2N+1).\pi n))\end{aligned}\quad \text{Equation 4.17}$$

where subscript o, is, ias represent the out of plane, in plane symmetric and in plane anti-symmetric modes, respectively, and N is the number of the mode

$$f_N(t) = \frac{N^*}{2.L_x} \sqrt{\frac{R_x}{m}} \quad \text{Equation 4.18}$$

where N^* equals to N for out of plane modes, 2N for in plane anti-symmetric modes and 2N+1 for in plane symmetric modes, and N is the number of the modes

$$f_N(t) = \frac{N^*}{L_F} C_w(t).V_{ns0}(t).Cos(\theta_0) \quad \text{Equation 4.19}$$

$$L_F = 4L_x \sqrt{\frac{\sqrt{6}.m.\sqrt{\beta-1}}{\rho C_d D L_x f_y}} \quad \text{Equation 4.20}$$

$$C_w(t) = \sqrt[4]{1 + \left[\frac{2.W}{\rho.C_d.V_{ns0}(t)^2.D.f_y.Cos(\theta_0)^2} \right]^2} \quad \text{Equation 4.21}$$

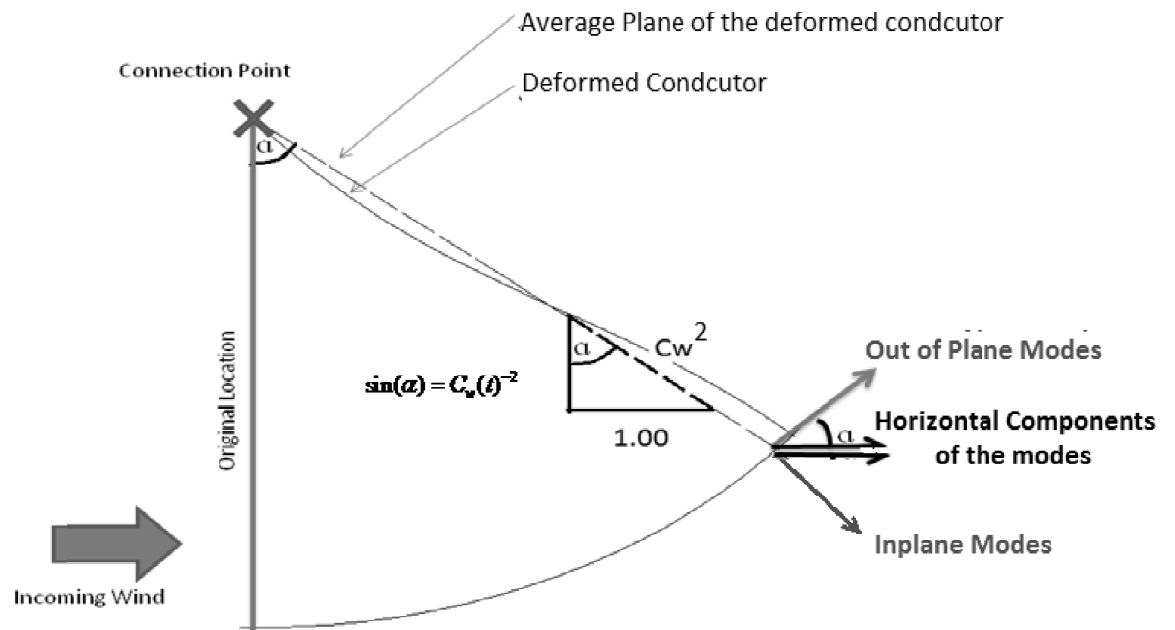
where

f_y : Load shape factor given in Figure (4.7)

L_F : Length scale which relates the 1st out of plane conductor natural frequency to the wind velocity at the origin, $V_{ns0}(t)$.

Table 4.1 Summary of the parametric study

Chosen Downburst Parameters (DPs)	Value
Span lengths $L_x = n_L \cdot D_j$	$n_L = 0.2, 0.4, 0.6, 0.8$ and 1.0
Radii $R = n_R \cdot D_j$	$n_R = 0.75, 1.0, 1.25, 1.5$ and 2.0
Angles θ	$0^\circ, 15^\circ, 30^\circ$ and 45°

**Figure 4.4 the stable location of the conductor**

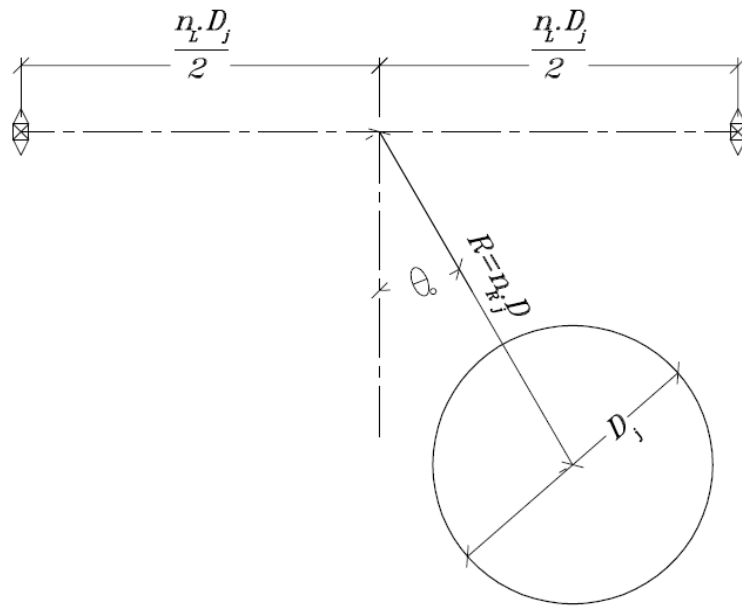


Figure 4.5 Downburst Parameters

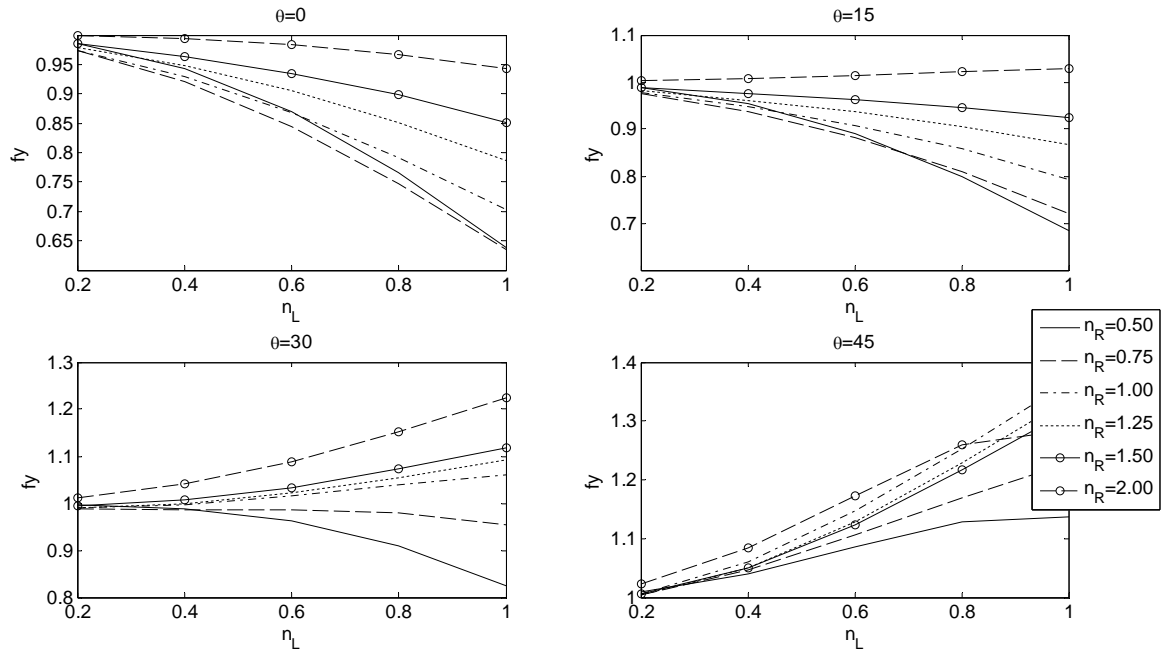


Figure 4.6 Variation of the load shape factor, f_y , with the Downburst Parameters

4.2.3 Conductor Aerodynamic Damping under Downbursts

Natural frequencies, $f_N(t)$, given by Equation 4.19, can be substituted in Equation 4.9 to obtain the aerodynamic damping. However, the expression given by Equation 4.9 requires knowledge about the horizontal component of the modes $\phi_y(n)$. Such a horizontal component is function of the conductor inclination angle, $\alpha(t)$, illustrated in Figure 4.4. By using the relationship between the inclination angle, α , and the factor $C_w(t)$, shown in Figure 4.5, expressions for the horizontal component of the modes, $\phi_y(n)$, is obtained is given in Equation 4.22. By substituting the horizontal component of the modes and the conductor frequencies obtained from Equations 4.22 and 4.19, respectively, into Equation 4.9, expression for the aerodynamic is obtained as shown in Equation 4.23. This expression shows the dependency on the Integral, I_N , defined by Equation 4.24. Such an integral is function of the DP and is obtained for the same DP summarized in Table 4.1. Values of the integral are shown in Figures 4.7, 4.8 and 4.9. It is found that beyond the first mode, $N > 1$, for the out-of plane modes, the integral I_N becomes independent of mode number, N . It is also found that the integral is almost independent of N for all the in-plane modes. Figures 4.7, 4.8 and 4.9 show that the integral I_N approaches unity for the small ratios of span length to downburst size, n_L .

$$\begin{aligned}\phi_{y-o}(n) &= \phi(n) \cdot \cos(\alpha) = \phi(n) \cdot \sqrt{1 - C_w(t)^4} \\ \phi_{y-i}(n) &= \phi(n) \cdot \sin(\alpha) = \phi(n) \cdot C_w(t)^2\end{aligned}\tag{Equation 4.22}$$

$$\begin{aligned}\zeta_{\text{air-o}} &= \frac{CdI_N}{4\pi N} \frac{\rho DL_F}{m \cdot \cos(\theta_0)} \sqrt{C_w(t)^{-2} - C_w(t)^{-6}} \\ \zeta_{\text{air-ias}} &= \frac{CdI_N}{8\pi N} \frac{\rho DL_F}{m \cdot \cos(\theta_0)} C_w(t)^{-3} \\ \zeta_{\text{air-is}} &= \frac{CdI_N}{4\pi(2N+1)} \frac{\rho DL_F}{m \cdot \cos(\theta_0)} C_w(t)^{-3} \frac{1.318}{1 + \frac{-1^{(N-1)}}{N\pi}}\end{aligned}\tag{Equation 4.23}$$

$$I_N = 2 \int_0^1 \phi_v(n) \cdot \phi_N^2(n) \cdot dn$$

$$I_{N-o} = a + \frac{b}{2} + \left(\frac{1}{3} - \frac{1}{4\pi^2 N^2} \right) \cdot c$$

$$I_{N-ias} = a + \frac{b}{2} + \left(\frac{1}{3} - \frac{1}{8\pi^2 N^2} \right) \cdot c$$

$$I_{N-is} = 0.7583 \cdot \left(\left(1 + \frac{-1^{N-1}}{N\pi} \right) \left(a + \frac{b}{2} \right) + \left(\frac{1}{3} - \frac{1.5(-1)^N}{\pi(1+2N)} - \frac{8}{\pi^2(1+2N)^2} + \frac{32(-1)^N}{\pi^3(1+2N)^3} \right) \cdot c \right)$$

Equation 4.24

where

subscripts o, i, a, s: out of plane, in plane, anti-symmetric and symmetric modes, respectively

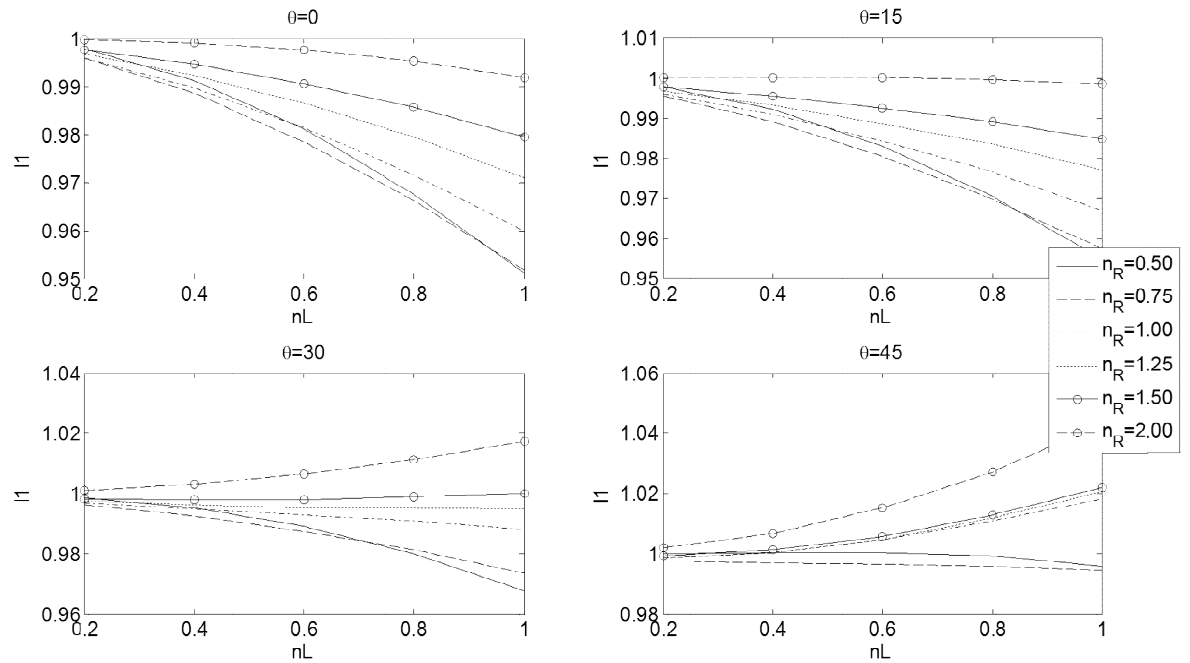


Figure 4.7 Variation of the Integral I_1 for first out of plane mode with the Downburst Parameters where $N=1$

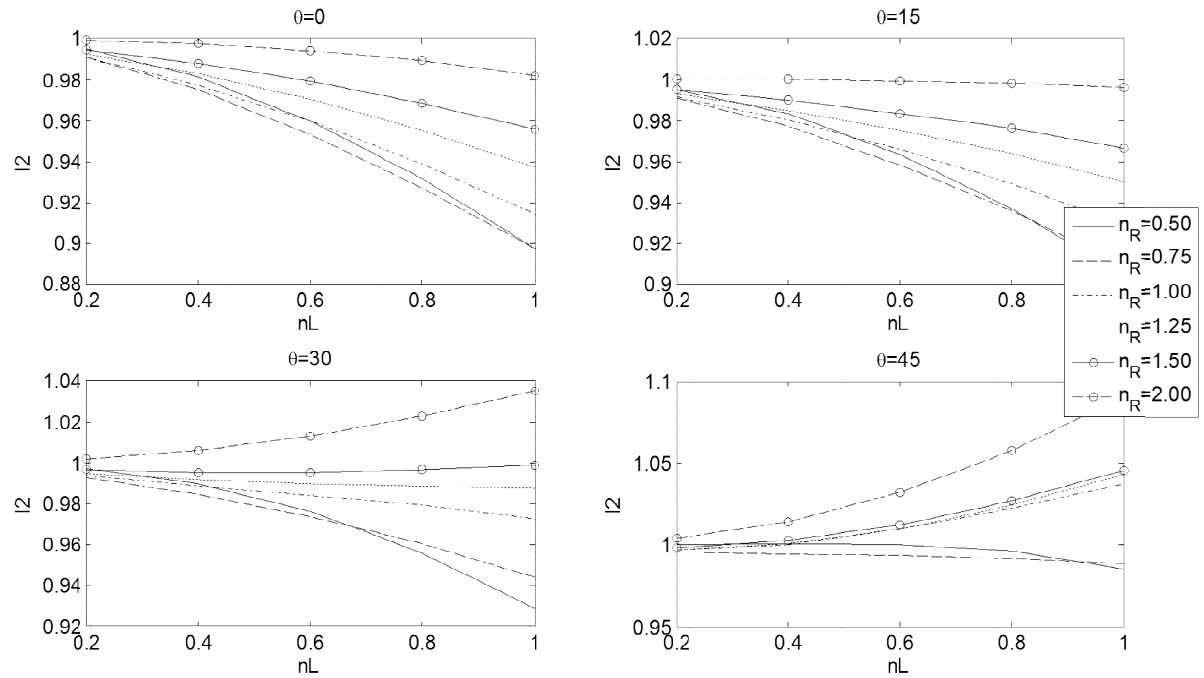


Figure 4.8 Variation of the Integral I_N with the Downburst Parameters for the in plane anti-symmetric modes where $N=1,2,\dots$ and for the out of plane modes where $N=2,3,\dots$

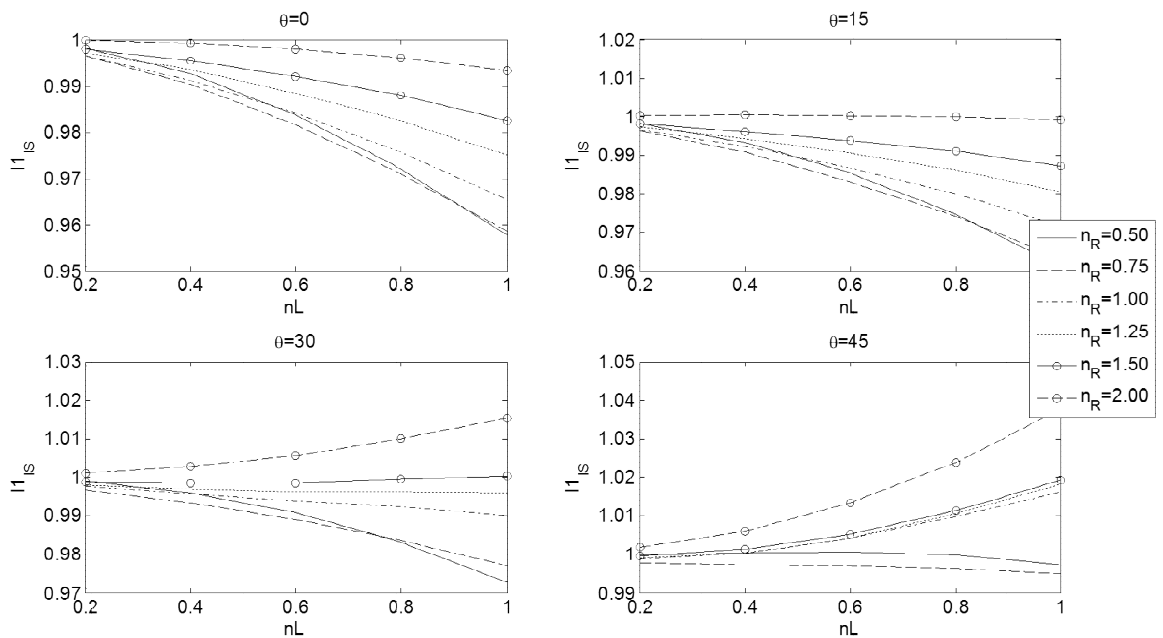


Figure 4.9 Variation of the Integral I_N with the Downburst Parameters for the in plane symmetric modes where $N=1,2,\dots$

4.3 Evaluation of the Aerodynamic Damping by CFD

In the previous section, a new analytical expression for the aerodynamic damping is derived. The accuracy of such expression needs to be assessed. Therefore, a technique based on CFD that is able to calculate the conductor damping is proposed in this section. Such a technique accounts for the Fluid Structure Interaction (FSI) that happening between the wind field and a vibrating conductor. Coupling between the wind flow and the structural deformation is considered by performing a dynamic analysis for the conductor and updating the conductor grids at each time step while solving for the wind flow using Navier-Stokes equations. In this manner, the response of a conductor placed in the wind is obtained and the aerodynamic damping from that response is evaluated as follows.

Cross sections of the conductors usually do not have sharp edges. Therefore, their drag coefficient are dependent on the Reynold's Number, Re , and the roughness of the section, as indicated by the ASCE 2010, Birjulin et al. (1960), Castanheta (1970), Engleman and Marihugh (1970), Richards (1965) and Watson (1955). Keyhan et al. (2013) performed CFD simulations to obtain the forces on a conductor subjected to gusty winds. The change of the drag coefficient, C_d , with the change of Reynolds number, Re , was considered. However, such a dependency on the Reynolds number, Re , further complicates the extraction of the damping from the obtained response, which is the main aim from this FSI technique. Therefore the Reynolds number dependency is neglected in the FSI technique. It should be mentioned that such a Reynolds number dependency can be accounted for while evaluating the aerodynamic damping using Equation 4.8 by using a velocity-dependent drag coefficient, $C_d(V_{ns0}(t))$ in the equation. Also, the developed analytical expression for aerodynamic damping can be used for a wider x-sections as long as the end-user is able to reasonably estimate the drag coefficients of the x-section under consideration.

In order to remove the dependency of the drag coefficient on Reynolds number, Re , a square conductor is used instead for validation purpose. Since the square section has different drag coefficient than the conductor section, a scaling factor is introduced to the forces obtained from the square section. Such a scaling factor is equal to the ratio

between the drag coefficient of the conductor, which is taken equal to 1.0 as recommended by the ASCE 2010, and that of the square. Properties of the conductor considered in this study are summarized in Table 4.2.

Table 4.2 Properties of the studied conductor

Length, L_x	200	m
Sag, S	10	m
Weight, W	8.96	N
Diameter, D	0.05	m
End Tension, R_x	14.5	kN
First Natural Frequency*, f_1	0.175	hz
Modal mass, M_1	91.3	N/(m/s ²)

*: Natural frequency is calculated assuming no wind case

4.3.1 CFD Technique to Obtain the Aerodynamic Damping

CFD simulations are performed using the Large Eddy Simulation (LES) sub grid scale model originally proposed by Smagorinsky (1963) and modified by Geomano et al. (1991) to tune the model constant based on the flow dynamics. The commercial software package Fluent (2006) is utilized to solve the governing flow expressed by Equations 4.25. Conductor velocity, V_c , is introduced into the governing equations to account for the conductor movement. Solving the FSI for an entire span of a conductor placed in the wind using LES can be very time consuming. That is because LES requires grid meshing in the order of the conductor cross section which is very smaller than the length of an entire span, making the entire process computationally expensive. Therefore, CFD simulations are performed on a conductor segment similar to what was used by Keyhan et al. (2013). The segment length is taken equal to 4 times the conductor diameter, D , similar to that used by Ochoa and Fueyo (2004). Murakami and Mochida (1995) indicated the importance of using a three dimensional domain to accurately predict the drag coefficient using LES. Summary of the proposed technique that performs the FSI is given by the flowchart shown in Figure 4.10. From the flowchart, a User Defined

Function (UDF) is developed as part this study and is integrated with the software FLUENT to solve for the conductor motion, which is treated as a single degree of freedom system considering the first out of plane vibration mode. Treating the conductor as a single degree of freedom system requires the modal force, $F(t)_{modal}$, to be known. Such a modal force can be calculated by integrating the applied forces along the entire span as indicated by Equation 4.26. By assuming a full correlation among those forces, a scaling is introduced to the force obtained from the computational segment, $F(t)_{seg}$, in order to obtain the required modal force, $F(t)_{modal}$, as indicated by Equation 4.27. Dimensions of the computational domain and the boundary conditions employed are shown in Figure 4.11. The domain length and width are chosen equal to 41D and 21D, respectively, to eliminate the effect of the boundary conditions on the flow near the conductor. The wall unit, y^+ , defined by Equation 4.28, is maintained less than 1.0 for all simulations. A number of 10 grids are used along the sides of the conductor to reasonably resolve the flow near the conductor. In order to resolve for the vortex shedding, dense grids are introduced near and behind the conductor with a grid size equal to $D/10$ as shown in Figure 4.11. Discretization schemes for the flow quantities and parameters of the utilized solver are summarized in Table 4.3.

Employing the technique summarized in Figure 4.10 provides time history of the conductor responses. For the cases of a conductor subjected instantaneously to a steady wind, the displacement response shows damped oscillatory movement towards the static displacement. By fitting the peaks of such decaying response with the logarithmic decrement of damping, conductor aerodynamic damping can be calculated. For the cases where the wind is non-stationary, as in downburst, there is no single value for the aerodynamic damping. Therefore instead of comparing the aerodynamic damping, the resulting displacement response can be directly compared with that obtained by solving the equation of motion employing the aerodynamic damping that is suggested in the current study. If compatible responses are found, that means it validates the suggested expression for estimating the aerodynamic damping.

Before the technique summarized in Figure 4.11 can be used to assess the accuracy of the suggested damping expression, the technique itself is examined by estimating the

aerodynamic damping of a conductor placed in a uniform steady wind and comparing the result with those obtained through well-established techniques as will be shown in section 4.3.2. Once accuracy of the technique is confirmed, it is used to assess the accuracy of the suggested damping expression, as will be shown in section 4.3.3.

$$\begin{aligned}
 \frac{\partial(\overline{u_i - V_{ci}})}{\partial x_i} &= 0 & \text{Equations 4.25} \\
 \frac{\partial \overline{u_i}}{\partial t} + (\overline{u_j - u_{gj}}) \frac{\partial \overline{u_i}}{\partial x_j} &= -\frac{1}{\rho} \frac{\partial \overline{P}}{\partial x_i} + \frac{\partial}{\partial x_j} (-\tau_{ij} + 2\nu \overline{S_{ij}}) \\
 \tau_{ij} &= \overline{u_i u_j} - \overline{u_i} \overline{u_j} \\
 \overline{S_{ij}} &= \frac{1}{2} \left(\frac{\partial \overline{u_i}}{\partial x_j} + \frac{\partial \overline{u_j}}{\partial x_i} \right) \\
 \tau_{ij} - \frac{1}{3} \delta_{ij} \tau_{kk} &= 2\nu_e \overline{S_{ij}} \\
 \nu_e &= (C_s \Delta)^2 \left(2\overline{S_{ij}} \overline{S_{ij}} \right)^2
 \end{aligned}$$

where

$i=1,2,3$ correspond to the directions x, y and z , respectively

The over bar represents the filtered quantities

$u_i, u_{gi}, p, t, \tau_{ij}$ and ν : fluid velocity, grid velocity, pressure, time, the SGS Reynolds stress and molecular viscosity coefficient, respectively.

$S_{ij}, \nu_e, \Delta, C_s$: strain rate tensor, eddy viscosity, grid size, Smagorinsky constant which is determined instantaneously based by the Geomano identity in the dynamic model (Geomano et al., 1991).

$$F(t)_{\text{modal}} = L_x \cdot \int f(n) \cdot \varphi_1(n) \cdot dn \quad \text{Equation 4.26}$$

where

$f(n)$: wind force applied on a conductor segment dn

$\varphi_1(n)$: value of the first mode shape at n

$$F(t)_{\text{modal}} = F(t)_{\text{seg}} \cdot \frac{L_x}{L_{\text{seg}}} \cdot \int \phi_1(n) \cdot dn = F(t)_{\text{seg}} \cdot \frac{2L}{\pi L_{\text{seg}}} \quad \text{Equation 4.27}$$

where:

L , L_{seg} : the conductor actual length and the conductor segment length in the CFD model

$$y^+ = \frac{y_p \cdot V_p}{\nu} \quad \text{Equation 4.4.28}$$

where

y_p : Distance to the conductor from the first grid

V_p : Velocity at the first grid point

ν : Kinematic viscosity

Table 4.3 Discretization schemes and solution technique for the CFD simulations

Parameter	Type
Time discretization	Second order implicit
Momentum discretization	Bounded central difference
Pressure discretization	Second order
Pressure-velocity Coupling	Pressure-implicit with splitting operators (PISO)
Under Relaxation Factors	0.7 for the Momentum and 0.3 for the Pressure

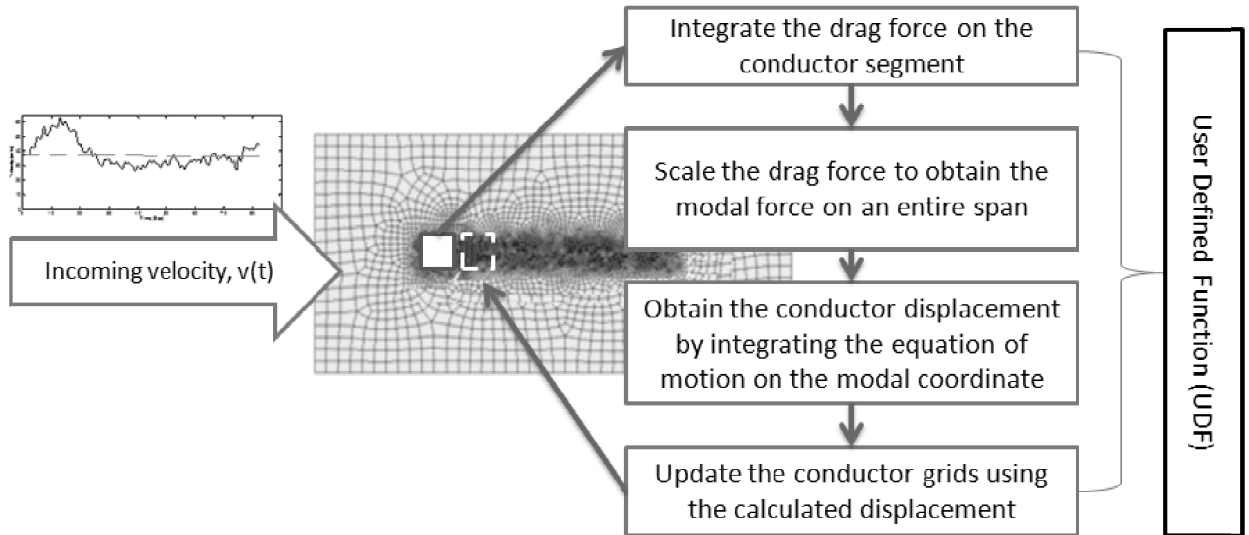


Figure 4.10 Schematic of the utilized technique to perform the FSI

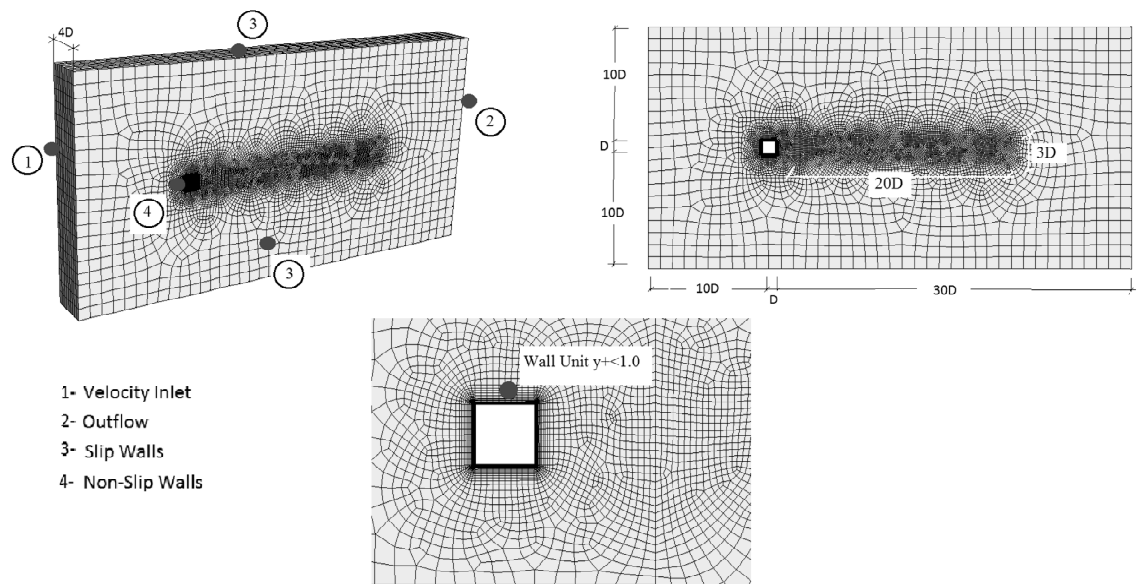


Figure 4.11 the CFD Domain and its Meshing

4.3.2 Simulating the Conductor under a Steady Uniform Winds

The conductor, whose properties are summarized in Table 4.2, is subjected to a uniform steady winds with a speed equals to 5.0 m/s. That corresponds to a Reynold's number, Re , with the order of $1.4E4$. Non dimensional time step $t^*=t.V/D=0.1$ is used to maintain the convergence, where t is the physical time step, V is the wind velocity=5m/s and D is the conductor diameter. The simulation is performed first on a stationary conductor to assess the quality of the employed grid, and then used for the movable conductor. The simulation is performed using the super computer facility available at Western University, SharcNET. Simulation for the stationary conductor employed 8 CPUs working for 6.5 hrs in order to solve for 6,500 time steps while simulation for the movable conductor, using the same number of CPUs, consumed 45 hrs in order to solve for 30,000 time steps. Simulation for the movable conductor consumes more time per time step because of updating the conductor grids.

The results of the stationary conductor are obtained in terms of the total drag force, $F_x(t)$. CFD simulation is continued until the drag force is statistically converged. Such a drag force, $F_x(t)$, is scaled to obtain the drag coefficient, $C_d(t)$, defined by Equation 4.29. Figure 4.12-a shows the variation of the drag coefficient with time. The mean, $\overline{C_d}$, and r.m.s, $\widetilde{C_d}$, drag coefficient are obtained equal to 2.2 and 0.18.

Table 4.4 compares the obtained mean and r.m.s coefficient with those from the literature. Both of the mean and r.m.s. drag coefficients fall within the published range in the literature, which gives a confidence on the employed grid. Figure 4.12-b, c. show the contour plots of the instantaneous velocity and vorticity normalized by the incoming velocity, V_{inc} , and the conductor width, D , after reaching the converged state. From both figures, it is clear that the wake structure behind the conductor is well resolved.

For the movable conductor, the results are obtained in terms of the conductor displacement response, which is represented by the continuous line in Figure 4.13. As predicted, the displacement response experiences a damping due to the conductor movement in the wind. A curve fitting for the displacement peaks is performed using the Logarithmic decrement of damping, given by Equation 4.30, as represented by the dotted

line in Figure 4.13. The predicted aerodynamic damping, ζ_{CFD} , is found equal to 6.94%. The theoretical estimation using Equation 4.9 proposed by Davenport (1962), ζ_{Th} , is found equal to 6.84% with a difference 1.5% with that predicted by the CFD. Such a small difference indicates the capability of the CFD technique to accurately estimate the aerodynamic damping.

$$C_d(t) = \frac{F_x(t)}{\frac{1}{2}\rho \cdot V^2 \cdot D \cdot L_{seg}} \quad \text{Equation 4.29}$$

Where:

ρ , L_{seg} : air density and conductor segment length, which is taken =4D

$$x(t) = x_{mean} \pm x_0 \cdot e^{-2\pi\zeta\omega_d t} \quad \text{Equation 4.30}$$

where

X_0 , X_{mean} : Displacement amplitude and the mean displacement, ω_d : Damped radial frequency $\omega_d(t) = \omega_0 \cdot \sqrt{1 - \zeta^2}$, ω_0 : Radial natural frequency

Table 4.4 the mean and RMS drag coefficient of a stationary square cylinder

Reference	$\overline{C_d}$	$\widetilde{C_d}$
Itoh and Tamura (2007)	2.05	0.25
Murakami and Mochida (1995).	2.05	0.12
Bearman and Obasaju (1982)	2.19	0.14
Ochoa and Fueyo (2004)	2.01	0.22
Current study	2.15	0.23

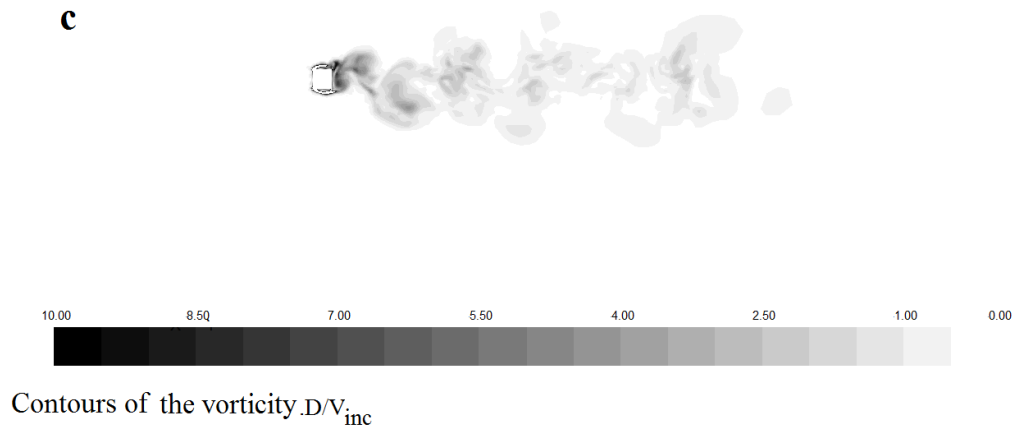
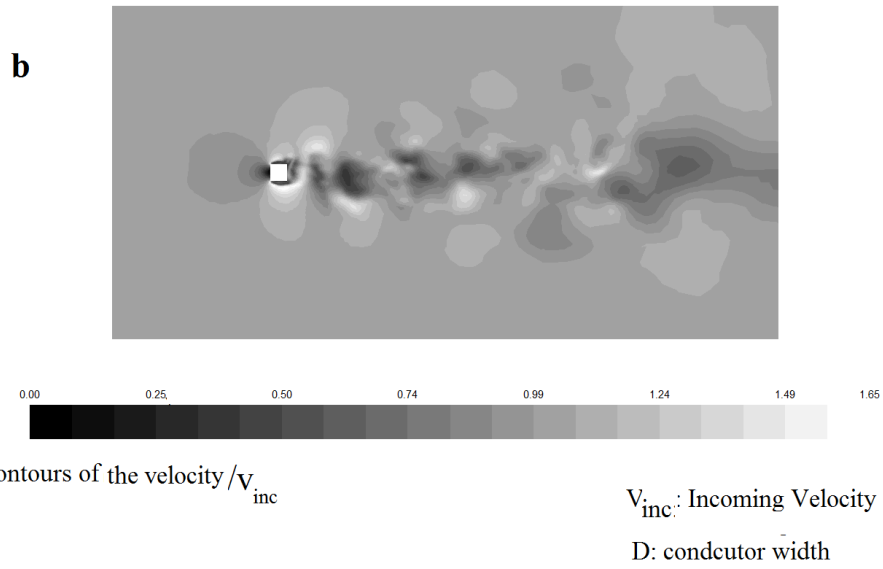
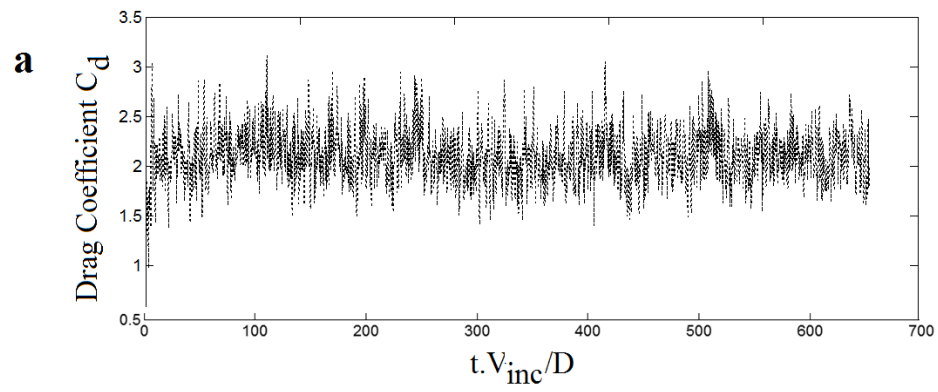


Figure 4.12 Results of the stationary conductor a-time history of the Drag Coefficient C_d b-instantaneous velocity contours c-instantaneous vorticity contours

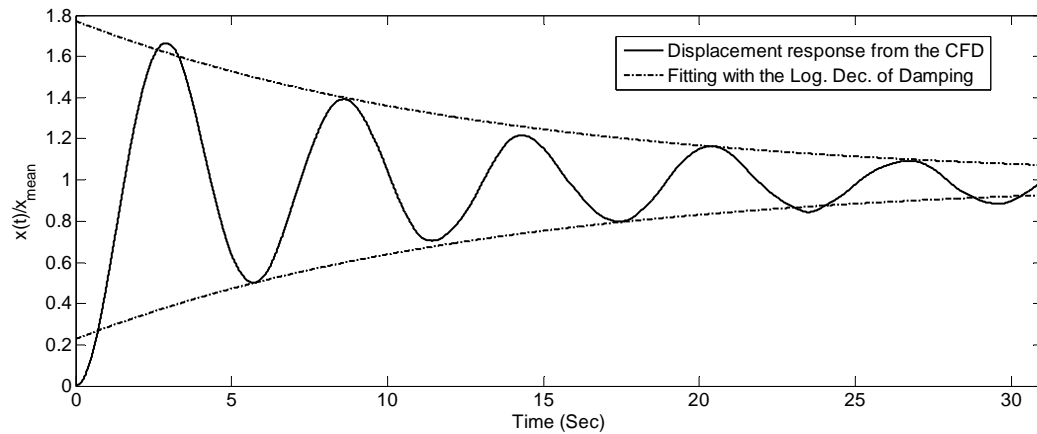


Figure 4.13 Fitting the peaks of the response with the logarithmic decrement of damping

4.3.3 Simulating the Conductor under Downburst Winds

As the technique, illustrated in Figure 10, showed reasonable accuracy of estimating the aerodynamic damping and the conductor response under a steady wind, it is used in this section to obtain the conductor response under downburst winds. Velocities associated with a downburst can be decomposed into a non-stationary mean component and a turbulent component. Mean component is extracted from the CFD simulation performed by Hangan and Kim (2007) and scaled by the technique described by Shehata et al. (2005) to represent an event of 500 m diameter with a jet velocity equals to 45m/s. Distance, R , and angle Θ , which defines the relative location between the downburst and the conductor, illustrated by Figure 3.1, are chosen to be 550 m and 0.0° , respectively. This represents the location that induces maximum conductor loads as indicated by Kim and Hangan (2007). Figure 4.14 shows a time history of the mean downburst velocity component at the conductor midpoint. The figure shows that the mean velocity needs approximately 250 seconds to pass the conductor. Simulating the entire 250 seconds using LES requires large computational demands. Therefore, only 80 seconds near the peak mean velocity, represented by the dotted line in Figure 4.14, are chosen the simulation. Turbulent velocity component is generated using the method indicated by Chen and Letchford (2004a,b) and Chay et al. (2006), where an evolutionary power

spectral density is used to describe the variation of the turbulent component along the time. Power Spectral Density (PSD) of von Karman spectrum is normalized and used in generating the fluctuating components. Turbulent Intensity is taken equal to 11% which is compatible with those reported by Holmes et al (2008) and Chan et al (2008) for real events. A cut off frequency equals to 0.5 hz is used in generating the turbulent component. Such a frequency is checked to be greater than the frequency of the 1st out of plane conductor mode, f_1 , which is calculated using Equation 4.19, and illustrated by Figure 4.15. The generated turbulent component is added to the mean component in order to obtain the total velocity at the span midpoint, as shown in Figure 4.16. CFD simulation is performed for the 80 seconds shown in Figure 16. The simulation consumed 312 hours to solve for 640,000 time steps utilizing 24 CPUs. The results are obtained in terms of the displacement response and are plotted using the continuous line shown in Figure 4.17. Such a response represents the total displacement response which can be decomposed into a mean component, a background component, and a resonant component. Resonant component, $x_r(t)$, is the only component affected by the aerodynamic damping. Therefore, such a component is extracted and plotted using the dotted line shown in Figure 4.17. The extraction is performed by calculating the summation of the mean and the backgrounds component, $x_{m+bg}(t)$, as indicated by Equation 4.31, and subtracting it from the total response. The proposed expression for the aerodynamic damping, given by Equation 4.18, is utilized to obtain the aerodynamic damping. The obtained aerodynamic damping shows variation with the time due to the change of the incoming mean velocity, as shown by Figure 18. The obtained damping is utilized in calculating the conductor response using step by step Newmark's method. More details about Newmark's method can be found in Bathe (1996). The total displacement response resulting from Newmark method is plotted by the dashed line in Figure 4.17. The resonant component is also extracted from the total response using the same way that is employed with the CFD results. Resonant displacement component is plotted using the dot-dashed line shown in Figure 4.17. It is clear from Figure 4.17 that both the total and resonant displacement resulting from employing the proposed aerodynamic formula in Newmark method and those resulting from the CFD have an excellent agreement. Such an agreement indicates

the capability of the proposed formula for predicting the aerodynamic damping under downburst winds.

$$x_{m+bg}(t) = \frac{1}{2} \frac{\rho \cdot V^2(t) \cdot D \cdot L_x \cdot I_{\phi v}}{K_1(t)} \tag{Equation 4.31}$$

Where:

$$I_{\phi v} = \int_0^1 \phi_v^2 \cdot \phi_1(n) \cdot dn = \frac{2}{\pi}$$

$K_1(t)$: modal stiffness for the first mode $= (2 \cdot \pi \cdot f_1(t))^2 \cdot M_1$, M_1 :
modal mass for the first mode $= 91.3 \text{ N/(m/s}^2)$

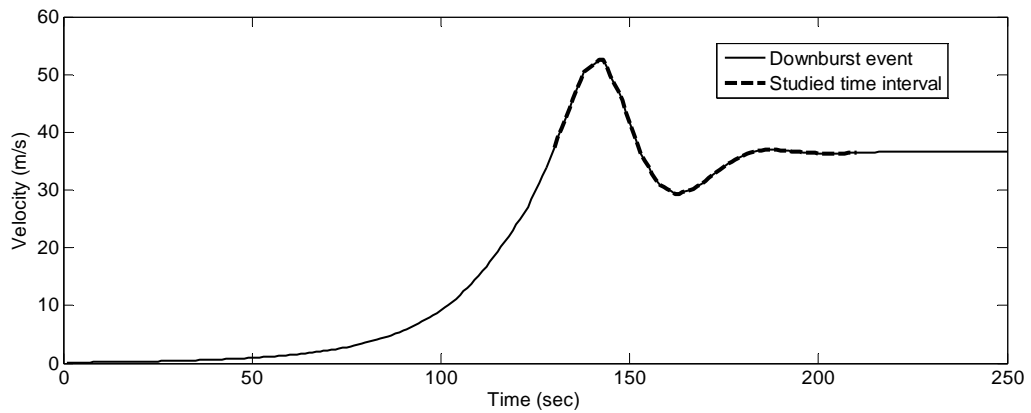


Figure 4.14 Time history of the non-stationary mean velocity component at the conductor midpoint

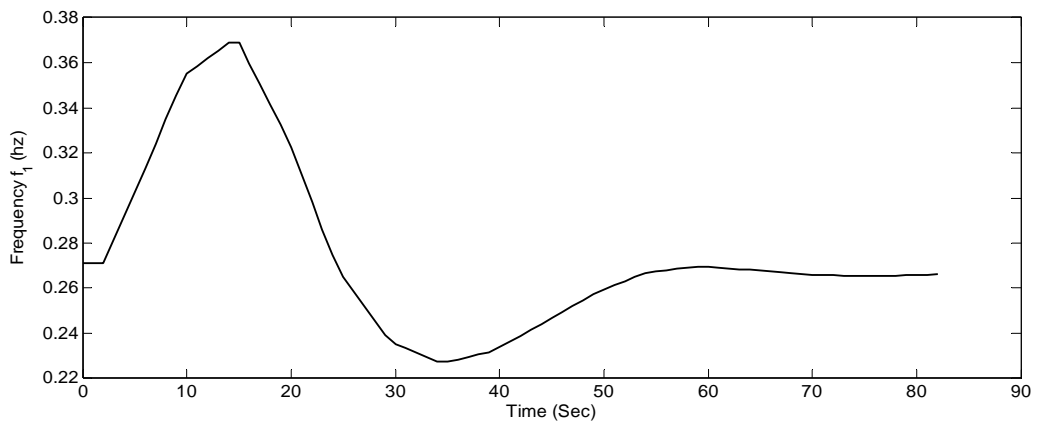


Figure 4.15 Variation of the 1st natural frequency with time

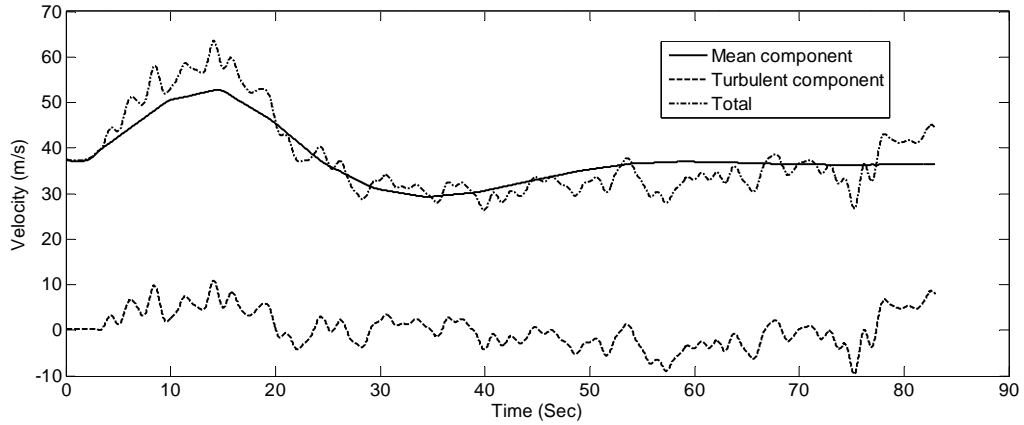


Figure 4.16 Mean, turbulent and total wind velocity at the conductor midpoint

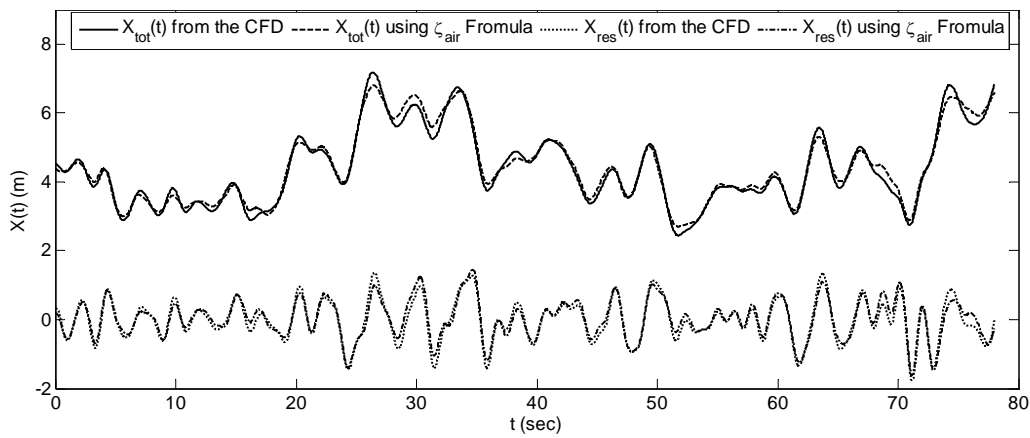


Figure 4.17 Total and resonant displacement responses resulted from the CFD and from employing the recent damping formula

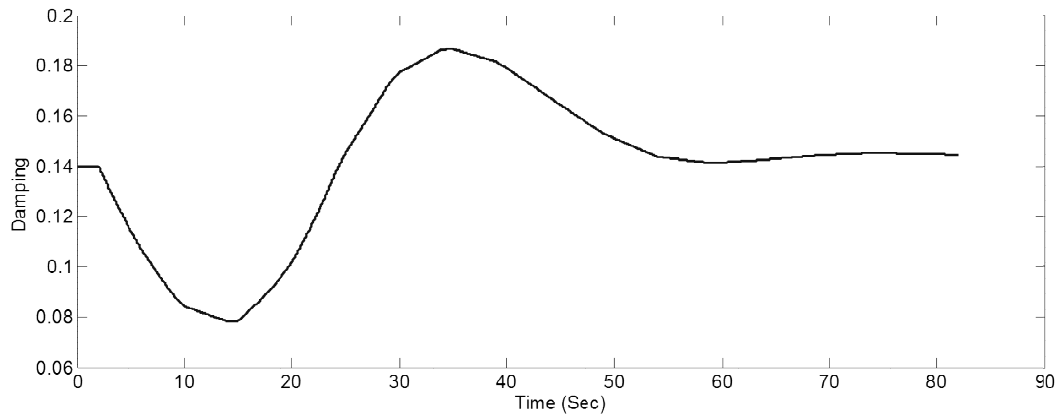


Figure 4.18 variation of the aerodynamic damping of the first mode with the time

4.4 Conclusions

An expression for the aerodynamic damping of a transmission line conductor subjected to downburst winds is analytically derived. The new expression accounts for the temporal variation of the natural conductor frequencies due to the temporal changes in the mean wind velocities. Such a variation does not appear in the case of normal winds, where wind velocities have a stationary mean component. Accounting for the temporal variation of the natural frequencies is performed by, first, deriving an expression for the conductor tension, and then, relating the conductor frequencies to such tension. The derived expression for the aerodynamic damping accounts for different downburst sizes and relative locations to the conductor. In order to assess the accuracy of such an expression, a CFD technique that is able to obtain the response of a conductor placed in the wind, is developed. Such a technique accounts for the Fluid Structure Interaction (FSI) between the wind and the conductor by allowing the conductor grids to move inside the wind domain. This CFD technique is used first to obtain the response of a conductor, which moves from rest, when subjected to a uniform steady wind. The conductor responds dynamically to the wind forces, with a damped motion. By fitting the peaks of that damped motion, aerodynamic damping of the conductor is estimated. The estimated damping shows good agreement when compared with the theoretical damping proposed by Davenport (1962), which validates the ability of the developed CFD technique to obtain the FSI between the wind and the conductor. The developed CFD technique is then utilized to assess the accuracy of the proposed aerodynamic damping expression under downburst winds. Since, there is no single value for the aerodynamic damping under downburst winds, conductor responses obtained from the CFD are compared with those using typical dynamic analysis, employing Newmark method, where the damping is obtained from the proposed expression. Compatible results are found between the responses obtained from the CFD and those obtained using dynamic analysis employing the proposed damping expression. Such results indicate the capability of the proposed expression of estimating the aerodynamic damping under downburst winds.

4.5 References

- Aboshosha, H., El Damatty, A., (2013)," Downburst Induced Forces on the Conductors of Electric Transmission Lines and the Corresponding Vulnerability of Towers Failure", CSCE 2013 Conference, Montreal, QC, Canada, May 29: June 1.
- ASCE, (2010), "Guidelines for electrical transmission line structural loading", ASCE Manuals and Reports on Engineering Practice, 74.
- Bathe, K.J. (1996), *Finite Element Procedures in Engineering Analysis*, Prentice-Hall, Englewood Cliffs, New Jersey.
- Bearman, P. and Obasaju, E. (1982), "An experimental study of pressure fluctuation on fixed and oscillating square-section cylinder", *J Fluid Mech*, 119, 297-321.
- Birjulin, A.P., Burgsdorf, V. V., and Makhlin, B.J. (1960), "Wind Loads on Overhead Lines", Paper 225, CIGRE, International Conference on Large Electric Systems, Paris, France.
- Braun, A. and Awruch, A. (2009), "Aerodynamic and aeroelastic analyses on the CAARC standard tall building model using numerical simulation", *Computer and Structures*, 87, 546-581.
- Castanheta, M. N. (1970) "Dynamic behavior of overhead power lines subject to the action of the wind", Paper No. 22-08 CIGRE, Session 22, Paris, France.
- Chay, M., Albermani, F., and Wilson, R. (2006). "Numerical and analytical simulation of downburst wind loads." *Eng. Struct.*, 28, 240–254.
- Chen, L., and Letchford, C.W. (2004a), A deterministic-stochastic hybrid model of downburst and its impact on a cantilevered structure. *Eng. Struct.*, 26(5), 619-629.
- Chen, L., and Letchford, C. W. (2004b). "Parametric study on the alongwind response of the CAARC building to downbursts in the time domain." *J. Wind. Eng. Ind. Aerodyn.*, 92_9_, 703–724.
- Darwish M., Damatty A.A.E.I. and Hangan, H. (2010), "Dynamic characteristics of transmission line conductors and behaviour under turbulent downburst loading", *Wind and Structures, An International Journal*, 13(4), 327-346.
- Darwish, M. and El Damatty, A.A. (2011), "Behavior of self supported transmission line towers under stationary downburst loading", *Wind and Structures, An International Journal*, 14(5), 481-498.

- Davenport, A.G. (1962), "Buffeting of a suspension bridge by storm winds", *J. ASCE Struct. Div.*, 88(3), 233-264.
- Engleman, C., Marihugh, D. (1970). "Forces on Conductors at High Wind Velocities", *Transmission and Distribution*, Oct.
- El Damatty, A., Aboshosha, H. (2012), Capacity of Electrical Transmission Towers under Downburst Loading. Proceedings of the First Australasia and South-East Asia Structural Engineering and Construction Conference, Perth, Australia, Nov 28-Dec 2, 2012, 317-322.
- Fluent, 6.2. (2005), "User's Guide, Fluent Inc., Lebanon".
- Fujita, T.T. (1990), "Downbursts: meteorological features and wind field characteristics", *Journal of Wind Engineering & Industrial Aerodynamics*, 36(1), 75-86.
- Geomano, M., Piomelli, U., Moin, P. and Cabot, W.H. (1991), "A dynamic subgrid-scale eddy viscosity model", *Physics and Fluids*, 3(7), 1760-1765.
- Hangan, H. and Kim, J. (2007), "Numerical simulations of impinging jets with application to downbursts", *J. Wind Eng. Ind. Aerodyn.*, 95(4), 279-298.
- Hangan, H. and Kim, J.D. (2004), "Numerical simulation of downbursts", Proceedings of the ASCE Structural Congress, Nashville, Te, USA, June 2004.
- Holmes, J.D., Hangan, H.M., Schroeder, J.L., Letchford, C.W. and Orwig, K.D. (2008), "A forensic study of the Lubbock-Reese downdraft of 2002", *Wind Struct.*, 11(2), 137-152.
- Hooman Keyhan, Ghyslaine McClure, Wagdi G. Habashi. "Dynamic analysis of an overhead transmission line subject to gusty wind loading predicted by wind-conductor interaction", *J. Wind Eng. Ind. Aerodyn.*, (In Press)
- Irvine, H.M. (1981), *Cable Structures*, MIT Press, Cambridge.
- Itoh, Y. and Tamura, T. (2007), "Overset grid method for large eddy simulation of turbulent flows around bluffbodies", Proceedings of FEDSM2007, 5th Joint ASME/JSME Fluids Engineering Conference, 1-9.
- Kwon, D. and Kareem, A. (2009), "Gust-Front Factor: New Framework for Wind Load Effects on Structures", *J. Struct. Eng.*, 135(6), 717-732.
- Li, C.Q. (2000), "A stochastic model of severe thunderstorms for transmission line design," *Probab. Eng. Mech.*, 15, 359-364.

- Lin, W.E., Savory, E., McIntyre, R.P., Vandelaar, C.S. and King, J.P.C. (2012), "The response of an overhead electrical power transmission line to two types of wind forcing", *J. Wind Eng. Ind. Aerod.*, 100(1), 58-69.
- Loredo-Souza, A. and Davenport, A.G. (1998), "The effects of high winds on transmission lines", *J. Wind Eng. Ind. Aerodyn.*, 74-76, 987-994.
- Macdonald, J.H.G. (2002), "Separation of the contributions of aerodynamic and structural damping in vibrations of inclined cables", *J. Wind Eng. Ind. Aerod.*, 90(1), 19-39.
- McCarthy, P. and Melsness, M. (1996), "Severe weather elements associated with September 5, 1996 hydro tower failures near Grosse Isle, Manitoba, Canada.", Manitoba Environmental Service Centre, Environment Canada, , 21.
- Murakami, S. and Mochida, A. (1995), "On turbulent vortex shedding flow past 2D square cylinder predicted by CFD", *Journal of Wind Engineering and Industrial Aerodynamics*, 54/55, 191-211.
- Ochoa, J.S. and Fueyo, N. (2004), "Large Eddy Simulation of the flow past a square cylinder", PHOENICS 10th International User Conference, Melbourne, Australia, CHAM Limited, London.
- Richards, D. (1965). "Aerodynamic properties of the severn crossing conductor" Paper 8, Symposium 16, National Physical Laboratory, Department of Scientific and Industrial Research, Teddington, Middle-sex, England.
- Savory, E., Parke, G., Zeinoddini, M., Toy, N. and Disney, P. (2001), "Modeling of tornado and microburst-induced wind loading and failure of a lattice transmission tower", *Eng. Struct.*, 23, 365-375.
- Shehata, A.Y. and El Damatty, A.A. (2007), "Behaviour of guyed transmission line structures under downburst wind loading", *Wind and Structures, An International Journal*, 10(3), 249-268.
- Shehata, A.Y., El Damatty, A.A. and Savory, E. (2005), "Finite element modeling of transmission line under downburst wind loading", *Finite Elements Anal. Des.*, 42(1), 71-89.
- Smagorinsky, J. (1963), "General circulation experiments with the primitive equations.", *Monthly Weather Review* :, 91, 99-164.

- Wang, X., Lou, W., Li, H. and Chen, Y. (2009), "Wind-induced dynamic response of high-rise transmission tower under downburst wind load", *J. Zhejiang Univ*, 43(8), 1520-1525.
- Watson, L. (1955)"Drag of bare standard cables."Technical Memorandum 114, Australian Aeronautical Research Laboratories Aerodynamics, Melbourne.

Chapter 5

5 Assessment of Dynamic Effect for Transmission Line Conductors under Downburst and Synoptic Winds

5.1 Introduction

Transmission lines (TLs) are used to carry electricity from sources of production to the distribution system. They consist of towers, conductors, ground wires and insulators. Conductors, which are responsible for transmitting the electricity, are supported by the towers through insulators. Ground wires are used as protection elements to transmit electrical charges to the ground in case of lightning. Transmission lines have been always designed to withstand forces induced by synoptic wind events. However, High Intensity Winds (HIW), in the form of downbursts or tornadoes, have not been typically considered in the design of the towers. By reviewing many cases of transmission line failures worldwide, it is revealed that more than 80% of weather-related failures of TLs are attributed to HIW as indicated by Dempsey and White (1996). Li (2000) reported that more than 90% of transmission line failures in Australia resulted from downburst events that are usually associated with thunderstorms. Dempsey and White (1996) also emphasized the possibility of multiple towers failure that could be triggered due to failure of a single tower. Failures that happened in Manitoba, Canada, in September 1996 and reported by McCarthy and Melsness (1996) represent a manifestation for this type of multiple towers failures. A downburst is a strong downdraft that induces an outburst of damaging winds near the ground as stated by Fujita (1990). Previous failure studies performed by Savory *et al.* (2001), Shehata and El Damatty (2008) and El Damatty and Aboshosha (2012) on different transmission towers subjected to downburst loading revealed the importance of including wind forces acting on the conductors. Most of the previous attempts to analyze the behaviour or the failure of transmission lines under downburst were performed using quasi-static analysis, assuming no dynamic effects and no interaction between the line components and the wind load (Savory *et al.* 2001 and Shehata *et al.* 2005, Shehata and El Damatty 2007, Darwish and El Damatty 2011). This assumption can be justified for typical towers with fundamental frequency in the order of

1 Hz or more (Holmes *et al.* 2008). However, this might not be the case for conductors which might be dynamically excited because of the proximity of their natural frequencies to the frequencies of the wind turbulence. Few attempts were done to investigate the dynamic response of the conductors. Loredo-Souza and Davenport (1998) studied the response of a single spanned conductor system subjected to synoptic winds. Their study showed that, depending on the amount of aerodynamic damping, the resonant response can be as important as the background response. Researchers such as Battista *et al.* (2003) and Gani and Legeron (2010) emphasized the importance of considering the dynamic effects. On the other hand, the study conducted by Darwish *et al.* (2010) for downburst loading reported that the dynamic response was mainly due to the background component, while the resonant component had a minor effect. Two reasons could be behind their findings. The first reason is related to the assumption made regarding the spatial distribution of the turbulent component. The wind field velocity associated with downbursts can be decomposed into a non-stationary mean component and a fluctuating turbulent component. In the study done by Darwish *et al.* (2010), the turbulent component was extracted from a real downburst event and was then assumed to be fully correlated along the conductors' spans. This assumption will tend to magnify the background responses compared to the resonant responses. The second reason is related to the estimation of the aerodynamic damping. Darwish *et al.* (2010) utilized the expression for aerodynamic damping derived by Davenport (1962), which is suitable for synoptic winds. This expression requires additional modifications to account for the increase of the conductor's tensile force and the consequent increase in the conductor natural frequencies when subjected to a downburst. Neglecting this effect exaggerates the aerodynamic damping and tends to attenuate the dynamic excitation. Lin *et al.* (2012) studied a single span conductor subjected to 57 simulated downbursts. Although most of their results were in favor of neglecting the dynamic effects, some of their results were not, and therefore the authors stated the need for additional research. In the current study, dynamic analyses are performed to investigate the response of two different conductor systems under both downburst and synoptic winds considering different wind velocities and different length spans. The objective of the study is to assess the importance of including the dynamic effect when predicting the response of the conductors under both

synoptic and downburst wind loading. Specifically, the paper focuses on the prediction of the transverse and longitudinal forces transmitted from the conductors to the tower due to these types of loading. The study considers the two conductor arrangements shown in Figs. 5.1a and 5.1b. The configuration shown in Fig. 5.1a represents the case of adjacent conductors not sharing a single insulator. In this case, modeling of a single span is sufficient to predict the response of the conductors. On the other hand, Fig. 5.1b represents the case where adjacent conductors share the same insulator. Modeling multiple conductors is needed in this case because of their mutual interaction. For such cases, and according to Shehata *et al.* (2005), modeling six conductor spans, three from each side of the tower of interest, is sufficient to obtain accurate prediction for the forces transmitted from the conductors to the tower.

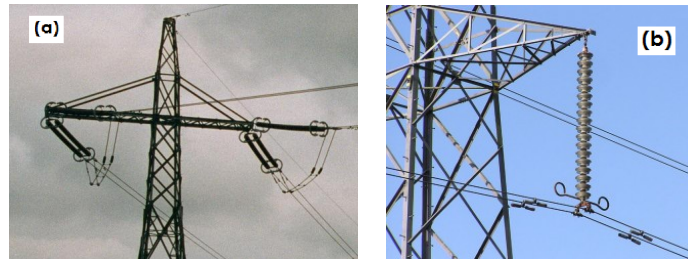


Figure 5.1 Insulator used in different systems: (a)-single spanned,
Wikipedia:http://en.wikipedia.org/wiki/Baltic_Cable (b)-six spanned,
<http://www.electrotechnik.net/2010/01/back-flashovers-introduction.html>

The paper starts by providing a description for different systems of conductors that are considered in the study. In addition, a detailed description of the downburst and synoptic wind fields is provided. Various steps applied to perform dynamic analyses and to obtain peak responses are then described. These steps include: (i) conducting a non-linear static analysis for the conductor system to obtain the conductor's time-dependent tension forces and displacements due to the running-mean wind velocities. These tension forces and displacements are used to calculate the time-dependent stiffness of the conductor, (ii) conducting a linear dynamic analysis under wind turbulence to calculate peak dynamic responses including resonant and background components using the time-dependent stiffness obtained in step (i), (iii) conducting a linear quasi-static analysis under wind

turbulence to determine the background component alone. The results of the dynamic analysis are then presented and discussed. Finally, conclusions and recommendations obtained from this study are provided.

5.2 Description of Different Cases Considered in the Analysis

A total of twelve different analysis cases are considered in this study for single-span and multiple-span conductor systems having properties summarized in Table 5.1. The twelve considered cases cover three loading scenarios: (i) four cases of downburst winds that cause maximum longitudinal reactions (ii) four cases of downburst winds that cause maximum transverse reactions (iii) four cases of synoptic winds.

Table 5.1 Properties of the conductor systems

Property	Value
Span Length L_x (m)	300 and 500 m
Sag Length S (m)	$L_x/30$
Elasticity Modulus $E(N/m^2)$	5.2E10
Weight $W(N/m)$	17.92
Projected Area in the wind direction (m^2/m)	0.022
Drag coefficient C_d according to the ASCE:74 (2010)	1.0
Cross sectional Area (m^2)	0.7E-04
Insulator Length $v(m)$	4.0
Average elevation (m)	43.0
Initial Tension $T_0=W.L_x^2/8.S$ (kN)	20

The cases of downbursts that cause maximum longitudinal and transverse reactions are chosen based on the recommendation of El Damatty *et al.* (2013) as will be discussed later in this section. For each of the three wind scenarios, the four considered cases cover two different mean wind velocities and two different span lengths. A summary of all considered cases is provided in Table 5.2. The mean wind velocity is selected as a variable in the parametric study since it is expected to affect the aerodynamic damping, which is the main source of attenuation for the resonant component as indicated by Loredou-Souza and Davenport (1998). At the same time, by varying the span length, the portion of the conductor affected by the correlated turbulence is expected to change and,

consequently, the magnitude of the fluctuating components (background and resonant) will change. These components are influenced by the turbulent length scale in the transverse direction, L_{uv} , as will be discussed in detail in section 3.1. In the following subsections, the considered wind fields, including both the mean and turbulent components are presented.

Table 5.2 Studied cases

Case	1	2	3	4	5	6	7	8	9	10	11	12
Type*	Db _x	Db _x	Db _x	Db _x	Db _y	Db _y	Db _y	Db _y	Sy	Sy	Sy	Sy
L _x (m)	300	300	500	500	300	300	500	500	300	300	500	500
V _{ref} (m/s)	40	20	40	20	40	20	40	20	40	20	40	20

Db_x, Db_y: Downburst case for the maximum longitudinal reaction R_x ($D=2.0 L_x$, $R=1.60 D_j$ and $\Theta=30^\circ$) and transverse reaction R_y ($D=2.0 L_x$, $R=1.20 D_j$ and $\Theta=0^\circ$)

Sy: Synoptic winds

V_{ref}: Reference mean velocity

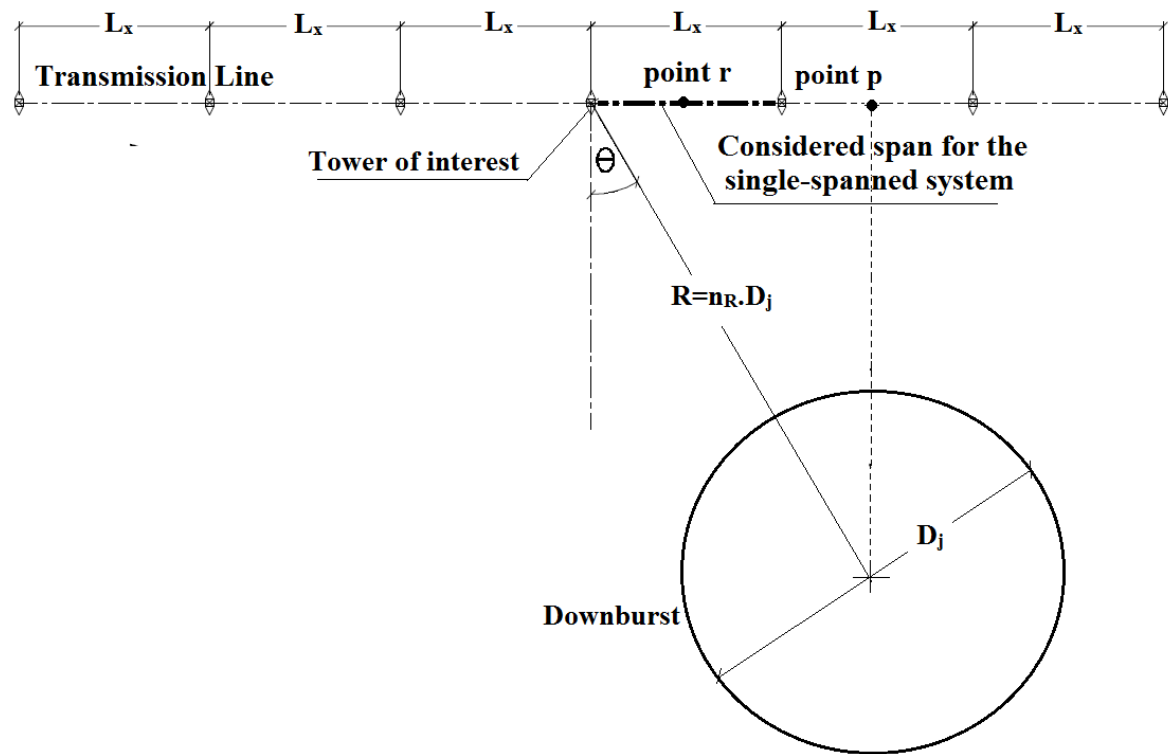


Figure 5.2 Downburst parameters D_j , R and Θ

5.3 Mean Wind Velocities

Wind velocities associated with downbursts and synoptic winds can be decomposed into a mean and a fluctuating component. However, the mean component associated with downbursts is different than that of synoptic winds because of its time and spatial dependency. As a result of the time dependency, it is usually named the “running-mean” or the “non-stationary mean” (Holmes *et al.* 2008, Kown and Kareem 2009). In the current study, the running-mean component of downbursts is extracted from the CFD simulation performed by Hangan and Kim (2007), based on the analogy between a falling downburst and a jet impinging to a wall (Fujita, 1985). In the CFD simulation, Unsteady Reynolds Averaged Navier Stoke’s (URANS) equations were solved together and the turbulence was accounted for using the Reynolds Stress Model (RSM). The running-mean component obtained from the CFD simulation is then scaled-up using the technique proposed by Shehata *et al.* (2005) to account for different event sizes and jet velocities. The mean component is evaluated at 10 points along each conductor span to account for the spatial variation. As indicated by Shehata and El Damatty (2007) and Darwish and El Damatty (2011), the running-mean velocities acting on the conductor are functions of the event size, D_j , and the downburst location relative to the conductor, which is identified by the polar coordinates, R and Θ shown in Fig. 5.2. According to El Damatty *et al.* (2013), an event having a jet diameter $D_j = 2 L_x$ and coordinates $R = 1.60 D_j$ and $\Theta = 30^\circ$ relative to the tower leads to peak longitudinal reactions at that tower. Similarly an event with the same diameter but with relative coordinates $R = 1.20 D_j$ and $\Theta = 0^\circ$ leads to peak transverse reactions. In the current study, the considered downburst scenario referring to peak longitudinal reactions is named Db_x , while that referring to peak transverse reaction is named Db_y as indicated in Table 5.2. Table 5.2 also summarizes the reference velocity, V_{ref} , considered in each case. This reference velocity, V_{ref} , is taken as the maximum running-mean velocity at the nearest point to the downburst centre (point “p” shown in Fig. 5.2). For the downburst cases, two reference velocities of 20 and 40 m/s are considered. For comparison purposes, the same two reference velocity values are assumed in the synoptic wind cases, where the mean velocities are time-independent in such cases.

5.4 Fluctuating Wind Velocities

The fluctuating wind velocities for both downbursts and synoptic winds can be generated numerically using the technique described by Chen and Letchford (2004) and Chay *et al.* (2006). This technique is general, which means that it can be applied for downburst winds with running-mean velocities and also for synoptic winds where the mean velocities are time independent. In this technique, the Power Spectrum Density (PSD), which describes the energy of the wind fluctuations in the frequency domain, proposed by von Karman (1948), is used to synthesize non-scaled turbulent velocities. These turbulent velocities are scaled using a modulation function. A time dependent modulation function is chosen for the case of downbursts while a constant function is employed for synoptic winds. This is done to account for the time variation of the turbulent fluctuations with the change of the mean velocity values. The employed modulation function is taken equal to the product of the turbulence intensity, I , and the mean velocity similar to Chay *et al.* (2006). The study conducted by Holmes *et al.* (2008) showed similarity between the spectra of the synoptic and the downburst winds. As such, von Karman's PSD is used in this study for both wind types. The turbulent length scale, L_u , which is required for the PSD of Von Karman, is taken equal to the event size, D_j , similar to the assumption made by Chay *et al.* (2006) for the downburst cases. Accurate estimation of the turbulent length scale, L_u , associated with downbursts requires additional research. For the cases of synoptic wind, the turbulent length scale, L_u , is calculated employing the approximate relationship $L_u = L_{uv}/0.3$, where L_{uv} is the turbulent length scale of the longitudinal fluctuations, u , along the transverse direction v . The length scale, L_{uv} , is considered equal to 52 m according to ASCE:74 (2010) assuming an open terrain. Correlations among the fluctuating components are introduced based on the coherency decay function proposed by Davenport (1986) using a coherency decay constant equal to 10, which is suitable for structural design purposes. The turbulent intensity is found to be in the order of 10% in a real downburst event as indicated by Holmes *et al.* (2008). For the case of synoptic winds, the turbulent intensity is found to be 14% according to the AS/NZS:7000 (2010). A single averaged value of 12% is considered for both events for comparison purposes. Turbulent velocities are generated at 10 points along each conductor span to account for the spatial variation.

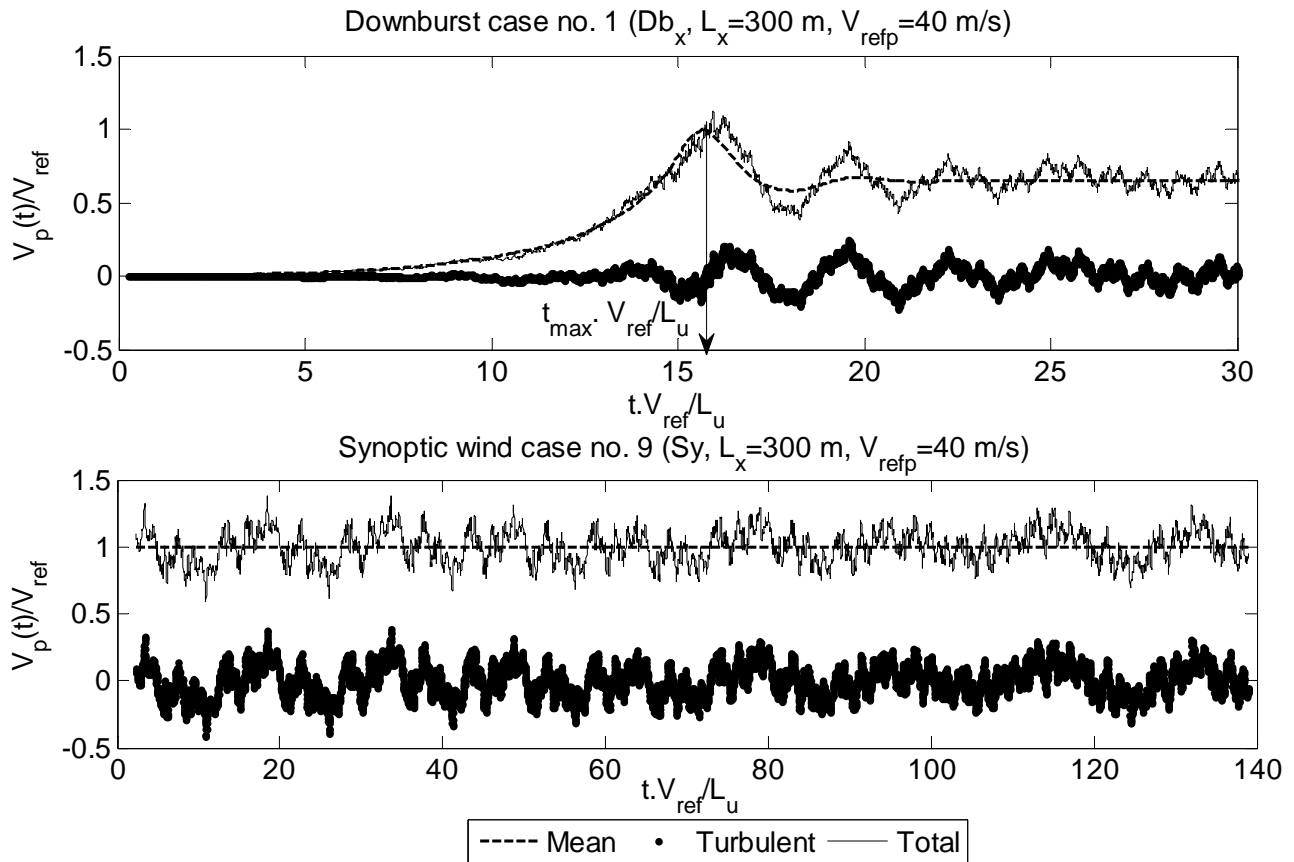
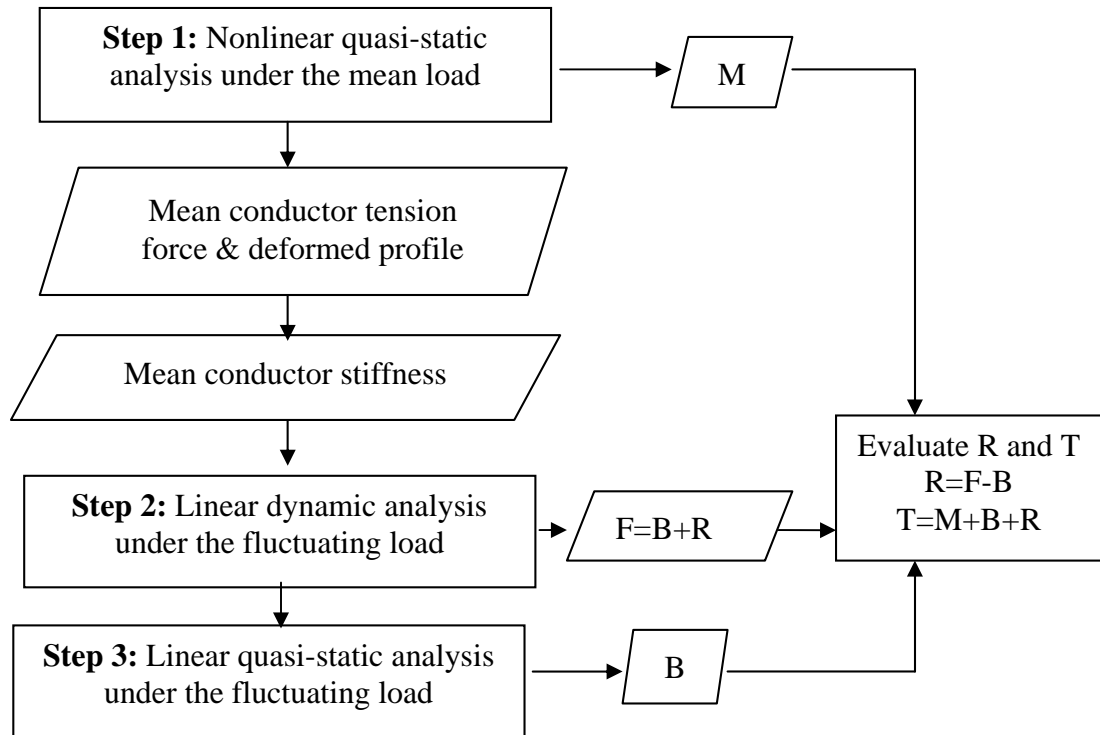


Figure 5.3 Velocity time history at point p for: (a) downburst case no. 1 ($Db_x, L_x=300, V_{refp}=40 \text{ m/s}$) (b) synoptic wind case no. 9 ($Sy, L_x=300, V_{refp}=40 \text{ m/s}$)

As a demonstration, Figs. 5.3a and 5.3b show samples of the mean and turbulent velocities taken at point p normalized by the reference velocity, V_{ref} , for downburst case (no. 1) and for synoptic wind case (no. 9), respectively. The horizontal axis represents a time t non-dimensional parameters involving the reference velocity V_{ref} and the longitudinal length scale L_u . The figures also show the time variation of the total velocity obtained by adding the mean and turbulent velocities.

5.5 Technique Used to Analyze Conductor Systems



M: mean response; F: fluctuating response; B: background component; R: resonant response; T: total response

Figure 5.4 Steps of the conductor analysis

Conductors and insulators are structural elements that behave non-linearly under the applied loads because of their low rigidity. This makes their dynamic analysis computationally very demanding. In order to reduce the computational demands, the dynamic analysis is conducted in the current study following the steps outlined in Fig. 5.4. The figure summarizes the steps of the analysis as follows: (i) The conductors are analyzed nonlinearly under forces resulting from mean wind velocities. The results of this analysis provide the conductor's mean response component, M, tension forces and deformed configuration. (ii) A linear analysis is conducted to evaluate the incremental response due to fluctuating velocities, F. In this analysis, the conductor stiffness corresponding to the deformed configuration and tension forces resulting from the mean

velocity analysis are employed. According to Sparling and Wegner (2007), this approach leads to a significant saving in terms of computational time without compromising the accuracy of the solution. This is mainly because of the small ratio between the fluctuating and the mean components. The fluctuating response, F , consists of the background and resonant components. In order to distinguish between the two components, a third analysis step is conducted as indicated in Fig. 5.4. In this step, a quasi-static analysis under the fluctuating forces is performed using the updated conductor stiffness resulting from the first analysis step to obtain the background component, B . This background component of the responses, B , is then subtracted from the fluctuating response, F , to separate the resonant component, R . By adding the velocity components together (the mean M , the background B , and the resonant R), the total response of the conductor is evaluated. More details about the steps utilized in the analysis are given below:

5.5.1 Step 1: Non-linear Quasi-Static Analysis under the Mean Wind

As previously mentioned, the "running mean" velocity of the downburst cases is adopted from the CFD simulation conducted by Kim and Hangan (2007), who indicated that the mean velocity has a horizontal and a vertical components. According to the findings by Kim and Hangan (2007) and Aboshosha and El Damatty (2014), the horizontal component of the mean velocity is the dominant and the vertical component can be neglected when calculating the forces acting on the conductor. This is also true for the synoptic wind cases where the mean velocities are typically in the horizontal direction. Consequently, as indicated in Fig. 5.5, the conductor systems will be subjected to a wind load g_y acting in the transverse direction Y in addition to the conductor weight W acting in the vertical direction Z . The intensity of the distributed load, $g_y(s)$, is calculated using Equation 5.1 as a function of the mean wind velocity, $V_m(s)$, at a general location s .

$$g_y(s) = \frac{1}{2} \cdot \rho \cdot C_d \cdot V_m(s)^2 \cdot D \quad \text{Equation 5.1}$$

where ρ is the air density which is taken equal to 1.25 kg/m^3 ; C_d is the drag coefficient of the conductor which is taken equal to 1.0 according to the ASCE:74 (2010), D is the

conductor facing area in the transverse direction per unit length. For a single bundled conductor, D is equal to the conductor diameter.

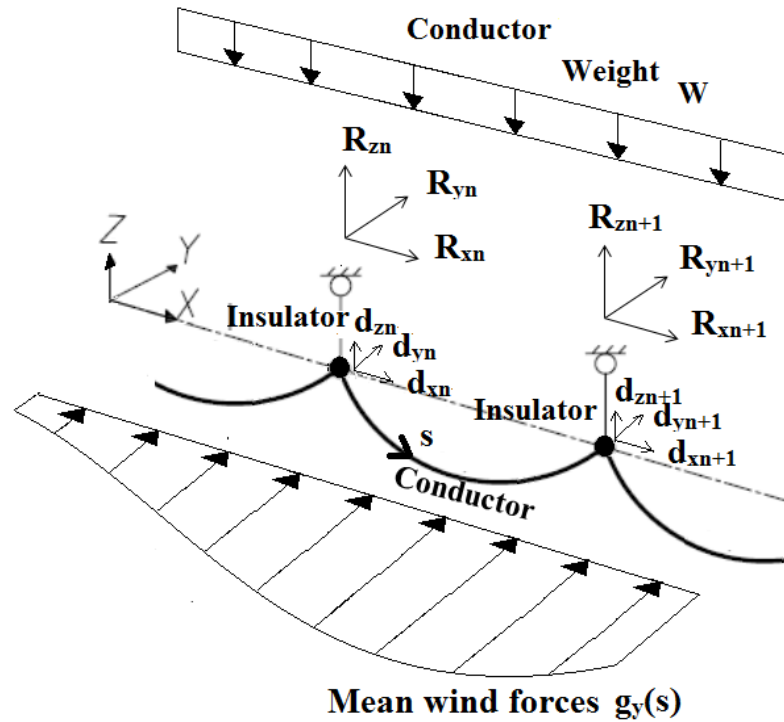


Figure 5.5 Schematic illustration of the conductor-system

The non-linear static analyses under the mean wind load, g_y , and the conductor weight, W , are conducted using the technique developed and validated by Aboshosha and El Damatty (2014). The technique treats each conductor span as a single element and thus reduces the unknown degrees of freedom by limiting them at the connections between the insulators and the conductors.

This technique is used to evaluate the reactions, R_{xi} , R_{yi} and R_{zi} at the supports and the displacements d_{xi} , d_{yi} and d_{zi} at the conductor-insulator connecting points as illustrated in Fig. 5.5, where i is the number of the insulator. According to the technique, vectors of the reactions, $\{R_x\}$, $\{R_y\}$ and $\{R_z\}$ and the displacements, $\{d_x\}$, $\{d_y\}$ and $\{d_z\}$ are calculated using Equations 5.2-5.4 according to the flowchart presented in Fig. 5.6.

$$\{R_y\} = \{R_y^F\} + [K_{yz}] \cdot \{dy\}, \quad \{R_z\} = \{R_z^F\} + [K_{yz}] \cdot \{dz\}$$

Equations 5.2

$$\{d_x\}^{i+1} = \{d_x\}^i + [K_x]^i \cdot \{f_x\}^i, \quad \{R_x\} = \left\{ d_x \cdot \frac{R_{res}}{v} \right\} \quad \text{Equations 5.3}$$

$$\{d_y\} = \left\{ v \cdot \frac{R_y}{R_{res}} \right\}, \quad \{d_z\} = \left\{ v - v \cdot \frac{R_z}{R_{res}} \right\} \quad \text{Equations 5.4}$$

Where $\{R_y^F\}$, $\{R_z^F\}$ are vectors of y and z reactions considering no displacements at the connection between the conductors and the insulators, which are defined in Appendix B; $[K_{yz}]$ is the stiffness matrix to account for the p-delta effect, which is defined in Appendix B; i is the iteration number; $\{f_x\}$ is the unbalanced load vector in x-direction, which is defined in Appendix B; $[K_x]$ is the tangential stiffness matrix for x-displacements that is given in Appendix B; the superscript i represents the iteration number; $\{R_{res}\}$ is the vector of the resultant forces in the insulators, $R_{res} = \sqrt{R_x^2 + R_y^2 + R_z^2}$.

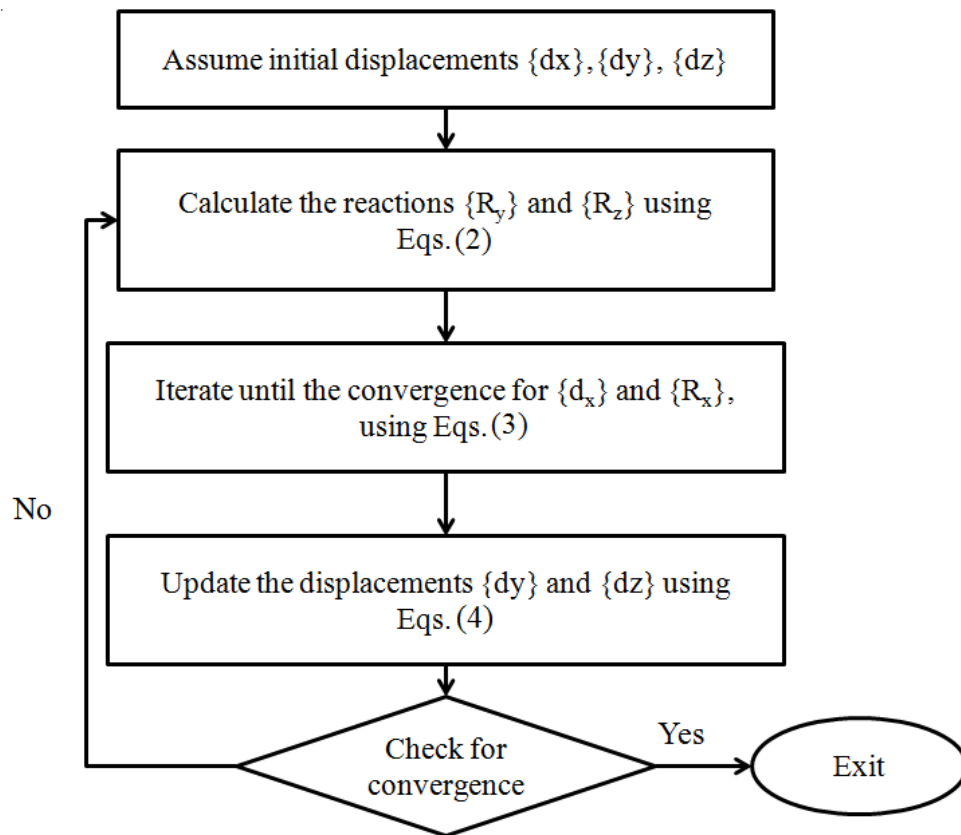


Figure 5.6 Flow chart of the employed technique (iterate until convergence)

As indicated in the flow chart, initial displacement vectors $\{d_x\}$, $\{d_y\}$ and $\{d_z\}$ are assumed and the corresponding reaction vectors $\{R_y\}$ and $\{R_z\}$ are calculated using Equations 5.2. The horizontal displacement and reaction vectors $\{d_x\}$ and $\{R_x\}$ are calculated by iterating through Equations 5.3 until no change in the results takes place between two subsequent iterations. This is followed by calculating the displacement vectors $\{d_x\}$ and $\{d_y\}$ using Equations 5.4, which satisfy the insulator equilibrium. The obtained solution is checked for convergence by comparing the displacement vectors obtained from the equations with the initial assumed values. If a difference greater than a chosen tolerance is found, the solution is considered not converged and the whole procedure is repeated as indicated in Fig. 5.6, until convergence takes place.

Fig. 5.7a shows the time variation of the mean wind load intensity acting at the midpoint of the span adjacent to the tower of interest (point r indicated in Fig. 5.2). As shown in Fig. 5.7a, the mean loads are time-dependent for the downburst cases and are time-independent for the synoptic wind cases. For the downburst cases non-linear static analyses are conducted using the technique presented in Fig. 5.6 at 250 time increments to capture the time history response under the time-varying mean component. One nonlinear analysis is only needed to obtain the mean response under synoptic wind. The conductor tension force and the deformed shape under the mean velocity component are obtained from the nonlinear static analysis. For the downburst cases, such parameters vary with time while they are constant for the synoptic cases. Those parameters are then used to calculate the stiffness of the conductors used in the subsequent linear dynamic analyses under the fluctuating wind component. The time history variation of the tension forces at the conductor span adjacent to the tower of interest, as obtained from the nonlinear analyses, are reported in Figs. 5.6b and 5.6c for the single and multiple spans, respectively. In these figures the tension forces are normalized by the initial tension force T_0 resulting from the conductor's own weight.

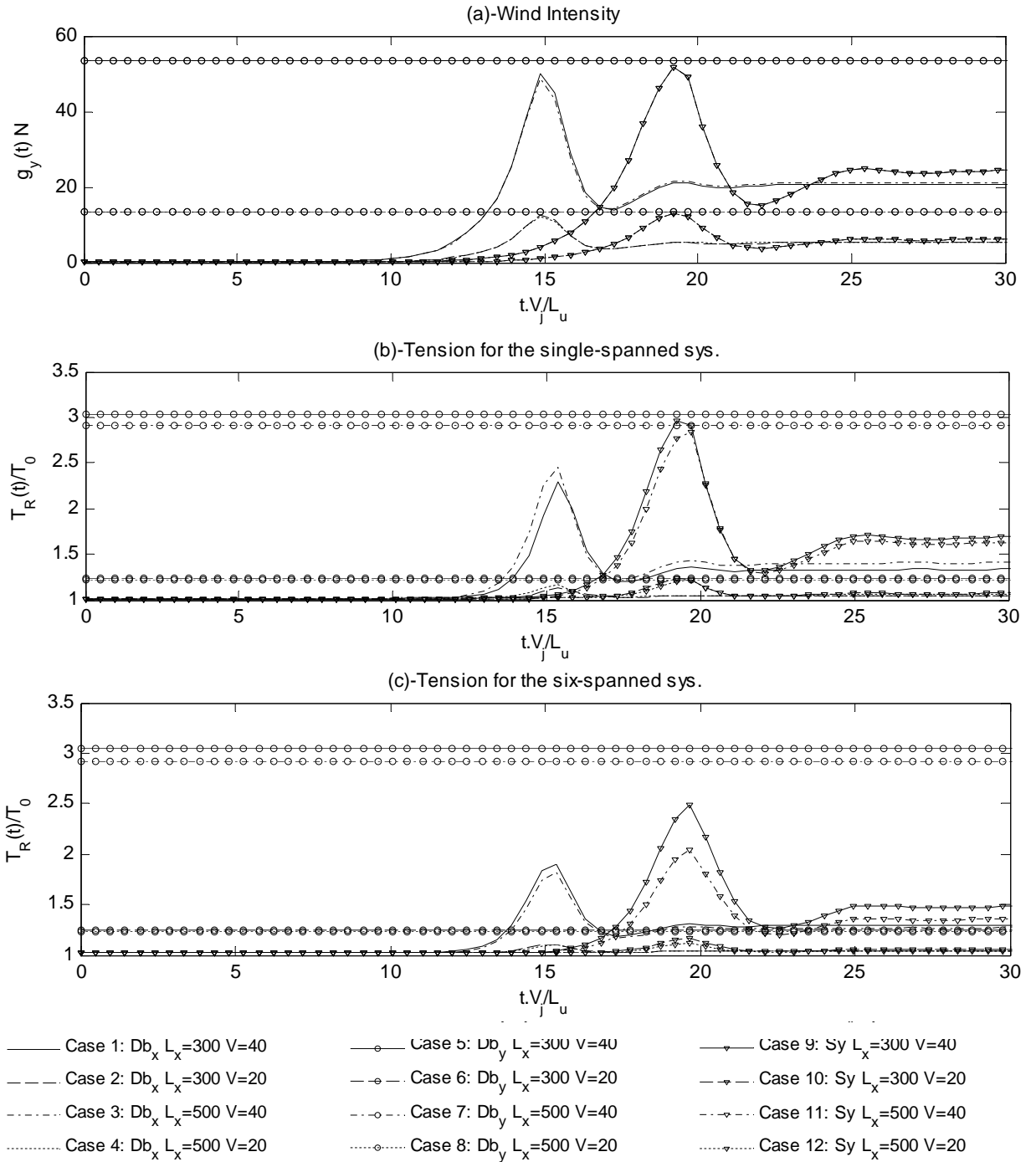


Figure 5.7 Time variation of the wind intensity, the tension force for the single-spanned and six-spanned systems

Fig. 5.8 shows the time variation of the transverse displacement, dy , and the vertical displacement, dz , at point r for both the single and six-spanned systems. By comparing the displacements obtained from load cases 1, 3, 5, 7, 9 and 11 to those from cases 2, 4, 6, 8, 10 and 12, respectively, it is found that the increase in the mean velocity leads to an increase in the transverse displacement dy and a decrease in the vertical displacement dz .

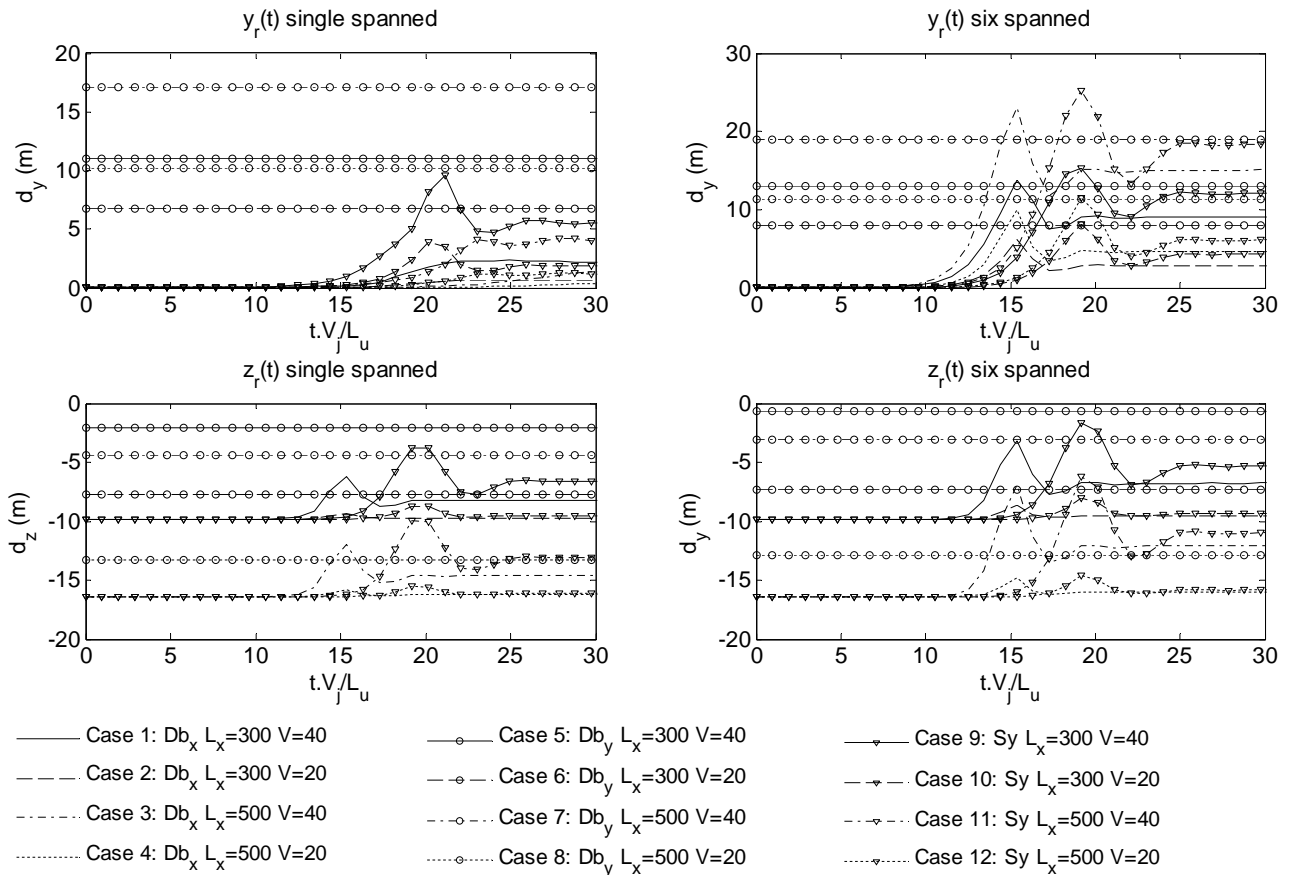


Figure 5.8 Time variation of the mean transverse displacement dy and vertical displacement dz at point r

Figs. 5.7 and 5.8 indicate that the applied wind loads lead to significant changes in the conductor tension and its profile, which need to be accounted for in the dynamic analysis. Examples of the instantaneous wind load, the deflected conductor shape for the single spanned system and the deflected conductor shape for the six spanned system are illustrated in Figs. 5.9, 5.10 and 5.11, respectively.

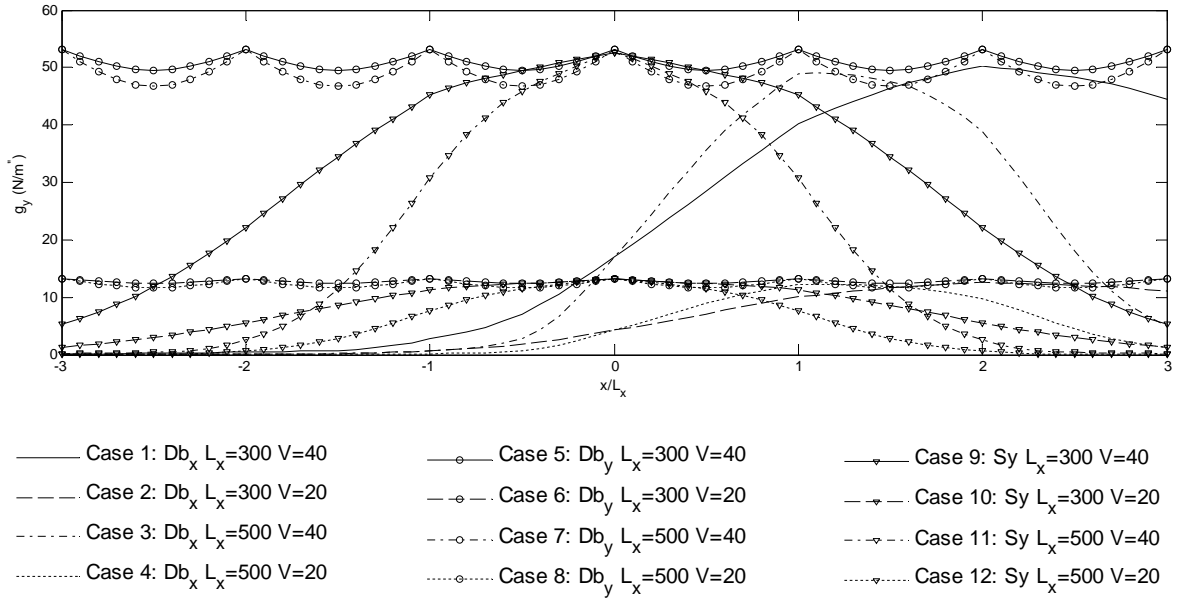


Figure 5.9 Distribution of the wind load g_y along the conductor spans at the time instance t_{max}

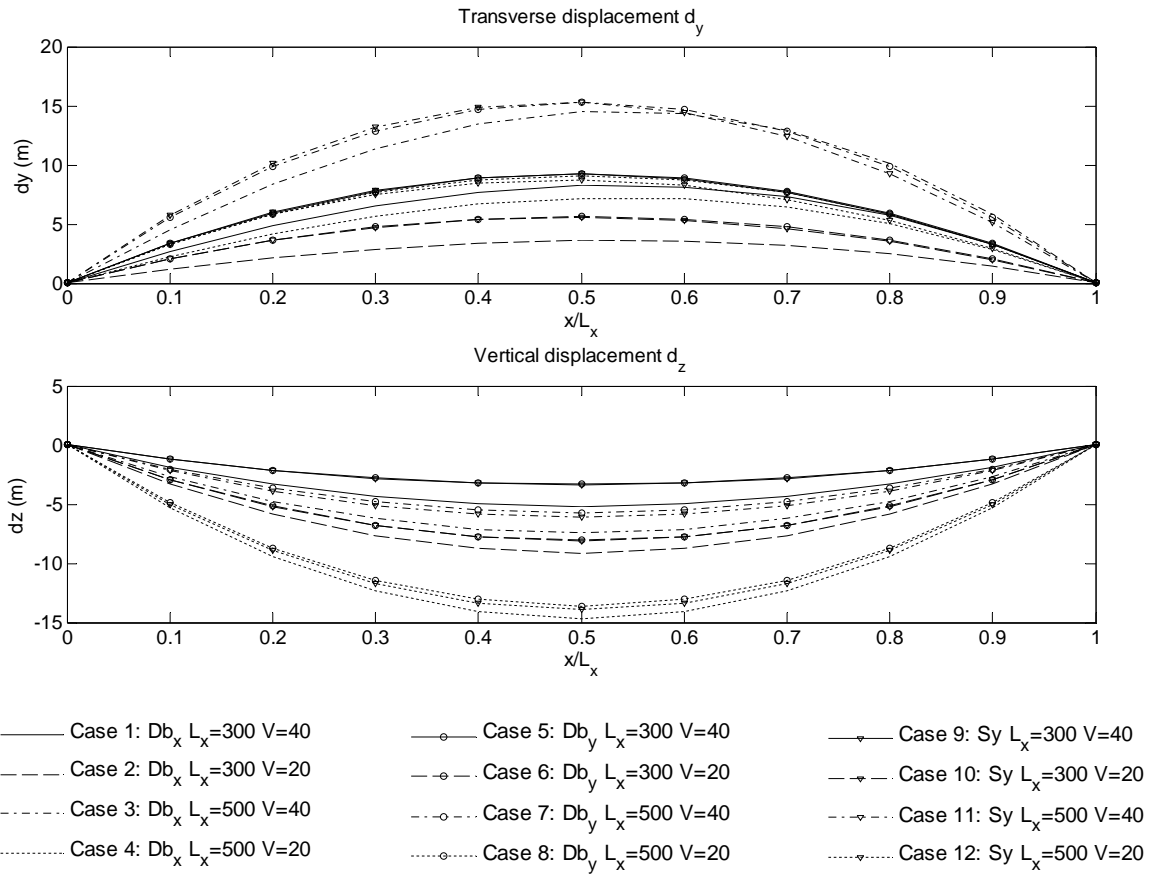


Figure 5.10 Conductor profile at the time instance t_{max} for the single-spanned system

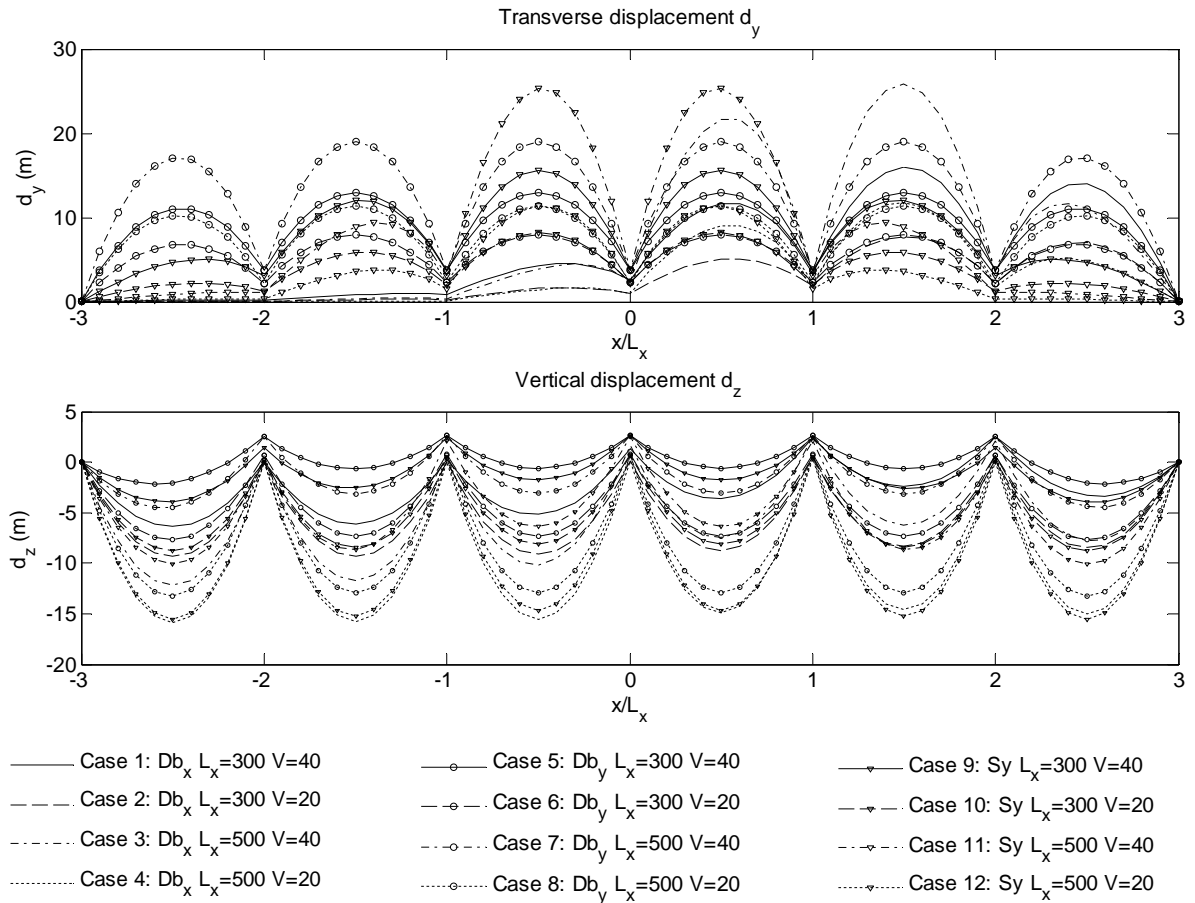


Figure 5.11 Conductor deformed configuration at the time instance t_{max} for the six-spanned system

The load and the deflected shape are plotted at the time instance, t_{max} , corresponding to the maximum mean wind speed at point p, which is indicated in Fig. 5.3. As shown in Fig. 5.9, wind load distribution due to downburst wind changes significantly in space in contrary to synoptic wind which is uniform. Figs. 5.10 and 5.11 indicate that under synoptic wind cases, the conductors have larger deflections in the transverse direction, d_y , compared to the downburst cases. This is expected because the considered loads, resulting from synoptic wind (cases 9, 10, 11 and 12), are higher than those due to downburst wind (Db_x : cases no. 1, 2, 3 and 4 and Db_y : cases no. 5, 6, 7 and 8), as indicated in Fig. 5.7a. The calculated tension forces and deformed shapes of the conductors are utilized in Step 2 to conduct the dynamic analyses.

5.5.2 Step 2: Linear Dynamic Analysis under the Fluctuating Wind Load

As previously mentioned, linear dynamic analysis is conducted under the fluctuating wind forces. The fluctuating wind force, $F_w(t)$, acting at a nodal point responsible of a tributary length L_e is calculated according to Equation 5.5 where $V_m(t)$ and $v(t)$ are the mean and the turbulent velocities happening at time t , respectively.

$$F_w(t) = \frac{1}{2} \cdot \rho \cdot C_d \cdot V_m(t) \cdot v(t) \cdot D \cdot L_e \quad \text{Equation 5.5}$$

The standard equation of motion of a multi-degree of freedom system subjected to a time-varying wind load is given below:

$$[M]\{\ddot{u}\} + [C(t)]\{\dot{u}\} + [K(t)]\{u\} = \{F_w(t)\} \quad \text{Equation 5.6}$$

where $[M]$ is the mass matrix; $[C(t)]$ is the time dependent damping matrix; $[K(t)]$ is the time dependent stiffness matrix; $\{F_w(t)\}$ is the load vector of the fluctuating forces.

What is unique in this analysis is that both the stiffness matrix $[K(t)]$ and the damping matrix $[C(t)]$ are considered to be time-dependent and are evaluated based on the internal forces and deformations corresponding to the mean wind load component, which vary with time for downburst cases.

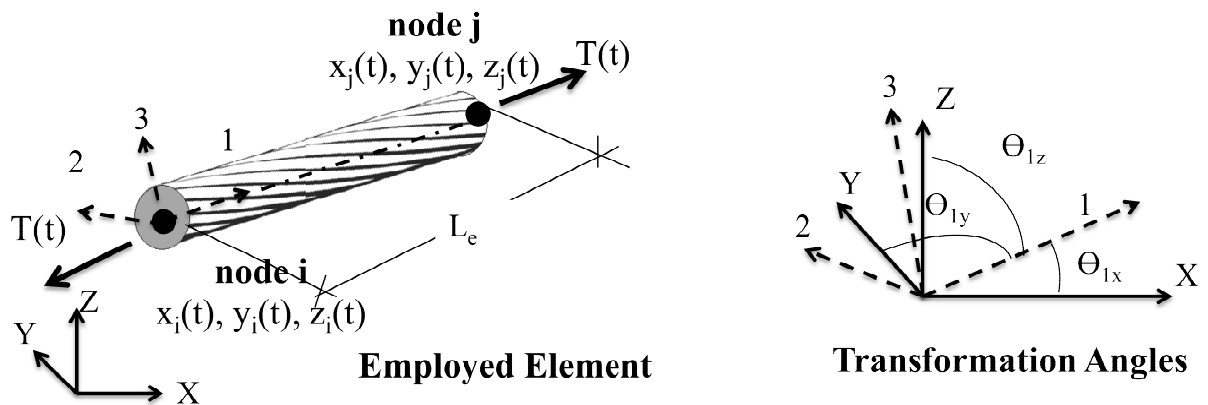


Figure 5.12 Employed two-noded cable element

In order to obtain the system stiffness matrix, $[K(t)]$, each conductor span is modeled using 10 two-nodded cable elements whose stiffness matrices, $[k_{eG}]$, in the global coordinates are calculated using Equation 5.7.

$$[k_{eG}] = T_e^T \cdot [k_{el}] \cdot T_e \quad \text{Equation 5.7}$$

$$T_e = \begin{bmatrix} [R] & [0] \\ [0] & [R] \end{bmatrix}, R = \begin{bmatrix} \text{Cos}(\theta_{1x}) & \text{Cos}(\theta_{1y}) & \text{Cos}(\theta_{1z}) \\ \text{Cos}(\theta_{2x}) & \text{Cos}(\theta_{2y}) & \text{Cos}(\theta_{2z}) \\ \text{Cos}(\theta_{3x}) & \text{Cos}(\theta_{3y}) & \text{Cos}(\theta_{3z}) \end{bmatrix},$$

$$k_{el} = \begin{bmatrix} [k] & -[k] \\ -[k] & [k] \end{bmatrix}, [k] = \frac{1}{L_e} \begin{bmatrix} EA & 0 & 0 \\ 0 & T(t) & 0 \\ 0 & 0 & T(t) \end{bmatrix}$$

Where $[k_{el}]$ is the element stiffness matrix in the local coordinates 1, 2 and 3; T_e is the Transformation matrix; R is the directional cosine matrix; θ_{ij} is the angle between axes i and j ; $T(t)$ is the element tension force; L_e is the element length.

As indicated in Equation 5.7, the element global stiffness matrix, $[k_{eG}]$, is calculated by transforming the element local stiffness matrix, $[k_{el}]$, from the local coordinates 1, 2, 3 to the global coordinates x , y and z , as illustrated in Fig. 5.12. This is achieved by using the transformation matrix T , which is formulated using the directional cosine matrix $[R]$, as indicated in Equation 5.7. It should be mentioned that in Equation 5.7, the element length L_e and the directional cosine matrix $[R]$ are functions of the deformed configuration of the conductor which is obtained from the non-linear analysis under mean wind forces performed in Step 1.

The mass, $[M]$, and the damping, $[C]$, matrices are expressed by Equations 5.8 and 5.9, using the lumped mass and the lumped damping at each node.

$$[M]_{3n \times 3n} = \begin{bmatrix} [M_1]_{3 \times 3} & [0] & [0] & [0] \\ [0] & [M_2]_{3 \times 3} & [0] & [0] \\ \vdots & \vdots & \ddots & \vdots \\ [0] & [0] & \dots & [M_{n-1}]_{3 \times 3} & [0] \\ [0] & [0] & \dots & [0] & [M_n]_{3 \times 3} \end{bmatrix}, [M_i]_{3 \times 3} = \begin{bmatrix} m & 0 & 0 \\ 0 & m & 0 \\ 0 & 0 & m \end{bmatrix} \quad \text{Equation 5.8}$$

$$[C]_{3n \times 3n} = \begin{bmatrix} [C_{a1}]_{3 \times 3} & [0] & [0] & [0] \\ [0] & [C_{a2}]_{3 \times 3} & & [0] \\ \vdots & \vdots & \ddots & \vdots \\ [0] & [0] & \dots & [C_{an-1}]_{3 \times 3} \\ [0] & [0] & \dots & [0] & [C_{an}]_{3 \times 3} \end{bmatrix}, [C_{ai}]_{3 \times 3} = \begin{bmatrix} 0 & 0 & 0 \\ 0 & c_{ai}(t) & 0 \\ 0 & 0 & 0 \end{bmatrix} \tag{Equation 5.9}$$

Where n is the number of nodes, which equals to 10 x (nSpan+1), where nSpan is the number of spans; $[M_i]$, $[C_{ai}]$ are the mass and damping matrices for node i; m is the nodal mass which is equal to $W.L_x / (20.g)$ for the first and last nodes and equal to $W.L_x / (10.g)$ for other nodes, where g is the gravitational acceleration which is equal to 9.81 m/s^2 , $c_{ai}(t)$ is the damping coefficient at node i.

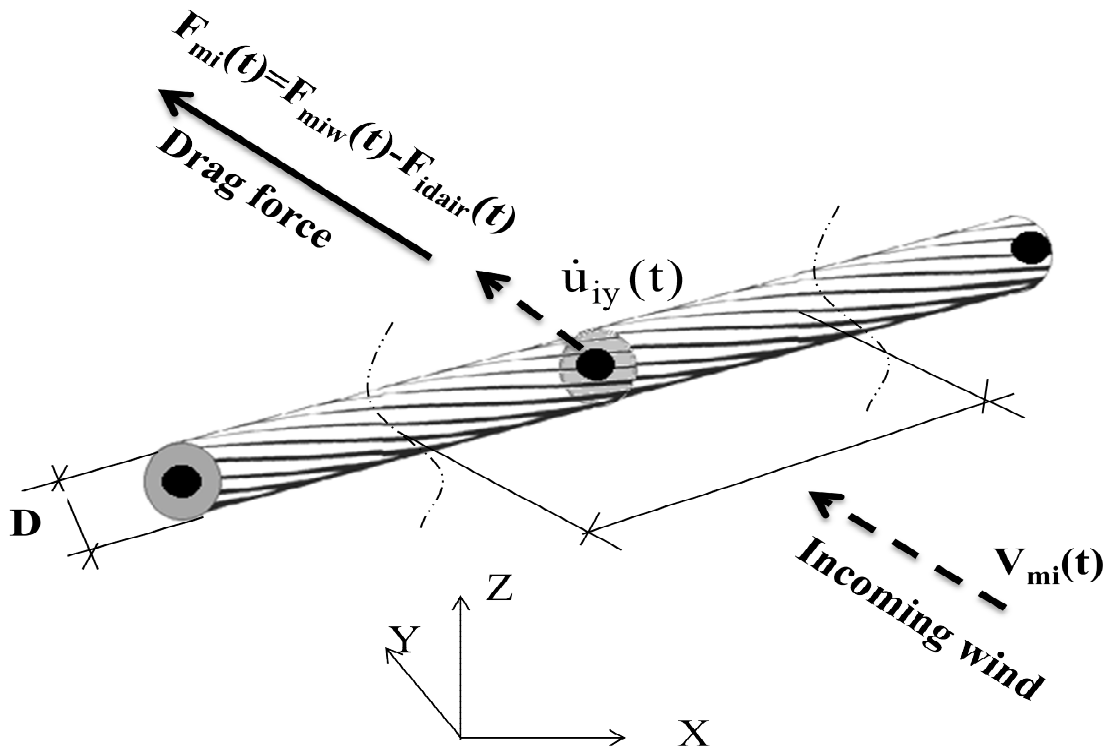


Figure 5.13 Drag force at node i due to incoming wind

According to Loredo-Souza and Davenport (1998), the aerodynamic damping of the conductor system is the dominant source of damping and plays a major role in attenuating the resonant component. Davenport (1962) proposed an expression for the aerodynamic damping ratio, ζ_a , based on the modal analysis procedure. Since the mode shapes are

expected to change with time as a result of the variation of the conductor's tension force and nodal coordinates with time, Davenport's expression cannot be used directly. Therefore, an expression for the time-dependent damping coefficient per each node, c_{ai} , is developed in the current study as follows:

- A conductor segment with a length L_e , as shown in Fig. 5.13, is considered. The segment moves with a velocity \dot{u}_{iy} in the transverse y -direction and is subjected to an incoming wind with a mean velocity, V_{mi} . The drag force applied on the segment due to the incoming mean wind velocity, F_{mi} , and the conductor movement can be expressed by Equation 5.10.

$$F_{mi}(t) = \frac{1}{2} \rho C_d D L_e (V_{mi}(t) - \dot{u}_{iy}(t))^2 \quad \text{Equation 5.10}$$

- This drag force, $F_{mi}(t)$, is expanded in Equation 5.11 as the addition of the drag force due to the mean incoming wind, $F_{miw}(t)$, and the aerodynamic damping force, $F_{idair}(t)$, due to conductor movement in the wind direction. It should be mentioned that in Equation 5.11 the conductor velocity, $\dot{u}_{iy}(t)$, is typically much smaller than the incoming wind velocity, $V_i(t)$, and thus the quadratic term of the conductor velocity is neglected.

$$F_{mi} = F_{miw} - F_{idair} = \frac{1}{2} \rho C_d D L_e V_{mi}(t)^2 - \rho C_d D L_e V_{mi}(t) \dot{u}_{iy}(t) \quad \text{Equation 5.11}$$

- The aerodynamic damping force, $F_{idair}(t)$, is equated to the viscous damping force as expressed by Equation 5.12, and the damping coefficient c_{ai} is accordingly evaluated using Equation 5.13.

$$F_{idair} = \rho C_d D L_e V_i(t) \dot{u}_{iy}(t) = c_{ai}(t) \dot{u}_{iy}(t) \quad \text{Equation 5.12}$$

$$c_{ai}(t) = \rho C_d D L_e V_i(t) \quad \text{Equation 5.13}$$

It should be mentioned that since the incoming wind velocities are mainly in the transverse y -direction, the aerodynamic damping coefficient, c_{ai} , is introduced only in the diagonal elements corresponding to the conductor velocities in the y -direction as shown in Equation 5.9. Dynamic analyses are performed using the Newmark's (Bathe, 1996) step by step integration technique. This in-house program is developed to overcome some limitations found in most of the commercial finite element software. For example, most of the available software do not allow defining time dependent damping forces as required in the current study. Also, most of commercial software do not have the option of conducting the analyses under the total wind load into two steps as done in the current study. This will require a significant computational time compared with the two steps approach (Sparling and Wegner, 2007). The in-house program is validated by employing it to analyze the six-spanned conductor system subjected to downburst load (case no. 4), and comparing the resulting reaction responses with the corresponding values obtained using SAP2000 CSI (2010). A constant damping ratio of 5% for the first two modes is considered in this example in order to be able to solve the problem within the capability of the commercial code.

Fig. 5.14a shows the time histories of the total and the fluctuating transverse reactions R_y obtained from the in-house and the SAP 2000 analyses. Similar time histories for the longitudinal reactions R_x are provided in Fig. 5.14b. The figures show a very good agreement between the two sets of analyses. In order to obtain a more detailed comparison, the time-dependent mean and root mean square (r.m.s.) components are calculated and are plotted in Fig. 5.14 c, d. As shown in the figures, both the mean and the r.m.s. components obtained from the developed in-house program are in an excellent agreement with those obtained from the SAP 2000 results. This provides confidence in the accuracy of the developed in-house code. This in-house program is then employed to conduct the dynamic analyses for the 12 considered cases. Results of these analyses are discussed in section 5.4.

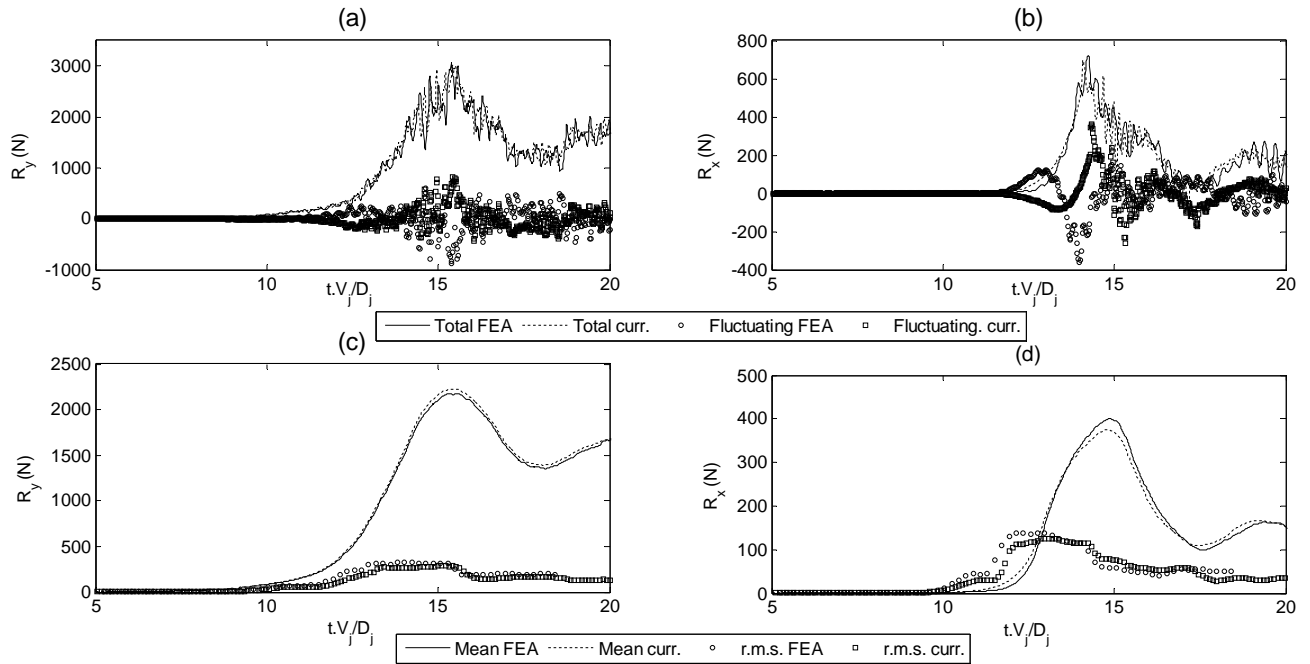


Figure 5.14 Comparison between the results of the in-house program and FEA (a) time history of R_x (b) time history of R_y (c) running R_y components (d) running R_x components

5.5.3 Step 3: Quasi-Static Linear Analysis under the Fluctuating Wind

As mentioned earlier, a quasi-static analysis of the conductor systems under the fluctuating wind is conducted in order to distinguish between the background and resonant components. The background component of the response is obtained by doing a static analysis through solving Equation 5.14. This is then subtracted from the total fluctuating component to identify the resonant component.

$$[K(t)]\{u\} = \{F_w(t)\}$$

Equation 5.14

where $\{F_w(t)\}$ is the fluctuating load vector due to the wind load; $[K(t)]$ is the time dependent stiffness matrix obtained using the conductor tension force and the location resulting from the quasi-static analysis under the mean loads

5.6 Results of the Dynamic Analyses

The three steps discussed above in section 5.3 are followed to analyze the conductor systems under the twelve wind cases summarized in Table 5.2. Reactions of the single-spanned system at the left tower, R_{x1} and R_{y1} , and those for the six-spanned system at the intermediate tower, R_{x6} and R_{y6} , in the longitudinal and the transverse directions, respectively, are calculated and plotted in Figs. C1-12 presented in Appendix C. The figures report the mean, the background and the resonant components, in addition to the overall response obtained from the summation of those three components. The reported reactions are normalized using the maximum mean reaction components (R_{y1}^* and R_{x1}^*) for the single-spanned system and (R_{y6}^* and R_{x6}^*) for the six spanned system. Also, the longitudinal reactions (R_{x1} and R_{x6}) reported in the figures are normalized on the right scale using the maximum mean transverse reactions (R_{y1}^* or R_{y6}^*), respectively. This is to allow comparison of the longitudinal reactions to the transverse reactions, thus identifying the cases where the longitudinal reactions are critical. It should be mentioned that for the cases of synoptic wind, the mean response is used for the scaling instead of the maximum mean response since the mean response does not vary with time. Also, for the cases of synoptic winds and the cases of downbursts corresponding to the maximum transverse reactions, the mean longitudinal reaction for the six spanned system, R_{x6} , is equal to zero due to symmetry and, thus is not used in the normalization.

In order to further assess the effect of turbulence, responses shown in Fig. C1-C12, located in Appendix C, are used to calculate the Gust Factor, GF, defined in Equation 5.15 as the ratio between the peak responses to the maximum-mean responses. Two gust factors are calculated based on how the peak responses are defined: (1) the first is named the dynamic gust factor, GF_{Dy} , where the peak responses result from the contribution of the mean, background and resonant components. (2) The second is named the quasi-static gust factor, GF_{QS} , where the contribution of the mean and the background components are only considered in calculating the peak responses.

$$GF = \frac{r_p}{r_{max}}$$

Equation 5.15

where:

r_p : Peak response

\bar{r}_{max} : Maximum mean response for the downburst winds or mean response for the synoptic winds

Table 5.3 Gust factors for the different wind cases

Resp. Type	Case	Downburst-(Peak R_x)			Case	Downburst-(Peak R_y)			Case	Synoptic Winds		
		GF _{Dy}	GF _{Qs}	Cont _R %		GF _{Dy}	GF _{Qs}	Diff _{Qs} %		GF _{Dy}	GF _{Qs}	Diff _{Qs} %
R _{y1}	1: L300 V 40	1.27	1.22	3.91	5: L300 V 40	1.40	1.36	3.01	9: L300 V 20	1.38	1.32	4.20
R _{x1}		1.27	1.21	4.57		1.59	1.53	3.94		1.49	1.42	5.26
R _{y6}		1.31	1.26	3.76		1.32	1.27	3.68		1.42	1.33	6.62
R _{x6}		1.18	1.15	2.92		**	**	1.96		**	**	11.52
R _{y1}	2: L300 V 20	1.27	1.22	3.76	6: L300 V 20	1.40	1.36	2.54	10: L300 V 20	1.36	1.32	3.14
R _{x1}		1.36	1.21	11.29		1.91	1.63	14.87		1.74	1.57	9.88
R _{y6}		1.27	1.25	1.63		1.30	1.27	2.08		1.41	1.32	6.24
R _{x6}		1.14	1.11	2.77		**	**	17.68		**	**	5.79
R _{y1}	3: L500 V 40	1.30	1.25	4.23	7: L500 V 40	1.25	1.21	3.27	11: L300 V 40	1.42	1.36	3.75
R _{x1}		1.37	1.32	3.22		1.27	1.25	1.83		1.48	1.39	6.02
R _{y6}		1.18	1.18	0.72		1.26	1.24	1.54		1.42	1.37	3.55
R _{x6}		1.15	1.14	0.82		**	**	1.70		**	**	9.81
R _{y1}	4: L500 V 40	1.28	1.25	2.73	8: L500 V 40	1.25	1.21	3.08	12: L500 V 40	1.42	1.36	4.36
R _{x1}		1.35	1.26	6.76		1.32	1.24	6.10		1.85	1.55	16.49
R _{y6}		1.20	1.18	1.78		1.25	1.24	1.34		1.40	1.36	2.90
R _{x6}		1.22	1.14	6.15		**	**	1.24		**	**	4.74

GFs in bold correspond to the peak reaction caused by the considered downburst size and location

** indicated that the mean response is equal to zero

Both the dynamic and the quasi-static gust factors, GF_{DY} and GF_{Qs}, are provided in Table 5.3 for the twelve considered cases. The contribution of the mean, $Cont_M$, background, $Cont_{BG}$, and resonant, $Cont_R$, components to the peak responses are calculated using Equations 5.16 and are plotted in Fig. 5.15.

$$Cont_M = \frac{1}{GF}, \quad Cont_{BG} = \frac{GF_{Qs} - 1}{GF}, \quad Cont_R = \frac{GF - GF_{Qs}}{GF} \quad \text{Equations 5.16}$$

The contribution of the resonant component, Cont_R , which is reported in Table 5.3, represents the error in the estimated peak response when the dynamic effect is not considered. High values of such a contribution imply the importance of conducting dynamic analysis. The following remarks points can be made by in view of the values of Cont_R calculated for different cases:

- (i) The contribution, Cont_R , to the peak longitudinal reaction R_{x1} for the single-spanned system reaches a maximum value of 15% for the downburst cases and 17% for the synoptic wind cases when considering the low reference velocity (20 m/s). The contribution reaches a maximum value of 4.5% and 6% for the downburst and the synoptic wind cases, respectively, for the high reference velocity (40 m/s). These results indicate that dynamic analysis is recommended to analyze single-spanned system subjected to low velocities for both downburst and synoptic winds. The contribution of the resonant component, Cont_R , to the peak transverse reaction R_{y1} is generally low and less than 5% under both the downburst and the synoptic wind cases.
- (ii) The contribution to the peak transverse reaction R_{y6} for the six-spanned system is in the order of 4% or less for the downburst cases and in the order of 6% for the synoptic wind cases. Also, the contribution to the peak transverse reaction R_{x6} of the six-spanned system is in the order of 6% or less for the downburst cases causing maximum longitudinal reactions (cases 1-4). These low contributions imply that conducting dynamic analysis may not be necessary for estimating the peak reactions for the six-spanned system.

By investigating the values of the GFs summarized in Table 5.3, it is found that for the twelve studied cases, GFs of both the longitudinal and transverse reactions for the single spanned system, R_{x1} and R_{y1} , are larger than those for the six spanned system, R_{x6} and R_{y6} . This is because correlated fluctuations characterized by the length scale, L_{uv} , cover a higher percentage of the conductor length for the single spanned system than that for the six spanned system. According to Davenport (1993), cases of high ratio of the turbulence

length scale L_{uv} to the system length have more correlated fluctuations than those of low ratios.

In Figs. C1-C12, located in Appendix C, time histories of the reactions are normalized by the maximum mean component for each case. This allows visualizing the difference between the peak reactions and their mean components caused by the wind turbulence. In order to compare the responses obtained from the 12 cases, a general normalization using a force, $g_{yp} \cdot L_x$, is applied to the reaction responses, as shown in Fig. 5.16. This normalization force is equal to product of the wind intensity applied at point p, g_{yp} , and expressed by Equation 5.17, and the span length L_x . This force, $g_{yp} \cdot L_x$, represents the maximum mean transverse force acting on the towers assuming a uniform distribution of the wind load.

$$g_{yp}^* = \frac{1}{2} \rho \cdot C_d \cdot V_{ref}^2 \cdot D, \quad \text{Equation 5.17}$$

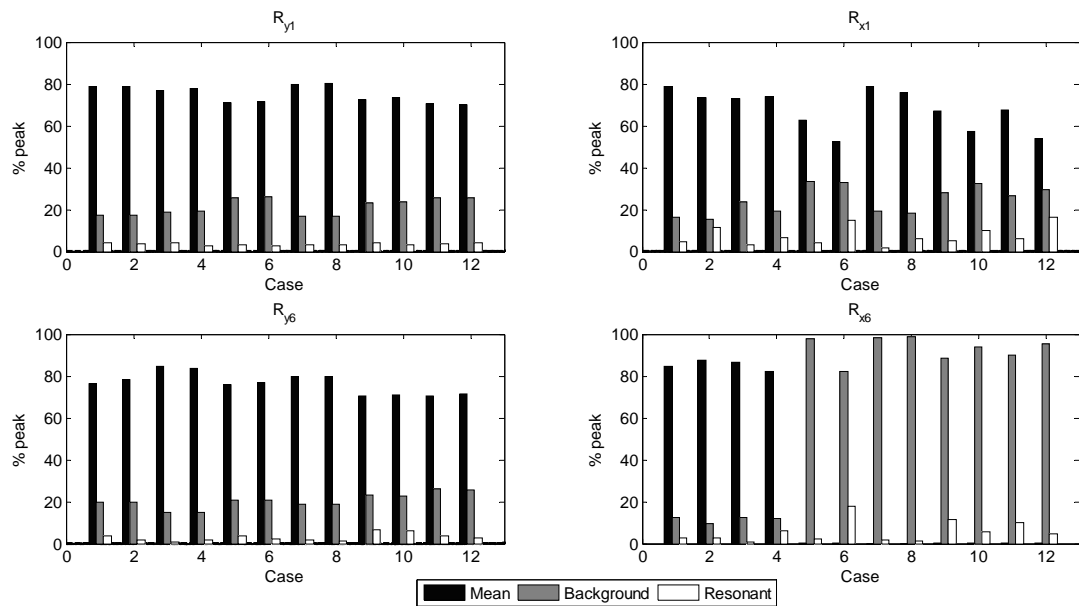


Figure 5.15 Contribution of different components in the peak responses

Fig. 5.16 shows the normalized peak reactions for the twelve considered cases. As shown in the figure, the maximum downburst peak transverse reactions R_{y1p} and R_{y6p} and longitudinal reaction R_{x1p} are associated with case no. 5 (Db_y: $L_x=300$ m, $V_{ref}=40$ m/s) and are equal to 70%, 125% and 390% of the force $g_{yp} \cdot L_x$, respectively. The maximum

downburst peak longitudinal reaction R_{x6p} occurs at case no.3 ($Db_x: L_x=500$ m, $V_{refp}=40$ m/s) and is equal to 45% of the force $g_{yp} \cdot L_x$. As indicated from those values, the developed longitudinal peak reactions, R_{x1p} and R_{x6p} are significantly high and, accordingly, should be included in the design of the line.

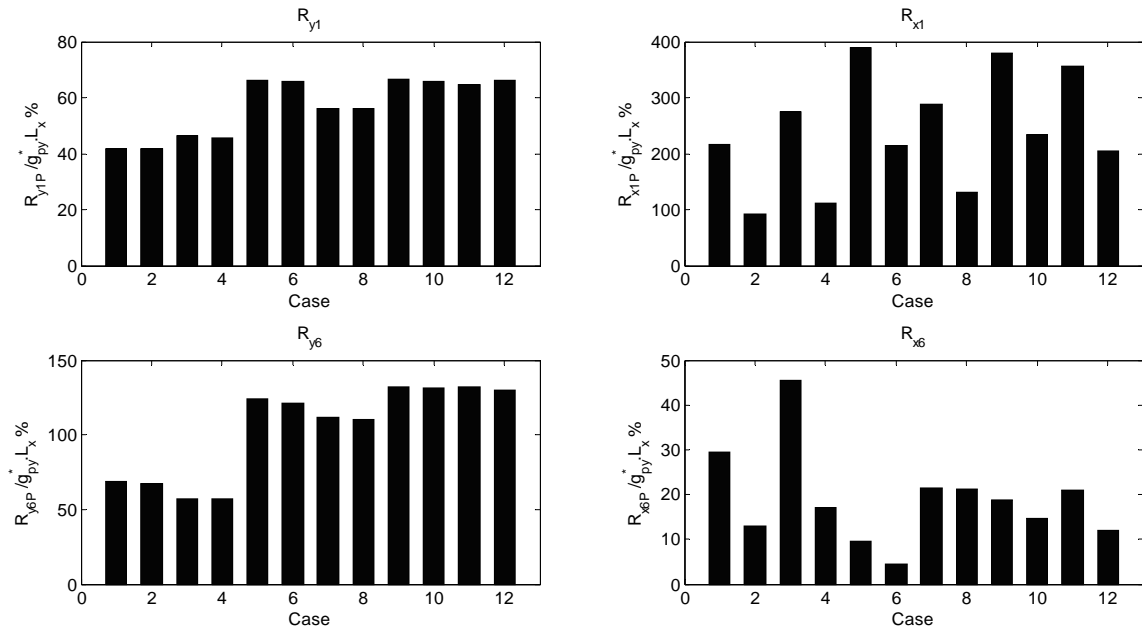


Figure 5.16 Normalized peak reactions

5.7 Conclusions

Dynamic analyses of single-spanned and multiple-spanned conductor systems are performed in the current study. The study includes twelve different cases with variation in the wind type, the mean wind velocity and the span length. Downburst and synoptic winds are used as the wind types. Two downburst loading scenarios causing maximum longitudinal conductor reaction, D_{bx} , and maximum transverse conductor reaction, D_{by} , are considered. Two mean wind velocities, ($V_{ref} = 20$ and 40 m/s) and two span lengths, ($L_x = 300$ and 500 m) are assumed in the analyses. A number of 6 spans (three on each side to the tower of interest) are considered in the study to model the multiple-spanned system based on a recommendation from the literature. The analyses of the two systems are conducted to obtain the longitudinal and the transverse reactions at the intermediate tower of the multiple-spanned system and at the left tower for the single spanned system.

The analysis of the conductor systems is conducted using three steps in order to distinguish between the mean, background and resonant components of the response. First, a non-linear quasi-static analysis under the running-mean wind velocities is conducted to obtain the conductor mean response in addition to the conductor tension force and its displaced profile, which are used to obtain the updated conductor's stiffness. Then, a linear dynamic analysis is conducted under the fluctuating wind forces using the updated conductor stiffness. The fluctuating response resulting from the dynamic analysis contains both the background and resonant components. A quasi-static analysis is conducted under the fluctuating wind forces to obtain the background component alone, which is then subtracted from the overall fluctuating response to estimate the resonant component. The ratio between the peak responses to the maximum mean responses, defined as the Gust Factor (GF), is calculated using both the dynamic analysis, GF_{Dy} , and the static analysis, GF_{QS} . The contribution of the different components to the peak response is calculated and the following conclusions are drawn:

- (i) The contribution, $Cont_R$, to the peak longitudinal reaction R_{x1} for the single-spanned system reaches a relatively high maximum value (in the order of 16%) for downburst and synoptic wind cases when considering the low reference velocity (20 m/s). Under the high reference velocity (40 m/s), the contribution $Cont_R$, reaches a relatively low maximum value (in the order of 5 %) for both downburst and synoptic wind cases. These results indicate that dynamic analysis is recommended to analyze single-spanned system subjected to downbursts and synoptic winds with low reference velocities.
- (ii) The maximum contribution to the peak transverse reaction R_{y6} and to the peak longitudinal reaction R_{x6} for the six-spanned system is found in the order of 5% and 6%, respectively, for both downburst and synoptic wind cases. These low contributions imply that conducting dynamic analysis may not be necessary for estimating the peak reactions for the six-spanned system.

- (iii) Gust factors of both the longitudinal and the transverse reaction for the single-spanned system are shown to be larger than those for the six-spanned system. This is because correlated fluctuations characterized by the length scale, L_{uv} , cover a higher percentage of the conductor length for the single-spanned system than that for the six-spanned system.
- (iv) Maximum peak transverse reactions for the single-spanned system, R_{y1p} and the six-spanned, system R_{y6p} , are found to be equal to 70%, 125% of the force $g_{yp} \cdot L_x$. The maximum peak longitudinal reaction for the single spanned system, R_{x1p} , and the six spanned system, R_{x6p} , are found to be equal to 390% and 45 % of the force $g_{yp} \cdot L_x$, respectively. As indicated from the values, the developed longitudinal reactions in the two systems are significant and should be included in the line design.

5.8 Acknowledgment

The authors would like to thank the National Research Council of Canada (NSERC), Hydro One Company and the Ontario Centre of Excellence (OCE) for their kind financial support of this research.

5.9 References

- Aboshosha, H., El Damatty, A. 2014. Effective Technique to Analyze Transmission Line Conductors under High Intensity Winds. *Wind and Structures, an International Journal* 18(3), 235-252.
- ASCE 2010. Guide lines for electrical transmission line structural loading. ASCE Manuals and Reports on Engineering Practice, 74.
- Australian Standard / New Zealand Standard AS/NZS: 7000. 2010. Overhead line design - Detailed procedures. Standards Australia Limited / Standards New Zealand, North Sydney, Australia.
- Bathe, K.J. 1996. Finite Element Procedures in Engineering Analysis, Prentice-Hall, Englewood Cliffs, New Jersey.

- Battista, R., Rodrigues, R., Pfeil, M. 2003. Dynamic behavior and stability of transmission line tower under wind forces. *J. Wind Eng. Ind. Aerod.* 91(8), 1051-1067.
- Chay, M., Albermani, F., Wilson, R. 2006. Numerical and analytical simulation of downburst wind loads. *Eng. Struct.* 28, 240–254.
- Chen, L., Letchford, C. 2004. A deterministic-stochastic hybrid model of downburst and its impact on a cantilevered structure. *Eng. Struct.* 26(5), 619-629.
- Computer and Structures, Inc. (2010), SAP2000 V.14, CSI Analysis Reference Manual, Berkeley, California, USA.
- Darwish, M., El Damatty, A. 2011. Behavior of self supported transmission line towers under stationary downburst loading. *Wind and Structures, An International Journal.* 14(5), 481-498.
- Darwish M., El Damatty A., Hangan, H. 2010. Dynamic characteristics of transmission line conductors and behaviour under turbulent downburst loading. *Wind and Structures, An International Journal.* 13(4), 327-346.
- Davenport, A.G. 1962. Buffeting of a suspension bridge by storm winds. *J. ASCE Struct. Div.*, 88 (3), 233-264.
- Davenport, A.G. 1986. The dependence of wind load upon meteorological parameters. *Proceedings of International Seminar on Wind Effects on Buildings and Structures*, Toronto, Canada: University of Toronto Press; 1968, p.19–82.
- Davenport, A.G. 1993. How can we simplify and generalize wind loads?, Presented at the Third Asia-Pacific Symposium on Wind Engineering. December 13-D15. Hong-Kong, Keynote Lecture.
- Dempsey, D., White, H.B. 1996. Wind wreak havoc on lines. *T&D World Mag.* 48 (6), 32-42.
- El Damatty, A., Aboshosha, H. 2012. Capacity of Electrical Transmission Towers under Downburst Loading. *Proceedings of the First Australasia and South-East Asia Structural Engineering and Construction Conference*, Perth, Australia, Nov 28-Dec 2, 2012, 317-322.
- El Damatty, A., Hamada, A., Alawady, A. 2013. Development of critical load cases simulating the effect of downbursts and tornados on transmission line structures.

- Key note lecture on the 8th Asia-Pacific Conference on Wind Engineering, APCWE8, Chennai, India. December 10th-14th 2013.
- Fujita, T.T. 1985. The downburst microburst and macroburst. University of Chicago, Department of Geophysical Sciences 128 pp.
- Fujita, T.T. 1990. Downbursts: meteorological features and wind field characteristics. *J. Wind Eng. Ind. Aerodyn.* 36(1), 75-86.
- Gani, F., and Legeron, F. 2010. Dynamic response of transmission lines guyed towers under wind loading. *Can. J. Civ. Eng.*, 37(3), 450-465.
- Hangan, H., Kim, J. 2007. Numerical simulations of impinging jets with application to downbursts. *J. Wind Eng. Ind. Aerodyn.* 95(4), 279-298.
- Holmes, J., Hangan, H., Schroeder, J., Letchford, C., Orwig, K. 2008. A forensic study of the Lubbock-Reese downdraft of 2002. *Wind Struct.* 11(2), 137-152.
- Kwon, D., Kareem, A. 2009. Gust-Front Factor: New Framework for Wind Load Effects on 499 Structures. *J. Struct. Eng.*, 135(6), 717-732.
- Li, C.Q. 2000. A stochastic model of severe thunderstorms for transmission line design. *Probab. Eng. Mech.* 15, 359-364.
- Lin, W., Savory, E., McIntyre, R., Vandelaar, C., King, P. 2012. The response of an overhead electrical power transmission line to two types of wind forcing. *J. Wind Eng. Ind. Aerodyn.* 100 58–69
- Loredo-Souza, A., Davenport, A. 1998. The effects of high winds on transmission lines. *J. Wind Eng. Ind. Aerodyn.* 74-76, 987-994.
- McCarthy, P., Melsness, M. 1996. Severe weather elements associated with September 5, 1996 hydro tower failures near Grosse Isle, Manitoba, Canada. Manitoba Environmental Service Centre, Environment Canada, 21 pp.
- Savory, E., Parke, G., Zeinoddini, M., Toy, N., Disney, P. 2001. Modelling of tornado and microburst-induced wind loading and failure of a lattice transmission tower, *Eng. Struct.*, 23, 365-375.
- Shehata, A., El Damatty, A. 2007. Behaviour of guyed transmission line structures under downburst wind loading. *Wind and Structures, An International Journal.* 10(3) (2007) 249-268, 98.

- Shehata, A., El Damatty, A., Savory, E. 2005. Finite element modeling of transmission line under downburst wind loading. *Finite Elements Anal. Des.* 42(1), 71-89.
- Shehata, A. and El Damatty, A. 2008. Failure analysis of a transmission tower during a microburst. *Wind and Structures*, 11(3)193-208.
- Sparling, B., Wegner, L. 2007. Estimating peak wind load effects in guyed masts. *Wind and Structures*. 10(4), 347-366.
- Von Karman T. 1948. Progress in the Statistical Theory of Turbulence. *Proceedings of the National Academy of Sciences of the United States of America*, 34(11), 530-539.

Chapter 6

6 LES of Wind Flow over Various Upwind Exposures

6.1 Introduction

With the recent development trends in computer and software technologies, the computational cost of carrying out large eddy simulation (LES) for ABL flows is becoming affordable. As a result LES is widely being used in building and wind engineering applications. Some examples include LES for building aerodynamics application (Dagneu and Bitsuamlak 2013), pollution dispersion (Tominaga and Stathopoulos et al. 2011), natural ventilation (Jiru and Bitsuamlak 2010, Jiang et al. 2013), wind-driven-rain/snow (Blocken and Carmeliet 2004, Beyers and Waechter 2008). Accurate simulation of the lower ABL flow and realistic application of the boundary conditions are essential steps for successful LES in building engineering. Boundary conditions represent the effect of the surroundings that have been cut off by the computational domain (CD) and idealize the influence of the actual flow environment under consideration. Boundary conditions dictate the solution inside the CD and have very significant effects on the accuracy of the solution. This study mainly focuses on the ground and inflow boundary conditions. There are several methods in the literature to account for the ground roughness while carrying out LES. Wall functions are perhaps the widely used approach and several variations were developed, such as those by Businger et al. (1971), Schumann (1975), Thomas and Williams (1999) and Xie et al. (2004). The main advantages of using wall functions are the simplicity of simulating a terrain with a specific target aerodynamic roughness z_0 . This is of great importance in wind engineering applications since it allows for simulating a prescribed incoming wind flow. However, wall functions are typically suitable to simulate smooth to moderately rough terrains with an aerodynamic roughness, z_0 , constrained by the practical grid size, Δ_z . The reasons behind this limitation can be summarized as follows: (i) In a typical wall function, drag forces induced by the terrain are introduced in a single grid layer using the velocity extracted at the mid-level of the layer height, $0.5 \Delta_z$, and the target roughness z_0 ; (ii) The level where the velocity is extracted (i.e. $0.5 \Delta_z$) has to be placed in the logarithmic flow

region, which is usually located above the physical roughness height, k_s or $\sim 30 z_0$ (Richards and Hoxey 1993, Franke et al. 2004, Fluent Inc. 2005, and Blocken et al. 2007). If the level where the velocity is extracted is placed below the physical roughness height, k_s or $\sim 30 z_0$, it means that the velocity is extracted from the canopy region. Although wall functions may be employed for such a case by using the shifted version of the logarithmic law i.e. by using displacement height (Vermeire et al. 2011), for very rough surfaces (i.e. large displacement heights) this approach becomes uncertain as indicated by Tsai and Tsuang (2005). These introduce a constraint on the maximum terrain roughness, z_0 , that can be simulated by wall functions while employing a specific grid with a height Δ_z as $60.z_0 < \Delta_z$. Such a constraint becomes very critical for moderately rough ($z_0=0.5$ m) and rough terrains (such as those encountered in heavily built environment $z_0>2$ m). Based on the modified Davenport classification (Wieringa 1992), the height of the first grid has to be 30 and >120 m for the two rough terrains respectively. This definitely limits the usability of the resulting flow in wind engineering applications as most of the important flow details near the ground are wiped out. The focus of the current study is to simulate the wind flow in and above rough terrains including the built-environment with a prescribed aerodynamic roughness, z_0 , that is not bounded by the constraint $60.z_0 < \Delta_z$.

Other than the wall functions approach, methods such as terrain following coordinates, immersed boundary methods (IBM) and canopy models do not have limitation on the terrain roughness that can be modelled. In the method of terrain-following-coordinates developed by Gal-Chen and Sommerville (1975a, b), as inferred by its name, grid coordinates are used to follow the topography of the terrain. Coordinate transformation is applied to convert the computational domain including the bottom topography to a rectangular domain. This method leads to accurate results. However, it is very complex and requires large computational resources (Anderson and Meneveau 2010). IBM is one of the robust methods to resolve for the terrain roughness. In the IBM additional forcing term is added to the momentum equation to account for the drag resulting from the obstacles. For grid points located inside an obstacle, the forcing term is used to instantaneously set the velocities to zeros as indicated by Iaccarino and Verzicco (2003) and Mittal and Iaccarino (2005). On the other hand for the first grid points located outside

the obstacle, forcing term is set to account for the drag and shear forces applied by the obstacle as indicated by Tamura (2009). Since IBM does not require a modification to the grid it is simpler to implement compared to the terrain-following-coordinates method. However, IBM still requires multiple fine grid layers at the bottom of the computational domain in order to account for the terrain roughness. For the cases where the roughness is due to the vegetation, canopy stress models can be used (Katul and Albertson 1998, Katul et al. 2004). LES based canopy stress models depend on the early contributions by Shaw and Schumann (1992) and Su et al. (1998) as reported by Albertson et al. (2001), Yang et al. (2006a, b) and Cassiani et al. (2008). In these models, each computational cell may contain obstacles with frontal area greater than the frontal area of the computational cell, which increases the aerodynamic drag coefficient. Such a drag coefficient is a function of the obstacle shape, computational resolution, and Reynolds number. Canopy stress models can also be used for different roughness sources other than the vegetation. Brown et al. (2001), for example, employed a canopy stress model to simulate ABL flow over a wavy surface, while Shiguang and Weimei (2004) employed canopy stress model to simulate ABL flow within and over an urban canopy.

Velocity profile resulting from the above mentioned methods: terrain-following grids, IBM and canopy model can be used to obtain the aerodynamic roughness by fitting the resulting velocity profile with the logarithmic law. However this represents a major challenge for LES of ABL flow over large complex built-environment terrain due to enormous computational demands.

Robust methods exist in literature such as those reported by Anderson and Meneveau's (2010) surface gradient-based drag (SGD) model. SGD model simulates terrains with topographic heights that are resolvable horizontally but require modeling vertically. Anderson and Meneveau (2010) employed the SGD model to calculate the vertical profiles of the velocities and Reynolds stresses for different terrain scenarios and compared them with those obtained from previous simulations in literature (Nakayama and Sakio 2002, Kanda et al. 2004, Coceal et al. 2007 and Xie et al. 2008). The terrain scenarios included roughness induced by uniform and staggered arrays of blocks, regular arrays of ellipsoidal roughness elements and a two sinusoidal wavy rough surface. The

comparison showed a good agreement between the resulting profiles from the SGD model and those from the literature. SGD model represents a robust method to simulate surface roughness with a given topography, however it does not allow for simulating a relatively rough surface with a prescribed z_0 , that are routinely encountered in wind engineering applications. This is mainly due to the following reasons: (i) In the SGD model and similarly in the previously discussed terrain-following grids, IBM, and canopy models, surface aerodynamic roughness, z_0 , is typically calculated as a result of the developed flow solution. In contrast, the present study focusses on characterizing inflow over a priori known or approximately estimated aerodynamic roughness z_0 of the ground surface; (ii) SGD model introduces the drag forces only at the first grid layer above the ground similar to the wall functions approach, therefore, the constraint ($60 \cdot z_0 < \Delta_z$) that limits the range of aerodynamic roughness that can be modelled for a particular grid density also exists.

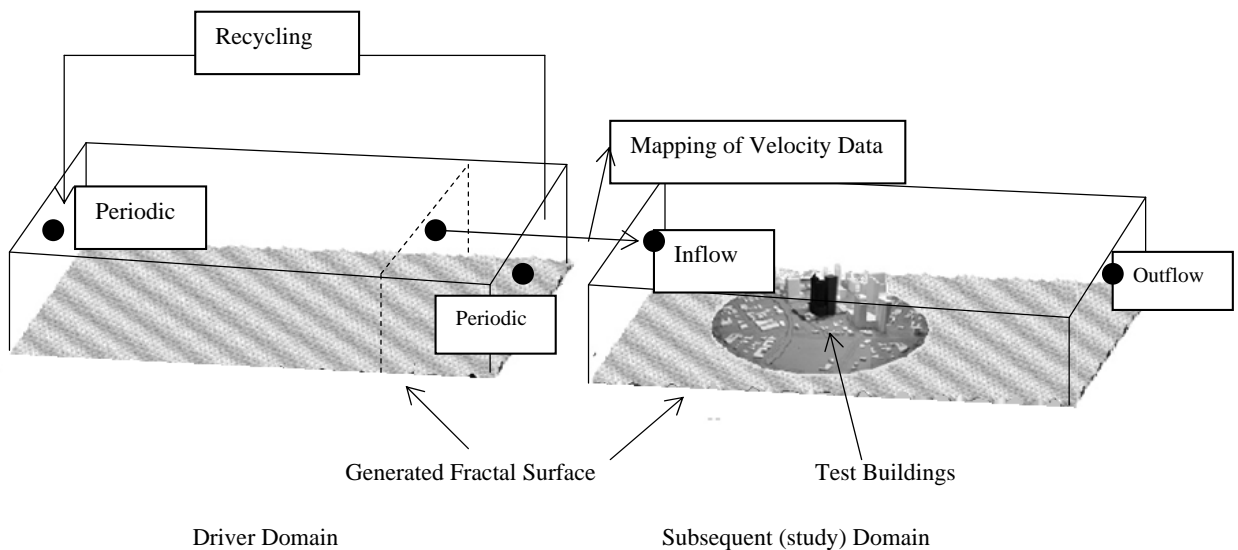


Figure 6.1 Schematic of driver and test domains

Anderson and Meneveau (2010) introduced the usage of random Fourier modes (RFM) to numerically generate random fractal surfaces. They studied two boundary layers induced from numerically generated fractal surfaces: a moderate rough and a very rough. The root mean square (r.m.s) topography heights was related to the resulting aerodynamic roughness, z_0 , but this area requires further research particularly with regard to the $60 \cdot z_0 <$

Δ_z constraint. In the current study, the SGD model developed by Anderson and Meneveau (2010) is modified to allow for simulating the flow within and above rough terrains with a prescribed aerodynamic roughness z_0 , that is not bounded by the constraint ($60.z_0 < \Delta_z$).

The present study has three parts. In the first part (Section 6.2), the original SGD model is modified to overcome the constraint $60.z_0 < \Delta_z$. In the second part (Section 6.3), a scaling technique is proposed to scale the fractal surfaces generated by RFM in order to produce the targeted aerodynamic roughness z_0 . In the third part (Section 6.4), LES of ABL flow over three different exposure conditions, represented by scaled fractal surfaces, is carried out by recycling the flow throughout a driver domain, as illustrated in Figure 6.1, using the modified SGD model. Simulations are performed by recycling the flow throughout a driver domain as shown in Figure 6.1. Recycling the flow enables obtaining a stabilized ABL using a relatively shorter computational domain. The resulting mean velocity, turbulence intensity and Reynolds stress profiles as well as the velocity spectra are compared with the profiles and spectra of the targeted aerodynamic roughness z_0 . Moreover, applicability of using the ABL velocities resulting from the driver domain as inflow boundary condition in the subsequent domain (as illustrated in Figure 6.1) is discussed. It is to be noted, however, performing subsequent LES on test buildings is not within the scope of the current study. Finally, conclusions and recommendations are given in Section 6.5.

6.2 Modified Surface Gradient Drag (MSGD) model

In this section, a modified version of the SGD model that was originally developed by Anderson and Meneveau (2010) is presented. SGD model was originally developed to simulate ABL flows above terrains that are slowly varying horizontally and with heights small enough to fall below the first vertical grid layer, such as those indicated by Figure 6.2a. According to Anderson and Meneveau (2010), drag force per unit mass inside a control volume, f_i , is calculated using Equation 6.1, while the shear stress at the top of the volume, τ_{i3} , is calculated by integrating the drag force along volume height as illustrated in Figure 6.2a and expressed by Equation 6.2.

$$f_i(x, y, \Delta_z / 2) = -\frac{1}{2 \cdot \Delta_z} C_d \cdot R(\hat{n}_k \frac{\partial h}{\partial x_k}) \tilde{u}_i U^{m\Delta} \tag{Equation 6.1}$$

where ρ is air density, C_d is drag coefficient of the roughness elements, which can be taken equal to 2 for rectangular-like roughness elements, Δ_z is vertical height of the first grid, \tilde{u}_i is resolved velocity at the reference height in the direction i , $U^{m\Delta}$: magnitude of the velocity at the reference height filtered using filtering width $m \cdot \Delta$ where m is taken equal to 2 and Δ is the grid length, \hat{n}_k : Unit vector of the velocity direction, $h(x, y)$: the height of the topography at x, y location, $R(x_k)$: is the ramp function $R(x_k) = (x_k/2 + |x_k|/2)$

$$\tau_{i3} = \rho \int_0^{\Delta_z} f_i dz = -\frac{1}{2} \rho \cdot C_d \cdot R(\hat{n}_k \frac{\partial h}{\partial x_k}) \tilde{u}_i U^{m\Delta} \tag{Equation 6.2}$$

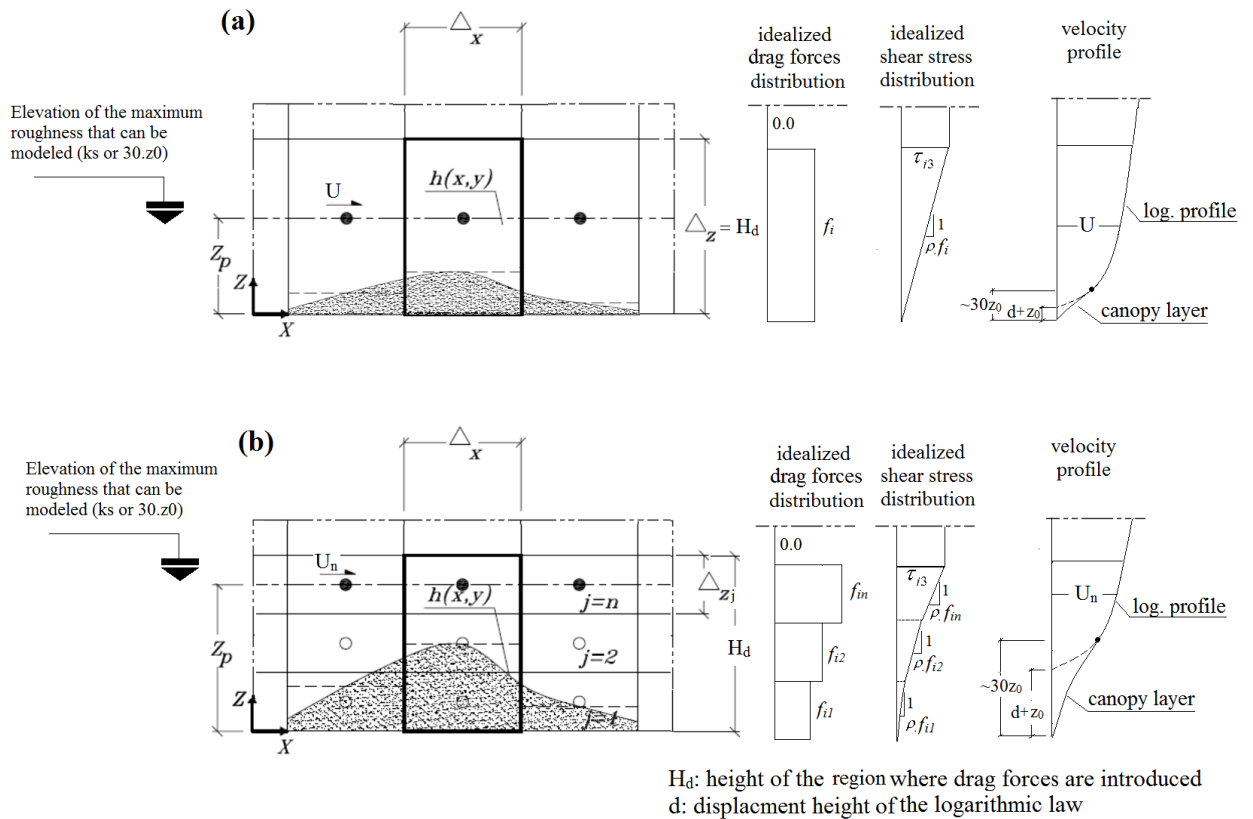


Figure 6.2 SGD models: (a) Anderson and Meneveau (2010) and (b) Modified

As discussed earlier, the constraint of $z_0 < \Delta_z$ is a result of applying the drag forces, f_i , on the first grid layer only due to the requirement of placing the level where the velocity is extracted, z_p , above the physical height of the roughness, k_s or $30z_0$ (in the logarithmic flow region). Such a constraint can be relaxed by using multiple n layers, with an overall height H_d , as illustrated in Figure 6.2b, which is the main concept of the modified SGD model. Shear stress, τ_{i3} , at the top of the grid layers is calculated using Equation 6.3, which is similar to the original expression given by Equation 6.2, except in the manner the drag coefficient, C_d^* , is calculated and the location where the velocity is extracted. In the modified model, shear stress, τ_{i3} , is related to the velocity at the upper layer, U_n , and the drag coefficient is modified accordingly as discussed in the following subsection.

$$\tau_{i3} = -\frac{1}{2} \rho \cdot C_d^* \cdot R(\hat{n}_k \frac{\partial h}{\partial x_k}) \tilde{u}_{in} U_n^{m\Delta} \quad \text{Equation 6.3}$$

It should be mentioned that the reason behind using multiple layers is not to account for the local variation of the roughness in the vertical direction, where some grid layers are located inside the roughness obstacle while other are located outside as in the IBM. Multiple layers are used instead to allow for extracting the velocity at mid-height of the upper layer, $H_d - 0.5 \Delta_{zn}$, which is placed in the logarithmic flow region above the physical height of the roughness (k_s or $30z_0$), as indicated by Figure 6.2b. This relaxes the constraint in the original SGD model to $30 \cdot z_0 < H_d - 0.5 \Delta_{zn}$ or $30 \cdot z_0 < (n - 0.5) \cdot \Delta_z$, for the case of a uniform layer height, Δ_z . This enables simulation of rougher surfaces by employing a specific grid provided that a sufficient number n of the layers is used. For the case of a single layer, $n=1$, the constraint $30 \cdot z_0 < (n - 0.5) \cdot \Delta_z$ converges to the constraint in the original SGD model by Anderson and Meneveau (2010). Multiple layers are also used to adopt to the target aerodynamic roughness, z_0 , before conducting the simulation, as will be discussed in details in Section 6.3.

Drag force in the i -direction at layer no. j , f_{ij} , can be expressed by Equation 6.4, as the multiplication of a coefficient C with the velocity component \widetilde{u}_{ij} and the velocity magnitude $U_j^{m\Delta}$.

$$f_{ij} = C \widetilde{u}_{ij} U_j^{m\Delta} \quad \text{Equation 6.4}$$

Such an expression is based on the analogy with vegetation canopies, where the coefficient C is the multiplication of the frontal area index (FAI) and the drag coefficient of the vegetation. In vegetation models, where the interest is in the averaged vegetation density rather than the localized vertical distribution (Inoue 1963 and Cowan 1968), that coefficient is usually considered constant along the canopy height. Similarly, by focusing on the averaged roughness distribution in the vertical direction, rather than the localized variations, the coefficient C can be assumed constant in all grid layers that share the same horizontal x - and y -coordinates. That is equivalent to the simulation of roughness elements that have a similar height and different shapes in plan. Shear stress at the top of the grid layers, τ_{i3} , can be calculated by integrating the drag forces, f_{ij} , from all layers, where $j=1:n$. By assuming a piece wise distribution of the drag forces, as shown in Figure 6.2b, shear stress at the top of the grid layers, τ_{i3} , can be expressed as a function of the coefficient C , according to Equation 6.5.

$$\tau_{i3} = \rho \int_0^{\Delta z} f_i dz = \rho \sum_{j=1}^n f_{ij} \cdot \Delta_z = \rho \cdot C \sum_{j=1}^n \widetilde{u}_{ij} U_j^{m\Delta} \Delta_z \quad \text{Equation 6.5}$$

By substituting the coefficient C as from Equation 6.5 into Equation 6.4, drag force at layer no. j in the direction i , f_{ij} , can be expressed by Equation 6.6.

$$f_{ij} = \frac{\tau_{i3} \widetilde{u}_{ij} U_j^{m\Delta}}{\rho \sum_{j=1}^n \widetilde{u}_{ij} U_j^{m\Delta} \Delta_{zj}} \quad \text{Equation 6.6}$$

Equations 6.3 and 6.6 calculate the shear stress and the drag forces at different layers using the modified SGD model, respectively. However, that requires the drag coefficient C_d^* to be known, which is discussed in the following subsection.

6.2.1 Calculation of the Drag Coefficient C_d^*

Anderson and Meneveau (2010) used a value of 2 for the drag coefficient, C_d , which is suitable for rectangular-like roughness elements. They chose the reference height, where the mean velocity is used to obtain the drag force, to be at the middle height of the first grid layer as illustrated by Figure 6.2a. On the other hand, in the modified SGD model, the reference height is chosen near the top of the canopy as illustrated in Figure 6.2b. Such a change in the reference height requires to be accounted for in the drag coefficient, C_d^* , employed in Equation 6.3. In the current study, drag coefficient, C_d^* , is calculated by scaling the drag coefficient, C_d , for rectangular like roughness elements with the ratio between the weightily averaged square velocity over the canopy grid layers, $\sum_{j=1}^n (\langle U(z)^2 \rangle \cdot \Delta z_j) / \sum_{j=1}^n (\Delta z_j)$, and the plane averaged square velocity at the reference height z_p , $\langle U(z_p)^2 \rangle$, as expressed by Equation 6.7. It should be mentioned that the two averaged square velocities are identical for the case of a single layer $n=1$, and consequently C_d^* equals to C_d .

$$C_d^* = C_d \cdot \frac{\sum_{j=1}^n (\langle U(z)^2 \rangle \cdot \Delta z_j) / \sum_{j=1}^n (\Delta z_j)}{\langle U(z_p)^2 \rangle} \quad \text{Equation 6.7}$$

where $\langle \dots \rangle$ represent horizontal plane averaging, C_d is drag coefficient for rectangular-like roughness elements which equals to 2. In order to obtain the drag coefficient, C_d^* , by using Equation 6.7, information regarding the velocity profile inside the canopy layer is required. Wang (2012) provided an analytical model that showed a reasonable accuracy for sparse canopies with a wide range, 0.03- 0.50, of frontal area index (FAI). The current study is focused in simulating the flow over rough terrains those representing urban canopies, which are usually sparse with a FAI in the order of 0.3 in downtown areas (Britter and Hanna 2003). This is within the range, where the analytical model by Wang

(2012) is reasonably accurate. Therefore, the same analytical model is used in the current study to scale the drag coefficient by Equation 6.7. According to Wang (2012), such a scaling ratio can be calculated using Equation 6.8, where $g(z)$ is a function that can be calculated by Equations 6.9 and depends on the elevation z and the canopy properties. More details about the employed parameters in Equations 6.9 are given by Wang (2012).

$$\frac{\sum_{j=1}^n \left(\langle U(z)^2 \rangle \cdot \Delta z_j \right) / \sum_{j=1}^n (\Delta z_j)}{\langle U(z_p)^2 \rangle} = \frac{\sum_{j=1}^n \left(\left(I_0(g(z)) - I_0(g(z_{01})) / k_0(g(z_{01})) \cdot k_0(g(z)) \right)^2 \right) \cdot \Delta z_j / \sum_{j=1}^n (\Delta z_j)}{\left(I_0(g(z_p)) - I_0(g(z_{01})) / k_0(g(z_{01})) \cdot k_0(g(z_p)) \right)^2} \quad \text{Equation 6.8}$$

where I_0 and k_0 are modified Bessel functions of first and second kinds of zero order, respectively.

$$g(z) = 2 \sqrt{\left(0.768X^2 + 0.9031X \right) \frac{z}{H_d}}$$

$$X = \frac{H_d}{H_d - d} \cdot \frac{1}{\ln\left(\frac{H_d - d}{z_0}\right)} - \left(\frac{H_d - d}{H_d} \frac{\ln\left(\frac{H_d - d}{z_0}\right)}{\ln\left(\frac{H_d}{z_{01}}\right)} \right)^{1.45} \cdot \frac{1}{\ln\left(\frac{H_d}{z_{01}}\right)} \quad \text{Equations 6.9}$$

where H_d : height of the region where the drag forces are introduced, which is taken in the current study in the order of 60 times the aerodynamic roughness of the surface z_0 , d : displacement height used to shift the logarithmic flow region above the canopy, z_{01} : Aerodynamic roughness due to the surroundings to the roughness elements, which is taken equal to H_d divided by $1e5$ similar to Wang (2012).

Equations 6.3, 6.6 and 6.7-6.9 represent the modified SGD model, which allows for simulating surfaces with an aerodynamic roughness, z_0 , that is not bounded by $60 \cdot z_0 < \Delta z$. In the next section, synthesizing fractal surfaces with a targeted aerodynamic roughness z_0 , is discussed.

6.3 Synthesizing Fractal Surfaces with a Targeted z_0

Synthesizing fractal surfaces with a targeted aerodynamic roughness is conducted in the following two steps: (i) random Fourier modes (RFM) are used to synthesize un-scaled fractal surfaces. Those surfaces are required to be scaled in order to have an aerodynamic roughness as the prescribed; and (ii) a procedure for scaling the surfaces is applied. The scaling is based on equating the average shear stress using the logarithmic law with the averaged shear stress resulting from the surface employing the modified SGD model. Details about those steps are illustrated in the following subsections.

6.3.1 Generating Unscaled Fractal Surfaces using RFM

Anderson and Meneveau (2010) employed RFM to synthesize heights, $h(x,y)$, of two different fractal surfaces by employing Equation 6.10. The roughness spectra, $S(k)$, described by Equation 6.11, was employed with a spectral slope β . Such a spectral slope characterizes the roughness of the generated surfaces.

$$h(x, y) = \sum_k S(k).e^{i(k.x+\varphi_k)} \quad \text{Equation 6.10}$$

where $S(k)$ is spectra of the roughness, k is wave length and φ_k is phase angles.

$$S(k) = c.k^{-\frac{1+\beta}{2}} \quad \text{Equation 6.11}$$

where c is constant to control the amplitudes of the fractal surface and β is spectral slope which is taken equal to -0.5 in the current study.

Anderson and Meneveau (2010) employed a spectral slope, β , equal to -0.5 for the very rough surface and to -0.8 for the moderate rough surface. In the current study, a single value of the spectral slope equal to -0.5 is used. A slight difference is introduced in the surfaces generated by RFM in the current study than Anderson and Meneveau (2010), which is related to the height variations in the y -direction. In the current study variation of the heights in the y -direction is introduced by relating the random phase angles, φ_k , to the y -coordinate as indicated by Equation 6.12. This leads to a Gaussian spectral distribution, with an average wave length $1/l_y$, in the y -direction as indicated by

Kraichnan (1970) and Smirnov et al. (2001). A high wave length in the order of $1/(2\Delta_y)$ is chosen. The Gaussian distribution of the spectra with a high characteristic wave length is chosen since it generates fractal surfaces with a height variation in the x -direction (dominant flow direction) that does not significantly change from section to section in the transverse y -direction. This allows for developing a boundary layer with homogeneous characteristics in the y -direction, which is preferable in wind engineering applications.

$$\varphi_k = \frac{y}{l_y} \tilde{k}_y + \varphi_0 \quad \text{Equation 6.12}$$

where \tilde{k}_y is Gaussian random numbers with zero mean and 0.5 standard deviation, l_y is characteristic wave length in y -direction, and φ_0 is random phase angles. Equations 6.10-6.12 can be used to describe the heights variation for an arbitrary generated fractal surface. The modified SGD model, described in section 6.2, can be used to introduce the drag forces resulting from such a surface. However, the aerodynamic roughness, z_0 , of the surface is not known yet. Therefore, a scaling factor that can be used to scale the fractal surfaces so that their aerodynamic roughness matches the target is suggested in the next subsection.

6.3.2 Scaling of the Fractal Surfaces

A scaling factor, a , is introduced to the heights generated by Equations 6.10-6.12 in order to have a specific value of the aerodynamic roughness when modeled using the modified SGD model, as indicated by Equation 6.13.

$$h_{scaled}(x, y) = h_c + a.h(x, y) \quad \text{Equation 6.13}$$

where h_c is a constant height that can be used to set the mean height of the surface to be equal to a specific value, which is chosen in the current study to be half the physical size of the targeted roughness, $0.5 k_s \sim 15 z_0$. That constant height does not affect the flow solution, but it affects the overall level of the surface.

In order to find the scaling factor, a , plane averaged shear stress opposing the mean flow, $\langle \tau_{13} \rangle$, induced by the scaled surface is equated with the averaged shear stress resulting from employing the logarithmic log law. Average shear stress resulting from the surface can be expressed by Equation 6.14, which require the terms between the parentheses to be averaged.

$$\langle \tau_{13} \rangle = -\frac{1}{2} \rho \cdot C_d^* \cdot \left\langle R(\widehat{n}_k \frac{\partial h_{scaled}}{\partial x_k}) \widetilde{u}_{1n} U_n^{m\Delta} \right\rangle \quad \text{Equation 6.14}$$

where $\langle .. \rangle$: horizontal plane averaging

Averaging of such terms can be approximated by Equation 6.15 as the multiplication of the averages of the sub terms, while assuming the flow to be dominated in the positive x -direction, $\widehat{n}_k \approx [1 \ 0 \ 0]$.

$$\left\langle R(\widehat{n}_k \frac{\partial h_{scaled}}{\partial x_k}) \widetilde{u}_{1n} U_n^{m\Delta} \right\rangle \approx \left\langle R(\frac{\partial h_{scaled}}{\partial x}) \right\rangle \left\langle (U_n^{m\Delta})^2 \right\rangle \quad \text{Equation 6.15}$$

Assuming the flow to be dominated in the positive x -direction is based on choosing the pressure gradient forces, which are used to enforce the flow in the computational domain, to be also in the positive x -direction. This is discussed in Section 6.4. By substituting the average of the terms between the parentheses from Equation 6.15, into Equation 6.14, average shear stress resulting from the scaled surface can be calculated by Equation 6.16, which involves some approximations. The influence of those approximations on the averaged shear and the resulting flow characteristics is discussed in Section 6.4.

$$\langle \tau_{13} \rangle \approx -\frac{1}{2} C_d^* \cdot \rho \cdot \left\langle (U_n^{m\Delta})^2 \right\rangle \left\langle R(\frac{\partial h_{scaled}}{\partial x}) \right\rangle \quad \text{Equation 6.16}$$

Mean shear stress due to the logarithmic law can be expressed by Equation 6.17, where C_{z_p} is the drag coefficient at the level of z_p and can be related to z_0 by Equation 6.18. Expressing the shear stress according to the logarithmic law is valid given that the velocity is extracted at a level z_p located in the logarithmic flow region, which is satisfied by maintaining $30 \cdot z_0 < H_d - 0.5 \Delta_{zn}$ as mentioned previously in Section 6.2.

$$\langle \tau_{13} \rangle = -C_{z_p} \cdot \rho \cdot \langle (U_n^{m\Delta})^2 \rangle \quad \text{Equation 6.17}$$

$$C_{z_p} = \left(\frac{\kappa}{\ln\left(\frac{z_p - d}{z_0}\right)} \right)^2 \quad \text{Equation 6.18}$$

where k is von Karman constant, which is taken as 0.41 and d is the displacement height. By equating the two averaged shear stresses, from Equations 6.16 and 6.17, the scaling factor, a , can be expressed by Equation 6.19.

$$a = \frac{2}{C_d^*} \cdot C_{z_p} \frac{1}{\left\langle R\left(\frac{\partial h}{\partial x}\right) \right\rangle} \quad \text{Equation 6.19}$$

The procedure adopted to generate the fractal surfaces that matches the targeted z_0 and how the resulting forces are introduced into the CFD code is summarized in Table 6.1. Following these steps three different fractal surfaces corresponding to different terrain exposures ranging from smooth to very rough terrain are generated, and subsequently used as ground boundary condition for the LES simulation as described in Section 6.4.

Table 6.1 Steps involved in simulating roughness associated with the fractal surfaces

Step	Description
1	Choose the number of layers n . Such a number is chosen in the current study so that the total height of layers H_d is in the order of 60 z_0 or more. Where z_0 is the target roughness with displacement height, d , to be simulated using a grid with dimensions, Δ_x , Δ_y , and Δ_z , in the x -, y - and z -directions, respectively.
2	Calculate the drag coefficient C_d^* according to the model by Wang (2012) using Equations 6.7-6.9.
3	Generate unscaled fractal surface using the coordinates of the grids in x - and y -directions using Equations 6.10-6.12. A high characteristic wave length, $1/l_y$, is recommended to maintain the x -distribution of the surface heights so that the changes at different y transverse locations are minimized. This helps to develop a

boundary layer with homogeneous characteristics in the transverse y -direction.

- 4 Scale the fractal surfaces using Equations 6.13, 6.18 and 6.19.
 - 5 In both driver and test domains, illustrated in Figure 6.1, introduce drag forces associated with the scaled surfaces using Equations 6.3 and 6.6. Those drag forces are to be assigned as source terms in the momentum equations. A user defined function (UDF) is built to introduce the drag forces into the CFD code.
-

6.4 LES Model

Three dimensional rectangular computational domains are chosen to perform the LES. The computational domain length, L_x , width, L_y , and height, L_z , are chosen to be 2 x 2 x 1 km. The computational domain is discretized in x -, y - and z -directions using two grids: G1 (64x64 x 64) and G2 (64x64x128) to assess the grid sensitivity.

Figure 6.3 illustrates the computational domain, the employed grids and the boundary conditions. While periodic boundary conditions are used for surfaces designated as 1, surface 2 implements slip wall and the ground surface 3 deploys the modified SGD model. The usage of periodic boundaries allows the boundary layer to be fully developed. Other researchers such as Basu and Porte'-Agel (2006), Stoll and Porte'-Agel (2006 and 2008), Anderson and Meneveau (2010), have also used periodic boundaries in order to obtain the developed boundary layer for their wall functions or roughness models. RFM is employed to generate three fractal surfaces corresponding to open country, suburban and urban terrain exposures as summarized in Table 6.2 by using Equations 6.10-6.12 and 6.11-6.14. The countryside, suburban, and urban exposures are also similar with those used by the ESDU (2001), which is widely used approach in most commercial boundary layer wind tunnels to generate target wind speed and turbulence profiles as well as the spectra.

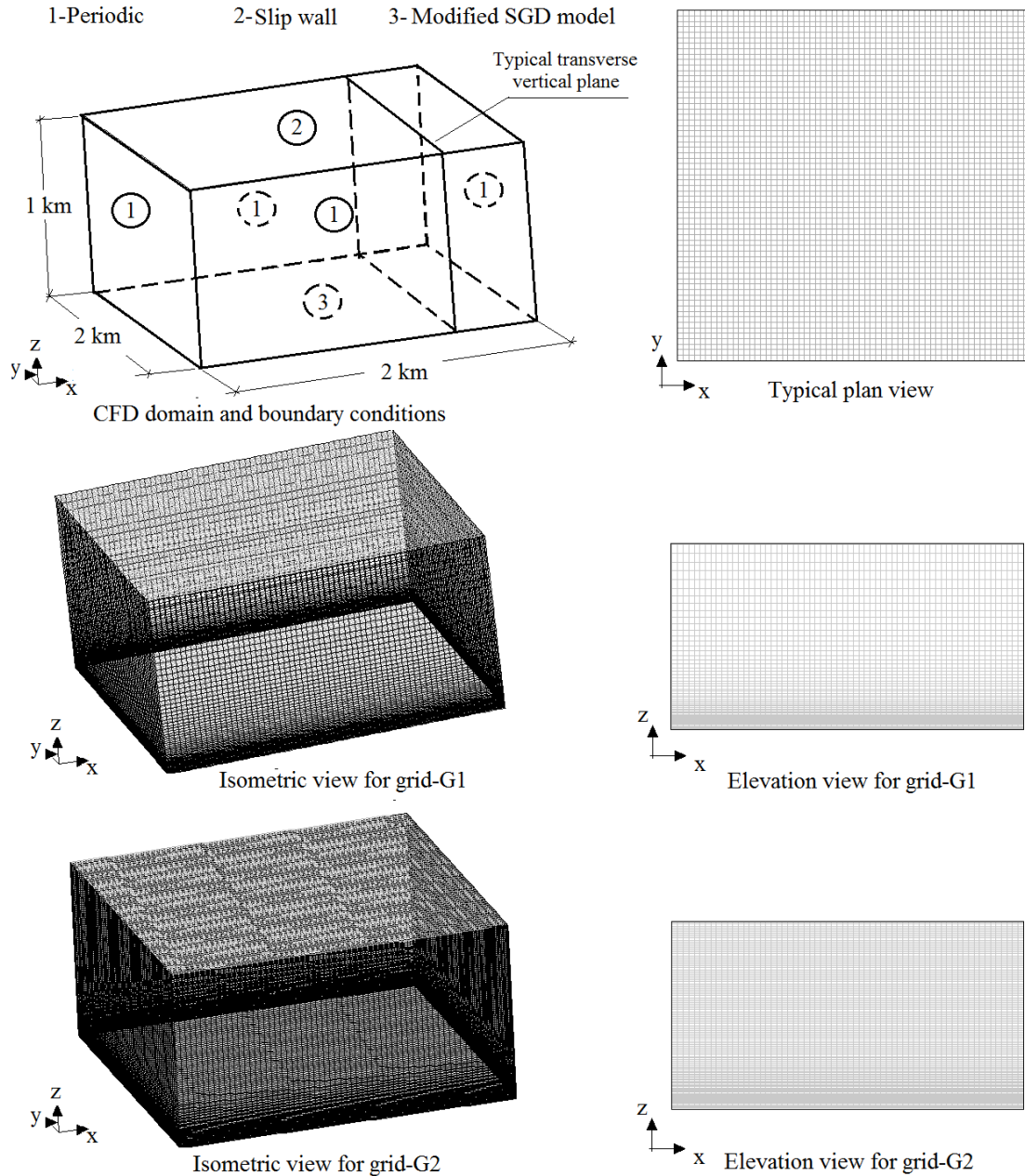


Figure 6.3 Computational domain, the employed grids and boundary conditions

In the surface generation process, 100 wave lengths, k , ranging from $1/(2\Delta_x)$ to $2\pi/L_x$ were used, while a high characteristic wave length in the y -direction, $1/l_y$, is chosen, $1/(2\Delta_y)$.

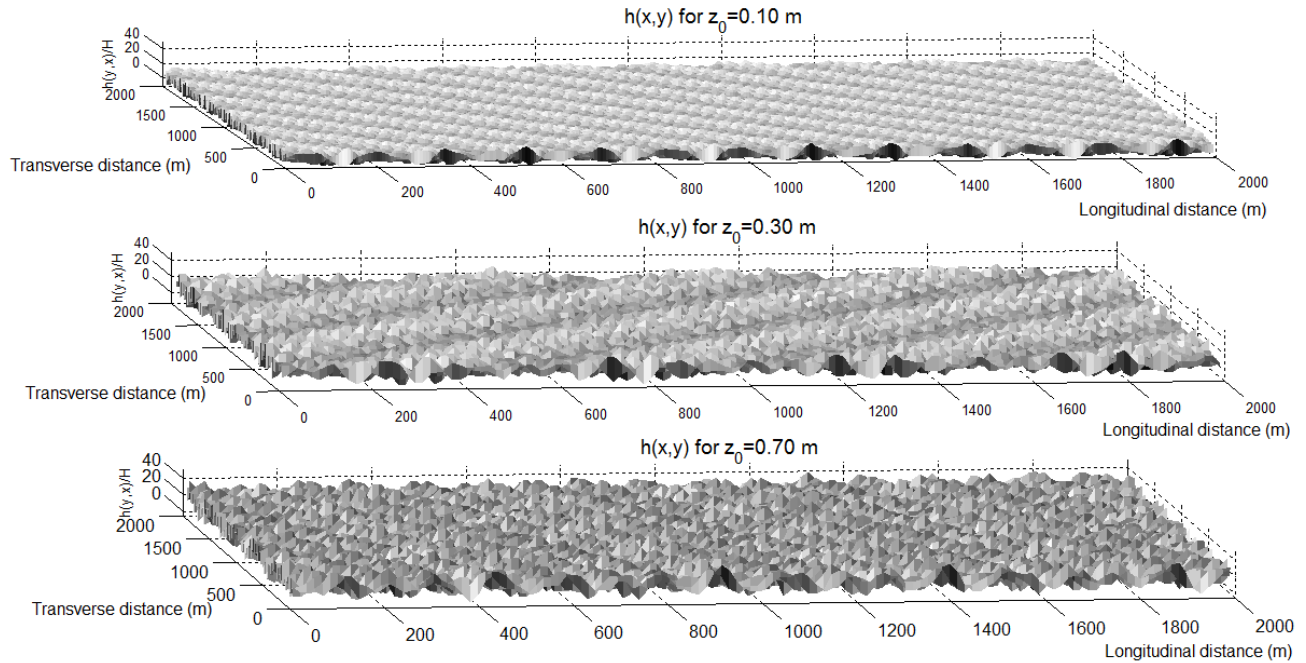


Figure 6.4 Generated fractal surfaces corresponding to $z_0=0.1, 0.3$ and 0.7m respectively

Illustrations of the generated terrains are given by Figure 6.4. In the surface generation process, the displacement height, d , is required. Such a displacement height is a function of the density of the roughness elements. The displacement height approaches zero for sparsely distributed roughness elements and it approaches the overall height of the canopy for heavily distributed elements as indicated by the ESDU 2002. In the current study, d is taken as summarized in Table 6.2, which is compatible with the findings of Tsai and Tsuang (2005). According to Tsai and Tsuang (2005), sensitivity of estimating z_0 due to uncertainty of the displacement height, d , decreases with the increase of the reference height, z_p . Such a reference height is chosen in the order of $60 z_0$ or more as summarized in Table 6.2, to reduce the error. Velocity, $U^{m\Delta}$, employed in calculating the shear stress, τ_{i3} , indicated by Equation 6.3, requires to be spatially averaged in order to represent the mean velocity around the roughness elements. Averaging of the velocities has a particular importance to satisfy the Monin and Obukhov similarity (Monin and Obukhov, 1954) and to introduce the required mean shear stress as indicated by Thomas and Williams (1999).

Table 6.2 Generated exposure conditions

Terrain Exposure	z_0 (m)	d/z_0^*	z_p/z_0^{**}
Countryside	0.1	0.0	75.0
Suburban	0.3	10	58.3
Urban (city center)	0.7	10	60.7

*: d/z_0 is taken from Tsai and Tsuang (2005), **: A number n of the layers equal to 2, 4 and 9 for $z_0=0.1, 0.3$ and 0.7 m, respectively, using a uniform layer height $\Delta z_j=5.0$ m.

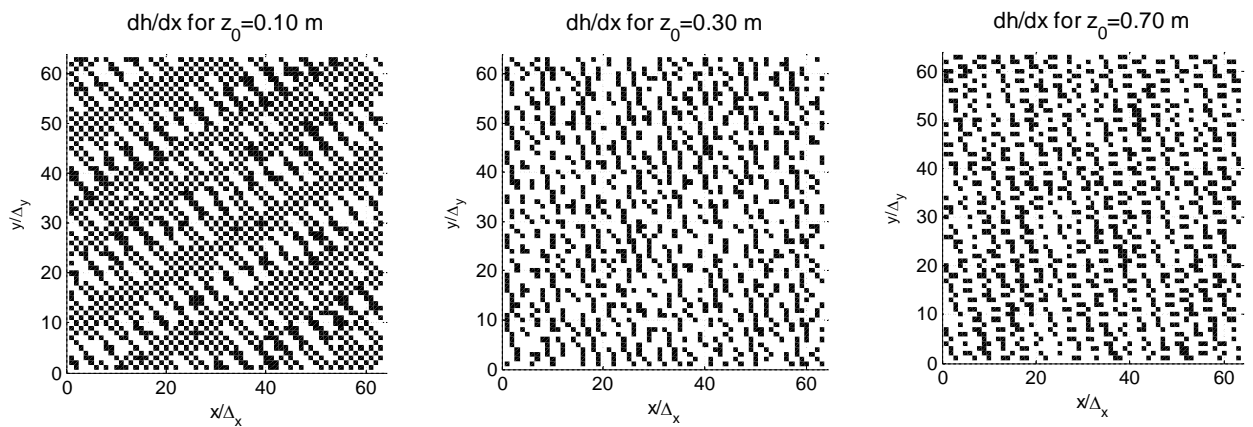


Figure 6.5 Generated surface grid points with positive $\frac{\partial h}{\partial x}$ (dark)

Anderson and Meneveau (2010) used a fixed filtering width of $1.\Delta$ while calculating the averaged velocity, $U^{m.\Delta}$, in their simulations. In the current study, however, the averaging width is related to the characteristics of the generated surface itself rather than using a fixed width. According to Equation 6.3, while considering the stream wise flow in the positive x -direction, only grid points that have positive derivative $\frac{\partial h}{\partial x}$ will affect the drag, and therefore, represent the presence of the roughness elements. Averaged distance between any two nearby zones, which have a positive derivative $\frac{\partial h}{\partial x}$, represents the averaged distance between the roughness elements. Such an averaged distance is calculated in both x - and y -directions i.e. l_x and l_y , respectively, and their resultant,

$l_{xy} = \sqrt{l_x^2 + l_y^2}$, is used as the width of the averaging filter $m\Delta$. Grid points that have a positive $\frac{\partial h}{\partial x}$ derivative are illustrated and marked in black in Figure 6.5 and the averaging distances l_x , l_y and the filter width, l_{xy} , are summarized in Table 6.3.

Table 6.3 Averaging lengths l_x , l_y , l_{xy}

Surface z_0 (m)	l_x/Δ_{xy}	l_y/Δ_{xy}^*	l_{xy}/Δ_{xy}
0.1	2.76	2.86	3.98
0.3	3.04	5.66	6.44
0.7	4.02	4.00	5.64

* Δ_{xy} : Grid length in x - and y -directions=2000/64 m

LES are performed using sub grid scale model originally proposed by Smagorinsky (1963) and modified by Geomano et al. (1991) to dynamically tune the model constant. The commercial software package Fluent 13 (2010) is utilized to solve the governing flow represented by Equations 6.15. A UDF is developed to calculate the drag forces, f_i , required in the momentum equations to account for the fractal surfaces as summarized by Table 6.1.

$$\begin{aligned} \frac{\partial(\overline{u_i})}{\partial x_i} &= 0 && \text{Equations 6.20} \\ \frac{\partial \overline{u_i}}{\partial t} + (\overline{u_j}) \frac{\partial \overline{u_i}}{\partial x_j} &= -\frac{1}{\rho} \frac{\partial \overline{P}}{\partial x_i} - \left(-\frac{1}{\rho} \Pi \delta_{ii}\right) + \frac{\partial}{\partial x_j} (-\tau_{ij} + 2\nu \overline{S_{ij}}) + f_i \\ \tau_{ij} &= \overline{u_i u_j} - \overline{u_i} \overline{u_j} \\ \overline{S_{ij}} &= \frac{1}{2} \left(\frac{\partial \overline{u_i}}{\partial x_j} + \frac{\partial \overline{u_j}}{\partial x_i} \right) \\ \tau_{ij} - \frac{1}{3} \delta_{ij} \tau_{kk} &= 2\nu_e \overline{S_{ij}} \\ \nu_e &= (C_s \Delta)^2 \cdot (2\overline{S_{ij}} \cdot \overline{S_{ij}})^2 \end{aligned}$$

where $i=1, 2, 3$ correspond to x -, y -, and z -directions, respectively, the over bar represents the filtered quantities, u_i , u_{gi} , p , t , τ_{ij} and ν represent fluid velocity, grid velocity, pressure, time, the SGS Reynolds stress and molecular viscosity coefficient, respectively.

$S_{ij}, \nu_e, \Delta, C_s$ represent strain rate tensor, eddy viscosity, grid size, Smagorinsky constant which is determined instantaneously based by the Geomano identity in the dynamic model (Geomano et al., 1991). δ_{ij} represent Kronecker delta, Π represent imposed pressure gradient to enforce the flow, f_i represent drag force obtained from the modified SGD model.

As indicated by Equations 6.20, pressure gradient, Π , is required in the flow governing equations to enforce the flow. The interest in the current research is the simulation of the ABL lower zone where the buildings exist. In this zone, the shear stress can be assumed constant and the velocity profile can be described approximately by the logarithmic law. In order to obtain a logarithmic velocity profile using the periodic boundary conditions illustrated in Figure 6.2, shear stress above the canopy layer needs to be maintained fairly constant. Therefore, stream-wise pressure gradient, Π , introduced in Equations 6.15, is lamped only at the upper 20% of the domain, H_{pG} , as indicated by Figure 6.6 a and expressed by Equation 6.21. This is similar to the case of using a uniform pressure gradient with high domains in the vertical direction.

$$\Pi = -\frac{\rho u_*^2}{H_{pG}} \quad \text{Equation 6.21}$$

where u_* is friction velocity which $=\sqrt{\tau/\rho}$, H_{pG} is height of the layer where the pressure gradient is lumped, and it is taken as 20% of the domain height H .

Figure 6.6a shows the balance between the imposed pressure gradient and the drag forces in addition to the corresponding shear stress for the modified SGD model while lamping the pressure gradient at the top 20% of the domain. For comparison purposes, Figure 6.6b shows the balance between the forces and the shear stress for the case of a uniform pressure gradient while using the SGD model by Anderson and Meneveau (2010). Simulation time step is chosen to maintain Courant Fredric Levy (CFL) number at the top of the computational domain, $z=1000$ m, less than one. This is to ensure the stability of the solution.

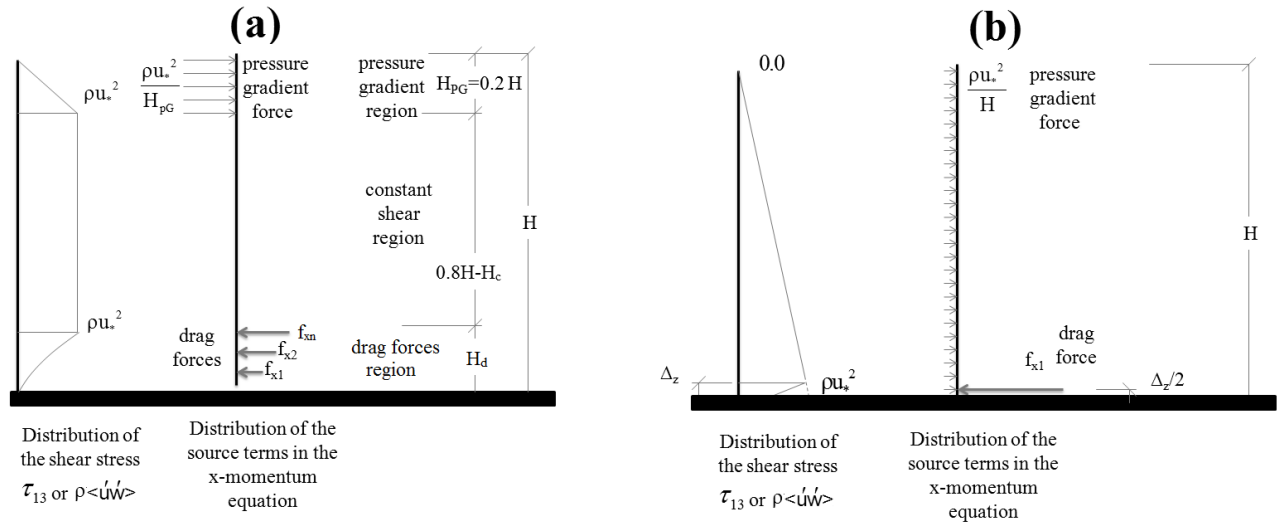


Figure 6.6 Balance between the imposed pressure gradient force and the drag forces (a) the modified SGD model with laminar pressure gradient force (b) original SGD model with uniform pressure gradient force

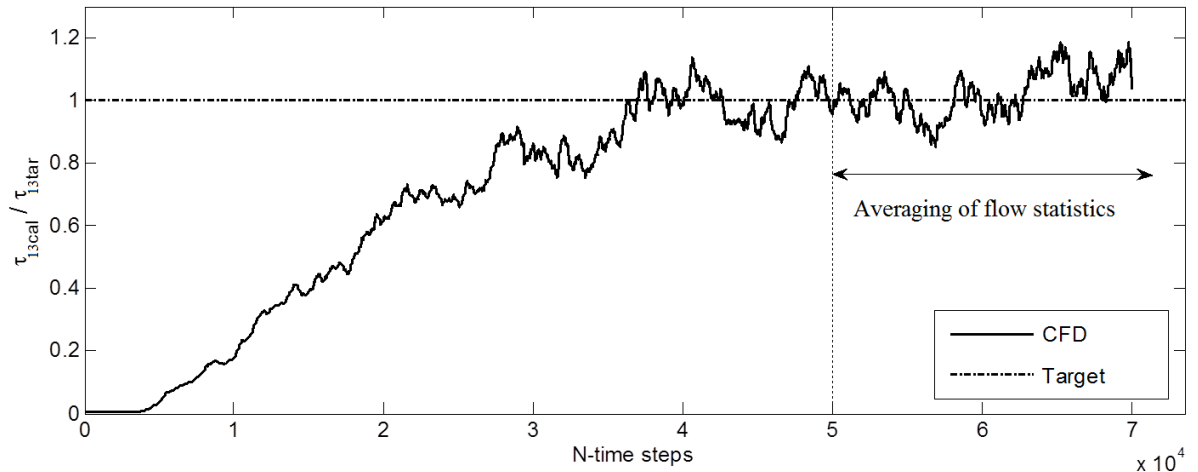


Figure 6.7 Time history of the calculated shear stress

Temporally averaged CFL of 0.67, 0.59 and 0.53 is used for the terrains with z_0 equals to 0.1, 0.3 and 0.7 m, respectively. Discretization schemes for the flow quantities and solver parameters are summarized in Table 6.4. All simulations are initialized from zero flow condition letting the imposed pressure gradient to enforce the flow until the balance is reached between the pressure gradient force and the shear force at the canopy layer at the bottom of the domain.

Normalized shear stresses, which is defined as the ratio between the calculated shear stress, $\tau_{13\text{calc}}$, and the targeted shear stress, $\tau_{13\text{tar}} = \rho \cdot u_*^2$, is plotted as shown in Figure 6.7. Convergence of the shear stress happens approximately after 50,000 time steps. After reaching the converged state, simulations are continued for 20,000 more time steps in order to extract the statistics for velocity and Reynolds stress profiles.

Table 6.4 Discretization schemes and solution technique for the CFD simulations

Parameter	Type
Time discretization	Second order implicit
Momentum discretization	Bounded central difference
Pressure discretization	Second order
Pressure-velocity coupling	Pressure-implicit with splitting operators (PISO)
Under relaxation factors	0.7 for the momentum 0.7 and 0.3 for the Pressure

6.4.1 Grid Sensitivity Study

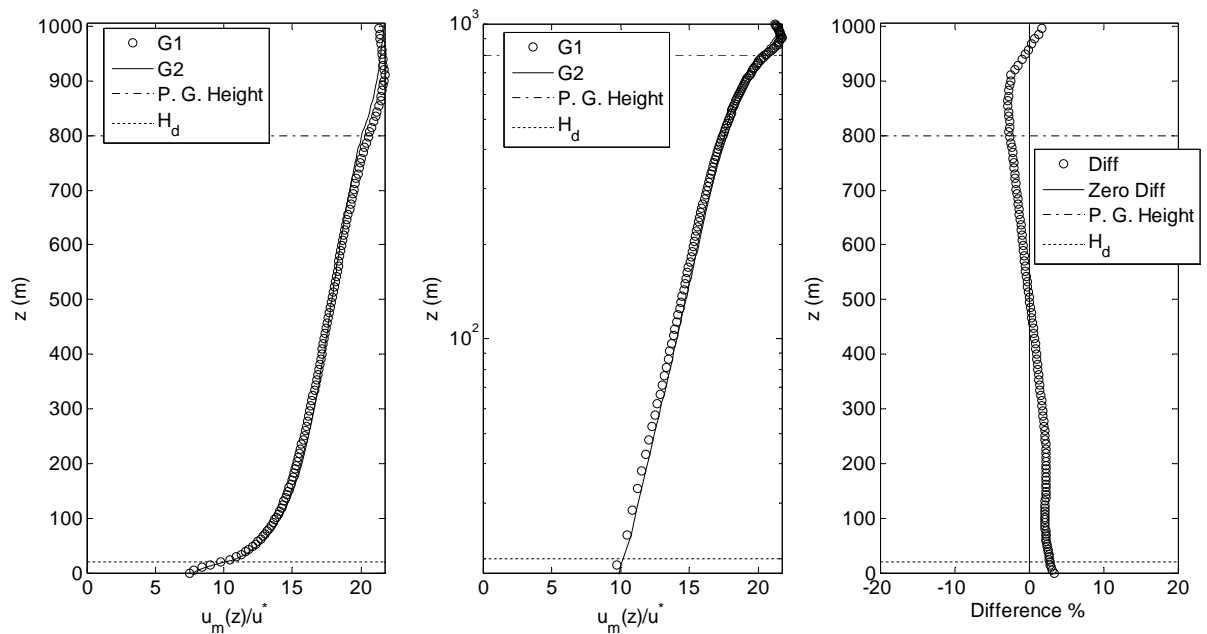


Figure 6.8 Mean velocity in the longitudinal direction $u_m(z)$: a) normal scale, b) logarithmic scale and c) difference percentile

Grid sensitivity analysis is performed for the case of suburban terrain, $z_0=0.3$ m. Mean velocity in the longitudinal direction, $u_m(z)$, is plotted for grids G1 and G2 as shown in Figures 6.8a, 6.8b using normal and logarithmic scale respectively. The heights of the canopy layer and where the pressure gradient is introduced are marked in the figures. Figures 6.8a, 6.8b indicate that both velocity profiles are in a good agreement. Difference ratio, Diff, in the mean longitudinal velocity defined by Equation 6.22 is plotted as shown in Figure 6.8-c.

$$Diff = \frac{u_{mG2}(z) - u_{mG1}(z)}{u_{mG2}(z)} \quad \text{Equation 6.22}$$

where $u_{mG1}(z)$, $u_{mG2}(z)$: mean velocity in the longitudinal direction resulting from the grid G1 and G2, respectively. Average difference along the height is found to be 0.89% which indicates the independency of the results on the employed grids. Therefore, only grid G2 results are shown in the following sections.

6.4.2 Results of the ABL Simulation

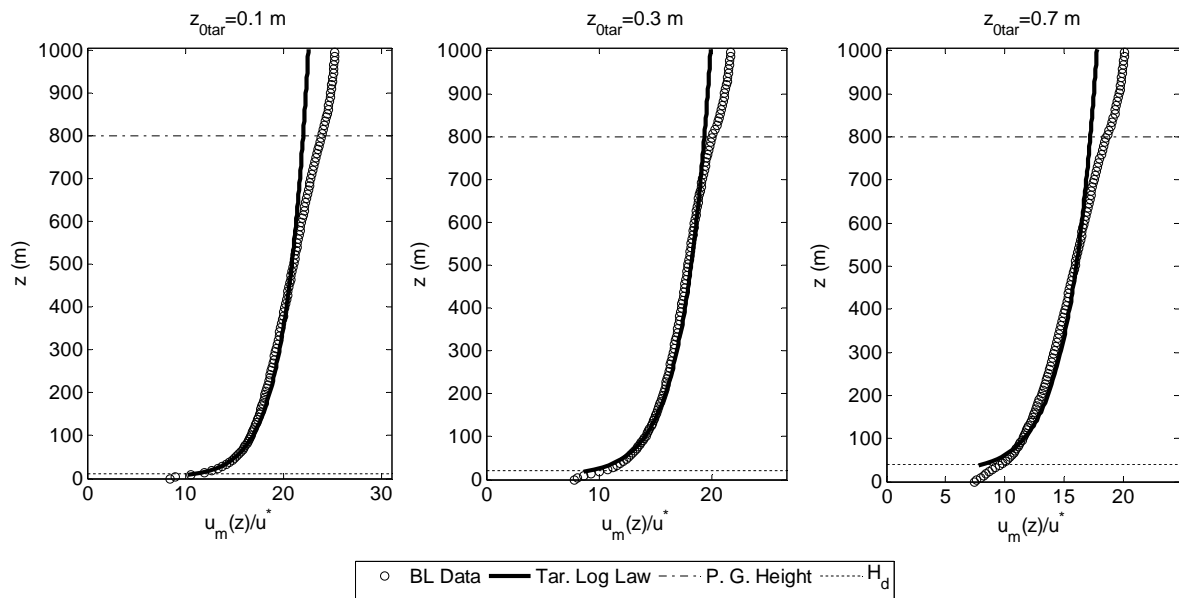


Figure 6.9 Mean velocity profile for the three generated surfaces using normal scale

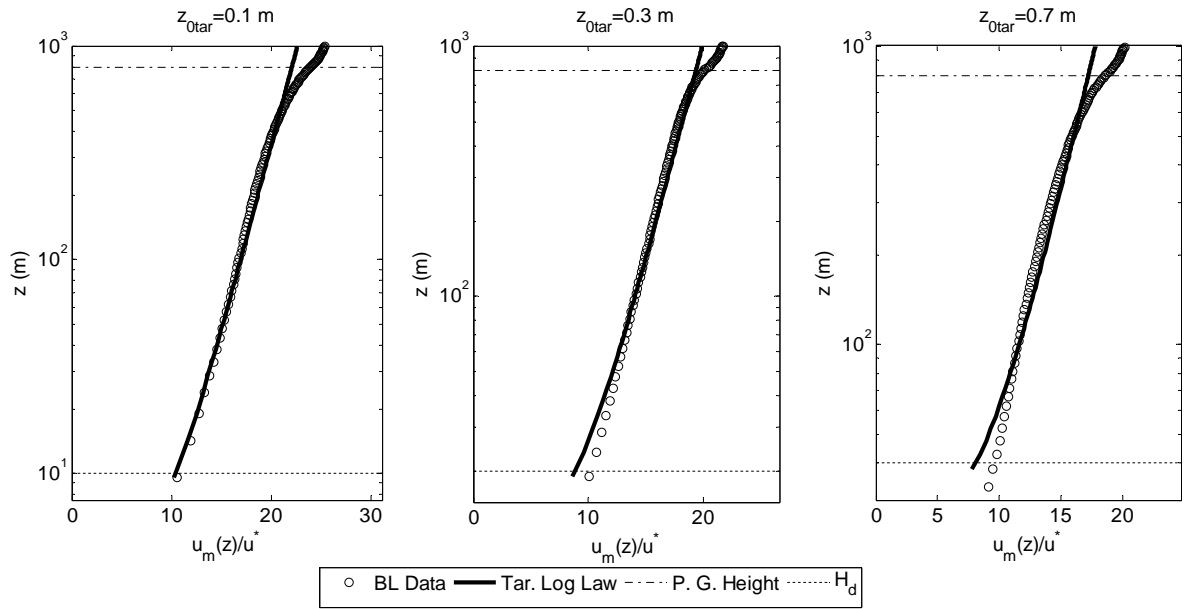


Figure 6.10 Mean velocity profile for the three generated surfaces using logarithmic scale

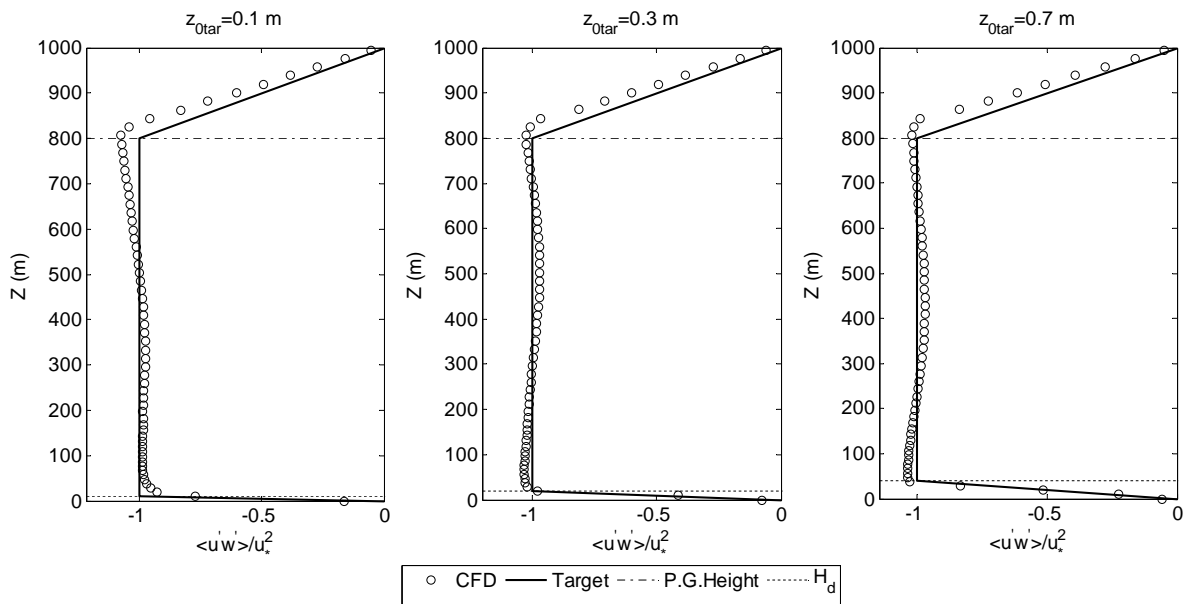


Figure 6.11 Normalized shear stress τ_{xz}

Mean velocity profiles obtained for the three generated surfaces are plotted and compared with those obtained from the logarithmic law as shown in Figures 6.9 and 6.10 using

normal and logarithmic scales, respectively. Generally CED predicted velocity profiles using the modified SGD match very well with those obtained from the logarithmic law for the zone where the shear stress remains constant. Average difference between the profiles resulting from the CFD and the targeted profiles, Err_{av} , defined by Equation 6.23 is found to be -0.4, 0.5 and 0.2% for z_0 equals to 0.1, 0.3 and 0.7 m, respectively. This indicates that the approximations involved in averaging the shear stress (Equation 6.15) as a step to scale the fractal surfaces so they have the prescribed aerodynamic roughness are reasonable. Shear stress is constant in the region above the canopy height and below the level where the pressure gradient is introduced. An illustration for the normalized shear stress, τ_{xz} , which is equal to the Reynolds stress $\langle u'w' \rangle$, normalized by the friction velocity u_*^2 is shown in Figure 6.11. Normalized shear stress starts with zero at the ground and reaches -1 at the height of the canopy layer. Normalized shear stress remains constant up to the elevation where the pressure gradient is introduced and finally reaches zero again at the top of the computational domain.

$$Err_{av} = \frac{1}{H - H_{PG} - H_{Canop}} \cdot \int_{z=H_{Canop}}^{z=H-H_{PG}} \frac{\bar{u}_{Log}(z) - \bar{u}_{CFD}(z)}{\bar{u}_{Log}(z)} dz \quad \text{Equation 6.23}$$

where $\bar{u}_{Log}(z)$ and $\bar{u}_{CFD}(z)$ represent mean velocity in the longitudinal direction resulting from the CFD and from the Logarithmic law, respectively, H is the domain height which is taken equal to 1000 m, H_{PG} is height of the layer where the pressure gradient is introduced and equals to 200 m and H_{Canop} is canopy height.

Root mean square fluctuations in the longitudinal direction, σ_u , is calculated and plotted for the three generated surfaces. Targeted fluctuations are calculated by integrating the power spectrum density, $S_{uu}(f)$, of Kaimal et al. (1972) as indicated by Equation 6.19 and plotted in Figure 6.12. As indicated from Figure 6.12, there is a gap between the r.m.s fluctuation calculated by the CFD and the targeted fluctuations calculated by integrating the PSD at the region starting above the canopy layer.

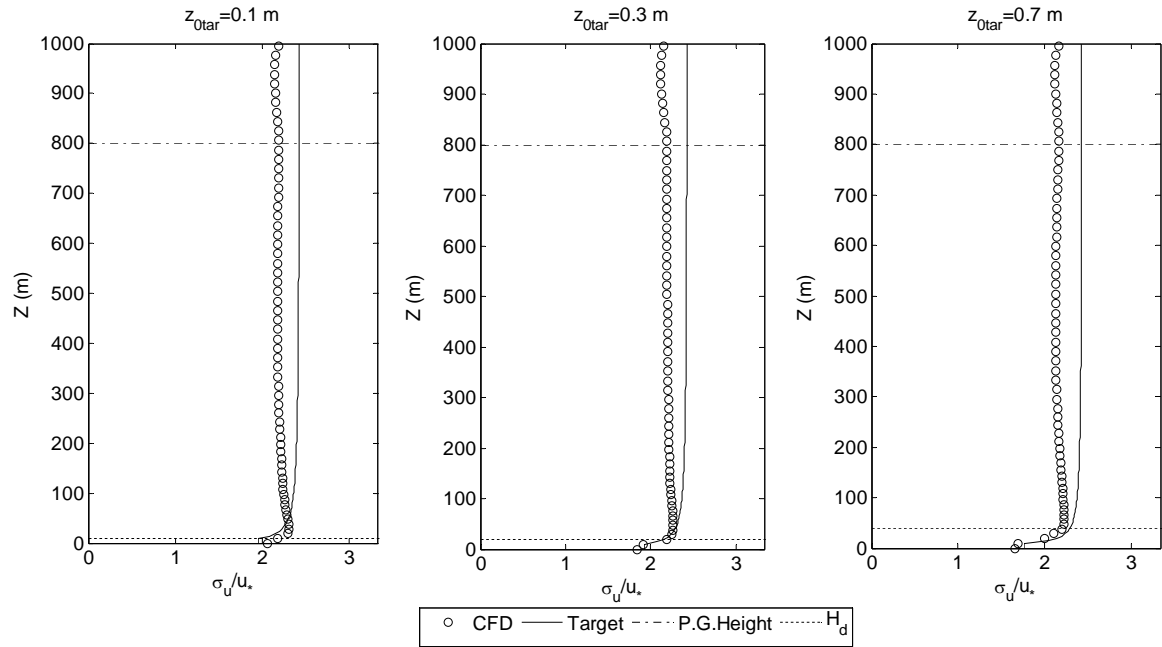


Figure 6.12 longitudinal r.m.s fluctuations

In order to investigate the reason behind such a gap, velocity time history at two elevations are extracted and their PSD is calculated and compared with Kaimal PSD. The two elevations are chosen at 100 and 200 m heights.

$$\sigma_u(z) = \sqrt{\int_0^{\infty} S_{uu}(f) \cdot df}$$

Equation 6.24

$$\frac{f \cdot S_{uu}(f)}{u_*^2} = \frac{100X}{(0.44 + 33X)^{5/3}}$$

$$X = \frac{f \cdot z}{u_m(10)}$$

where $S_{uu}(f)$ is PSD of the longitudinal fluctuations which is taken according to Kaimal et al. (1972), f is frequency and $u_m(10)$ is mean longitudinal velocity at 10 m height.

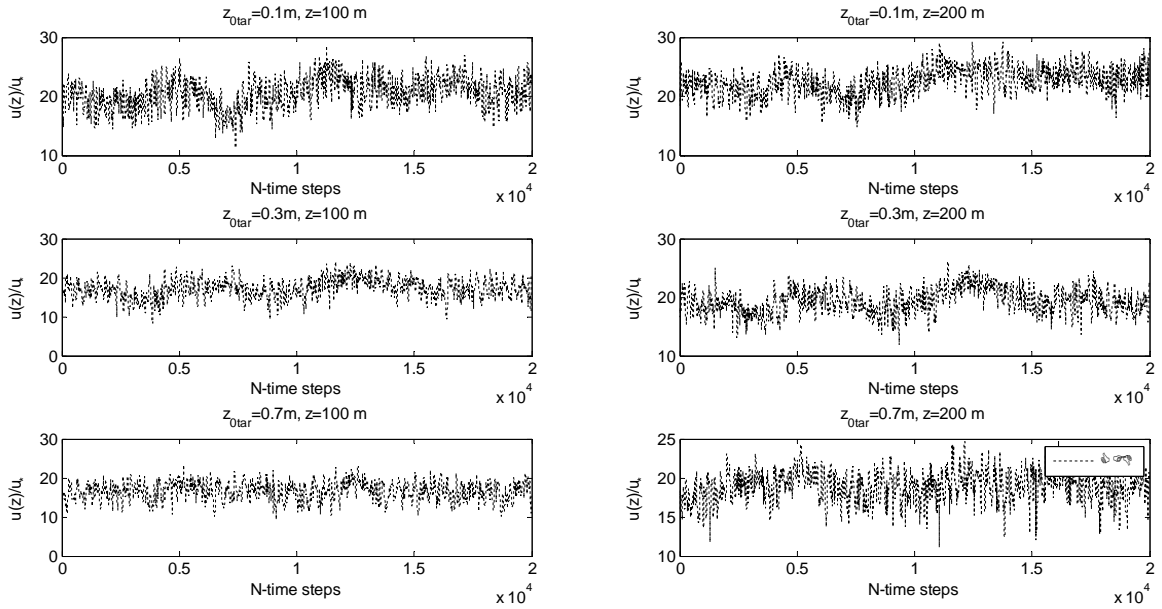


Figure 6.13 Velocity time history at two different elevations and three different roughness conditions

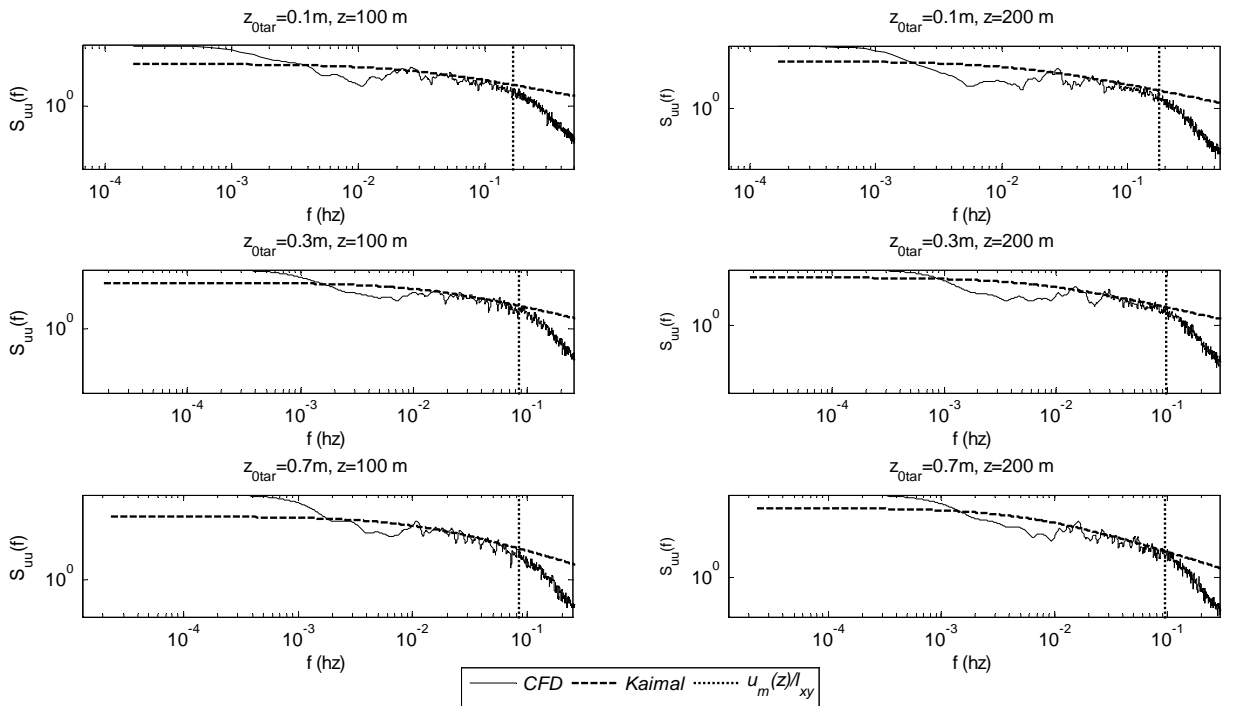


Figure 6.14 PSD of the velocities at two different elevations and three different roughness conditions

Time histories of the longitudinal velocity are shown in Figure 6.13. PSD of the extracted velocities are shown in Figure 6.14. It appears from Figure 6.14 that the resulting PSD from the velocities obtained from the CFD can be classified into two zones based on how the PSD resulting from the CFD matches the targeted PSD of Kaimal. The first zone with lower frequencies represent large scale fluctuations that are temporally resolved. Such a zone starts from a zero frequency and reaches a cut off frequency, f_{cut} , which represents the maximum frequency of fluctuations those are captured by the modified SGD model. That cut off frequency equals to the mean velocity, $\bar{u}(z)$, divided by the averaging length, l_{xy} , summarized in Table 6.3, and is shown in Figure 6.14. The second zone represents the small scale fluctuations with high frequencies greater than f_{cut} . As shown in Figure 6.14, the temporal variation of the small scale fluctuations is filtered out. Such a filtration is attributed for the underestimation of the longitudinal fluctuation, σ_u , as shown in Figure 6.12. For the cases where the small scale fluctuations are important, finer grids can be used. The usage of finer grids decreases the averaging length l_{xy} and subsequently increases the cut off frequency, f_{cut} .

6.4.3 Application for Inflow Boundary Condition Generation

Most of the velocity spectra are well reproduced by following the technique employed in the current study as shown in Figure 6.14. This allows the technique to produce the inflow BC for a subsequent simulation as illustrated in Figure 6.1 and performed previously by Lund et al. (1998) and Nozawa and Tamura (2002). Inflow BC for a subsequent LES can be easily extracted from the velocity history at a typical transverse vertical plane in the computational domain shown in Figures 6.1 and 6.3. However, generation of inflow BC using the current technique has a main advantage compared to the other recycling techniques. One of the main advantage represents the ability to generate flow statistics for different estimated target ground roughness z_0 without detail knowledge about the shapes and the arrangements of the roughness elements. Also, the current technique has another advantage for inflow generation over the methods based on statistically generating the inflow turbulence. This advantage applies to all recycling methods. Generated inflow BC from the current technique is a result solving Navier-Stokes equations that satisfy the continuity condition. In addition, the present method can

be applied to maintain the desired inflow statistics reaching up to the incident flow (i.e. close to the study object) by introducing desired roughness at the bottom of the study domain (Figure 6.1). Thus avoiding significant inflow degradation expected over the upstream fetch (between the inlet and the study building location) as reported by Tamura (2008) and Dagneu and Bitsuamlak (2013).

6.5 Conclusions

Flow characterization of a neutrally stratified ABL flow above three fractal surfaces that represent countryside, suburban and urban terrain exposures with specific roughness, z_0 , is performed by relaxing the constraint of $60.z_0 < \Delta_z$. Surface gradient drag-based (SGD) model developed by Anderson and Meneveau (2010), which is originally developed for fairly rough surfaces, is modified to be able to simulate very rough surfaces encountered in the built environment. This was enabled by allowing the drag forces to be applied in multiple grid layers above the ground. Height variation in the three surfaces is introduced using random Fourier modes (RFM). The resulting heights are then scaled by the new scaling technique so that the resulting roughness matches its prescribed target value. LES was performed using the commercial CFD software Fluent 13 and user defined functions (developed as part of the current study) by using periodic boundary conditions and pressure gradient to enforce the flow. The resulting mean wind profile for the three surfaces matches well with the targeted logarithmic profile in the region of the constant shear stress. The average error between the resulting profiles from the CFD and the targeted profiles is found equal to -0.3, -0.5 and 0.2 % for z_0 equals to 0.1, 0.3 and 0.7 m, respectively. Root mean square of the longitudinal fluctuations resulting from the CFD appear to be underestimated above the canopy height with an average ratio of 10%. Such an underestimation appears to be due to the filtration of the small scale turbulence smaller than the average distances between the roughness elements l_{xy} . This observation was made by comparing the longitudinal velocity spectra from the CFD with those of Kaimal et al. (1972). The comparison showed that the two spectra well match each up to a cut off frequency, f_{cut} , which equals to $u_m(z)/l_{xy}$. For the cases where the small scales are important, a finer grid in the longitudinal direction can be used which will result in roughness elements with smaller width, l_{xy} . The current technique can be used to generate

the Inflow Boundary Condition for subsequent LES of flow over the built-environment. That can be done by extracting the velocity records at a typical transverse vertical plane and introducing them at the inflow boundary condition of the subsequent domain. The current technique has a particular advantage over the other recycling techniques, which is the ability to simulate any roughness z_0 without detail priori knowledge about the shape and the distribution of the roughness elements. Also, the current technique has another advantage of satisfying the continuity condition for inflow generation over the methods based on statistically generating the inflow turbulence, which applies for all recycling methods. The generated velocities are a result of solving Navier-Stokes equations and automatically satisfy the continuity condition.

6.6 Acknowledgments

The authors would like to thank the National Research Council of Canada (NSERC), Hydro One Company and the Ontario Centre of Excellence (OCE) for their kind financial support of this research and Sharcnet for providing access to their high performance computation facility. Last but not least the Canada Research Chair support for the last author is greatly acknowledged.

6.7 References

- Albertson J.D., Katul, G. Wiberg, P. 2001. Relative importance of local and regional controls on coupled water, carbon, and energy fluxes. *Advances in Water Resources* 24(9–10), 1103–1118.
- Anderson W., Meneveau C. 2010. A Large-eddy simulation model for boundary-layer flow over surfaces with horizontally resolved but vertically unresolved roughness elements. *Boundary-Layer Meteorology* 137, 397–415.
- Basu S., Porte´-Agel, F. 2006. Large-eddy simulation of stably stratified atmospheric boundary layer turbulence: A scale-dependent dynamic modeling approach. *Journal of the Atmospheric Sciences* 63, 2074-2091.
- Beyers, M., Waechter, B. 2008. Modeling transient snowdrift development around complex three-dimensional structures. *Journal of Wind Engineering and Industrial Aerodynamics* 96(10), 1603-1615.

- Blocken B., Carmeliet, J. 2004. A review of wind-driven rain research in building science. *Journal of Wind Engineering and Industrial Aerodynamics* 92(4), 1079-1130.
- Blocken, B., Stathopoulos, T., Carmeliet, J., 2007. CFD simulation of the atmospheric boundary layer: wall function problems, *Atmospheric Environment*, 41, 38-252.
- Britter R.E., Hanna, S.R. 2003. Flow and dispersion in urban areas. *Annual Review of Fluid Mechanics* 35(1), 469–496. doi:10.1146/annurev.fluid.35.101101.161147
- Brown A.R., Hobson J.M., Wood N. 2001. Large-eddy simulation of neutral turbulent flow over rough sinusoidal ridges. *Boundary-Layer Meteorology* 98, 411–441
- Businger, J.A., Wynagaard, J.C., Izumi, Y., Bradley, E.F. 1971. Flux–profile relationships in the atmospheric surface layer. *Journal of the Atmospheric Sciences* 28, 181–189.
- Cassiani, M., Katul, G., Albertson, J., 2008. The effects of canopy leaf area index on airflow across forest edges: Large-eddy simulation and analytical results. *Boundary-Layer Meteorology* 126, 433–460.
- Coccal O, Dobre, A., Thomas, T.G., Belcher S.E. 2007. Structure of turbulent flow over regular arrays of cubical roughness. *Journal of Fluid Mechanics* 589, 375–409.
- Cowan, I.R. 1968. Mass, heat and momentum exchange between stands of plants and their atmospheric environment. *Quarterly Journal of the Royal Meteorological Society* 94:523–544.
- Dagnew, A., Bitsuamlak, G.T. 2013. Computational evaluation of wind loads on buildings: a review. *Wind and Structures*, 16(6), 629-660.
- Engineering Sciences Data Unit (ESDU) 85020. 2001. Characteristics of atmospheric turbulence near the ground. Part II: single point data for strong winds.
- Engineering Sciences Data Unit (ESDU) 82026. 2002. Strong winds in the atmospheric boundary layer. Part 1: hourly-mean wind speeds.
- Fluent Inc., 2005. *Fluent 6.2 User's Guide*, Fluent Inc., Lebanon.
- Fluent 13.0. 2010. *User's Guide*. Fluent Inc., Lebanon.
- Gal-Chen, T., Somerville, R.C.J. 1975a. On the use of a coordinate transformation for the solution of the Navier–Stokes equations. *Journal of Computational Physics* 17, 209–228.

- Gal-Chen, T., Somerville, R.C.J. 1975b. Numerical solution of the Navier–Stokes equations with topography. *Journal of Computational Physics* 17, 276–310.
- Germano, M., Piomelli, U., Moin, P., Cabot, W.H. 1991. A dynamic subgrid-scale eddy viscosity model. *Physics of Fluids A* 3(7), 1760–1765.
- Iaccarino, G., Verzicco, R., 2003. Immersed boundary technique for turbulent flow simulations. *Applied Mechanics Reviews* 56, 331–347.
- Inoue, E., 1963. On the turbulent structure of air flow within crop canopies. *Journal of the Meteorological Society of Japan* 41, 317–326.
- Jiang, Y., Alexander, A., Jenkins, H., Arthur, R., Chen, Q. 2003. Natural ventilation in buildings: measurement in a wind tunnel and numerical simulation with large-eddy simulation. *Journal of Wind Engineering and Industrial Aerodynamics* 91(3), 331-353.
- Jiru, T.E., Bitsuamlak, G.T., 2010. Application of CFD in Modelling Wind-Induced Natural Ventilation of Buildings-A Review. *International Journal of Ventilation*, 9(2), 131-147.
- Kaimal, J. C., Wyngaard, J. C., Izumi, Y., & Cote', O. R. 1972. Spectral characteristics of surface-layer turbulence. *Quarterly Journal of the Royal Meteorological Society* 98 (417), 563-589.
- Kanda, M., Moriwaki, R., Kasamatsu, F. 2004. Large-eddy simulation of turbulent organized structures within and above explicitly resolved cube arrays. *Boundary-Layer Meteorology* 112, 343–368.
- Katul, G., Albertson, J. 1998. An investigation of higher-order closure models for a forested canopy. *Boundary- Layer Meteorology* 89(1), 47–74.
- Katul, G., Mahrt, L., Poggi, D., Sanz, C. 2004. One and two equation models for canopy turbulence. *Boundary-Layer Meteorology* 113, 81–109.
- Kraichnan, R. 1970. Diffusion by a random velocity field, *Physics of Fluids* 13, 22.
- Lund, T.S., Wu, X., Squires, K.D. 1998. Generation of turbulent inflow data for spatially developing boundary layer simulations. *Journal of Computational Physics* 140, 233–258.
- Mittal, R., Iaccarino, G. 2005. Immersed boundary methods. *The Annual Review of Fluid Mechanics* 37, 239–261.

- Monin, A. S. and Obukhov, A. M. 1954. Basic laws of turbulent mixing in the ground layer of the atmosphere, *Trans. Geophys. Inst. Akad. Nauk. USSR* 151, 163–187.
- Nakayama, A., Sakio, K. 2002. Simulation of flows over wavy rough boundaries. Center for Turbulence Research, Annual Research Briefs, Stanford University/NASA Amers Research Center, 313–324
- Nozawa, K., Tamura, T. 2002. Large eddy simulation of the flow around a low-rise building in a rough-wall turbulent boundary layer. *Journal of Wind Engineering and Industrial Aerodynamics* 90, 1151-1162.
- Richards, P.J., Hoxey, R.P. 1993. Appropriate boundary conditions for computational wind engineering models using the k-e turbulence model. *Journal of Wind Engineering and Industrial Aerodynamics* 46&47, 145-153
- Schumann, U., 1975. Subgrid scale model for finite difference simulations of turbulent flows in plane canals and annuli. *Journal of Computational Physics*. 18, 376-404.
- Shaw, R.H., Schumann, U. 1992. Large-eddy simulation of turbulent flow above and within a forest. *Boundary- Layer Meteorology* 61:47–64
- Shiguang, M., Weim, J. 2004. Large Eddy Simulation and Study of the Urban Boundary Layer. *Advances in Atmospheric Sciences*. 21: 650-661
- Smagorinsky, J. 1963. General circulation experiments with the primitive equations, i. the basic experiment. *Monthly Weather Review*, 91: pp 99-164, 1963.
- Smirnov, R., Shi, S., Celik, I. 2001. Random flow generation technique for large eddy simulations and particle-dynamics modeling. *Journal of Fluids Engineering* 123, 359-371.
- Stoll, R., Porte´ -Agel, F. 2006. Effect of roughness on surface boundary conditions for large-eddy simulation. *Boundary-Layer Meteorology* 118, 169–187.
- Stoll, R., Porte´ -Agel, F. 2008. Large-eddy simulation of the stable atmospheric boundary layer using dynamic models with different averaging schemes. *Boundary-Layer Meteorology* 126, 1–28.
- Su, H.B., Shaw, R.H., Paw U.K.T., Moeng C.H., Sullivan P.P. 1998. Turbulent statistics of neutrally stratified flow within and above a sparse forest from large-eddy simulation and field observation. *Boundary-Layer Meteorology* 88, 367–397.

- Tamura, T. 2008. Towards practical use of LES in wind engineering. *Journal of Wind Engineering and Industrial Aerodynamics* 96, 1451–1471.
- Tamura, T. 2009. Large Eddy Simulation of Building Aerodynamics. The Seventh Asia-Pacific Conference on Wind Engineering, November 8-12, 2009, Taipei, Taiwan.
- Thomas, T.G., Williams, J.J. 1999. Generating a wind environment for large eddy simulation of bluff body flows *Journal of Wind Engineering and Industrial Aerodynamics* 82, 189-208.
- Tominaga, Y., Stathopoulos, T. 2011. CFD modeling of pollution dispersion in a street canyon: Comparison between LES and RANS. *Journal of Wind Engineering and Industrial Aerodynamics* 99(4), 340-348.
- Tsai J., Tsuang B. 2005. Aerodynamic roughness over an urban area and over two farmlands in a populated area as determined by wind profiles and surface energy flux measurements. *Agricultural and Forest Meteorology* 132 (2005) 154–170.
- Vermeire, B., Orf, L. Savory, E. 2011. Improved modelling of downburst outflows for wind engineering applications using a cooling source approach. *Journal of Wind Engineering and Industrial Aerodynamics* 99, 801–814.
- Wang, W. 2012. An analytical model for mean wind profiles in sparse canopies. *Boundary-Layer Meteorology* 142, 383–399.
- Whittingham, H. 1964. Extreme wind gust in Australia. Bureau of Meteorology (Melbourne), Department of Science, Bulletin 46.
- Wieringa, J. 1992. Updating the Davenport roughness classification. *Journal of Wind Engineering and Industrial Aerodynamics* 41-44, 357-368.
- Xie, Z., Coceal, O., Castro, I.P. 2008. Large-eddy simulation of flows over random urban-like obstacles. *Boundary-Layer Meteorology* 129,1–23.
- Xie, Z., Voke, P., R., Hayden, P., Robins, A.G. 2004. Large eddy simulation of turbulent flow over a rough surface. *Boundary-Layer Meteorology* 111, 417–440, 2004.
- Yang, B., Raupach, M.R., Shaw R.H., Paw K.T., Morse A. 2006a. Large-eddy simulation of turbulent flow across a forest edge. Part I: flow statistics. *Boundary-Layer Meteorology* 120, 377–412.

Yang B., Morse A., Shaw R.H., Paw K.T. 2006b. Large-eddy simulation of turbulent flow across a forest edge. Part II: momentum and turbulent kinetic energy budget. *Boundary-Layer Meteorology* 121, 433–457.

Chapter 7

7 Turbulent Downburst Wind Field and Corresponding Dynamic Behavior of Transmission Line Conductors

7.1 Introduction

Downburst is a strong downdraft that induces an outburst of damaging wind near the ground as defined by Fujita (1985). Hazards associated with downburst winds on different structures including Transmission Lines (TLs) are extensively discussed in the literature (Whittingham, 1964; Fujita, 1990; Vickery, 1992; Holmes, 1999; Li 2000; Choi, 2002). Previous field studies such as the Joint Airport Weather Studies (JAWS), the Northern Illinois Meteorological Research on Downbursts (NIMROD), and the Federal Aviation Administration Lincoln Laboratory Operational Weather Studies (FLOWS; Fujita, 1985), showed that the maximum downburst wind speeds happen at 50 m above the ground, as indicated by Fujita and Wakimoto (1981), Wilson et al. (1984), and Hjelmfelt (1988). Although field studies can provide actual velocities, they represent a challenging task due to the unpredictability of the event occurrence in time and in space. This challenge motivated researchers in the past to study downbursts either experimentally (Osegura and Bowles 1988, Lundgren et al. 1992, Alahyari and Longmire 1994, Yao and Lundgren 1996, Wood et al. 2001 and Chay and Letchford 2002) or computationally (Selvam and Holmes 1992; Hadz'iabdic' 2005; Chay et al. 2006; Kim and Hangan 2007; Sengupta and Sarkar 2008; Gant 2009; Mason et al. 2009, 2010a). In computational studies of downbursts, the following methods are currently used: the Impinging Jet (IJ) method proposed by Fujita (1985), Cooling Source (CS) method suggested by Anderson et al. (1992) and the method of simulating the downburst-producing thunderstorm indicated by Orf et al. (2012). Both IJ and CS methods are computationally less expensive compared with the simulation of the downburst-producing thunderstorm. The latter requires significant computational resources which makes it unaffordable for the current study.

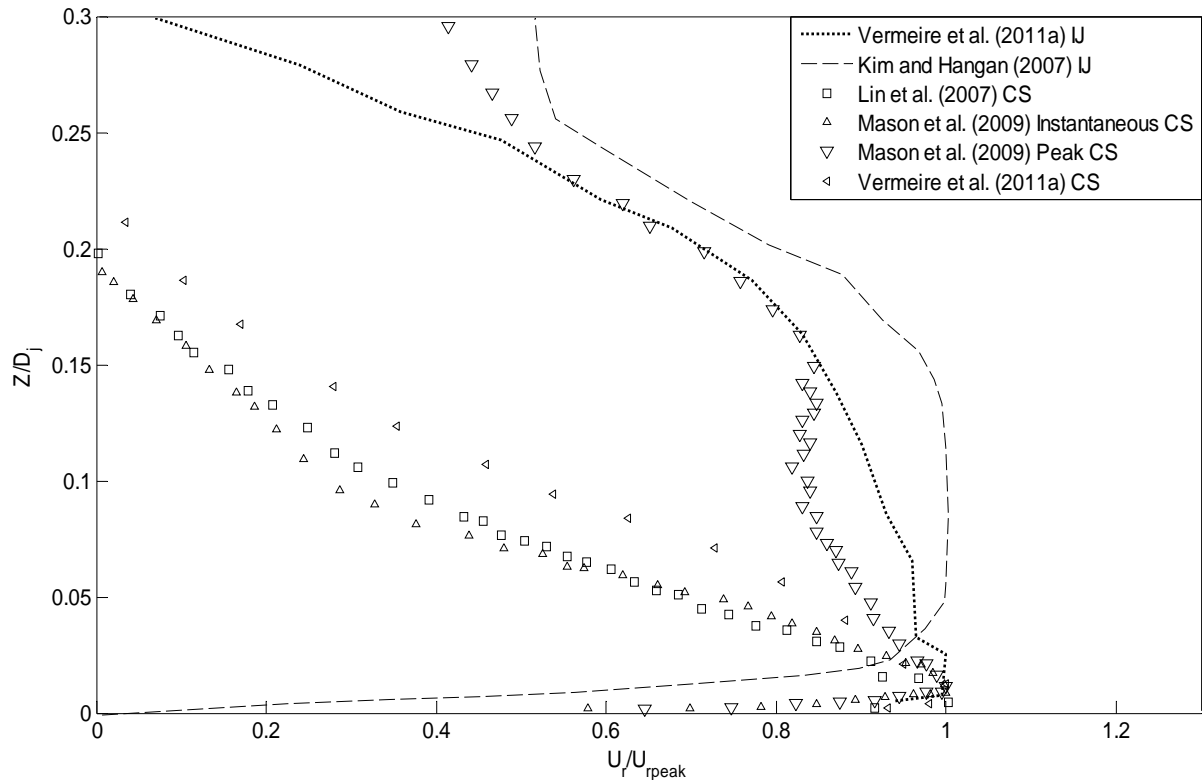


Figure 7.1 Comparison between the vertical velocity profile of downbursts using IJ and CS methods

There are several attempts over the last decades to simulate downbursts either using the IJ or the CS method. For example, Kim and Hangan (2007) used the IJ method to obtain the running mean downburst wind velocities employing an axi-symmetric two dimensional domain. Sengupta and Sarkar (2008) simulated downbursts using the IJ method employing k-epsilon, k-omega, shear stress transport (SST) and LES turbulence models and compared the resulting profiles with those obtained from experiments. Their results showed a reasonable agreement between the profiles obtained from the LES and from the experiment. The applicability of using LES to simulate downbursts is also reported by Hadz'iabdic' (2005), Chay et al. (2006) and Gant (2009). Mason et al. (2009, 2010a) used the CS method to simulate downbursts on two and three dimensional domains, respectively. Mason et al. (2009, 2010a) used the Shear Adaptive Simulation (SAS) by Menter and Egerov (2005). However, SAS model might over-predict the turbulent viscosity of jet-type flows, as indicated by Gant (2009). Mason et al. (2009, 2010a) also

used the neutral wall function to model the terrain roughness. This was justified by using small height of the first grid layer, Δ_z , i.e. 1.0 m according to Teske and Lewellen (1977). Richards and Hoxey (1993), Franke et al. (2004), Fluent Inc. (2005), and Blocken et al. (2007) reported that the physical roughness, k_s or $\sim 30 z_0$, that can be modeled by a wall function cannot exceed the mid height of the first grid layer, $0.5 \Delta_z$, which leads to the constraint $\Delta_z > 60 z_0$. This constraint shades doubts on the results obtained by Mason et al. (2009) for a terrain roughness greater than 0.016 m. Mason et al. (2010b) investigated the effect of topography on the wind velocities. They estimated speed-up factors for a downburst and compared them with speed-up factors for synoptic wind. Vermeire et al. (2011a) simulated downbursts over various terrains, with z_0 equals to 0.001-0.1 m, using the CS method employing LES to resolve for turbulence. Similar to Mason et al. (2009), they utilized a neutral wall function with a first grid layer height, Δ_z , of 1.0 m. Later, Vermeire et al. (2011b) used the CS method to study the interaction between multiple downburst events and reported a 55% increase in the velocity magnitude compared to that of a single event. A comparison between the velocity profiles obtained using the IJ and the CS method is shown in Figure 7.1. The profiles obtained by Lin et al. (2007) and Vermeire et al. (2011a) and the instantaneous profile obtained by Mason et al. (2009) using the CS method appear to have maximum velocity close to the ground and quickly drop with height. This could be a result of employing a ramp function to enforce the flow in the conducted simulations using the CS method, compared with an instantaneous enforcing in the conducted simulations using the IJ method. However, the overall peak profile obtained by Mason et al. (2009b) using the CS method appears to be in a reasonable agreement with those from IJ methods (Vermeire et al. 2011a, Kim and Hangan 2007). It should be mentioned that in Figure 7.1 the velocity profiles generated using the CS method are normalized vertically, assuming that the peak velocity happens at a radius equal to $1.2 D_{jeq}$, where D_{jeq} is the equivalent diameter of the downdraft formulated by the CS. This allows for a consistent scaling of the data obtained by both the CS and the IJ method. The choice of $1.2 D_{jeq}$ is based on the results reported by Kim and Hangan (2007).

All of the above mentioned studies do not discuss the turbulent characteristics (such as turbulence intensities, length scales, spectra and peak factors) of the flow near the

ground. Holmes et al. (2008) studied the turbulent characteristics for a real downburst event that happened near Lubbock, Texas on 2002. Unfortunately, the obtained characteristics are limited to the few locations where the velocities were measured and, are suitable for open terrain exposure only. Turbulent characteristics for other terrain exposures need further research. These characteristics are essential to quantify the peak loads on different structures including TLs and their responses that are experienced as indicated by Chen and Letchford (2004a, b), Chay and Albermani (2005), Chay et al. (2006), Holmes et al. (2008) and Kwon and Kareem (2009). Savory *et al.* (2001), Shehata and El Damatty (2008) and El Damatty and Aboshosha (2012) conducted failure studies on different transmission towers subjected to downburst loading and their results revealed the importance of including wind forces acting on the conductors. The current study is an attempt to fill some of these gaps, therefore, it focuses on turbulent wind field of downburst falling on various exposure conditions and its effect on the response of TL conductors. As a result LES that is capable of modeling turbulent characteristics of downburst has been chosen over other Unsteady Reynolds Averaged Navier-Stokes (URANS) equations based-simulation that averages out some of the time scales (Sengupta and Sarkar 2008). Four exposures namely; open, country side, suburban, and urban are considered in the LES (z_0 , equal to 0.03, 0.1, 0.3 and 0.7 m, respectively). Ground roughness corresponding to these exposures is modeled implicitly by using fractal surfaces generated by means of random Fourier modes (RFM) and scaled, as necessary, to represent the targeted aerodynamic roughness of the chosen exposure. Drag forces resulting from the fractal surfaces are then introduced in the flow simulations using the surface gradient drag (SGD) model, originally proposed by Anderson and M (2010) and latter modified for rougher surfaces by Aboshosha et al. (2013). This model is adopted because (i) it is not bounded by the constraint $\Delta_z > 60.z_0$, and therefore allows for modeling rough terrains without losing the accuracy near ground flow simulations where structures are engulfed, and (ii) it is computationally less expensive compared to explicit roughness element based LES modeling. Simulations are performed in the current study using the IJ method. Although the IJ method does not predict the buoyancy characteristics of the flow as indicated by Vermeire et al. (2011a), it produces an easily scalable wind field as indicated by Shehata et al. (2005) and Kim and Hanagan (2007).

The current study is divided into five parts: The first part (section 7.2) details the numerical model. The second part (section 7.3) discusses the decomposition of the resulting wind field into running mean and turbulent components. The third part (section 7.4) discusses simulation results and main findings. The fourth part (section 7.5) discusses the dynamic response of TL conductors to downburst wind fields obtained from the simulations. The fifth part (section 7.6) shows the applicability of using the turbulent wind field characteristics with the gust factor (GF) approach to evaluate the peak forces acting on TL conductors.

7.2 LES Model Setup

The commercial CFD package FLUENT (2010) solver is utilized to solve the LES represented by Equation 7.1. A Dynamic Sub-Grid Scale model proposed by Smagorinsky (1963) and Geomano et al. (1991) is used to account for the turbulence. Parameters used to handle flow quantities as well as solution technique are summarized in Table 7.1.

$$\begin{aligned}
 \frac{\partial(\overline{u_i})}{\partial x_i} &= 0 \\
 \frac{\partial \overline{u_i}}{\partial t} + (\overline{u_j}) \frac{\partial \overline{u_i}}{\partial x_j} &= -\frac{1}{\rho} \frac{\partial \overline{P}}{\partial x_i} + \frac{\partial}{\partial x_j} (-\tau_{ij} + 2\nu \overline{S_{ij}}) + f_i \\
 \tau_{ij} &= \overline{u_i u_j} - \overline{u_i} \overline{u_j} \\
 \overline{S_{ij}} &= \frac{1}{2} \left(\frac{\partial \overline{u_i}}{\partial x_j} + \frac{\partial \overline{u_j}}{\partial x_i} \right) \\
 \tau_{ij} - \frac{1}{3} \delta_{ij} \tau_{kk} &= 2\nu_e \overline{S_{ij}} \\
 \nu_e &= (C_s \Delta)^2 \cdot (2\overline{S_{ij}} \cdot \overline{S_{ij}})^2
 \end{aligned}
 \tag{Equation 7.1}$$

where $i=1, 2, 3$ correspond to the x -, y - and z -directions, respectively. The over bar represents the filtered quantities, u_i , u_{gi} , ρ , t , τ_{ij} and ν which represent fluid velocity, grid velocity, pressure, time, the SGS Reynolds stress and molecular viscosity coefficient, respectively. S_{ij} , ν_e , Δ , C_s represent strain rate tensor, eddy viscosity, grid size,

Smagorinsky constant, which is determined instantaneously based on the Geomano identity in the dynamic model (Geomano et al., 1991), respectively. δ_{ij} represents Kronecker delta, f_i represents drag force obtained from the modified SDG (Aboshosha et al. 2014).

Table 7.1 Discretization schemes and solution technique

Parameter	Type
Time discretization	Second order implicit
Momentum discretization	Bounded central difference
Pressure discretization	Second order
Pressure-velocity coupling	Pressure-implicit with splitting operators (PISO)
Under relaxation factors	0.7 for the momentum 0.7 and 0.3 for the pressure

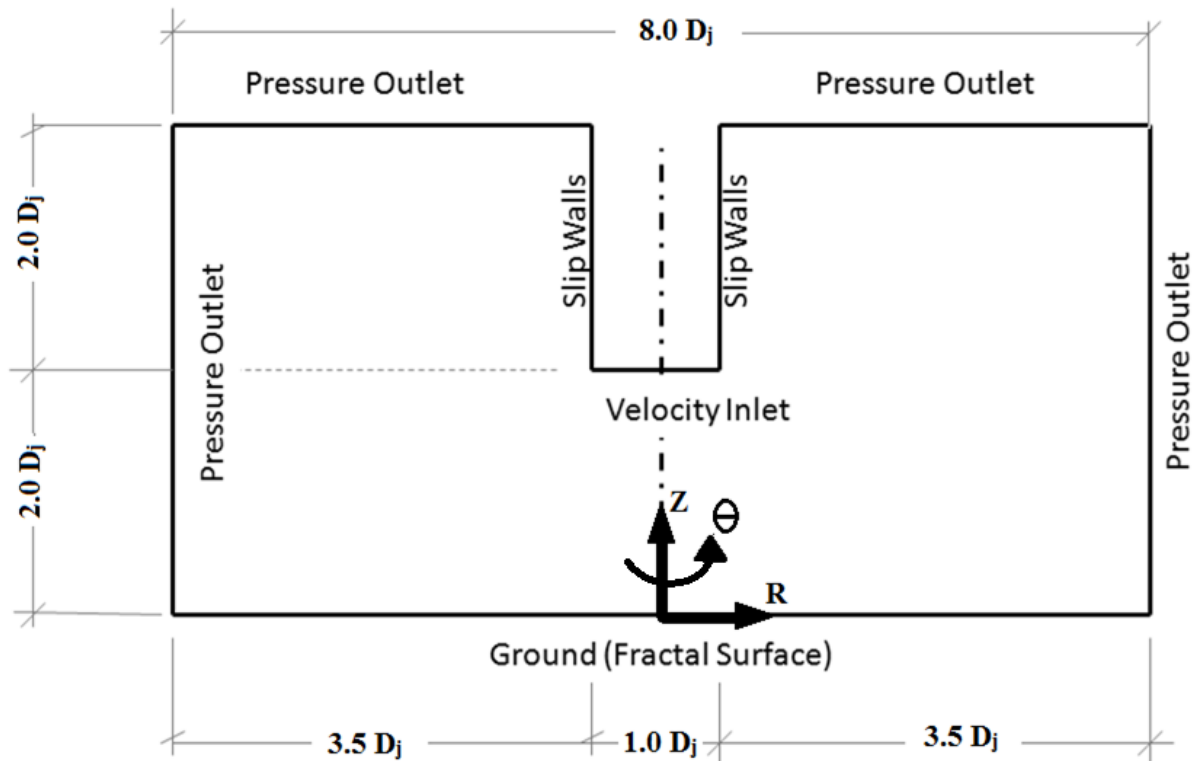


Figure 7.2 Computational domain and boundary conditions.

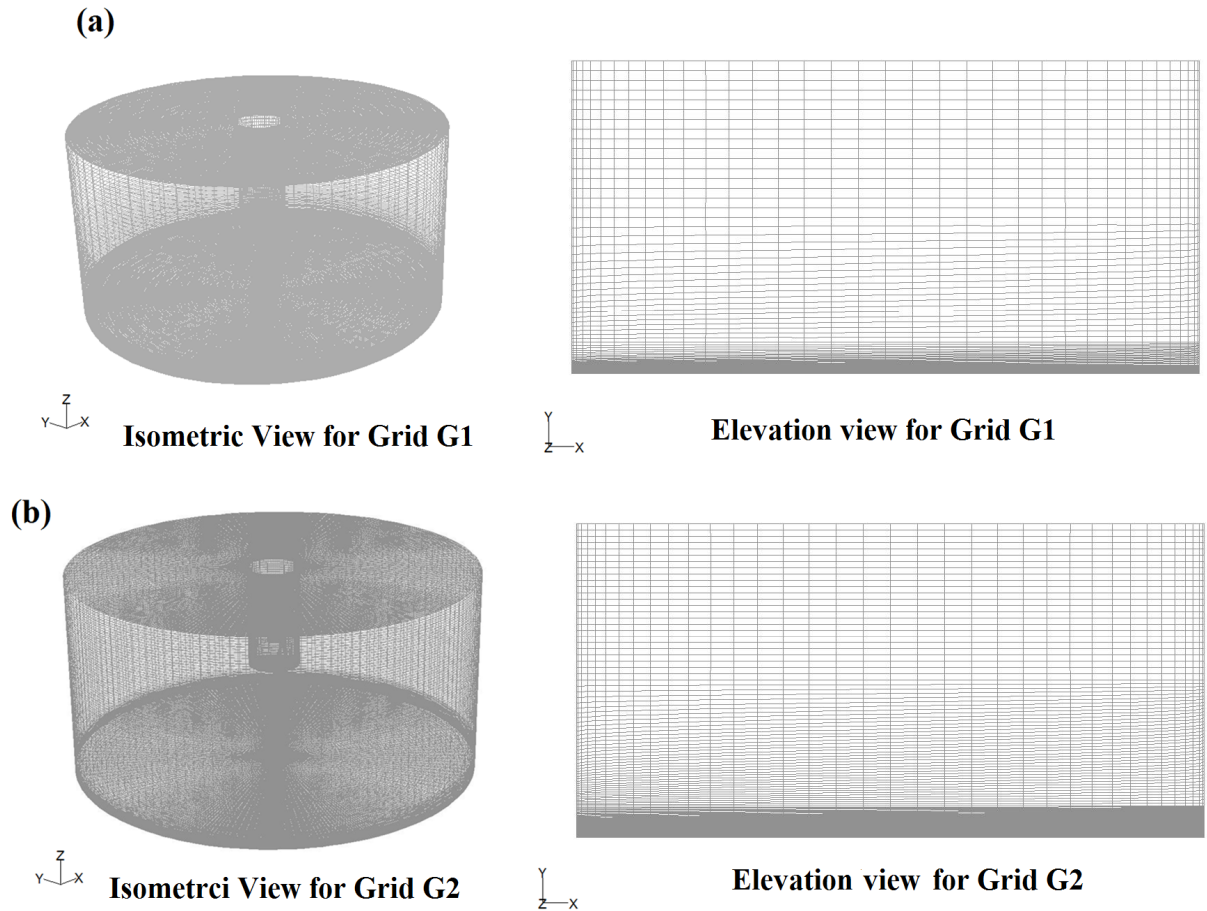


Figure 7.3 Employed Grids

A three dimensional cylindrical domain is employed to perform the LES, as illustrated in Figure 7.2. A full cylindrical domain is used in the current study compared with only a quadrant domain used by Vermiere et al. (2011). This avoids bounding the flow by the quadrant walls thus allowing evaluation of the turbulent length scales along the circumferential direction. A jet diameter, D_j , is considered equal to 1 km, which represents a typical size of a downburst, as indicated by Holmes et al. (2008). The computational domain is chosen to be $8D_j \times 4D_j$ for the radial and vertical dimensions, respectively, which is slightly larger than those employed by Vermier et al. (2011). Two

grids, Grid 1 and Grid 2 are used to check the grid independency of the results, as shown in Figure 7.3 and summarized in Table 7.2.

Table 7.2 Properties of the employed grids

Grid	Grid 1	Grid 2
Radial discretization	400 with 0.01 D_j each	400 with 0.01 D_j each
Circumferential discretization	72 with $\frac{2.\pi}{72}$ each	72 with $\frac{2.\pi}{72}$ each
Vertical discretization	Starts with 0.005 D_j and increases gradually to 0.10 D_j . Total number of vertical grids is 100	Starts with 0.005 D_j and increases gradually to 0.07 D_j . Total number of vertical grids is 150
Number of Grids	2.9 E+6	4.3 E+6

In the simulation, a jet velocity, V_j , equals to 40 m/s is used to enforce the flow. This jet velocity is used because it represents a typical value, as indicated by Savory et al. (2001). A time step of 0.0625 sec is chosen to keep Courant Friedrichs-Lewy (CFL) number at the bottom of the computational domain less than one in order to maintain the stability of the solution. The simulations started from a zero flow condition letting the downburst to develop in the computational domain by the introduced jet. The simulations continued until the main vortices induced near the inflow by the Helmholtz instability exit the computational domain.

7.2.1 Modeling of Terrain Roughness

Terrain roughness effect is modeled by using fractal surfaces. Heights of the fractal surfaces, $h(r, \theta)$, are generated according to Equation 7.2 using random Fourier modes (RFM).

$$h(r, \theta) = \sum_k S(k).e^{i(k.r+\phi_k)}$$

Equation 7.2

where $S(k)$ is the spectra of the roughness $S(k) = c.k^{-\frac{1+\beta}{2}}$, k is the wave length, c is a constant to control the amplitudes of the fractal surface, β is spectral slope which is taken as equal to -0.5, the phase angles $\varphi_k = \tilde{k}_\theta.\theta/l_\theta + \varphi_0$; φ_0 represent random phase angles and \tilde{k}_θ represent Gaussian random numbers with zero mean and 0.5 standard deviation, $1/l_\theta$ represent characteristic wave length in the θ direction which is taken equal to $1/(2.\Delta_\theta)$, where Δ_θ is the grid size in the θ direction.

Heights of the fractal surfaces generated by Equation 7.2, need to be scaled such that the surface aerodynamic roughness, z_0 , matches the targeted roughness, z_{0tar} . Scaling is performed using the procedure proposed by Aboshosha et al. (2013) and is expressed by Equation 7.3, where h_c represents a constant height that can be used to set the mean height of the surface to be equal to a specific value, which is chosen in the current study to be half of the physical size of the targeted roughness, $0.5 k_s \sim 15 z_{0tar}$. The constant height does not affect the flow solution, but it affects the overall level of the surface. The scaling factor a is estimated as shown in Equation 7.4, where C_d^* represent drag coefficient of the roughness elements which relates the drag force to the velocity measured at the reference height z_p , $\langle \dots \rangle$ represent horizontal plane averaging, $R(xx)$ is the ramp function $R(xx) = (xx/2 + |xx|/2)$, κ is von Karman constant and is taken as 0.41, and d represent the displacement height of the logarithmic flow region.

$$h_{scaled}(r, \theta) = h_c + a.h(r, \theta) \quad \text{Equation 7.3}$$

$$a = \frac{2}{C_d^* \left\langle R\left(\frac{\partial h}{\partial r}\right) \right\rangle} \cdot \left(\frac{\kappa}{\ln\left(\frac{z_p - d}{z_{0tar}}\right)} \right)^2 \quad \text{Equation 7.4}$$

Drag forces resulting from the scaled surface, $h_{scaled}(r, \theta)$, are introduced into the computational domain using the surface gradient-based drag (SGD) model, proposed originally by Anderson and Meneveau (2010) and modified by Aboshosha et al. (2013). The original SGD model showed very accurate velocity and Reynolds stress profiles of

the flow passing above different surfaces, previously examined in the literature (Nakayama and Sakio 2002, Kanda et al. 2004, Coceal et al. 2007 and Xie et al. 2008). The main drawback of the original model is the requirement of placing the physical roughness k_s or $\sim 30.z_0$ below the centre of the first grid layer, $0.5 \Delta_z$ (Richards and Hoxey 1993, Franke et al. 2004, Fluent Inc. 2005, Ansys Ltd., 2005, and Blocken et al. 2007). This constraint is similar to those encountered while using wall functions, which results from introducing drag forces in the first grid layer. Aboshosha et al. (2013) modified the SGD model, as shown in Figure 7.4, by introducing the drag forces into multiple n layers. In the modified model, n can be chosen to place the height z_p , or $n \cdot 0.5 \Delta_z$ in the case of a uniform layer height Δ_z , above the physical size of the roughness elements, k_s or $\sim 30z_0$, as illustrated in Figure 7.4. This relaxes the constraint on the maximum roughness that can be modeled using a particular grid, provided that a sufficient number of the layers n is used. In the modified model, shear stress at the top of the layers, τ_{i3} , at the level, H_d , is calculated using Equation 7.5, while drag force per unit mass at any layer j , f_{ij} , is expressed by Equation 6.10.

$$\tau_{i3} = -\frac{1}{2} \rho \cdot C_d^* \cdot R(\widehat{n}_k \frac{\partial h_{scaled}}{\partial x_k}) \widetilde{u}_{in} U_n^{m\Delta} \quad \text{Equation 7.5}$$

$$f_{ij} = \frac{\tau_{i3} \cdot \widetilde{u}_{ij} U_j^{m\Delta}}{\rho \sum_{j=1}^n \widetilde{u}_{ij} U_j^{m\Delta} \Delta_{zj}} \quad \text{Equation 7.6}$$

where ρ is the air density, \widehat{n}_k is a unit vector of the velocity direction, \widetilde{u}_{in} is the resolved velocity at the reference height (layer n) in the direction i , $U_n^{m\Delta}$ is the magnitude of the velocity at the reference height (layer n) filtered using a filtering width $m \cdot \Delta$, where m is calculated according to Aboshosha et al. (2013) as a function of surface heights $h_{scaled}(r, \theta)$, Δ_{zj} is height of layer no. j

The drag forces are expressed by Equation 7.6 based on considering an average distribution of the roughness elements in the vertical direction, which is equivalent to the case of roughness elements with the same height but having different shapes in plan

(Aboshosha et al. 2014). In the current study four fractal surfaces are generated using Equations 7.2-7.4, as shown in Figure 7.5.

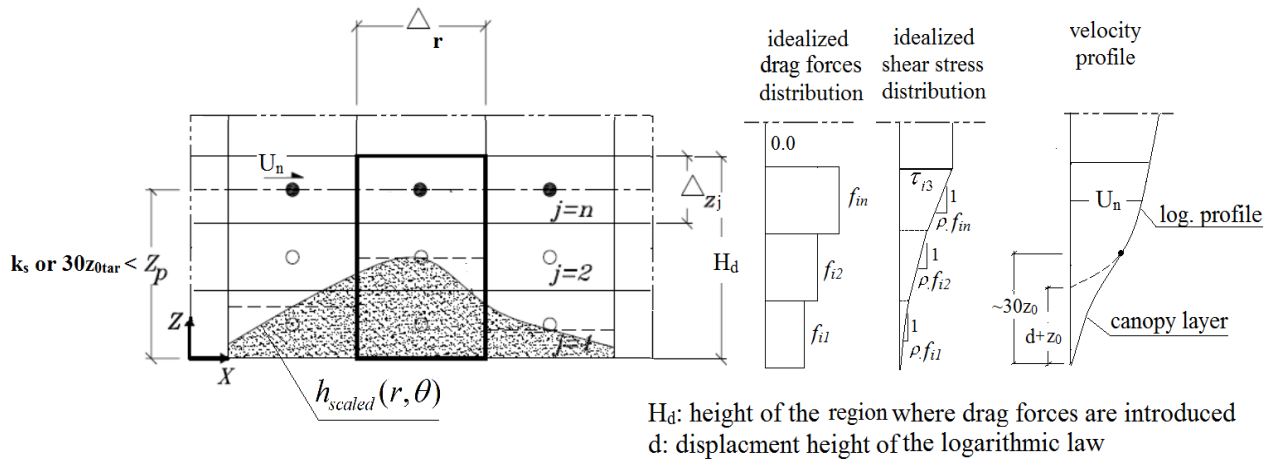


Figure 7.4 Illustration of the modified SGD model by Aboshosha et al. (2014)

The generated surfaces represent open, country side, suburban and urban exposures with aerodynamic roughness, z_0 , equal to 0.03, 0.1, 0.3 and 0.7 m, respectively. This classification is following the ESDU (2001) definition. Drag forces induced by the fractal surfaces are calculated using the modified SGD model using Equations 7.5 and 7.6 and introduced into the set of expressions presented in Equation 7.1, which governs the flow.

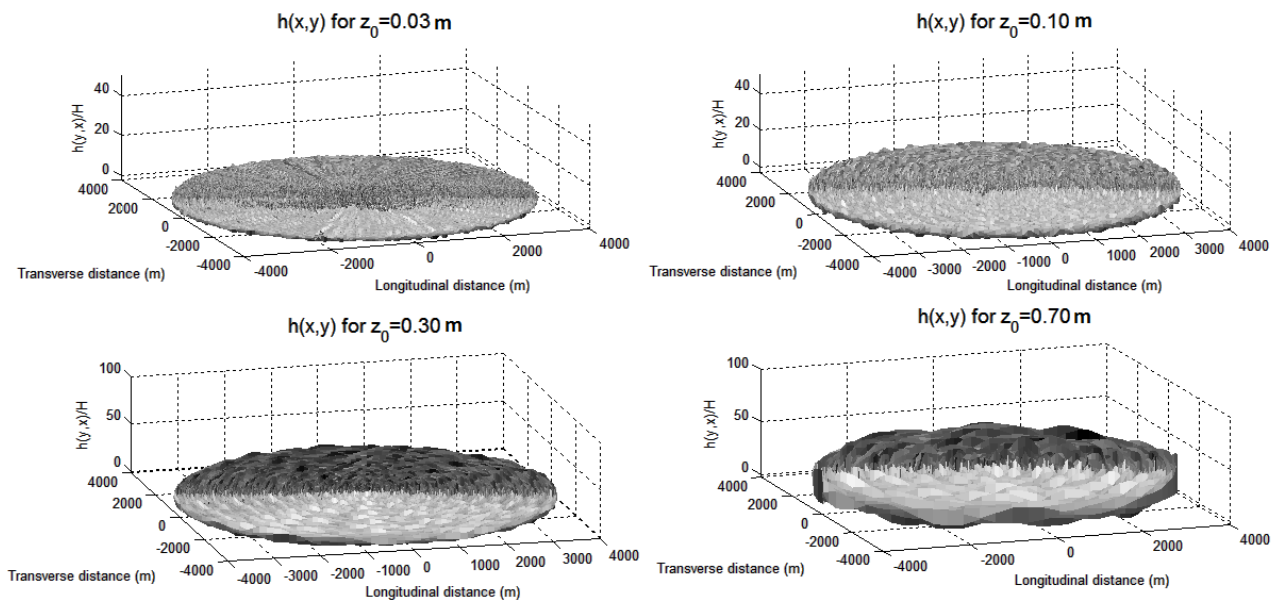


Figure 7.5 Roughness produced by using fractal surfaces for four different exposures

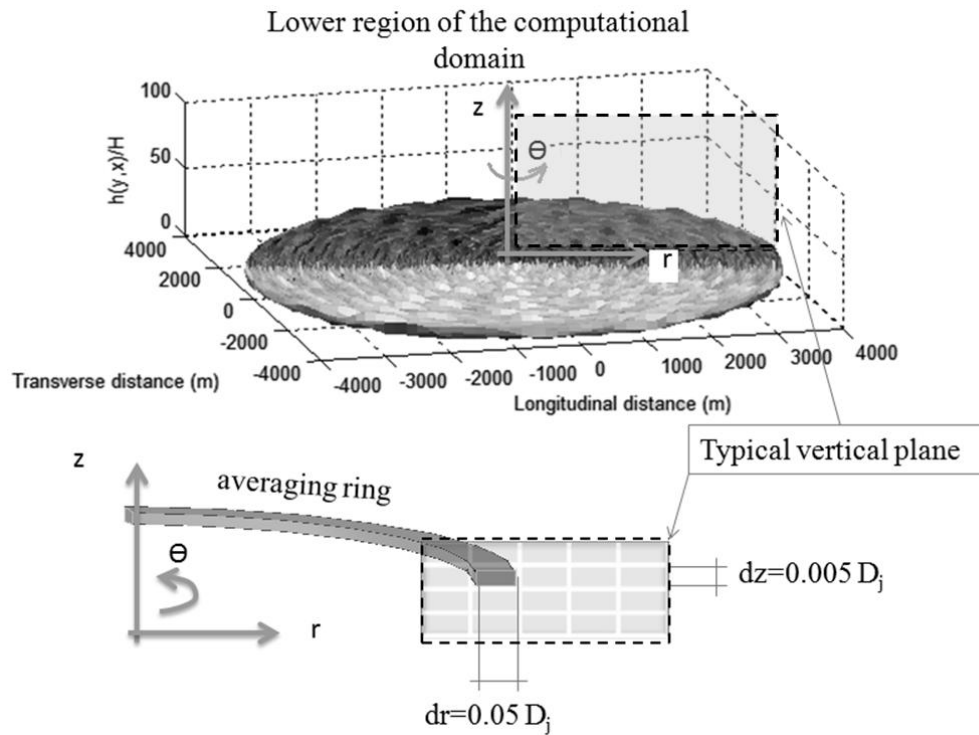


Figure 7.6 Spatial averaging of the instantaneous velocities

7.3 Running Mean and Turbulent Wind Decomposition

The main difference between decomposing a downburst wind field from synoptic is the time-dependency of its mean component. The wind field is usually decomposed into a running mean and a turbulence component Choi and Hidayat (2002) and Holmes et al. (2008). The method adopted for the present study is similar to that used by Jeong and Hussain (1995) to decompose the wind field into a phase average and a random component. A spatial averaging is applied circumferentially at all computational points using a spatial window size having a radial width $d_r = 0.05 D_j$ and vertical height $d_z = 0.005 D_j$, as illustrated in Figure 7.6. Resulting velocities from the spatial averaging are also temporally averaged by passing low frequencies smaller than a cut off frequency f_{cut} . This cut off frequency, given by Equation 7.7, is chosen to be twice the shedding frequency,

f_{shedd} , of the main vortices. This is to keep the fluctuations due to the main vortices, generated by Helmholtz instability, in the mean component. Shedding frequency is taken according to Kim and Hangan (2007) to represent the main vortices happening near the ground at a radius equal to $1.0 D_j$.

$$f_{cut} = 2.f_{shedd} = 2 \frac{0.3X.V_j}{D_j} = 0.6 \frac{V_j}{D_j} \quad \text{Equation 7.7}$$

where X is the distance from the jet centre to the point of interest which is taken as $2.D_j$ to represent the points close to the ground.

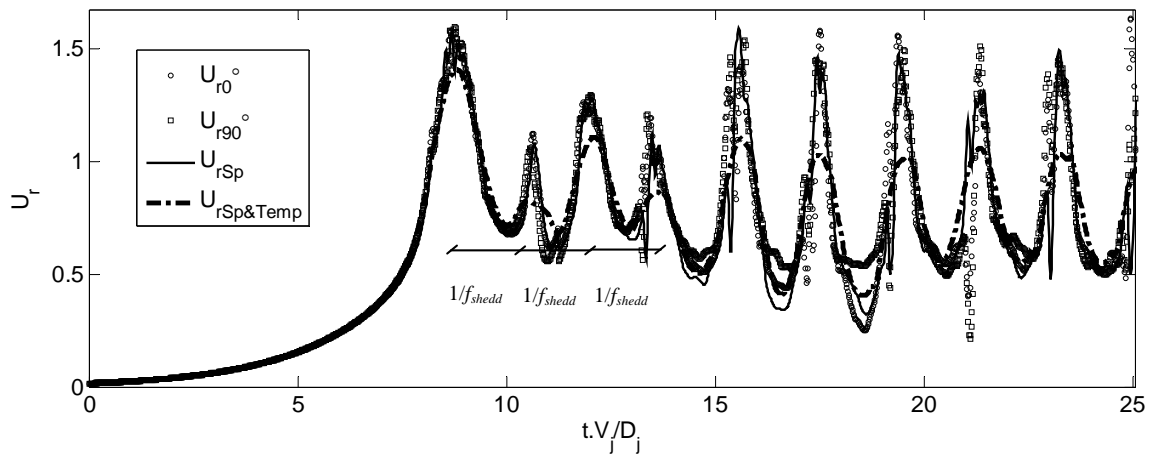


Figure 7.7 Spatial and temporal averaging of the instantaneous radial velocity at $R=1.25 D_j$ and $Z=0.05 D_j$

Accordingly, a 0.048 Hz cut off frequency, f_{cut} , is used in the current study. This cut off frequency is equivalent to a 69 sec averaging period for the real event that happened near Lubbock, Texas, USA in June 2002. This particular event has a jet velocity, V_j , of 29 m/s and a jet diameter, D_j , of 1200 m (Kim and Hangan 2007). This is in agreement with a (40-80 sec) range recommended for the averaging period by Holmes et al. (2008) and Darwish et al. (2010). Figure 7.7 shows the time history of the instantaneous radial velocity U_{r0° located at $R=1.25 D_j$, $Z=0.05 D_j$ and $\Theta=0^\circ$ and the velocity U_{r90° located at $R=1.25 D_j$, $Z=0.05 D_j$ and $\Theta=90^\circ$. The same figure also shows the resulting time histories

after applying the spatial average, U_{rSp} , and after applying both the spatial and the temporal averages, $U_{rSp\&Temp}$. It is clear from the figure that the averaged velocities in the space and time, $U_{rSp\&Temp}$, still contains strong fluctuations due to the main vortices similar to those found by Hangan and Kim (2007) for jets with high Reynolds number.

7.4 LES Results and Discussion

7.4.1 Grid Independence

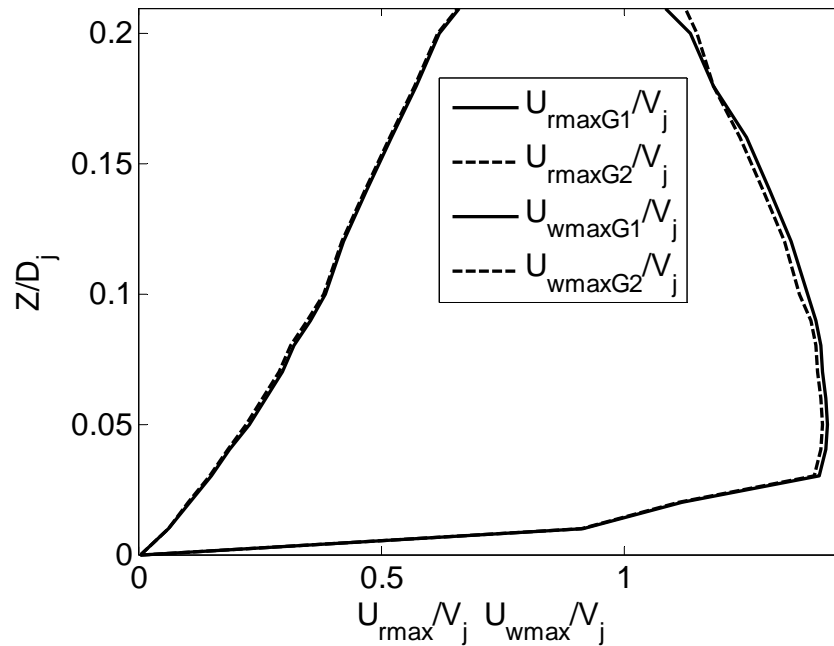


Figure 7.8 Maximum averaged radial and vertical velocity profiles obtained from Grid 1 (G1) and Grid 2 (G2)

Grid independence study is performed for the case of the country side exposure, where z_0 equals to 0.1 m. Maximum averaged velocities in the radial, U_{rmax} , and in the vertical, U_{wmax} , directions are used to check the sensitivity of the results on the employed grids, as illustrated in Figure 7.8. Profiles of the radial and vertical velocities obtained from the two grids are in a very good agreement. The maximum difference between the two profiles are found to be 0.83% and 0.98 % for the cases of the radial and vertical velocities, respectively. This indicates the independency of the results on the employed grids and therefore, only Grid 1 is used for simulating downbursts on the other exposure

conditions. Figure 7.8 also indicates that the maximum vertical velocities are significantly lower than the maximum radial velocities near the ground, where most structures are located. Therefore, only the radial velocities are discussed in the remaining portion of the paper.

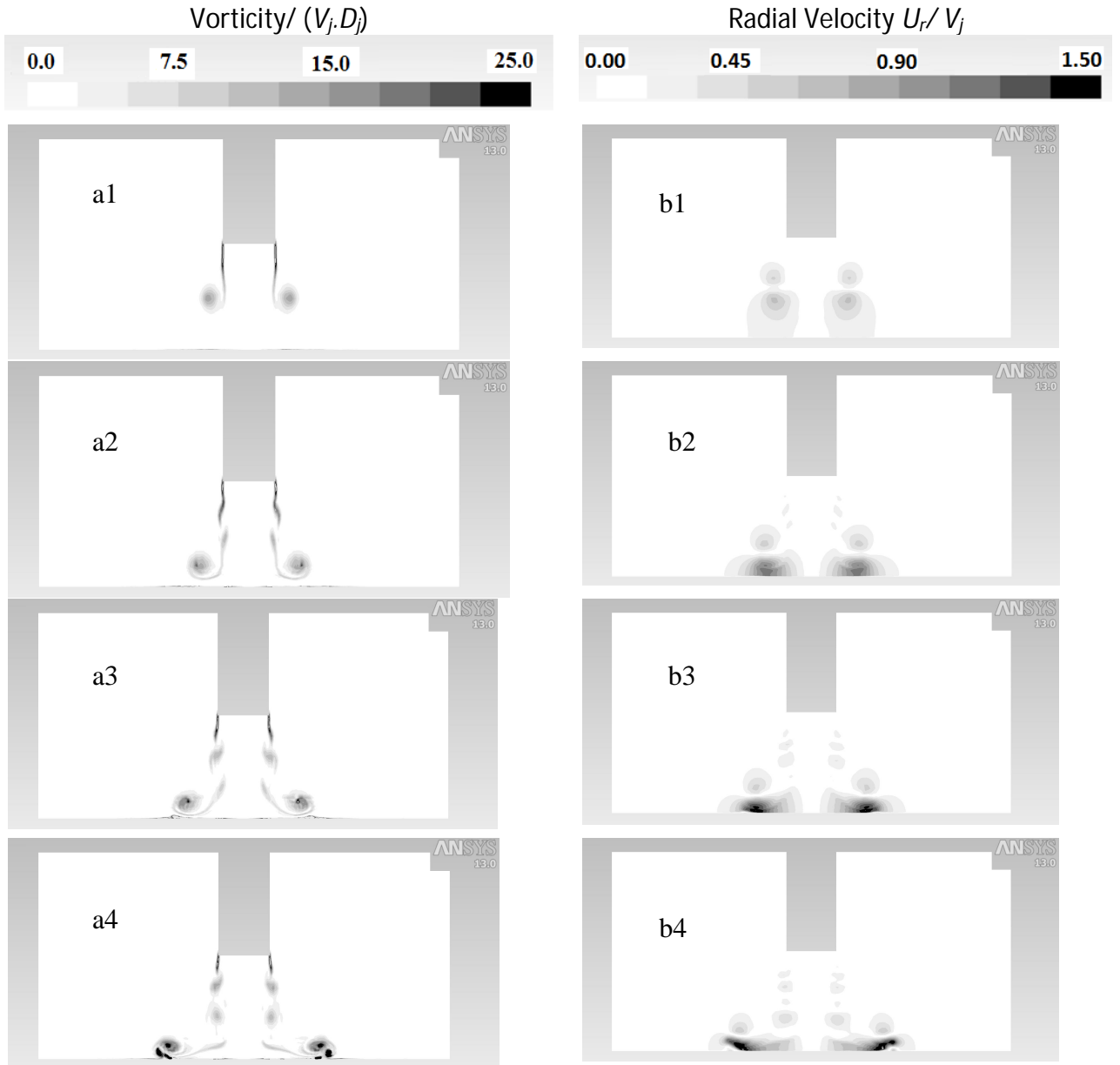




Figure 7.9 Evolution of the (a) normalized vorticity and (b) radial velocity for the open terrain condition with the time: (1) $T_n=8$, (2) $T_n=10$, (3) $T_n=12$, (4) $T_n=14$, (5) $T_n=16$; Where $T_n=T \cdot D_j/V_j$

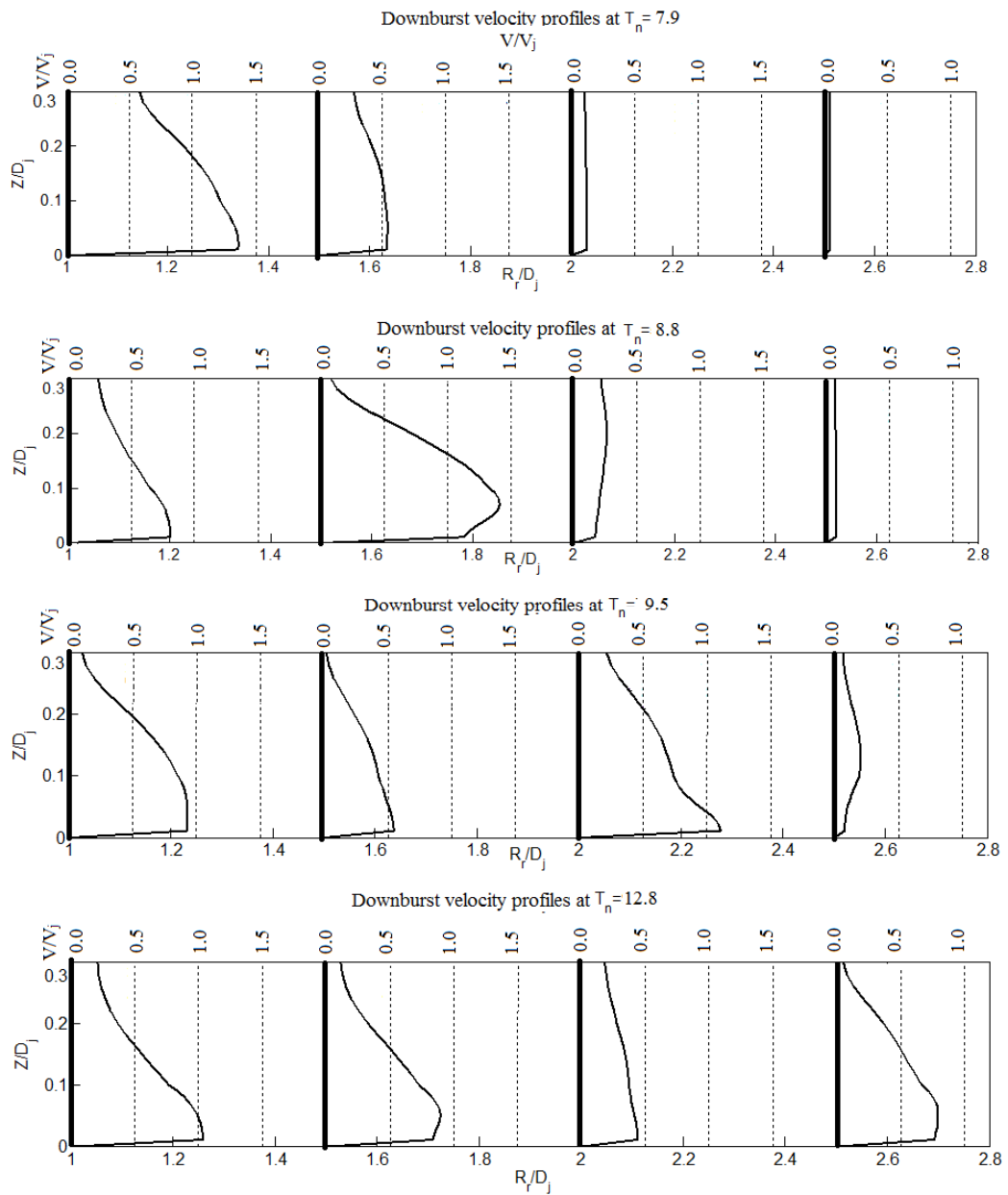


Figure 7.10 Radial averaged velocity at $R/D_j=0.5, 1.0, 1.5$ and 2.0 at $T_n=7.9, 8.8, 9.5$ and 12.8 ; Where $T_n=Time \cdot V_j/D_j$

7.4.2 Evolution of the Wind Field with Time

Downburst is a transient event in which the downdraft impinges towards the ground and convects radially with high velocities. Evolution of the downburst falling on an open exposure with $z_0=0.03$ m is illustrated in Figure 7.9. In this figure, radial velocity and the vorticity contours are plotted at different non dimensional time T_n , where $T_n=Time \cdot V_j/D_j$. It appears from Figures 7.9 (a1-a3) that a main vortex is formed right below the velocity inlet boundary due to Helmholtz instability then the vortex travels downward with the jet. After the main vortex hits the ground, as shown in Figures 7.9 (a4 and a5), it is broken down into multiple smaller vortices that are convected radially. Figures 7.9 (b1-b5) indicate that high radial velocities are associated with the location of the formed vortices similar to the findings by Kim and Hanagan (2007) and Veremier et al. (2011).

7.4.3 Mean Wind Field

Evolution of the vertical profile of the radial velocity, U_r , for the open terrain condition is illustrated in Figure 7.10. Instantaneous vertical profiles are plotted at different radii ($R=1.0, 1.5, 2.0$ and $2.5 D_j$) from the centre. The profiles are plotted at non dimensional time, $T_n=8.4, 9.2, 11.4$ and 13.0 representing the time instances when the maximum radial velocity occur at those radii ($R=1.0, 1.5, 2.0$ and $2.5 D_j$), respectively.

Profiles of the instantaneous maximum radial velocity and the peak radial velocity (extracted from the entire simulation time) are plotted for the case of open exposure as shown in Figure 7.11. The plotted profiles are normalized by the peak radial velocity, U_{rpeak} , based on the entire computational domain. For comparison purposes, other profiles obtained from field measurements, experiments and simulations in the literature are also plotted in the same figure. As shown in Figure 7.11, profiles obtained in the current study show a good agreement with the experimental results reported by Mason and Wood (2004) and Mason et al. (2005), field measurements by JAWS Data (Hjelmfelt, 1988) and simulation results by Proctor (1998) and Vermeire et al. (2011a). It is observed that both the instantaneous and the peak profiles obtained in the current study are consistent with

the profiles obtained previously. However, the profile predicted by Kim and Hangan (2007) appears to be maximum at higher elevation and covers broader elevations. This can be attributed to the small scale adopted for their simulations which may have overestimated the thickness of the developed boundary layer (Mason et al. 2009).

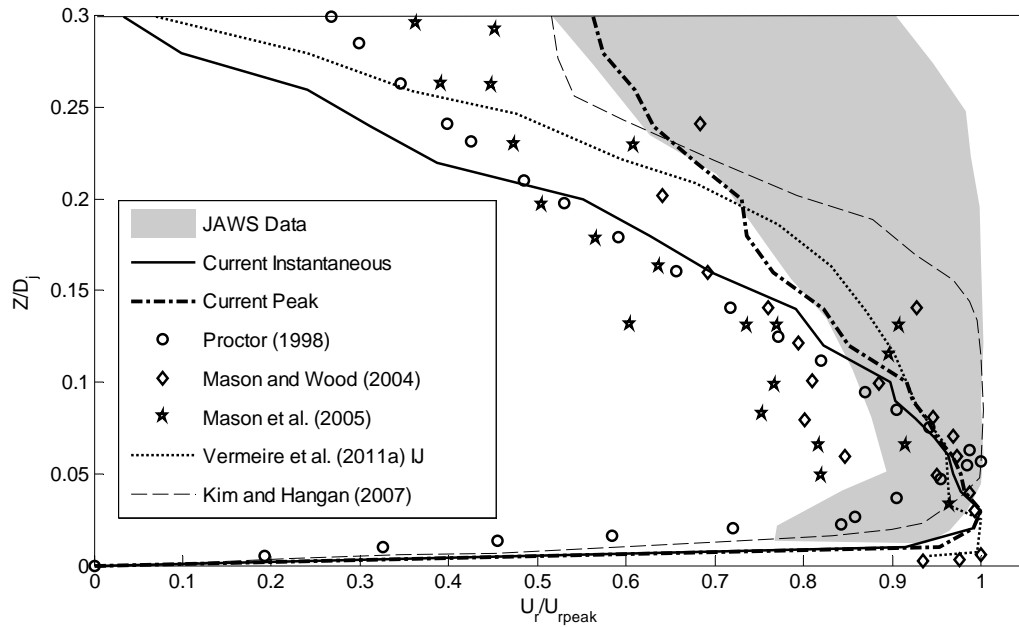


Figure 7.11 Radial velocity profile comparisons for the open exposure

7.4.3.1 Ground Roughness Effect

The effect of exposure roughness on the instantaneous maximum radial and envelope peak (i.e. maximum value of radial velocity at that height at any time) of radial velocities are shown in Figure 7.12. It appears that both the maximum instantaneous and envelope peak profiles tend to decrease with the increase of the roughness length of the exposure. It is also observed that the location of the maximum velocity shifts in the upward direction with the increase of the ground roughness length. Figure 7.13 shows the contour plots of the peak radial velocities obtained for the four studied exposure conditions. Representative height of the fractal surfaces is marked in the contour plots. Figure 7.13 shows that the location of the peak radial velocity lies within the range of $R=1.1-1.3D_j$ and tends to increase in z -direction with the increase of the ground roughness length, as

indicated in Figure 7.12. The reduction of the peak velocity with the increase of the roughness length, and the location of the peak velocity show good agreement with the trends reported by Mason et al. (2009) for downbursts enforced by Cooling Sources. However, a detailed comparison with the profiles obtained by Mason et al. (2009) was not possible because Mason et al. (2009) used different values of the aerodynamic roughness, z_0 .

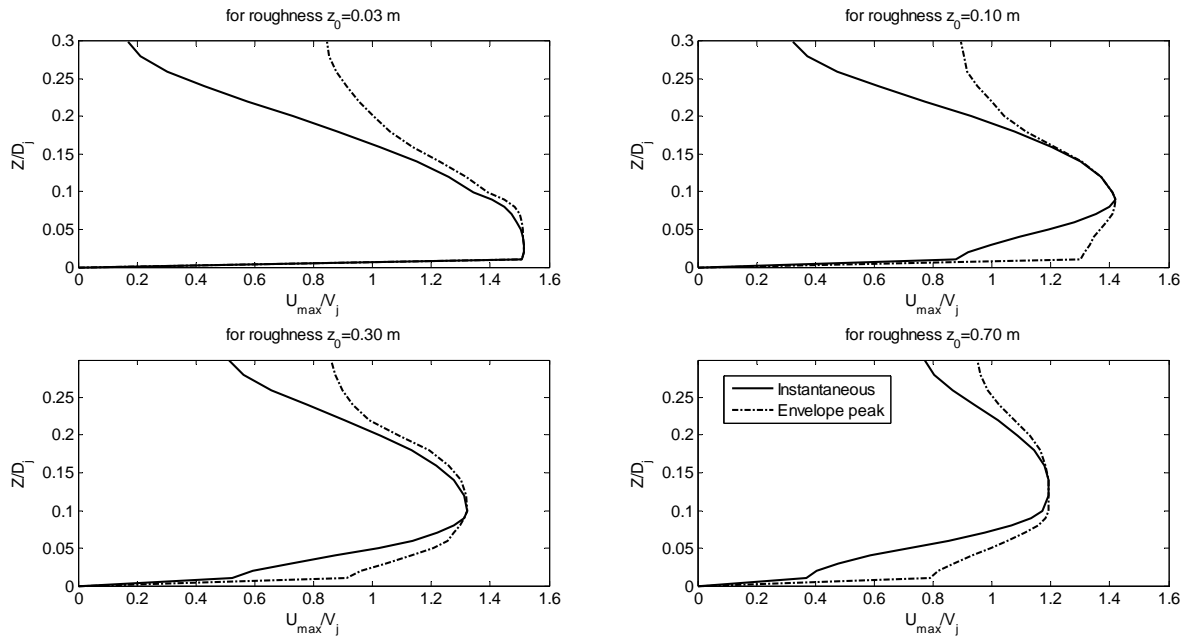


Figure 7.12 Instantaneous and envelope peak radial velocity

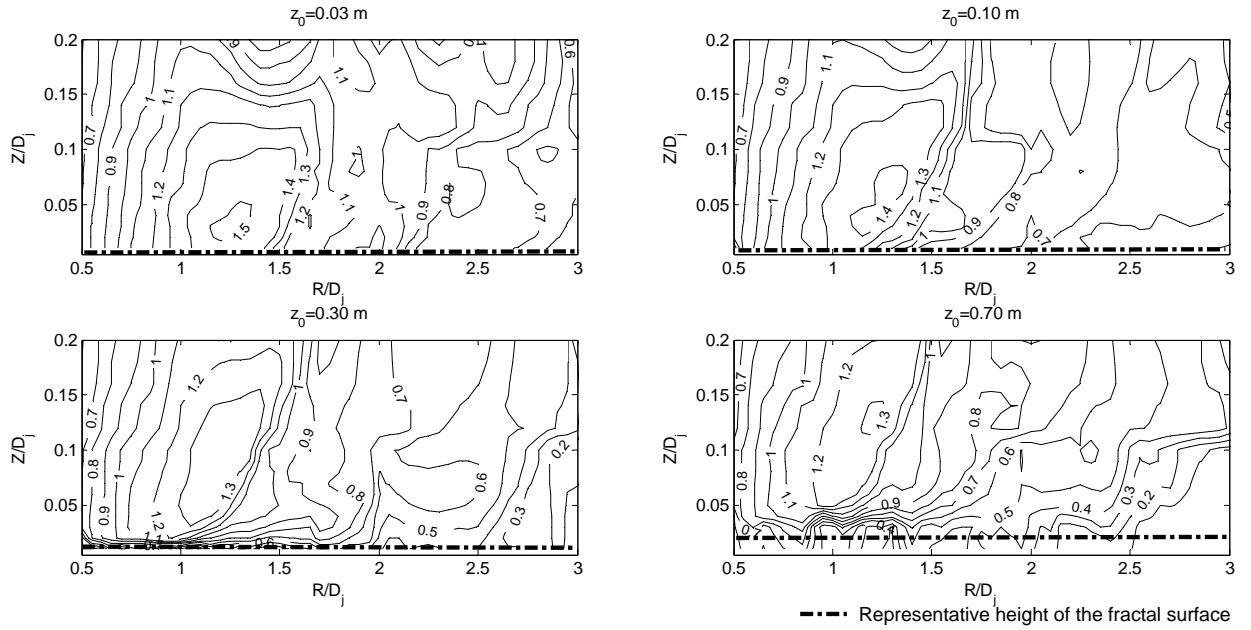


Figure 7.13 Maximum mean radial velocity V_j

7.4.4 Turbulent Wind Field

7.4.4.1 Turbulence Intensity

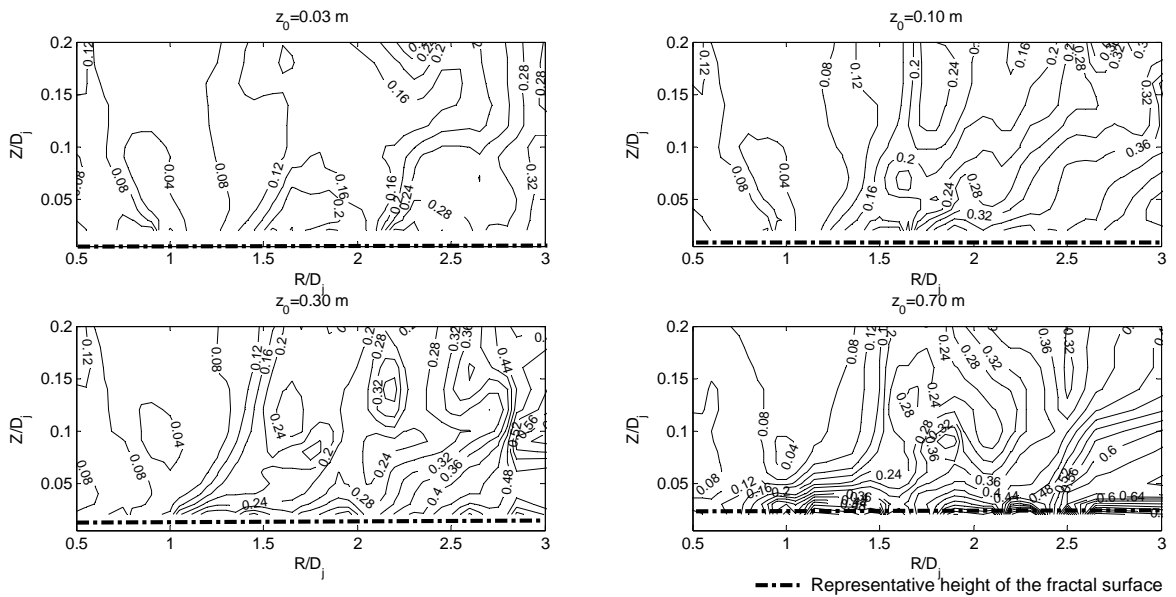


Figure 7.14 Turbulent intensity I_{ur} measured at the time instance of the maximum mean radial velocity

As discussed in Section 3, wind field resulting from the current simulations is decomposed into a running mean and a turbulent component. Downbursts are transient events and their mean and turbulent characteristics change with time. However, with respect to their effects on structures, characteristics near the time instances of the maximum mean velocities are of great importance as they mostly govern peak loads associated with these events. Therefore turbulent characteristics are obtained at those time instances similar to a study reported by Holmes et al. (2008). This is equivalent to treating the downburst turbulence as a piece-wise stationary process and focusing on the time interval close to the occurrence of the maximum mean velocities.

Turbulent Intensity, I_{ur} , defined by Equation 7.8, is calculated and plotted in Figure 7.14 for the four exposure conditions considered in the current study. As shown in Figure 7.14, turbulent intensity is high near the ground and decreases with the increase in height. By relating the turbulent intensity obtained from Figure 7.14 to the maximum mean velocity obtained from Figure 7.13, it is found that the turbulent intensity decreases in locations where the maximum mean velocity is high. This indicates that the peak velocities are mostly due to the mean component. Turbulent intensity near ground at locations of maximum mean velocities ranges between 0.08-0.12, 0.08-0.16, 0.08-0.24, 0.08-0.36, for open, countryside, suburban, and urban exposures, respectively. It is worth noting that the average intensity obtained in the current study for the open terrain, $I_{ur} \sim 0.10$, agrees with the findings reported by Holmes et al. (2008) based on a real downburst event.

$$I_{ur} = \frac{\sigma_{ur\max}}{U_{r\max}} \quad \text{Equation 7.8}$$

where $U_{r\max}$ is the maximum radial velocity, $\sigma_{ur\max}$ is r.m.s of the fluctuating velocity calculated from the period of $t_{\max} - \frac{1}{2 \cdot f_{cut}} : t_{\max} + \frac{1}{2 \cdot f_{cut}}$, where t_{\max} is the time instance corresponding to the maximum mean velocity.

7.4.4.2 Turbulence Correlation in the Wide Frequency Band

Effect of turbulence on a specific structure is assessed with parameters such as turbulence intensity, turbulence length scales, and turbulence spectra in addition to the dynamic

properties of the structure. In the current study, turbulence length scales in the circumferential, L_θ , radial, L_r , and vertical, L_w , directions are evaluated. Circumferential and vertical length scales, L_θ and L_w , are obtained directly, as the fitting parameters, from fitting the spatial correlation functions, $R(d\theta)$ and $R(dz)$, given by Equations 7.9 and 7.10, respectively.

$$R(d\theta) = \exp\left(-\frac{r \cdot d\theta}{L_\theta}\right) \quad \text{Equation 7.9}$$

$$R(dz) = \exp\left(-\frac{dz}{L_w}\right) \quad \text{Equation 7.10}$$

where $d\theta$, dz are the magnitude of angular and vertical separations, respectively.

Radial length scales, L_r , can be expressed as a function of the mean velocity and the turbulence time scale, τ_{turb} , as given by Equation 7.11. Maximum mean radial velocity, U_{rmax} , is used to represent the mean velocity in Equation 7.11, as the turbulence is extracted near the time instance of the maximum mean, t_{max} . Turbulent time scale, τ_{turb} , is evaluated by integrating the autocorrelation function, $R(\tau)$, as given by Equation 7.12. It should be mentioned that the autocorrelation function may have a negative sign. In such cases, the integration is stopped at the time of the first zero crossing, $\tau_{0-cross}$, similar to Katul and Parlange (1995).

$$L_r = U_{rmax} \cdot \tau_{turb} \quad \text{Equation 7.11}$$

$$\tau_{turb} = \int_0^{1/f_{cut} \cdot \tau_{0-cross}} R(\tau) \cdot d\tau \quad \text{Equation 7.12}$$

where $\tau_{0-cross}$ is the time corresponding to the first zero crossing of the autocorrelation function $R(\tau)$.

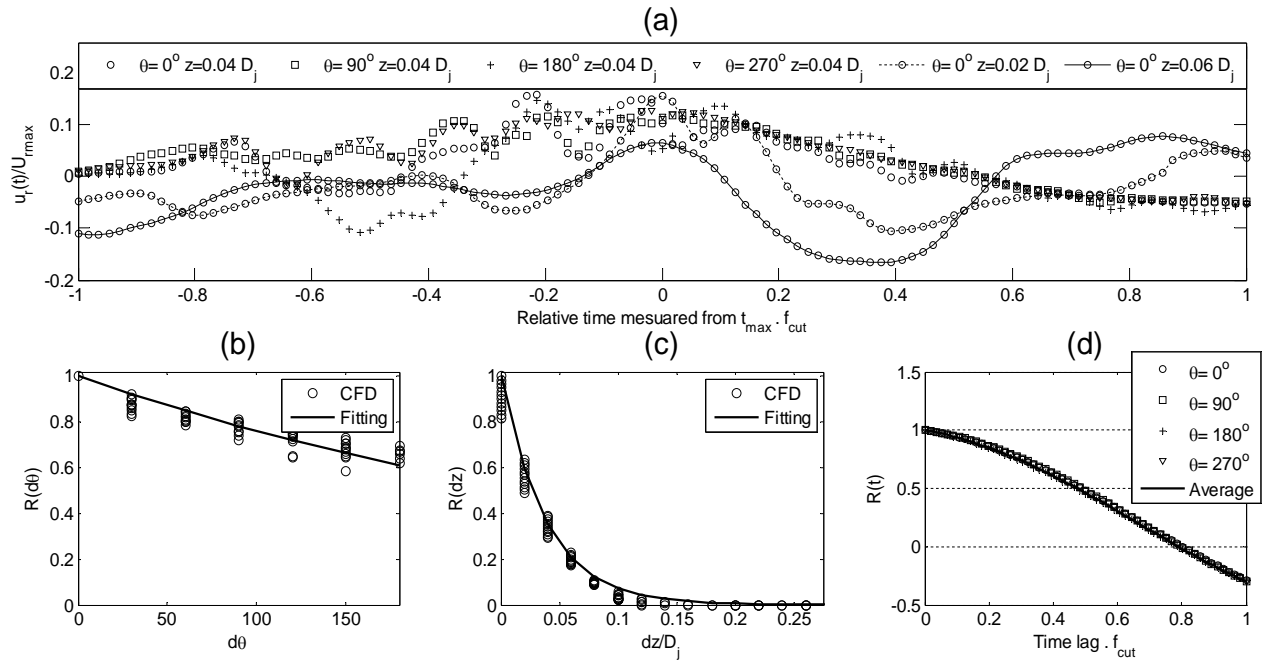


Figure 7.15 Procedure of obtaining the length scales from the fluctuating velocities
(a) fluctuating radial velocities (b) fitting the circumferential correlation function
 $R(dz)$ (c) fitting the vertical correlation function $R(\theta)$ and (d) averaging the
autocorrelation function

Sample plot of turbulent velocities at a location of $R=1.5D_j$ for the open terrain condition obtained at different angles θ and heights Z is shown in Figure 7.15.a, and the correlation functions in the circumferential, vertical, and radial directions are plotted in Figures 7.15(a, b, c), respectively. A circumferential correlation function, $R(\theta)$, is calculated using twelve turbulent velocity vectors extracted at every 30° and then fitted with the expression given by Equation 7.9, as shown in Figure 7.15(b). A vertical correlation function, $R(dz)$, at typical height, Z , is calculated by employing 10 velocity vectors, five on each side of the height extracted at every $0.005 D_j$ and then fitted by using Equation 7.10, as shown in Figure 7.15(c). Autocorrelation function, $R(\tau)$, is calculated by averaging the autocorrelation functions of the velocity vectors taken at every 30° , as shown in Figure 7.15(d).

Contour plots of the circumferential length scale, L_θ , are plotted in Figure 7.16. It appears from this figure that the circumferential length scale, L_θ , reaches up to 9 times the jet diameter D_j . This large value indicates that turbulence associated with downbursts is very well correlated in the circumferential direction, which agrees with the findings reported by Holmes et al. (2008). It is found that large values of, L_θ , cover wider areas in the case of smoother exposures ($z_0=0.03$ and 0.1 m) than areas in case of rougher exposures ($z_0=0.3$ and 0.7 m). This emphasizes that rougher exposures are able to breakdown the correlated turbulence into a random turbulence.

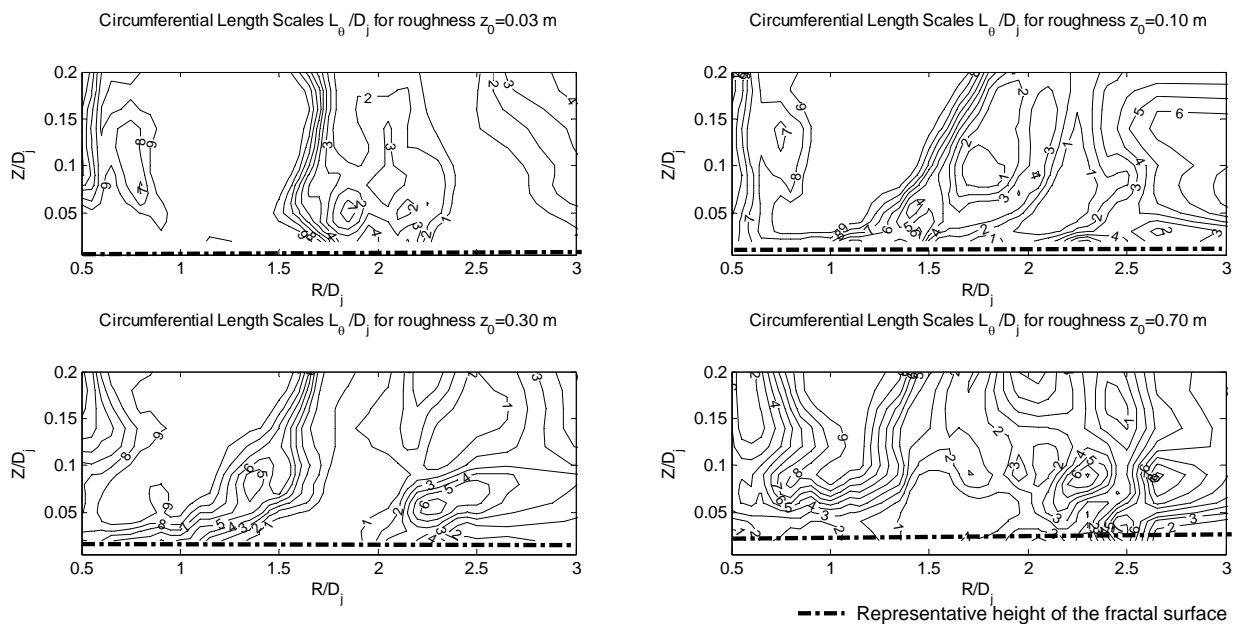


Figure 7.16 Circumferential length scale of turbulence L_θ

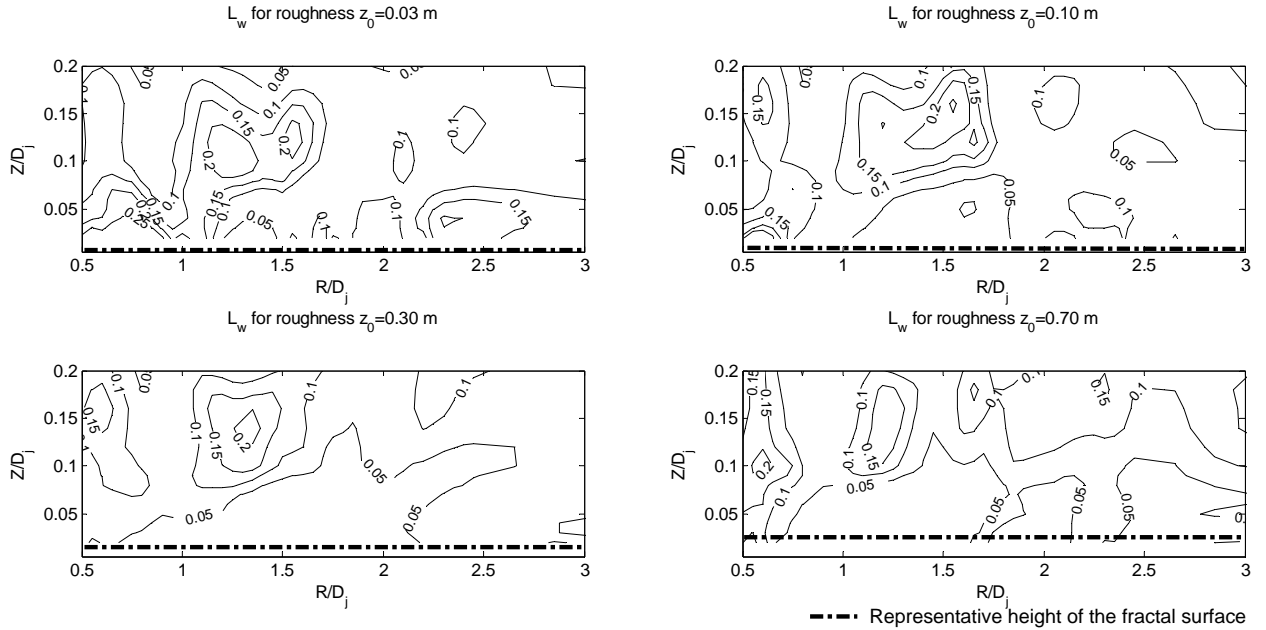


Figure 7.17 Vertical length scales of turbulence L_w

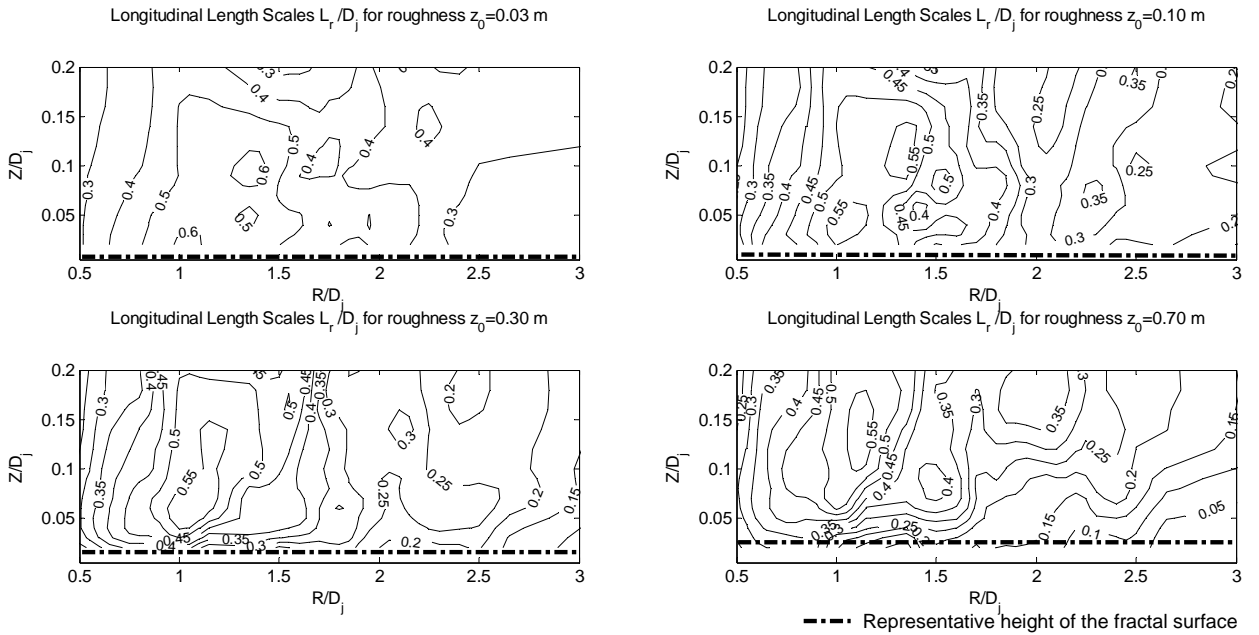


Figure 7.18 Radial turbulence length scale L_r

Contour of vertical length scales, L_v , are plotted in Figure 7.17. As shown in the figure, vertical length scales L_v generally ranges between $0.05-0.25D_j$, which is relatively smaller compared with circumferential length scales by at least an order of magnitude. This

emphasizes that the turbulence associated with downbursts is less correlated in the vertical direction compared to the circumferential direction, which is favorable in designing tall structures. Turbulent length scale in the vertical direction, L_v , at the location of the maximum mean velocity ($R=1.1-1.3D_j$) is found to be in the order of $0.05D_j$. This represents a 50 m length scale for a typical downburst with 1000 m diameter, which is compatible with the length scales defined in the ASCE (2010) for normal wind. Radial length scales, L_r , are plotted in Figure 7.18. It appears that a length scale ranges between $0.3-0.6D_j$ in the zone where mean velocities are maximum ($R=1.1-1.3D_j$) above the height of the roughness elements. For a typical downburst with 1000 m diameter, this represents a length scale of 300-600 m which is larger than the longitudinal length scales for synoptic winds 85-150 m according to the AS/NZS (2011). Larger length scales indicate that downburst turbulence is better correlated in the wind direction than the turbulence associated with normal winds. Turbulent length scales, L_θ , L_v and L_r , characterize the correlation in the wide frequency band. This is of a particular importance to quantify background forces on structures.

7.4.4.3 Turbulence Spectra

Power spectrum density of turbulent velocities at four points located at R and Z equal to $(0.02, 1.0)D_j$, $(0.04, 1.0)D_j$, $(0.02, 1.5)D_j$ and $(0.04, 1.5)D_j$ are calculated and plotted in Figure 7.19. These points are chosen as they bound the area where the peak velocities are expected. It is worth mentioning that frequencies smaller than f_{cut} are not shown in the figure as they correspond to the mean component. For comparison purposes with normal wind, Von Karman spectra, represented by Equation 7.13 (AS/NZS 2011), is also plotted in Figure 7.19.

$$S_{ur} = \frac{4 \cdot \sigma_u^2 \cdot \frac{L_r}{U_m}}{\left(1 + 70.8 \left(\frac{f \cdot L_r}{U_m}\right)^2\right)^{5/6}} \quad \text{Equation 7.13}$$

As shown in Equation 7.13, σ_u is the r.m.s fluctuation, U_m is mean velocity, which is taken equal to the maximum mean velocity U_{max} , f represent frequency, L_r represent turbulent length scale in the radial direction which is taken from Figure 7.18.

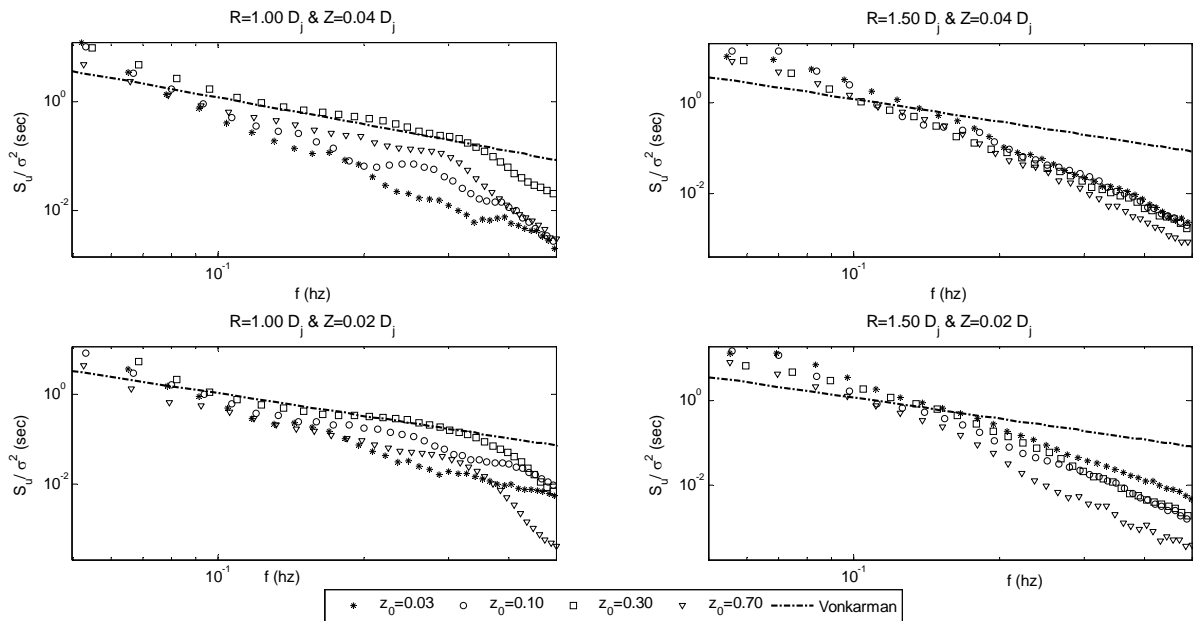


Figure 7.19 Turbulent spectra

Figure 7.19 shows that the spectra obtained at a radius R equals to $1.0D_j$ shows a reasonable agreement with VonKarman's especially for rougher exposures. With the increase of the radius, a steeper slope more than $-2/3$ of VonKarman is found. This agrees with the finding reported by Holmes et al. (2008) for a real downburst event although they reported a less steep slope. Generally, the steeper slope indicates that flexible structures with natural frequencies, 0.1-1 Hz, are less susceptible to dynamic excitation by downburst turbulence than by normal wind turbulence. Figure 7.19 also shows the roughness effect on the spectra. It is found at radius R equals to $1.0 D_j$, that the turbulent fluctuation associated with small eddies is higher for the rough terrain exposures, $z_0=0.3$ and 0.7 m, than the fluctuations for moderate rough exposures, $z_0=0.03$ and 0.1 m. However, with increasing the distance from the downburst jet, $R=1.5D_j$, energy associated with smaller eddies becomes higher in moderate rough exposures $z_0=0.03-0.1$

m. This indicates that rough exposures are able to breakdown the turbulence into smaller eddies in shorter distances than moderate rough exposures.

7.4.4.4 Peak Radial Wind Velocity

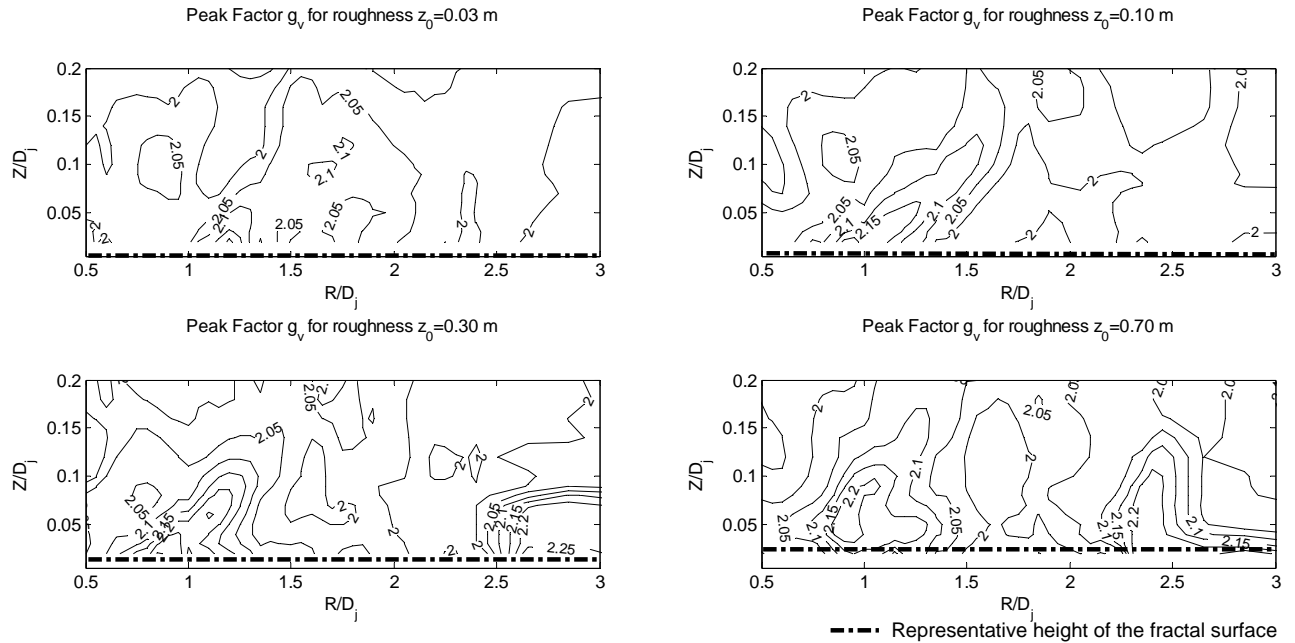


Figure 7.20 Peak factor g_v

In the current study, peak factor of the radial velocity fluctuations, g_v , is estimated statistically. This peak factor quantifies the peak velocities, \hat{U}_r , as expressed by Equation 7.14. A peak factor, g_v , represents the ratio between the peak fluctuations to the r.m.s fluctuations and can be calculated from Equation 7.15. Estimating the peak factor statistically is more stable than the estimation using absolute peak velocities.

$$\hat{U}_r = U_{r\max} (1 + g_v \cdot I_r) \quad \text{Equation 7.14}$$

$$g_v = \sqrt{2 \ln(2\nu T)} + \frac{0.5772}{\sqrt{2 \ln(2\nu T)}} \quad \text{Equation 7.15}$$

where ν is the rate of zero crossing of the fluctuating velocity, T is averaging time which is equal to $1/f_{cut}$.

An average rate of zero crossing ν , which represents the average frequency of the turbulence, is required in order to obtain the peak factor, g_ν , using Equation 7.15. Expression given by Equation 7.16, is used to obtain such average rate, ν . The resulting peak factor, g_ν , is plotted in Figure 7.20. As shown in Figure 7.20, peak factor, g_ν , is less sensitive to the location in the domain and ranges between 2.00-2.20.

$$\nu = \sqrt{\frac{\int_{f_{cut}}^{f_s/2} (f - f_{cut})^2 \cdot S_u(f) df}{\int_{f_{cut}}^{f_s/2} S_u(f) df}} + f_{cut} \tag{Equation 7.16}$$

where $S_u(f)$: spectra of the radial velocity, f_s : sampling frequency

7.4.4.5 Turbulent Correlations in the Narrow Frequency Band

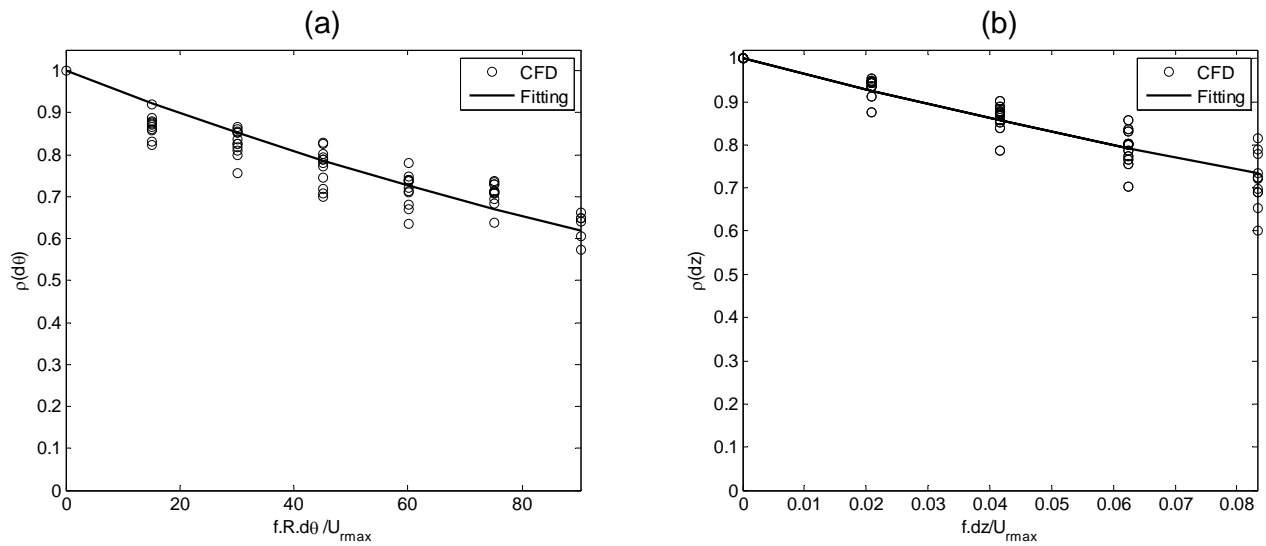


Figure 7.21 Fitting the root coherence function

Turbulent correlations in the narrow frequency band are required for cases where structures are susceptible to dynamic excitations by wind turbulence. Turbulent correlations in the narrow frequency band can be represented by the root coherence, $\rho(f)$, given by Equation 7.17.

$$\rho(f) = \exp\left(\frac{-C \cdot f \cdot d}{U_{\max}}\right) \quad \text{Equation 7.17}$$

where f is the frequency, U_{\max} is maximum mean velocity, C is coherency decay constant, and d is distance between velocity pairs, which is taken equal to dz and $R \cdot d\theta$ for vertical and circumferential directions, respectively.

The constant C in Equation 7.17 is called the coherency decay constant. It characterizes the correlations in the narrow frequency band. High values of C represent low correlations, while low values indicate high correlations. Variation of the narrow band correlations characterized by the coherency decay constant, C , is studied. Root coherence, $\rho(f)$, is plotted for the turbulent velocity vectors obtained at different vertical and circumferential locations. Sample root coherences for velocity vectors that vary in the vertical and circumferential directions at radius R of $2.0D_j$ and elevation Z of $0.004D_j$ are plotted in Figure 7.21(a), b, respectively. By fitting the root coherence with the expression in Equation 7.17, coherency decay constants C_w and C_θ are obtained as the fitting parameter in the vertical and circumferential directions, respectively. These constants are shown in Figure 7.21(a), and (b), respectively. Variation of the coherency decay constants, C_w , and, C_θ , is shown by the contour plots in Figures 7.22 and 7.23, respectively. As shown in these figures, the constant, C_w , generally decreases with the increase of height, which agrees with the findings reported by Chen and Letchford (2005). It is found that the constant C_w is of the order of 10 at the location of maximum mean velocities, i.e. $R=1.1-1.3D_j$. This is consistent with the range of values used for normal winds, 5-15 (Holmes et al. 2008). The decay constant in the circumferential direction, C_θ , has relatively smaller values, which is expected because of the well correlation of the turbulent in the circumferential direction. This means that downbursts, with a well correlated turbulence having frequencies close to the structures' frequencies, might excite flexible long horizontal structures more than normal winds.

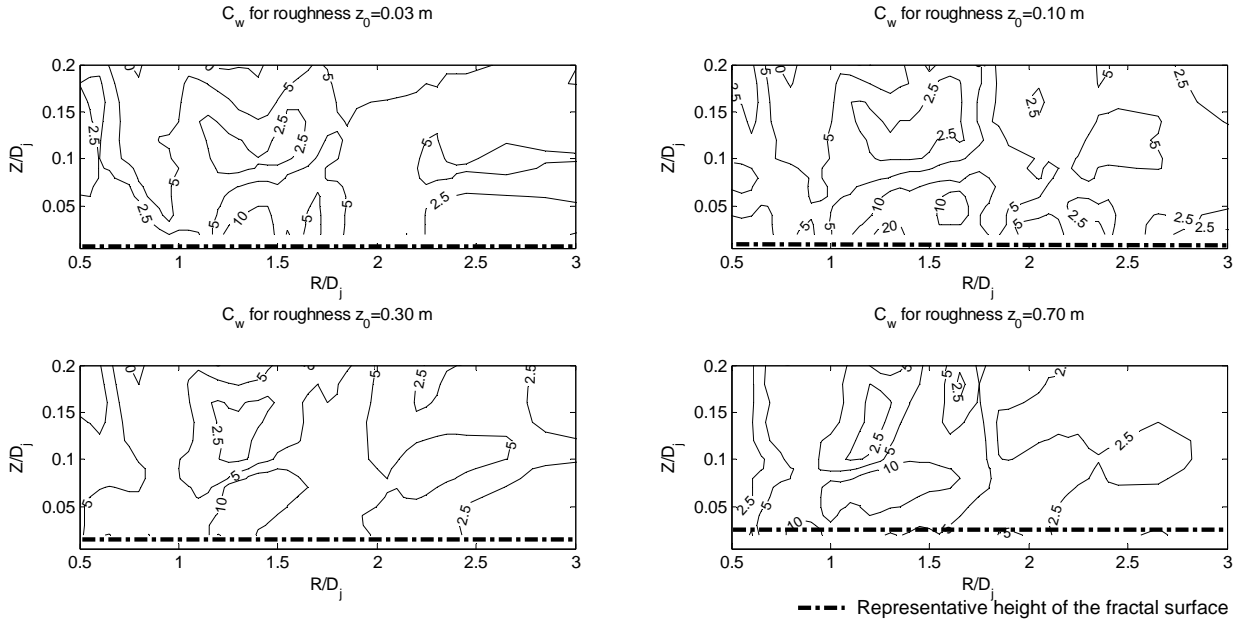


Figure 7.22 Coherency decay constant in the vertical direction C_w

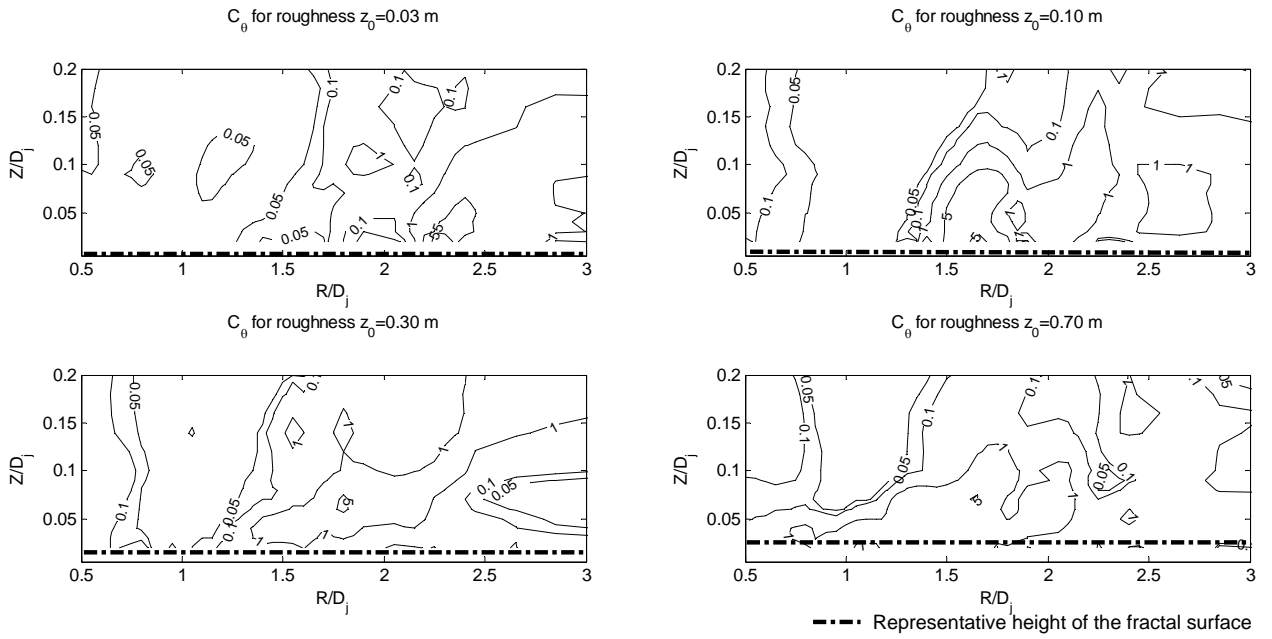


Figure 7.23 Coherency decay constant in the circumferential direction C_θ

7.5 Assessing the Dynamic Effect on Transmission Line Conductors

In the previous section, downburst wind fields resulting from LES considering various terrain exposures are investigated in detail. In this section, the resulting wind fields are employed to assess the importance of including the dynamic effect on the responses of TL conductors. TL conductors with single-spanned and six-spanned systems, previously investigated in Chapter 5 considering an open terrain exposure, are reconsidered here for further assessment. This assessment accounts for different terrain exposures. It also employs wind fields with a detailed turbulent component that was not investigated in Chapter 5.

Assessment of the dynamic response of the conductors is performed considering the eight downburst cases previously considered in Chapter 5 and summarized in Table 7.3. These cases cover two downburst scenarios: (i) four cases leading to maximum longitudinal reactions (ii) four cases leading to maximum transverse reactions. Each four cases covers two conductor spans with two reference velocities, as summarized in Table 7.3. A reference velocity, V_{ref} , is taken as the maximum mean velocity at the nearest point on the conductor to the downburst centre (point “p” shown in Figure 5.2). Figure 7.24 shows samples of the mean, turbulent and total velocity time histories taken at point p for the downburst case (no.1).

Table 7.3 Studied cases

Case	1	2	3	4	5	6	7	8
Type*	Db _x	Db _x	Db _x	Db _x	Db _y	Db _y	Db _y	Db _y
L _x (m)	300	300	500	500	300	300	500	500
V _{ref} (m/s)	40	20	40	20	40	20	40	20

Db_x, Db_y: Downburst case for the maximum longitudinal reaction R_x (D=2.0 L_x, R=1.60 D_j and $\Theta=30^\circ$) and transverse reaction R_y (D=2.0 L_x, R=1.20 D_j and $\Theta=0^\circ$); V_{ref}: Reference mean velocity

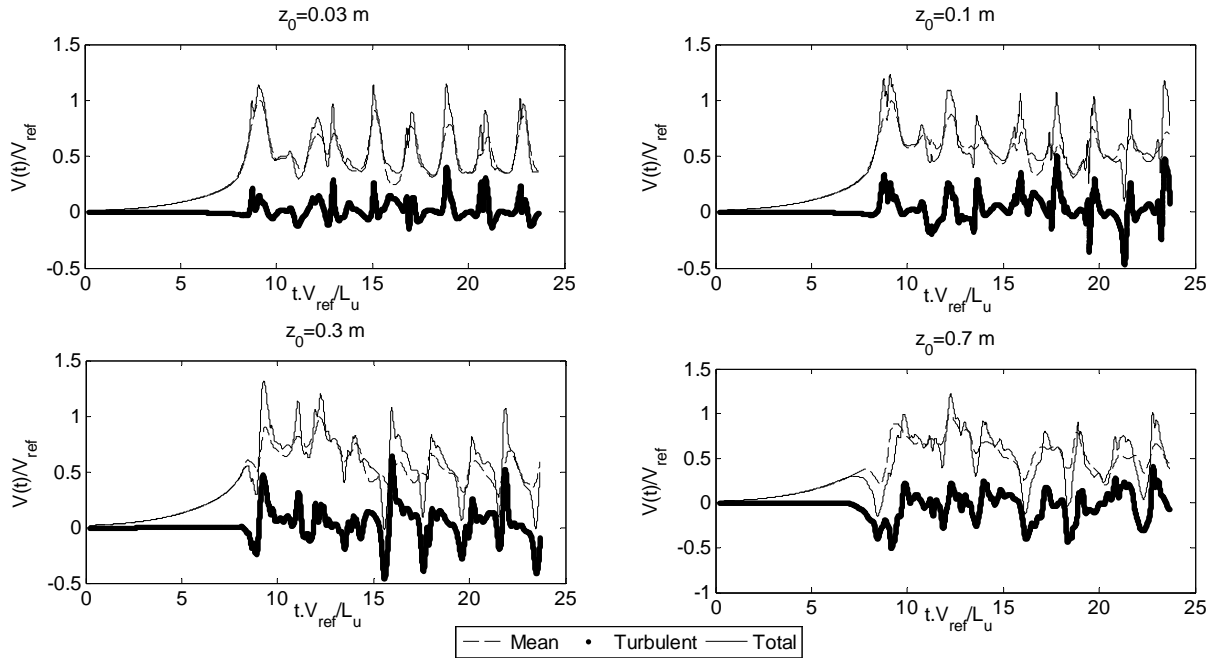


Figure 7.24 Velocity time history at point p for downburst case no. 1 (Dbx, $L_x=300$, $V_{refp}=40$ m/s)

Mean and fluctuating forces acting on the conductor, resulting from downburst velocities, are calculated as described in section 5.3. Responses of the conductor systems under the applied forces are obtained using the three steps technique described in the same section to distinguish between the mean, background and resonant components. Sample responses obtained for downburst case (no. 1) falling over open, countryside, suburban and urban exposures are illustrated in Figures D.1-D4, respectively, provided in Appendix D. In these figures R_{y1} and R_{y6} represent the transverse reactions and R_{x1} and R_{x6} represent the longitudinal reactions resulting from the single-spanned system and the six-spanned system, respectively. The resulting responses are used to calculate the Gust Factor, GF , defined as the ratio between the peak responses to the maximum-mean responses. Two gust factors are calculated based on how the peak responses are defined: (1) the first is called the dynamic gust factor, GF_{Dy} , where the peak responses result from the contribution of the mean, background and resonant components. (2) The second is called the quasi-static gust factor, GF_{QS} , where only the contribution of the mean and the background components is considered in calculating the peak responses. The gust factors

are summarized in Tables D1, D2, D3, and D4, located in Appendix D, for open, countryside, suburban and urban terrain exposures, respectively. The contribution of the mean, $Cont_M$, background, $Cont_{BG}$, and resonant, $Cont_R$, components to the peak responses are calculated using the expressions shown in Equation 7.18 and they are plotted in Figures 7.25-7.28 for the considered terrain exposures.

$$Cont_M = \frac{1}{GF_{Dy}}, \quad Cont_{BG} = \frac{GF_{QS} - 1}{GF_{Dy}}, \quad Cont_R = \frac{GF_{Dy} - GF_{QS}}{GF_{Dy}} \quad \text{Equation 7.18}$$

The contribution of the resonant component, $Cont_R$, which is reported in Tables D1-D4, represents the error in the estimated peak response when the dynamic effect is not considered. High contribution implies the importance of conducting dynamic analysis. The following remarks can be deduced by observing the values of $Cont_R$ calculated for different cases. It should be noted that these remarks are based on the values of $Cont_R$ for the longitudinal reaction, considering solely downburst cases which are critical for the longitudinal reaction, and for the transverse reaction considering only downburst cases which are critical for the transverse reaction. This is because these critical cases are responsible for the maximum reactions.

- For moderately rough exposures (open and countryside), maximum contribution $Cont_R$ of the longitudinal reaction is found to be 10% for the high reference velocity (40 m/s) and 21% for the low reference velocity (20 m/s). Maximum $Cont_R$ for the transverse reaction is found to be in the order of 6% for both reference velocities. This indicates that, when considering moderately rough exposures, the dynamic effect may be neglected for high reference velocities but has to be considered for low reference velocities. This observation is compatible with the findings made in Chapter 5 considering solely an open terrain exposure.
- For rough exposures (suburban and urban), the dynamic effect is shown to be important under both low and high reference velocities. For example, maximum $Cont_R$ is found to be 16% for the longitudinal reaction at the low reference velocity (20 m/s) and 38% for the transverse reaction at the high reference velocity (40 m/s).

- Increasing the span length tends to decrease the contribution of the resonant component $Cont_R$ for all cases. This is because the correlation between the turbulent velocities decreases with the increase in the span length.

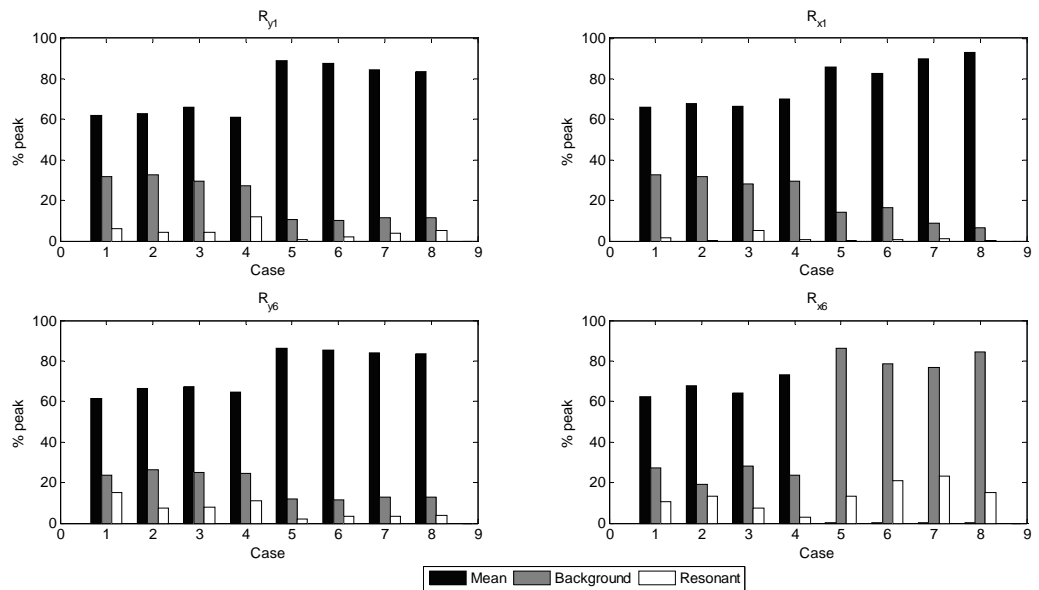


Figure 7.25 Mean, background and resonant contributions to the peak response - open terrain ($z_0=0.03$ m)

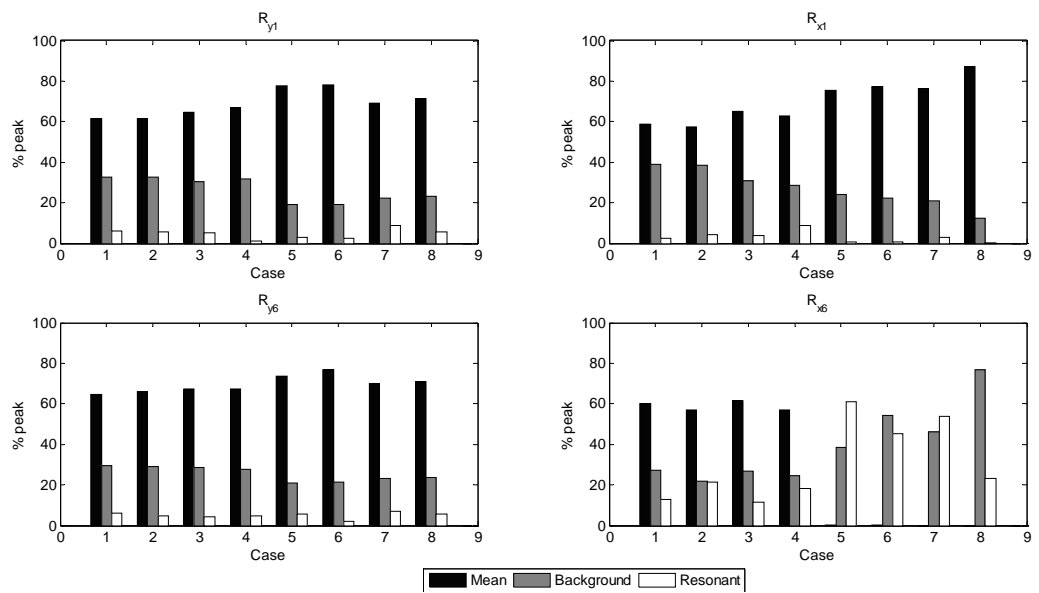


Figure 7.26 Mean, background and resonant contribution to the peak response- country side terrain ($z_0=0.1$ m)

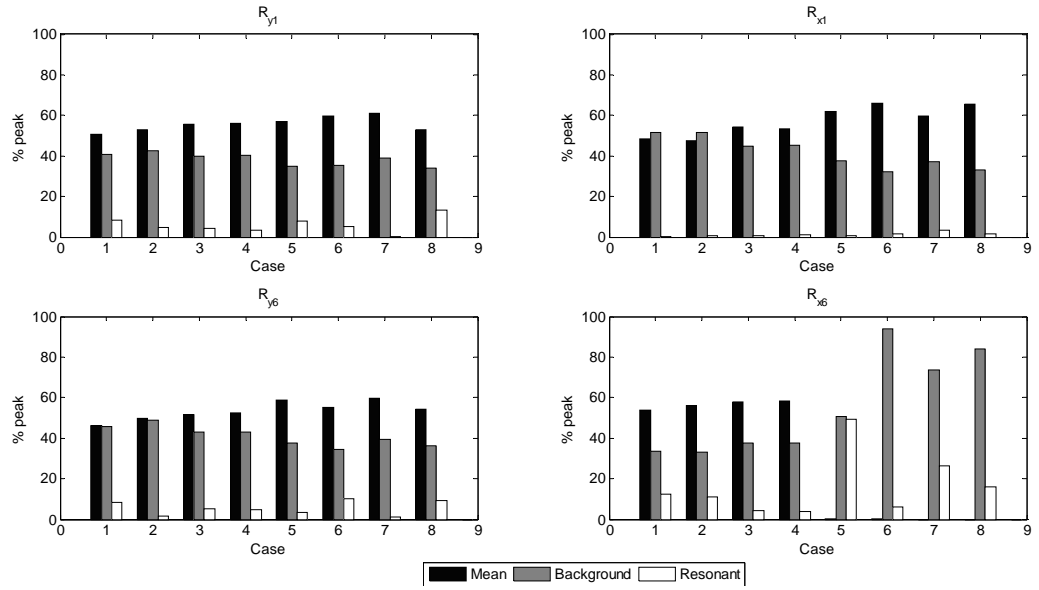


Figure 7.27 Mean, background and resonant contribution to the peak response- suburban terrain ($z_0=0.3$ m)

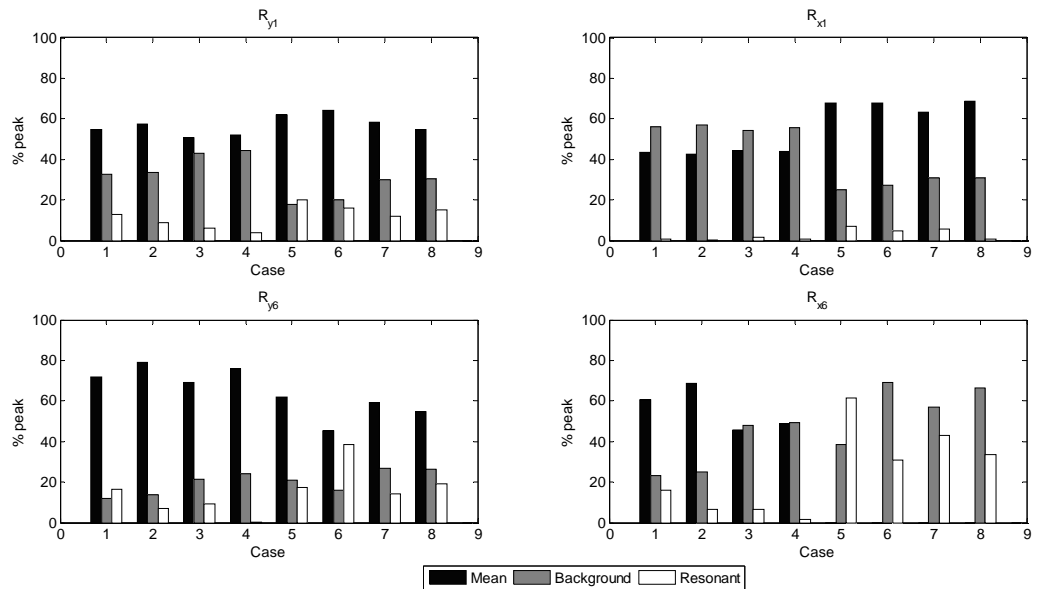


Figure 7.28 Mean, background and resonant contribution to the peak response - urban terrain ($z_0=0.7$ m)

In order to compare the responses obtained from different cases, a general normalization using a force, $g_{yp} \cdot L_x$, is applied to the reaction responses, as shown in Figure 7.29. This normalization force is equal to the product of the wind intensity applied at point p , g_{yp}^*

(expressed by Equation 5.17), and the span length L_x . This force, $g_{yp} \cdot L_x$, represents the maximum mean transverse force acting on the towers assuming a uniform distribution of wind load.

$$g_{yp}^* = \frac{1}{2} \rho \cdot C_d \cdot V_{ref}^2 \cdot D, \tag{Equation 7.19}$$

Figure 7.29 shows the normalized peak reactions for the four considered terrain conditions. As shown in the figure, the maximum normalized peak transverse reactions R_{y1p} and R_{y6p} happen under rough terrain exposures (suburban with $z_0=0.3$ m and urban with $z_0=0.7$ m), and are equal to 75% and 80%, respectively. The maximum normalized peak longitudinal reactions R_{x1p} and R_{x6p} happen under smooth terrain exposures (open with $z_0=0.03$ m and countryside with $z_0=0.1$ m), and are equal to 290% and 45%, respectively. These values indicate that the developed longitudinal peak reactions, R_{x1p} and R_{x6p} are significant and accordingly are recommended to be included in the design of the line.

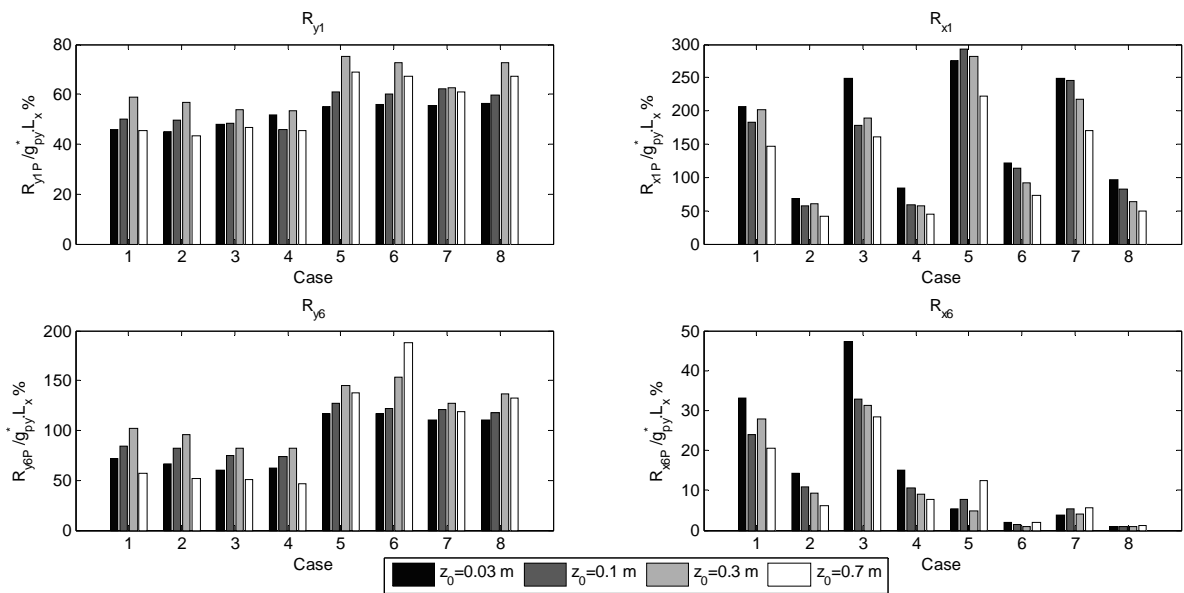


Figure 7.29 Peak response normalized by $g_{py} \cdot L_x$ for the different terrain exposures

7.6 Application of the Gust Front Factor (GFF) Approach to Obtain the Peak Responses of Transmission Line Conductors

Gust factor for a structure, originally proposed by Davenport (1967) represents the ratio between the peak displacement and the mean displacement. Such a GF is extensively examined by Solari (1993a,b) and Simiu and Scanlan (1996). Later Zhou and Kareem (2001), suggested a new definition for the gust factor as the ratio between the peak base moment and the mean base moment. The new definition is believed to allow for a more accurate estimation of the effective forces experienced by the structures. Gust factor approach widely used in the design codes, such as the ASCE (2010) and the AS/NZS (2011), is valid for synoptic winds. Kown and Kareem (2009) suggested a new framework called the gust front factor (GFF) which is valid for both synoptic and non-synoptic winds including downbursts. The new GFF includes some factors to account for the non-stationarity associated with the non-synoptic winds. Those factors converge to unity for the case of stationary wind letting the new GFF converging to the original GF. Unfortunately, the new GFF requires the characteristics of the non-synoptic event and involves heavy calculations. Both can delay the implementation of the GFF in design codes. Downburst characteristics obtained in the current study can be used directly in the new GFF. With regard to the computational demand involved in this process, properties of the structure and the dynamic characteristics of the event play a significant role. For the case of transmission line (TL) structures for instance, the dynamic behaviour can be decoupled into behaviour of tower and behaviour of conductor, separately. That is because of the gap between their natural frequencies. Typical towers, with overall height less than 50 m, have a fundamental frequency larger than 1 Hz. This makes them far from being excited by wind turbulence. Conductors have lower frequencies than towers, which makes them susceptible to be excited by turbulence. Fortunately, as indicated from the results obtained in the previous section, the dynamic effect of the conductor is minor when considering moderate rough terrains (open and suburban) under high velocities, typically encountered during downburst events. This can simplify the GFF for this type of structures by considering only the mean and the background components. Considering the mean and the background components is a common practice in design codes for

typical TL structures under synoptic winds, as in the ASCE (2010), IEC (2003) and the AS/NZ (2010). By considering mean and background components, GFF for a response R can be expressed by Equation 7.20 using the statistical method proposed by Davenport (1993). This requires information about the normalized mean velocities, φ_u , turbulent intensities, I_{ur} , turbulent length scales, L_{Db} , and peak factor, g_v , that can be easily obtained from the current study.

$$GF = \frac{\hat{R}}{\bar{R}} = 1 + 2 \cdot g_v \cdot \sqrt{J_{LDb}} / I_m$$

where,

$$J_{LDb} = \iint I_{ur}(n_1) \cdot I_{ur}(n_2) \cdot \varphi_u(n_1)^2 \cdot \varphi_u(n_2)^2 \cdot i_R(n_1) \cdot i_R(n_2) \cdot e^{\left(\frac{-L_x |n_1 - n_2|}{L_{Db}}\right)} dn_1 \cdot dn_2 \quad \text{Equation 7.20}$$

$$I_m = \int \varphi_u(n_1)^2 \cdot i_R(n_1) dn_1$$

As shown in Equation 7.20, \hat{R} and \bar{R} are the peak and the mean responses, respectively; J_{LDb} is called the joint acceptance function and it depends on the length scales of the downburst turbulence L_{Db} in the direction of the conductor; n is a local axis. For the six spanned system n is equal to -3, 0 and 3 at the far left, intermediate and far right towers, respectively. For the single spanned system, n is equal to 0 and 1 for the left and right towers, respectively; $i_R(n)$ is the influence line of the response R ; φ_u is the normalized mean velocity along the structure, where $\varphi_u = U_r(n)/U_{ref}$, and U_{ref} is the reference velocity.

It should be noted that the usage of the above expression, requires the influence line, i_R , of different responses to be known. Influence lines for transverse reactions for a single spanned system, i_{Ry1} , and for a six spanned system, i_{Ry6} , are straight forward and can be expressed by Equations 7.21 and 7.22, respectively. On the other hand, influence lines for the longitudinal reactions require further study since they do not have available expressions yet.

$$i_{Ry1} = \begin{cases} 1-n & n = 0:1 \\ 0 & \text{otherwise} \end{cases} \quad \text{Equation 7.21}$$

$$i_{Ry6} = \begin{cases} 1-|n| & n = -1:1 \\ 0 & otherwise \end{cases}$$

Equation 7.22

7.7 Conclusions

In the current study, Large Eddy Simulation (LES) of downbursts falling on various exposure conditions are performed. Ground roughness is simulated by fractal surfaces generated using the RFM and scaled to produce an aerodynamic roughness, z_0 , equals to 0.03, 0.1, 0.3 and 0.7 m corresponding to open, country side, suburban and urban exposures, respectively. Wind field resulting from simulations is decomposed into mean and turbulent components. Mean component is extracted using spatial and temporal averaging. By subtracting the mean component from the wind field, turbulent component is obtained. Results of the mean wind field show the following:

- Vertical component of the velocities appear to be minor when compared with the radial component.
- Profiles of the peak and instantaneous maximum radial velocity, obtained in the current study for open exposure, are in a good agreement with the profiles obtained from field measurements, experiments and simulations available in the literature.
- Ground roughness is found to affect the profiles of the peak velocities. It is observed that with increasing the roughness, the peak velocity decreases and the height where the peak velocity takes place increases. This observation agrees with the trends found in the literature.

Analysis of the turbulent wind field indicates that the turbulent intensity, I , decreases at locations where the mean velocities are maximum. Generally, turbulent intensity, I , at the locations of maximum mean velocities ranges between 0.08-0.12, 0.08-0.16, 0.08-0.24, 0.08-0.36 for open, country side, suburban and urban exposures, respectively. The average turbulence intensity obtained for the open exposure, $I \sim 0.10$, agrees with the turbulence intensity reported by Holmes et al. (2008) for a real event. Turbulence correlations in the wide frequency range characterized by turbulent length scales, are investigated. Turbulence length scales in the circumferential, L_θ , and the vertical, L_v , and radial direction, L_r are evaluated and the following are deduced:

- Circumferential length scale, L_θ , reaches up to 9 times the jet diameter D_j for the four studied exposures. These large length scales indicate that turbulence associated with downbursts is very well correlated circumferentially. It is observed that large values exist on wider areas for moderate rough exposures, $z_0=0.03$ and 0.1 m, than in the rough exposures, $z_0=0.3$ and 0.7 m. This emphasizes that rough terrains are more able to breakdown the correlated turbulence into a random turbulence.
- Vertical length scales ranges between $0.05-0.25D_j$, which is smaller than the circumferential length scales by an order of magnitude. This is favorable for the case of tall vertical structures compared to long horizontal structures as the fluctuating forces are less correlated. Average turbulence length scale for a typical downburst of 1000 m diameter, at locations where mean velocities are maximum, is found to be compatible with the vertical length scale for normal winds.
- Radial length scales, L_r , ranges between $0.3-0.6D_j$ in the zone where mean velocities are maximum. These represent 300-600 m radial length scales for the case of a typical downburst of 1000 m diameter, which are larger than typical longitudinal length scales for synoptic winds.

Turbulence spectra are plotted for four points, which bound the area where the peak velocities are expected, and compared with von Karman spectrum for synoptic winds. The spectra obtained at the radius $R=1.0D_j$ is close to the spectra of normal wind especially for the case of rough exposures, $z_0=0.3$ and 0.7 m. With the increase of the radius, the spectra tend to have a steeper slope than the $-2/3$ of the normal wind. This is favorable for wind sensitive structures with frequencies (0.1-1 hz) as they may not be excited by the turbulence from the downbursts. The spectra belonging to small eddies at the locations where the radius R is equal to D_j , is less for the cases of moderate rough exposure compared to rough exposures. At the larger radius, $R=1.5D_j$, however, the spectra corresponding to the small eddies becomes higher in the cases of moderate rough exposures. This indicates that rough exposures are able to breakdown the turbulence into smaller eddies in shorter distances than by moderate rough terrains.

Peak factor of the radial wind fluctuations is insensitive to the spatial location and generally ranges in between 2 to 2.2.

Turbulent correlations in the narrow frequency band characterized by the coherency decay constants are studied in the vertical and the circumferential directions. Decay constant in the vertical direction, C_w , is found to decrease with the increase in the height. The constant has a value in the order of 10 near the ground at the locations of the maximum mean velocities that is compatible with the normal winds. Decay constant in the circumferential direction, C_θ , is found to be smaller by an order of magnitude than the constant in the vertical direction. This indicates that downburst turbulence is very well correlated in the circumferential direction compared to the vertical direction, which could be unfavorable for long horizontal structures.

Downburst wind fields resulting from LESs are employed to assess the importance of including the dynamic effect while obtaining the responses of transmission line (TL) conductors and the following observations are made for the considered cases:

- For moderate rough terrains (open and countryside), the dynamic effect is low (up to 10 % for the longitudinal reaction and 6% for the transverse reaction) and may be neglected when considering the high reference wind speed (40 m/s). Under the low reference speed (20 m/s), dynamic effect is high (21 % for the longitudinal reaction) and has to be accounted for.
- For rough terrains (suburban and urban), the dynamic effect is high (up to 16 % for the longitudinal reaction for the high reference wind speed and 38% for the transverse reaction for the low reference wind speed) and has to be accounted for under both high and low reference wind speeds.
- Increasing the span length tends to decrease the contribution of the resonant component $Cont_R$ for all cases. This is because the correlation between the turbulent velocities decreases with the increase in the span length.

Finally, the applicability of using the gust front factor (GFF) approach to evaluate the peak responses of TL conductors is emphasized. It is found that the characterization of

the wind field conducted throughout this study is very useful and the resulting flow characteristics can be implemented directly in the GFF approach.

7.8 References

- Aboshosha, H., El Damatty, A., Bitsuamlak, G. 2014. LES of wind in the built-environment: Inflow and roughness induced by fractal surfaces. Paper submitted to *Wind and Structures an International Journal*. (WAS47999H)
- Alahyari, A., Longmire, E.K. 1994. Particle image velocimetry in a variable density flow: application to a dynamically evolving downburst. *Experiments in Fluids* 17, 434–440.
- Anderson, J.R., Orf, L.G., Straka, J.M., 1992. A 3-D model system for simulating thunderstorm microburst outflows. *Meteorology and Atmospheric Physics* 49, 125–131.
- Anderson W., Meneveau C., 2010. A Large-eddy simulation model for boundary-layer flow over surfaces with Horizontally resolved but vertically unresolved roughness elements. *Boundary-Layer Meteorology* 137, 397–415.
- Ansys Ltd., 2005. Ansys CFX-solver, Release 10.0: Theory. Canonsburg.
- American Society of Civil Engineers (ASCE). 2010. Guidelines for electrical transmission line structural loading. ASCE Manuals and Reports on Engineering Practice, No. 74, New York, NY, USA.
- AS/NZS1170.2. 2011. Standards Australia, Structural design actions. Part 2: Wind actions, Australian-New Zealand Standard.
- Blocken, B., Stathopoulos, T., and Carmeliet, J. 2007. CFD simulation of the atmospheric boundary layer: wall function problems. *Atmospheric Environment*, 41, 38-252.
- Chay, M.T., Albermani, F., Wilson, R. 2006. Numerical and analytical simulation of downburst wind loads. *Engineering Structures* 28, 240–254.
- Chay, M.T., Letchford, C.W., 2002. Pressure distributions on a cube in a simulated thunderstorm downburst - part a: stationary downburst observations. *Journal of Wind Engineering and Industrial Aerodynamics* 90, 711–732.

- Chay, M., and Albermani, F., 2005. Dynamic response of a SDOF system subjected to simulated downburst winds. Proc., Asia-Pacific Conf. on Wind Engineering (APCWE-VI), 1562–1584.
- Chay, M., Albermani, F., and Wilson, R. 2006. Numerical and analytical simulation of downburst wind loads. *Engineering Structures* 28(2), 240–254.
- Chen, L., and Letchford, C. W. 2004a. A deterministic-stochastic hybrid model of downbursts and its impact on a cantilevered structure. *Engineering Structures* 26(5), 619–629.
- Chen, L., and Letchford, C. W. 2004b. Parametric study on the along wind response of the CAARC building to downbursts in the time domain. *Journal of Wind Engineering and Industrial Aerodynamics* 92(9), 703–724.
- Chen, L. and Letchford, C.W. 2005. Proper orthogonal decomposition of two vertical profiles of full-scale non-stationary correlated downburst wind speeds. *Journal of Wind Engineering and Industrial Aerodynamics* 93, 187-216.
- Chen, L. and Letchford, C.W. 2006. Multi-scale lateral correlation analyses of two lateral profiles of full-scale downburst wind speeds. *Journal of Wind Engineering and Industrial Aerodynamics* 94, 675-696.
- Choi, E.C.C. and Hidayat, F.A. 2002. Dynamic response of structures to thunderstorm winds, *Prog. Struct. Eng. Mech.* 4, 408-416.
- Coccal, O., Dobre ,A., Thomas, T.G., Belcher, S.E. 2007. Structure of turbulent flow over regular arrays of cubical roughness. *J Fluid Mech* 589:375–409
- Darwish, M., Damatty, A., Hangan, H. 2010,. Dynamic characteristics of transmission line conductors and behaviour under turbulent downburst loading, *Wind and Structures, An International Journal*, 13(4), 327-346.
- Davenport, A. G. 1967. Gust loading factors. *ASCE J. Struct. Div.*, 93(3), 11–34.
- Davenport, A.G. 1993. How can we simplify and generalize wind loads?, Presented at the Third Asia-Pacific Symposium on Wind Engineering. December 13-D15. Hong-Kong, Keynote Lecture.
- El Damatty, A., Aboshosha, H. 2012. Capacity of Electrical Transmission Towers under Downburst Loading. *Proceedings of the First Australasia and South-East Asia*

- Structural Engineering and Construction Conference, Perth, Australia, Nov 28-Dec 2, 2012, 317-322.
- Engineering Sciences Data Unit (ESDU) 85020. 2001. Characteristics of atmospheric turbulence near the ground. Part II: single point data for strong winds.
- Fluent Inc. 2005. Fluent 6.2 User's Guide, Fluent Inc., Lebanon.
- Fluent 13.0. 2010. User's Guide. Fluent Inc., Lebanon.
- Franke, J., Hirsch, C., Jensen, A.G., Krüs, H.W., Schatzmann, M., Westbury, P.S., Miles, S.D., Wisse, J.A., Wright, N.G. 2004. Recommendations on the use of CFD in wind engineering. Proceedings of the International Conference on Urban Wind Engineering and Building Aerodynamics, in: van Beeck JPAJ (Ed.), COST Action C14, Impact of Wind and Storm on City Life Built Environment, von Karman Institute, Sint-Genesius-Rode, Belgium, 5 - 7 May 2004.
- Fujita, T. T. 1990. Downbursts: Meteorological features and wind field characteristics. *Journal of Wind Engineering and Industrial Aerodynamics* 36(1), 75–86.
- Fujita, T.T. 1985. The downburst microburst and macroburst. University of Chicago, Department of Geophysical Sciences 128 pp
- Fujita, T.T., Wakimoto, R.M. 1981. Five scales of airflow associated with a series of downbursts on 16 July 1981. *Monthly Weather Review* 109, 1438–1456.
- Germano, M., Piomelli, U., Moin, P., Cabot, W.H. 1991. A dynamic subgrid-scale eddy viscosity model. *Phys. Fluids A* 3 (7), 1760–1765.
- Gant, S.E. 2009. Reliability issues of LES-related approaches in an industrial context. *Flow, Turbulence and Combustion* 84, 325–335.
- Hadz'iabdic', M. 2005. LES, RANS and Combined Simulation of Impinging Flows and Heat Transfer. Ph.D Thesis. University of Sarajevo 185pp.
- Hjelmfelt, M.R. 1988. Structure and life cycle of microburst outflows observed in Colorado. *Journal of Applied Meteorology* 27, 900–927.
- Holmes, J.D. 1999. Modeling of extreme thunderstorm winds for wind loading and risk assessment, Proceedings, of the 10th International Conference on Wind Engineering, Copenhagen 1999, Balkema Press, Amsterdam 1409-1455.
- Holmes, J., Hangan, H., Schroeder, J., Letchford, C., Orwig, K. 2008. A forensic study of the Lubbock-Reese downdraft of 2002. *Wind and Structures* 11(2), 137-152.

- International Electrotechnical Commission (IEC) 60826. 2003. Design criteria of overhead transmission lines, Geneva, Switzerland.
- Jeong, J. and Hussain, F. 1995. On the identification of a vortex, *Journal of Fluid Mechanics* 285 69-94.
- Kanda M, Moriwaki R, Kasamatsu, F. 2004. Large-eddy simulation of turbulent organized structures within and above explicitly resolved cube arrays. *Boundary-Layer Meteorology* 112, 343–368.
- Katul, G.G. and Parlange, M.B. 1995. Analysis of Land Surface Heat Fluxes using the OrthonormalWavelet Approach, *Water Resource Research*, 31, 2743–2749.
- Kim, J., Hangan, H. 2007. Numerical simulations of impinging jets with application to thunderstorm downbursts. *Journal of Wind Engineering and Industrial Aerodynamics* 95, 279–298.
- Kwon, D. and Kareem, A. 2009. Gust-Front Factor: New Framework for Wind Load Effects on Structures, *Journal of Structural Engineering* 135(6), 717-732.
- Li, C.Q. 2000. A stochastic model of severe thunderstorms for transmission line design, *Probab. Eng. Mech.* 15, 359-364.
- Lundgren, T.S., Yao, J., Mansour, N.N. 1992. Microburst modelling and scaling. *Journal of Fluids Mechanics* 239, 461–488.
- Mason, M., Wood, G., Fletcher, D. 2009. Numerical simulation of downburst winds. *Journal of Wind Engineering and Industrial Aerodynamics* 97, 523–539.
- Mason, M., Fletcher, D., Wood, G. 2010a. Numerical simulation of idealized three-dimensional downburst wind fields. *Engineering Structures* 32, 3558–3570.
- Mason, M. Wood, G., Fletcher, D. 2010b. Numerical investigation of the influence of topography on simulated downburst wind fields. *Journal of Wind Engineering and Industrial Aerodynamics* 98, 21–33.
- Menter, F.R., Egorov, Y. 2005. A scale adaptive simulation model using two- equation models. In: 43rd AIAA Aerospace Sciences Meeting and Exhibit, American Institute of Aeronautics and Astronautics.
- Nakayama A, Sakio K. 2002. Simulation of flows over wavy rough boundaries. Center for Turbulence Research, Annual Research Briefs, Stanford University/NASA Amers Research Center, 313–324

- Orf, L. Kantor, E., Savory, E. 2012. Simulation of a downburst-producing thunderstorm using a very high-resolution three-dimensional cloud model. *Journal of Wind Engineering and Industrial Aerodynamics* 104–106. 547–57.
- Osegura, R.M., Bowles, R.L. 1988. A simple, analytic 3-dimensional downburst model based on boundary layer stagnation flow. NASA Technical Memorandum, 100632 National Aeronautics and Space Administration.
- Proctor, F.H. 1988. Numerical simulation of an isolated microburst. Part I: dynamics and structure. *Journal of the Atmospheric Sciences* 45, 3137–3160.
- Richards, P.J., Hoxey, R.P. 1993. Appropriate boundary conditions for computational wind engineering models using the k-e turbulence model. *Journal of Wind Engineering and Industrial Aerodynamics* 46&47, 145-153.
- Savory, E., Parke, G.A.R., Zeinoddini, M., Toy, N. and Disney, P. 2001. Modeling of tornado and microburst-induced wind loading and failure of a lattice transmission tower, *Engineering Structures*, 23(4), 365-375
- Selvam, R., Holmes, J.D. 1992. Numerical simulations of thunderstorm down-bursts. *Journal of Wind Engineering and Industrial Aerodynamics* 44, 2817–2825.
- Sengupta, A., Sarkar, P.P. 2008. Experimental measurement and numerical simulation of an impinging jet with application to thunderstorm microburst winds. *Journal of Wind Engineering and Industrial Aerodynamics* 96, 345–365.
- Shehata, A.Y., El Damatty, A.A. and Savory, E. 2005. Finite element modeling of transmission line under downburst wind loading, *Finite Elements Anal. Des.* 42(1), 71-89.
- Shehata, A. and El Damatty, A. 2008. Failure analysis of a transmission tower during a microburst. *Wind and Structures*, 11(3)193-208.
- Simiu, E., and Scanlan, R. H. 1996. *Wind effects on structures*, 3rd Ed., Wiley, New York.
- Smagorinsky, J. 1963. General circulation experiments with the primitive equations, i. the basic experiment. *Monthly Weather Review* 91, 99-164.
- Solari, G. 1993a. Gust buffeting. I: Peak wind velocity and equivalent pressure. *Journal of Structural Engineering* 119(2), 365–382.

- Solari, G. 1993b. Gust buffeting. II: Dynamic along-wind response. *Journal of Structural Engineering* 119(2), 383–397.
- Standards Australia Limited / Standards New Zealand AS/NZS:7000. 2010. Overhead line design - Detailed procedures, Standard Australia, North Sydney, Australia.
- Teske, M.E., Lewellen, W.S. 1977. Turbulent transport model of a thunderstorm gust front. In: *Proceedings of the 10th Conference on Severe Local Storms*, American Meteorological Society, Omaha.
- Vermeire, B., Orf, L. Savory, E. 2011a. Improved modelling of downburst outflows for wind engineering applications using a cooling source approach. *Journal of Wind Engineering and Industrial Aerodynamics* 99, 801–814
- Vermeire, B., Orf, L. Savory, E. 2011b. A parametric study of downburst line near-surface outflows. *Journal of Wind Engineering and Industrial Aerodynamics* 99, 226–238
- Vicroy, D. 1992. Assessment of microburst models for downdraft estimation. *J. Aircr.*, 29(6), 1043–1048.
- Wilson, J.W., Roberts, R.D., Kessinger, C., McCarthy, J. 1984. Microburst wind structure and evaluation of Doppler radar for airport wind shear detection. *Journal of Climate and Applied Meteorology* 23, 898–915.
- Whittingham, H. 1964. Extreme Wind Gust in Australia. Bureau of Meteorology (Melbourne), Department of Science, Bulletin 46.
- Wood, G.S, Kwok, K.C.S., Motteram, N.A., Fletcher, D.F. 2001. Physical and numerical modelling of thunderstorm downbursts. *Journal of Wind Engineering and Industrial Aerodynamics* 89, 535–552.
- Xie Z., Coceal O, Castro I.P. 2008. Large-eddy simulation of flows over random urban-like obstacles. *Boundary-Layer Meteorology* 129, 1–23.
- Yao, J., Lundgren, T.S. 1996. Experimental investigation of microbursts. *Experiments in Fluids* 21, 17–25.
- Zhou, Y., and Kareem, A. 2001 . Gust loading factor: New model. *Journal of Structural Engineering*, 127(2), 168–175.

Chapter 8

8 Conclusions and Recommendations

The current thesis investigates the behaviour of TL conductors under downburst wind considering various terrain exposures. The study is motivated by the lack of information about (i) the response of TL conductors under downburst wind, (ii) the wind field of downburst events happening over different terrain exposures typically encountered by TLs. The research conducted in this thesis involves the following phases:

1. Development and validation of an effective numerical technique to calculate the reactions of a multi-spanned transmission line conductor system under loads generated by High Intensity Wind (HIW) events in the form of tornadoes and downbursts. The technique is based on a semi-closed form solution for obtaining the displacements and the reactions at the ends of each conductor span.
2. Derivation and validation of a closed-form solution, suitable for structural practitioner engineers, to calculate the reactions of a multi-spanned transmission line conductor subjected to downbursts loads. This closed-form solution is derived for two cases: (i) downburst with arbitrary size and relative location to the tower of interest (ii) downburst with critical size and location causing maximum transmitted forces from the conductor to the tower of interest.
3. Derivation and validation of a new analytical expression for the conductor aerodynamic damping under downburst wind accounting for the localized nature of the downburst represented in the event size and its relative location to the conductor.
4. Assessment of the dynamic response of single and multiple spanned TL conductor systems subjected to fluctuating downburst and synoptic wind fields corresponding to open terrain exposure. Two critical downburst configurations, recommended in the literature and expected to cause the maximum conductor reactions, are considered in the study.
5. Development and validation of a new model to simulate terrain roughness using Large Eddy Simulation (LES) based on the usage of fractal surfaces. This new

model does not have the maximum roughness constraint that exists in the commonly used wall functions for simulating terrain roughness.

6. Characterization of the turbulence associated with the downbursts falling over various terrain exposures typically encountered by TLs. The roughness model developed in phase (5) is utilized to simulate the terrain roughness. This is followed by dynamic analyses of the conductor systems similar to the conducted analyses in phase (4) for open terrain exposure while covering other exposures.

The general conclusions obtained from the six conducted phases are presented below.

8.1.1 Effective Technique to Analyze Transmission Line Conductors under High Intensity Winds

In this chapter, an effective numerical technique to evaluate the reactions of a multi-spanned transmission line conductor system under loads varying along the spans such as those induced by HIW is developed. A semi-closed form solution to obtain the displacements and reactions at the ends of each conductor span is derived. The derivation of the semi-closed form solution led to a system of non-linear equations. A numerical scheme is proposed to solve these simultaneous non-linear equations. The technique is employed to analyze two TL conductors subjected to downburst and tornado load cases. In order to assess the accuracy of the technique, Finite Element Analysis (FEA) is conducted for the same conductors under the same loads. The responses calculated from the proposed technique and those obtained from the FEA are compared and the following observations are noticed:

- Reactions and displacements calculated using the new technique show good agreement with the FEA. The maximum difference in the displacements between the two methods is 4% and 5% for downburst and tornado cases, respectively. For the reactions, the maximum difference is found to be 5% for downbursts and 6% for tornadoes.
- The new technique shows a significant reduction in the computational time compared to FEA. The new technique is 185 times faster than the FEA, for the considered cases. Analysis of transmission lines under HIW requires conducting a large number of analyses to capture the critical sizes and locations of these

localized events. Consequently, a reduction in the computational time for each analysis becomes very important for such applications.

8.1.2 A Closed Form Solution for the Reactions of a Transmission Line Conductor under Downburst Winds

A closed form solution to evaluate the reactions of a transmission line conductor subjected to downburst loads is derived. A simplified multi-spanned conductor-insulator system is considered in the derivation where the supporting insulators to the right and the left of the tower of interest are modeled using a combination of roller supports and linear springs. The considered system accounts for the coupling effect between adjacent spans while reducing the system complexity. The solution is derived to cover two cases: (1) downburst with arbitrary size and relative location to the tower of interest (2) downburst size and location responsible for inducing the peak longitudinal reaction and previously recommended for the line design. Accuracy of the derived solution is assessed by comparing its results with those obtained from Finite Element Analysis (FEA). Both the derived solution and the FEA are employed to analyze thirty two cases of downburst with a generic size and location, and eighteen cases of downbursts that produce maximum longitudinal reactions. Based on the results of these analyses, the following conclusions are made:

- A reasonable accuracy of the model is found when compared with FEA results. A maximum difference in longitudinal reactions is found to be in the order of 15% while for transverse reactions the difference is in the order of 7%.
- The derived solution is substantially easy to obtain the reactions of the conductors under downbursts. The proposed closed form solution is considered as a novel technique that can directly be used to obtain maximum longitudinal reactions for downbursts. This expression can be of a significant importance for line designers.

8.1.3 Aerodynamic Damping of Transmission Line Conductors under Downburst Winds

A new analytical expression for the aerodynamic damping of transmission line conductors subjected to downburst winds is developed. The expression accounts for the changes in the conductor's frequencies due to the changes of the downburst mean

velocities with the time. Also the expression accounts for the localized effect of the downburst, represented by the event size and its relative location to the conductor. The developed expression is validated using a CFD technique that is able to obtain the conductor wind induced response. The accuracy of this CFD technique to predict the Fluid Structure Interaction (FSI) between the incoming wind and the conductor is first validated. Then, the technique is used to obtain the conductor response under the effect of downburst winds. The conductor response is compared with that obtained from dynamic analysis, using Newmark's method, where the damping is evaluated by the proposed analytical expression. An excellent agreement between the responses obtained from CFD and dynamic analysis employing the proposed damping expression is found. The results of this comparison indicate the capability of the proposed expression to accurately estimate the aerodynamic damping under downburst winds.

8.1.4 Assessment of Dynamic Effects for Transmission Line Conductors under Downburst and Synoptic Winds

Dynamic analyses of single-spanned and multiple-spanned conductor systems are performed to assess the need of conducting dynamic analysis. The study includes twelve different cases by varying the wind type, the mean wind velocity and the span length. Downburst and synoptic winds corresponding to open terrain exposure are used as different types of wind loading. Two downburst loading scenarios leading to maximum longitudinal conductor reaction, D_{bx} , and maximum transverse conductor reaction, D_{by} , are considered. Two mean wind velocities, ($V_{ref} = 20$ and 40 m/s) and two span lengths, ($L_x = 300$ and 500 m) are used in the analyses. A number of 6 spans (three on each side to the tower of interest) are used in the study to model the multiple-spanned system based on a recommendation given in the literature. Analysis of the two systems is conducted to obtain longitudinal and transverse reactions at the intermediate tower of the multiple-spanned system and at the left tower for the single spanned system. Analysis of the conductor systems is conducted using the following three steps in order to distinguish between mean, background and resonant components of the responses: (i) non-linear quasi-static analyses under running-mean wind velocities are conducted to obtain the conductor time dependent mean responses and stiffness. Time-dependent stiffness is

calculated from conductor tension forces and deformed profile. (ii) linear dynamic analysis is then conducted under fluctuating wind forces using the updated conductor stiffness. Fluctuating responses resulting from the dynamic analysis contain both background and resonant components. (iii) quasi-static analysis is conducted under fluctuating wind forces to obtain the background component, which is subtracted from the overall fluctuating responses to get the resonant component. The ratio between the peak responses to the maximum mean responses, defined as the Gust Factor (GF), is evaluated using both the dynamic analysis, GF_{Dy} , and the quasi static analysis, GF_{QS} . The contribution of different components to the peak response is evaluated and the following conclusions are drawn from the results:

- Peak transverse reactions for the single-spanned system, R_{y1p} , and the six-spanned system, R_{y6p} , are found to be equal to 70%, 125% of the force $g_{yp} \cdot L_x$. This force, $g_{yp} \cdot L_x$, represents the maximum mean transverse force acting on the towers assuming a uniform distribution of the wind load. The peak longitudinal reaction for the single spanned system, R_{x1p} , and the six spanned system, R_{x6p} , are found to be equal to 390% and 45 % of the force $g_{yp} \cdot L_x$, respectively. As indicated from the values, the developed longitudinal reactions in the two systems are significant and accordingly are recommended to be included in the line design.
- The contribution of the resonant component, $Cont_R$, to the peak longitudinal reaction R_{x1} for the single-spanned system reaches a maximum value of 16% for downburst and synoptic wind cases when considering the low reference velocity (20 m/s). Under the high reference velocity (40 m/s), the contribution $Cont_R$, reaches a maximum value of 5% for both downburst and synoptic wind cases. These results indicate that dynamic analysis may be not neglected under high velocities but is recommended for the line desing under low velocities due to both downbursts and synoptic winds.
- The maximum contribution to the peak transverse reaction R_{y6} and to the peak longitudinal reaction R_{x6} for the six-spanned system is found in the order of 5% and 6%, respectively, for both downburst and synoptic wind cases. These low contributions imply that conducting dynamic analysis may not be necessary for estimating the peak reactions for the six-spanned system.

- Gust factors of both the longitudinal and the transverse reaction for the single-spanned system are shown to be larger than those for the six-spanned system. This is because correlated fluctuations characterized by the length scale, L_{uv} , cover a higher percentage of the conductor length for the single-spanned system than that for the six-spanned system.

8.1.5 LES of Wind in the Built-Environment: Inflow and Roughness Induced by Fractal Surfaces

In this chapter, the limitation on the maximum terrain roughness that can be simulated using Large Eddy Simulation (LES) is discussed. This limitation is found to be very influential for the cases of moderately rough to rough surfaces typically encountered by TLs. For such cases, this limitation acts as an obstacle for obtaining the turbulent characteristics of downbursts using LES, which are essential to evaluate the peak downburst loads. Therefore, in this chapter, a modification is applied to an existing model, called the surface gradient drag-based (SGD) developed by Anderson and Meneveau (2010), to relax the constraint of the maximum roughness that can be modeled. This is enabled by applying the drag forces on multiple grid layers above the ground. The modified model is used to simulate synthesized fractal surfaces representing three terrain exposures named countryside, suburban and urban. Large eddy simulations of the boundary layers formed above the synthesized surfaces are conducted and the following observations are made:

- The resulting mean wind profile for the generated surfaces perfectly matches the targeted logarithmic profile in the region of the constant shear stress. The average error between the resulting profiles from the CFD and the targeted profiles is found to be equal to -0.3, -0.5 and 0.2 % for z_0 equals to 0.1, 0.3 and 0.7 m, respectively.
- Root mean square of the longitudinal fluctuations resulting from the CFD appears to be underestimated with an average ratio of 10%. This underestimation is due to the filtration of the small scale turbulence that is smaller than the average distance between the roughness elements l_{xy} . This observation is made by comparing the

longitudinal velocity spectra from the CFD with those from the literature. This comparison showed that the two spectra are well matched up to a cut off frequency, f_{cut} , which is equal to $u_m(z)/l_{xy}$. For the cases where small scales are required, a finer grid can be used in the longitudinal direction which will result in roughness elements with smaller width, l_{xy} .

- The results indicate the applicability of using fractal surfaces with the modified SGD model to simulate terrain roughness for moderate rough to rough terrains typically encountered by TLLs.

8.1.6 Turbulence Characterization of Stationary Downbursts using LES

Large Eddy Simulations (LES) of downbursts acting on different terrain conditions are performed. Terrain roughness is simulated by fractal surfaces generated using the Random Fourier Modes (RFM) and scaled to have an aerodynamic roughness, z_0 , that is equal to 0.03, 0.1, 0.3 and 0.7 m. These values correspond to open, country side, suburban and urban terrain conditions, respectively, according to the Engineering Sciences Data Unit 85020: (2001). Drag forces due to the fractal surfaces are introduced into the governing flow equations using the modified surface gradient drag SGD model proposed in Chapter 6. The wind field resulting from the simulations is decomposed into mean and turbulent components. The former is extracted using a spatial and a temporal averaging, while the later is obtained by subtracting the mean component from the overall wind field. By analyzing the resulting mean component, the following conclusions are deduced:

- The vertical mean component of the velocities appears to be minor when compared with the radial component near the ground.
- Profiles of the peak and instantaneous maximum radial velocity, obtained in the current study for the open terrain condition, are in a good agreement with the profiles obtained from field measurements, experiments and simulations in the literature.
- Terrain roughness affects the profiles of the peak maximum velocity. By increasing the aerodynamic roughness z_0 , the peak maximum velocity decreases

and the height where the peak takes place increases, which agrees with the findings reported in the literature.

Analysis of the turbulent wind field indicates that the turbulent Intensity, I , decreases at locations where mean velocities are maximum. Generally, turbulent intensity, I , at these locations lies in the range of 0.08-0.12, 0.08-0.16, 0.08-0.24, 0.08-0.36 for open, countryside, suburban and urban terrains, respectively. This indicates that the turbulence intensity increases with the increase of roughness. The average intensity found for the open terrain condition, $I \sim 0.10$, agrees with the intensity reported in the literature for a real event. Turbulent correlations in the wide frequency range, characterized by the turbulent length scales, are studied and the following observations are noticed:

- Circumferential length scale, L_{θ} , reaches up to 9 times the jet diameter, D_j , for the four studied terrains. This high value indicates that turbulence associated with downbursts is well correlated circumferentially. It is also found that high values exist on further distances measured from the event centre for moderate rough terrains (open and countryside) than for rough terrains (open and countryside). This emphasizes that rough terrains have the nature of breaking down the correlated turbulence into a random turbulence.
- Vertical length scales lie within the range of 0.05-0.25 D_j , which is smaller than circumferential length scales by an order of magnitude. This is favorable for the case of tall structures compared to long horizontal structures as the fluctuating forces are less correlated. Average turbulent length scale for a typical downburst of 1000 m diameter, at locations where mean velocities are maximum, is found to be compatible with the vertical length scale for normal winds.
- Radial length scales, L_r , are found to be in the range of 0.3-0.6 D_j in the zone where mean velocities are maximum. These represent 300-600 m radial length scales for the case of a typical downburst of 1000 m diameter, which are greater than the longitudinal length scales for synoptic winds.
- Turbulence spectra are plotted for four points, which bind the area where the peak velocities are expected. They are then compared with Von karman spectrum for synoptic winds. The spectra obtained at a radius $R=1.0 D_j$ is noticed to be close to

the spectra of normal wind especially for the case of rough terrains, $z_0=0.3$ and 0.7 m. With the increase of the radius, the spectra tend to have a steeper slope than $-2/3$ of the normal wind. This is favorable for wind sensitive structures with frequencies ($0.1-1$ Hz) as they might not be excited by turbulence from downbursts as by those from synoptic wind. The spectra which belong to small eddies at the points where the radius R equals to $1.0 D_j$, is less for the case of moderate rough terrains compared to the spectra for the case of rough terrains. On the other hand, at a large radius, $R=1.5 D_j$, the spectra corresponding to small eddies become higher in the case of smooth terrains. This indicates that rough terrains are able to breakdown the turbulence into small eddies in shorter distances compared to smooth terrains.

- Peak factors of the radial wind fluctuations are evaluated statistically. It is found that the peak factors are insensitive to the spatial location and generally lies within the range of 2-2.2.
- Turbulent correlations in the narrow frequency band characterized by the coherency decay constants are studied in the vertical and circumferential directions. A decay constant in the vertical direction, C_w , is found to be decreasing with the increase in the height. The constant has a value in the order of 10 near the ground at locations of maximum mean velocities, which is compatible with normal winds. Another decay constant in the circumferential direction, C_θ , is found to be smaller by an order of magnitude than the constant in the vertical direction. This indicates that downburst turbulence is significantly more correlated in the circumferential direction than in the vertical direction, which could be unfavorable for long horizontal structures.

Downburst wind fields resulting from the current LES are employed to investigate the dynamic behavior of TL conductors. The single-spanned and multiple-spanned conductor systems, previously investigated in Chapter 5 under open terrain exposure, are considered for further assessment under other exposures. The study is conducted for eight cases that cover two downburst scenarios: (i) four cases of downburst winds that cause maximum longitudinal reactions (ii) four cases of downburst winds that cause maximum transverse

reactions. Each four cases covers two conductor spans (300 and 500 m) and two reference velocities (40 and 20 m/s). Responses of the conductor systems are obtained using the approach previously utilized in Chapter 5 to distinguish between the mean, background and resonant components. By investigating the contribution of the resonant component, $Cont_R$, to the peak responses the following conclusions can be withdrawn:

- For moderate rough terrains (open and countryside), dynamic effect is low (up to 10 % for the longitudinal reaction and 6% for the transverse reaction) and may be neglected when considering the high reference wind velocity (40 m/s). Under the low reference velocity (20 m/s), dynamic effect is high (21 % for the longitudinal reaction) and has to be accounted for.
- For rough terrains (suburban and urban), the dynamic effect is high (up to 16 % for the longitudinal reaction for the high reference wind velocity and 38% for the transverse reaction for the low reference wind velocity) and has to be accounted for under both high and low reference wind velocity.
- For all terrains, increasing the span length tends to decrease the contribution of the resonant component $Cont_R$. This is because the correlation between the turbulent velocities decreases with the increase in the span length.

The obtained turbulent characteristics coupled with the gust front factor (GFF) approach is applicable to evaluate the peak responses of TL conductors.

8.2 Recommendation for Future Research

The current thesis discusses several topics related to the static and dynamic response of transmission lines due to downburst winds occurring over various terrain exposures. For future research, the following investigations are suggested:

- Check the uncertainty of the employed CFD models in comparison with physical experiments such as the newly constructed WindEEE dome.
- Reassess the dynamic effect on the peak transmission line conductor reactions using downburst turbulence generated by the newly immersing techniques such as wavelet transform and the usage of evolutionary spectra. These techniques can be

used instead of the method adopted in the present study and described by Chen and Letchford (2004) and Chay *et al.* (2006).

- Estimate the Gust Front Factor (GFF) by employing the turbulent characteristics of downburst happening over different terrain conditions. This allows for calculating peak design loads under downburst.
- Expand the study conducted in Chapter 7 on the turbulence characterization to include tornadoes.
- Expand the closed form solution developed in Chapter 3 to account for tornado loading.
- Propose new formulations for the GFF under tornado loading for both conductors and towers.
- Study the downburst wind field including the turbulent characteristics for different topographies including hills and escarpments for both downbursts and tornadoes.
- Propose topography multipliers for the design loads resulting from downbursts and tornadoes to account for the topography effects similar to the multipliers commonly used for synoptic winds.

Appendix A: Parameters of the Numerical Technique Used to Analyze TL Conductors under HIW

Definition for the reaction vectors $\{R_y^F\}$ and $\{R_z^F\}$ and for the matrix $[K]_{NdxNd}$

$$\{R_y^F\} = \left\{ \begin{array}{c} \frac{M_{zgyA1}}{L_x} \\ \frac{M_{zgyB1} + M_{zgyA2}}{L_x} \\ \frac{M_{zgyB2} + M_{zgyA3}}{L_x} \\ \vdots \\ \frac{M_{zgyB Nd-2} + M_{zgyA Nd-1}}{L_x} \\ \frac{M_{zgyB Nd-1}}{L_x} \end{array} \right\}, \quad \{R_z^F\} = \left\{ \begin{array}{c} \frac{M_{ygzA1}}{L_x} \\ \frac{M_{ygzB1} + M_{ygzA2}}{L_x} \\ \frac{M_{ygzB2} + M_{ygzA3}}{L_x} \\ \vdots \\ \frac{M_{ygzB Nd-2} + M_{ygzA Nd-1}}{L_x} \\ \frac{M_{ygzB Nd-1}}{L_x} \end{array} \right\}$$

$$[K]_{NdxNd} = \begin{bmatrix} \frac{R_{x1}}{L_x} & -\frac{R_{x1}}{L_x} & 0 & 0 & \dots & 0 \\ -\frac{R_{x1}}{L_x} & \frac{R_{x1}}{L_x} + \frac{R_{x2}}{L_x} & -\frac{R_{x2}}{L_x} & 0 & \dots & 0 \\ 0 & -\frac{R_{x2}}{L_x} & \frac{R_{x2}}{L_x} + \frac{R_{x3}}{L_x} & -\frac{R_{x3}}{L_x} & \dots & 0 \\ \vdots & \vdots & \vdots & \vdots & \ddots & \vdots \\ 0 & 0 & 0 & -\frac{R_{xNd-2}}{L_x} & \frac{R_{xNd-2}}{L_x} + \frac{R_{xNd-1}}{L_x} & -\frac{R_{xNd-1}}{L_x} \\ 0 & 0 & 0 & 0 & -\frac{R_{xNd-1}}{L_x} & \frac{R_{xNd-1}}{L_x} \end{bmatrix}$$

Where:

M_{igK} : The first order moment around i axis at point K induced by a loading $g_j(s)$

L_x : Span Length

Definition for the unbalanced load vector, $\{f_x\}_{Ndx1}$, and the tangential stiffness matrix, $[K_x]_{NdxNd}$, in x-direction

$$\{f_x\}_{Ndx1} = \left\{ \begin{array}{c} R_{x1} - d_{x1} \frac{R_{res1}}{V} \\ R_{x2} - R_{x1} - d_{x2} \frac{R_{res2}}{V} \\ \vdots \\ R_{xNd-1} - R_{xNd-2} - d_{xNd-1} \frac{R_{resNd-1}}{V} \\ R_{xNd-1} - d_{xNd} \frac{R_{resNd}}{V} \end{array} \right\}$$

$$[K_x]_{NdxNd} = \left[\begin{array}{cccccc} \frac{R_{res1}}{V} + C_1 & -C_1 & 0 & 0 & \dots & 0 \\ -C_1 & C_1 + \frac{R_{res2}}{V} + C_2 & -C_2 & 0 & \dots & 0 \\ 0 & -C_2 & C_2 + \frac{R_{res3}}{V} + C_3 & -C_3 & \dots & 0 \\ \vdots & \vdots & \vdots & \ddots & \vdots & \vdots \\ 0 & 0 & \dots & -C_{Nd-2} & C_{Nd-2} + \frac{R_{resNd-1}}{V} + C_{Nd-1} & -C_{Nd-1} \\ 0 & 0 & \dots & 0 & -C_{Nd-1} & C_{Nd-1} + \frac{R_{resNd}}{V} \end{array} \right]$$

Where

$$C_n = \frac{L_0 \cdot b_n \cdot a_n}{2(L_x + dx_{N+1} - dx_N)^2 \cdot \left(\frac{L_0 \cdot b_n}{L_x + dx_{N+1} - dx_N} - 1\right)^{3/2}}$$

Appendix B: Parameters of the Numerical Technique Used to Analyze TL Conductors under Downburst Wind

Definition for the reaction vectors $\{R_y^F\}$ and $\{R_z^F\}$ and for the matrix $[K_{yz}]$

$$\{R_y^F\} = \left\{ \frac{M_{gyA1}}{L_x} \quad \frac{M_{gyB1} + M_{gyA2}}{L_x} \quad \frac{M_{gyB2} + M_{gyA3}}{L_x} \quad \dots \quad \frac{M_{gyB Nd-2} + M_{gyA Nd-1}}{L_x} \quad \frac{M_{gyB Nd-1}}{L_x} \right\}^T,$$

$$\{R_z^F\} = W.L_x \left\{ \frac{1}{2} \quad 1 \quad 1 \quad \dots \quad 1 \quad \frac{1}{2} \right\}^T$$

$$[K_{yz}] = \begin{bmatrix} \frac{T_1}{L_x} & -\frac{T_1}{L_x} & 0 & 0 & \dots & 0 \\ -\frac{T_1}{L_x} & \frac{T_1}{L_x} + \frac{T_2}{L_x} & -\frac{T_2}{L_x} & 0 & \dots & 0 \\ 0 & -\frac{T_2}{L_x} & \frac{T_2}{L_x} + \frac{T_3}{L_x} & -\frac{T_3}{L_x} & \dots & 0 \\ \vdots & \vdots & \vdots & \vdots & \ddots & \vdots \\ 0 & 0 & 0 & -\frac{T_{Nd-2}}{L_x} & \frac{T_{Nd-2}}{L_x} + \frac{T_{Nd-1}}{L_x} & -\frac{T_{Nd-1}}{L_x} \\ 0 & 0 & 0 & 0 & -\frac{T_{Nd-1}}{L_x} & \frac{T_{Nd-1}}{L_x} \end{bmatrix}$$

where M_{gyAj}, M_{gyBj} is the moment at the left and right ends of span no. j due to the applied load g_y ; N_d is the number of conductor-insulator connections; T_j is the tension force is span j; L_x is the span length.

Definition for the unbalanced load vector, $\{f_x\}_{Nd \times 1}$, and the tangential stiffness matrix,

$[K_x]_{Nd \times Nd}$, in x-direction

Definition for the unbalanced load vector, $\{f_x\}_{Nd \times 1}$, and the tangential stiffness matrix, $[K_x]_{Nd \times Nd}$, in x-direction

$$\{f_x\}_{Nd \times 1} = \left\{ \begin{array}{c} T_1 - d_{x1} \frac{R_{res1}}{V} \\ T_2 - T_1 - d_{x2} \frac{R_{res2}}{V} \\ \vdots \\ T_{Nd-1} - T_{Nd-2} - d_{xNd-1} \frac{R_{resNd-1}}{V} \\ T_{Nd-1} - d_{xNd} \frac{R_{resNd}}{V} \end{array} \right\}$$

$$[K_x] = \begin{bmatrix} \frac{R_{res1}}{V} + C_1 & -C_1 & 0 & 0 & \dots & 0 \\ -C_1 & C_1 + \frac{R_{res2}}{V} + C_2 & -C_2 & 0 & \dots & 0 \\ 0 & -C_2 & C_2 + \frac{R_{res3}}{V} + C_3 & -C_3 & \dots & 0 \\ \vdots & \vdots & \vdots & \ddots & \vdots & \vdots \\ 0 & 0 & \dots & -C_{Nd-2} & C_{Nd-2} + \frac{R_{resNd-1}}{V} + C_{Nd-1} & -C_{Nd-1} \\ 0 & 0 & \dots & 0 & -C_{Nd-1} & C_{Nd-1} + \frac{R_{resNd}}{V} \end{bmatrix}$$

where C_n is defined below; V : insulator length; d_{xJ} is the x-displacement at node no. J ; R_{resJ} is the resultant force in the insulator no J ; L_0 is the conductor length that is calculated as $L_0 = L_x \cdot (1 + 8/3 \cdot (\text{sag}/L_x)^2)$; Q_{yn} is the shear force in span n due to the downburst load; d_{yN} is the y-displacement at node N .

$$C_n = \frac{L_0 \cdot \frac{1}{\sqrt{2}} \sqrt{\int_0^1 Q_{yn}(s)^* ds + \frac{W^2 L_x^2}{12} + 2 \cdot \frac{T_n}{L_x} \left((dy_{N+1} - dy_N) \int_0^1 Q_{yn}(s)^* ds \right)}}{2(L_x + dx_{N+1} - dx_N)^2 \cdot \left(\frac{L_0}{L_x + dx_{N+1} - dx_N} - 1 \right)^{3/2}}$$

Appendix C: Figures for the reaction time responses

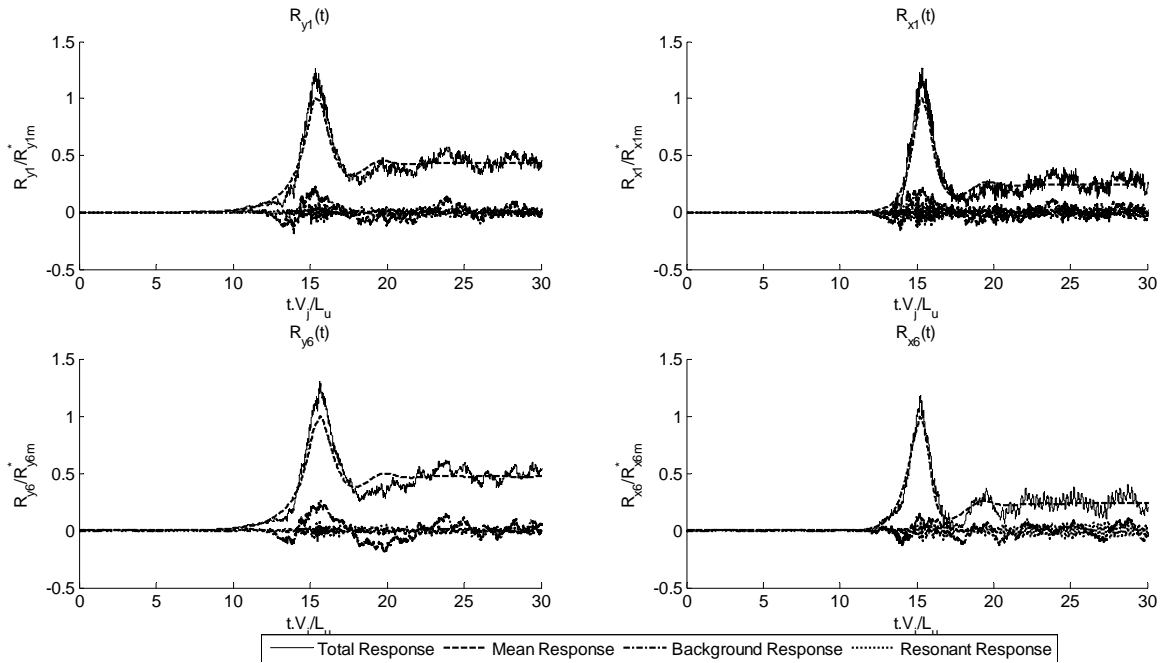


Figure C1 Reaction Responses for Case 1 ($Db_x, L_x=300$ m, $V_{ref}=40$ m/s)

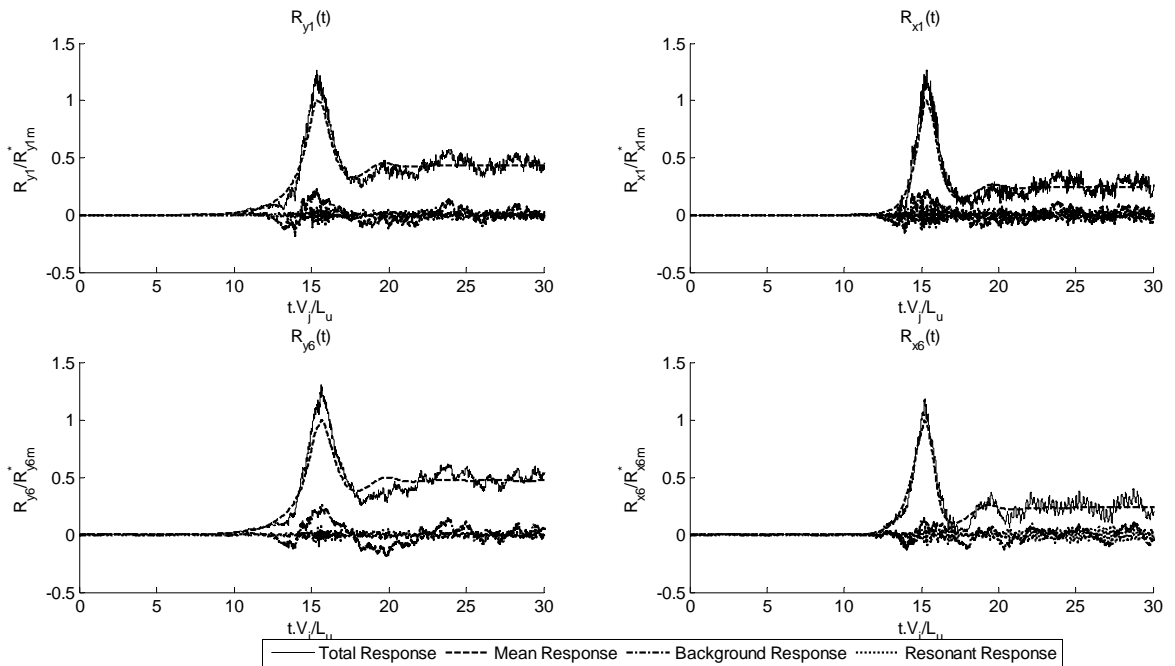


Figure C2 Reaction Responses for Case 2 (Dbx, Lx=300 m, Vref= 20 m/s)

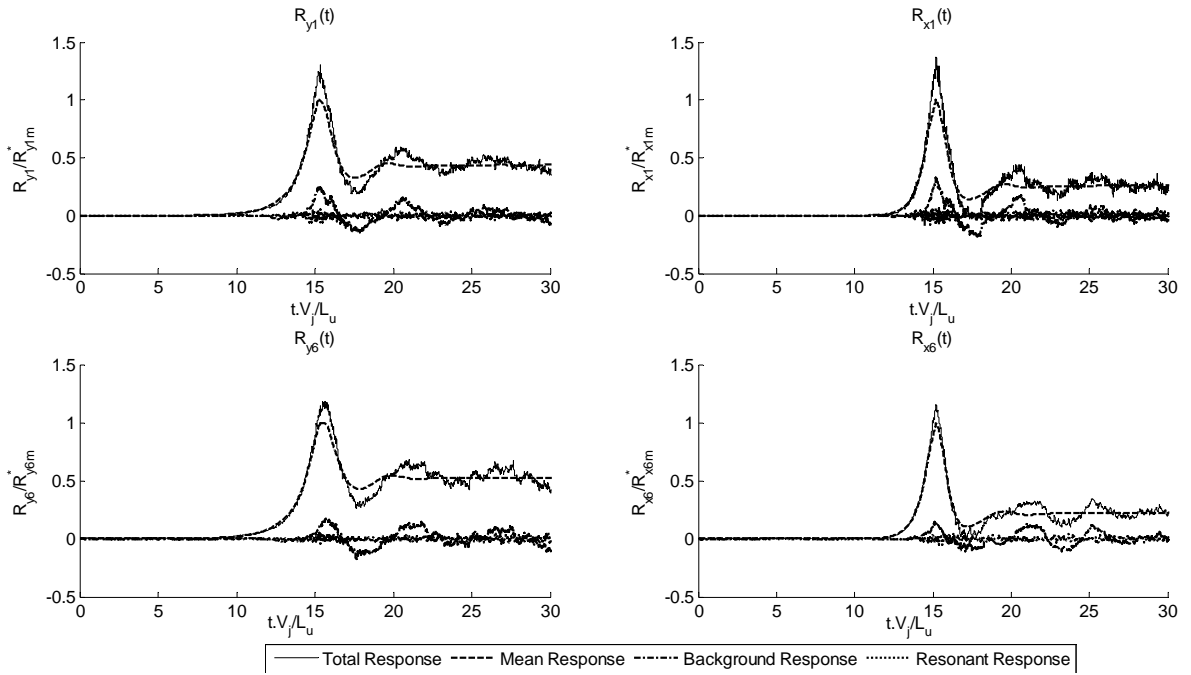


Figure C3 Reaction Responses for Case 3 (Dbx, Lx=500 m, Vref= 40 m/s)

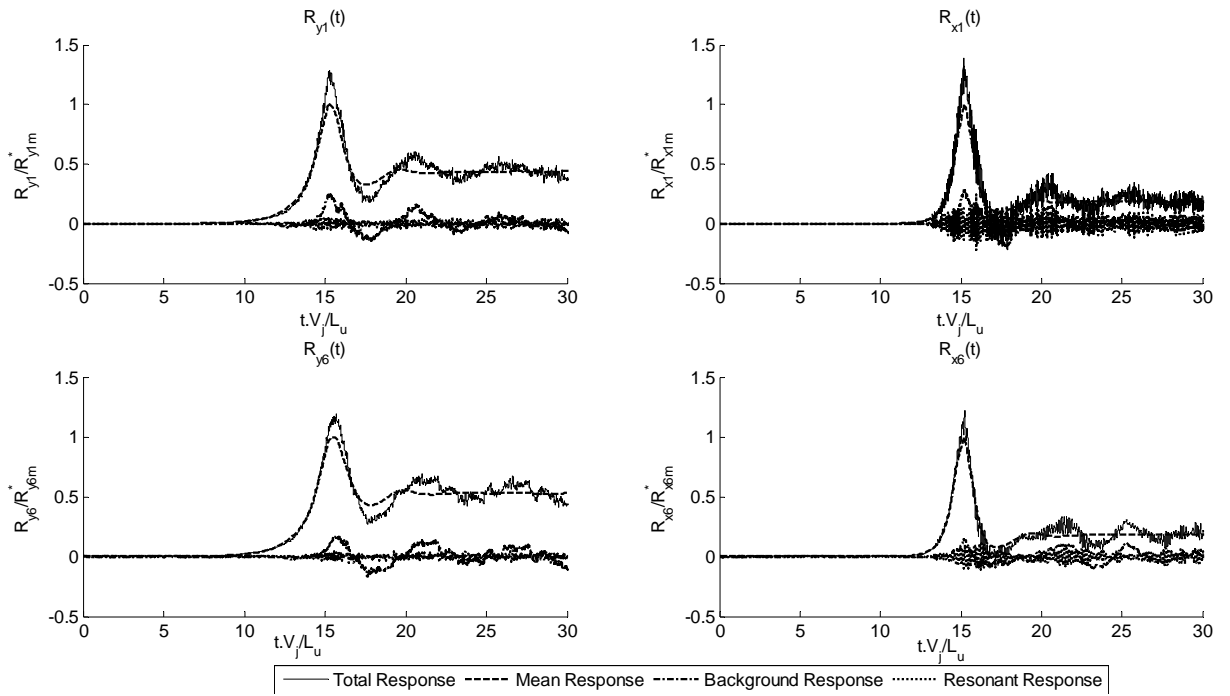


Figure C4 Reaction Responses for Case 4 (Db_x, L_x=500 m, V_{ref}= 20 m/s)

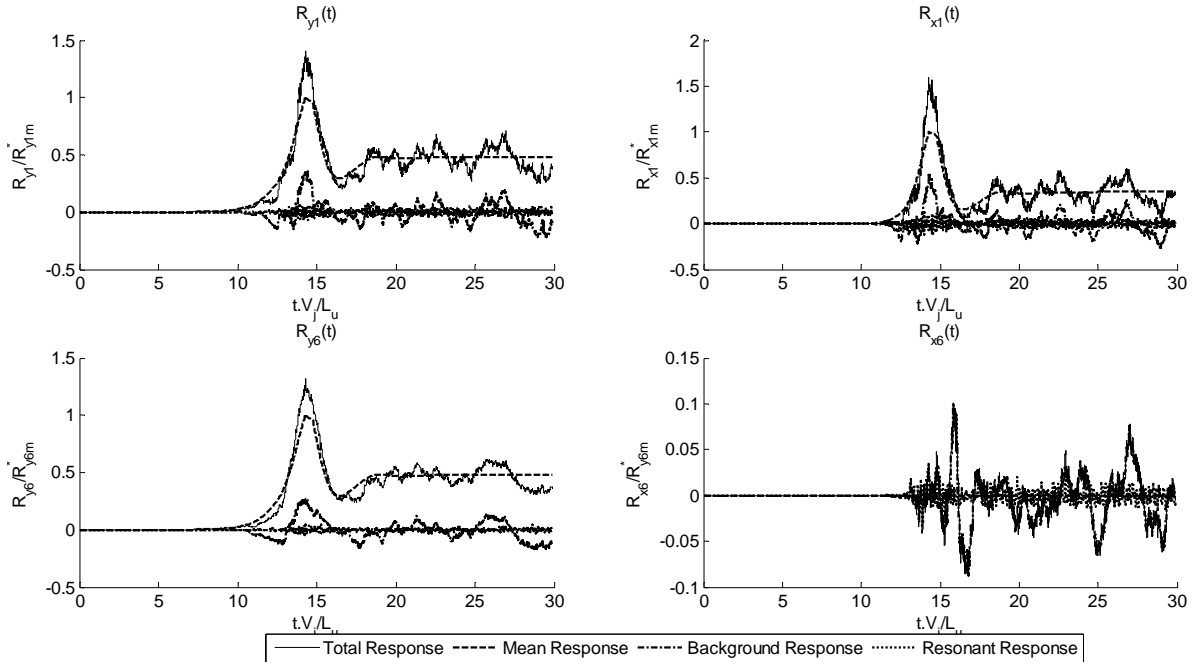


Figure C5 Reaction Responses for Case 5 (Db_y, L_x=300 m, V_{ref}= 40 m/s)

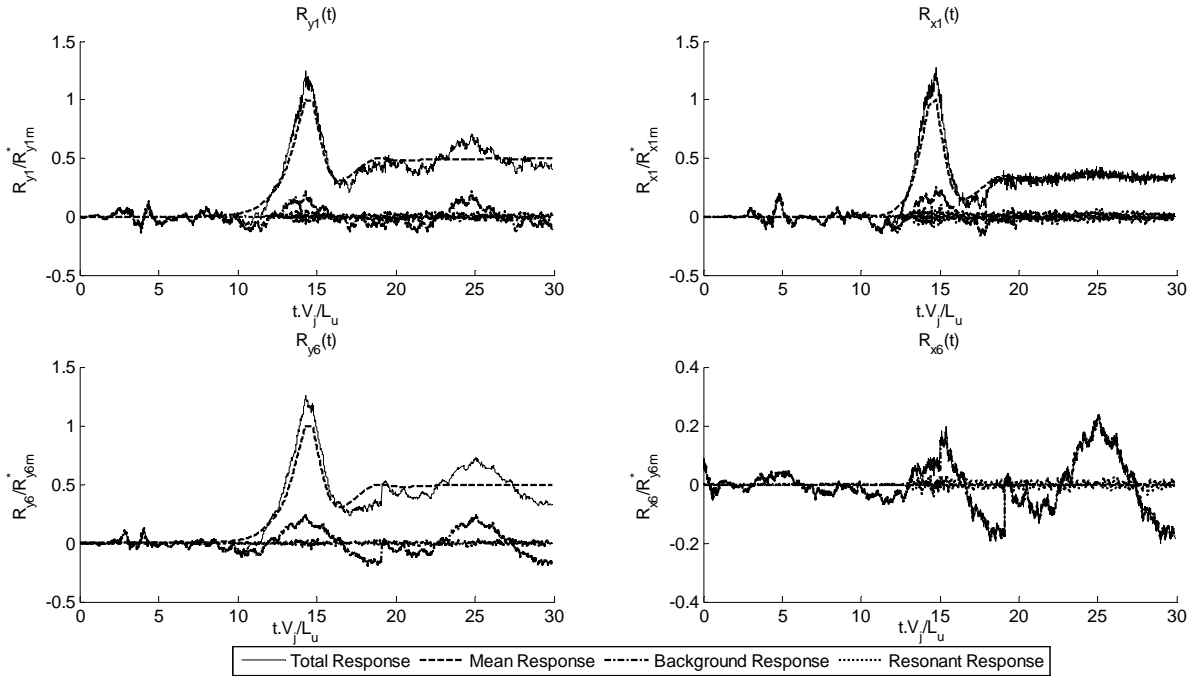


Figure C6 Reaction Responses for Case 6 (Db_y, L_x=300 m, V_{ref}= 20 m/s)

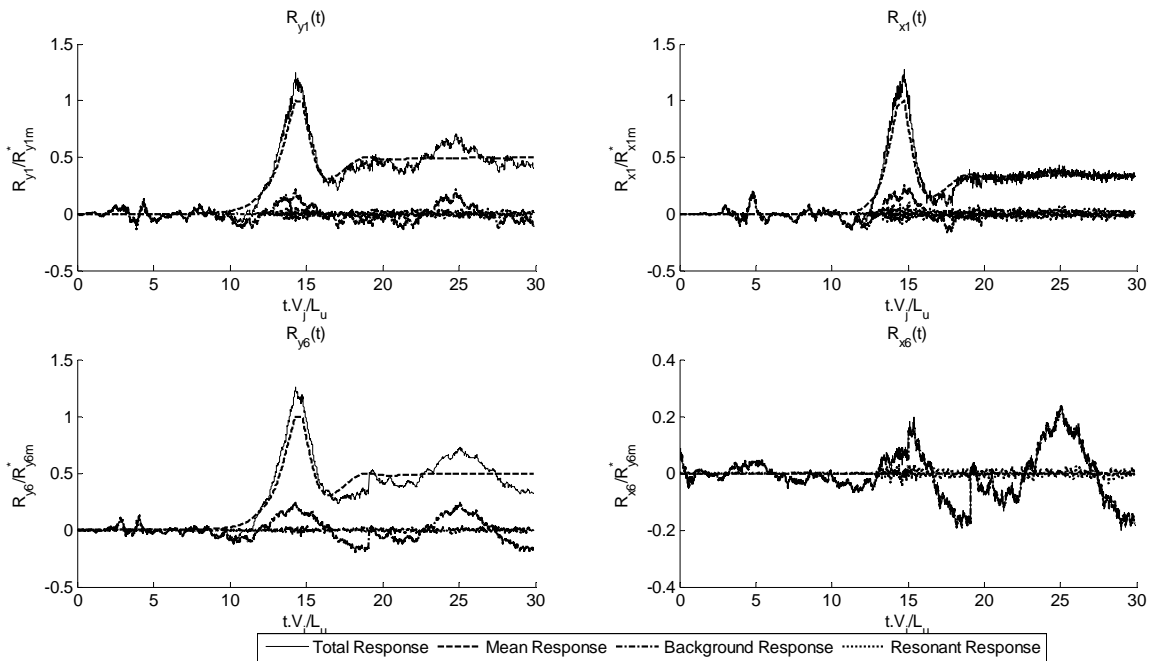


Figure C7 Reaction Responses for Case 7 (Db_y , $L_x=500$ m, $V_{ref}= 40$ m/s)

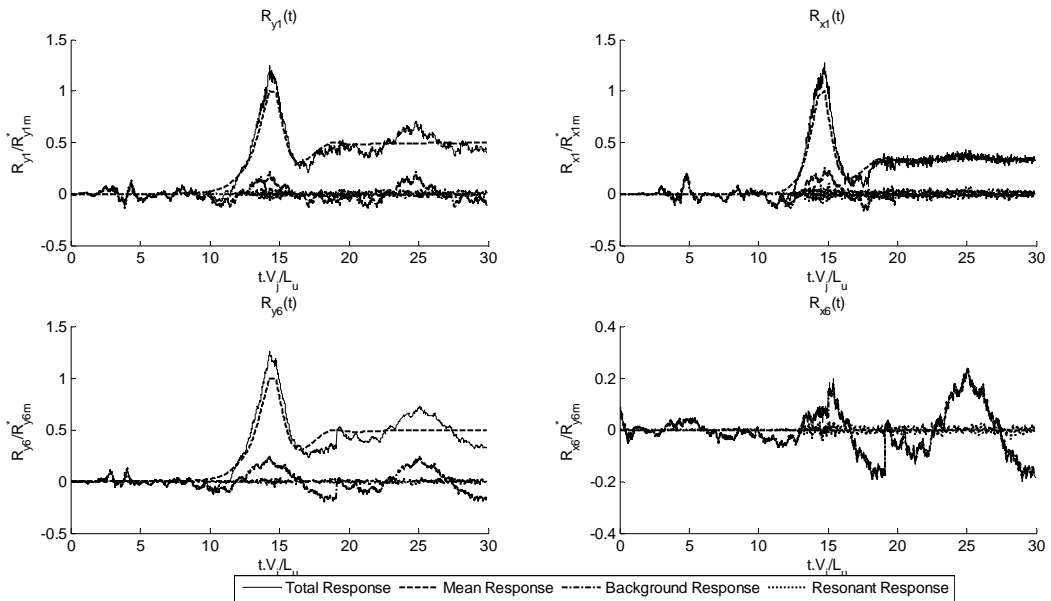


Figure C8 Reaction Responses for Case 8 (Db_y , $L_x=500$ m, $V_{ref}= 20$ m/s)

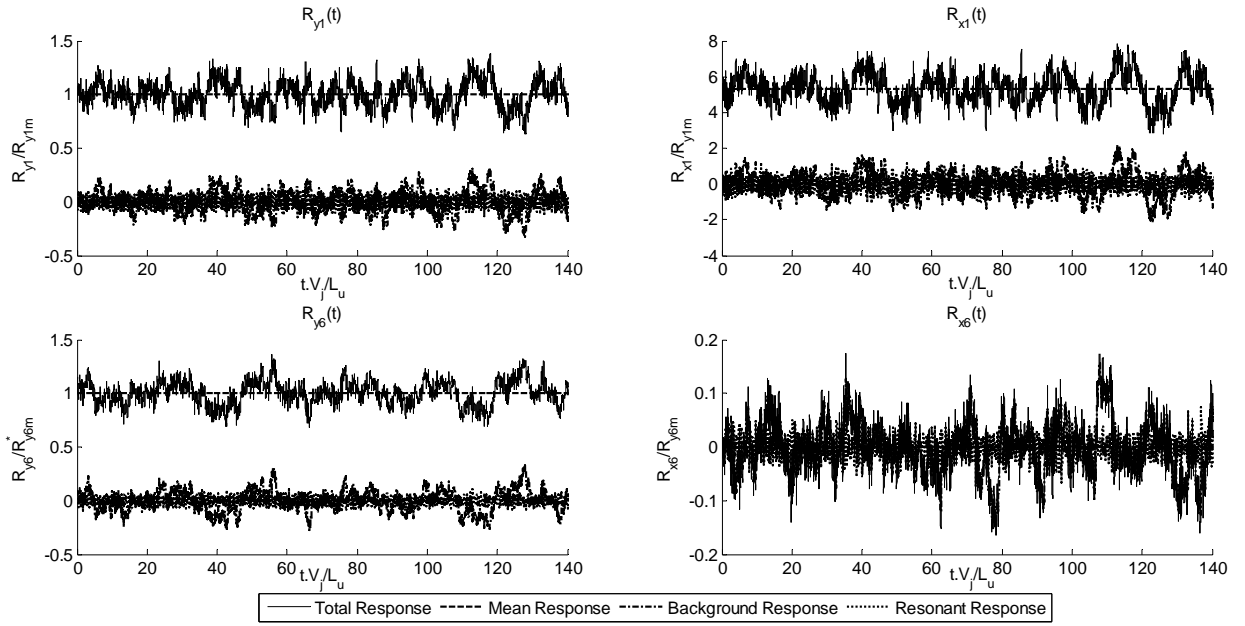


Figure C9 Reaction Responses for Case 9 (Sy Lx=300 m, Vref= 40 m/s)

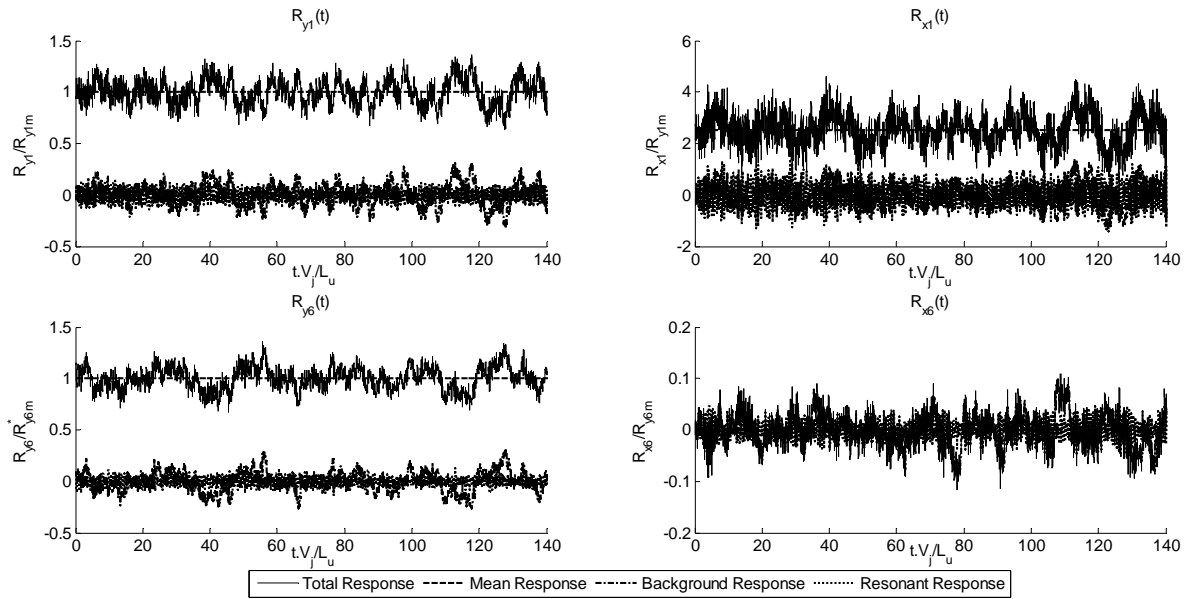


Figure C10 Reaction Responses for Case 10 (Sy, Lx=300 m, Vref= 20 m/s)

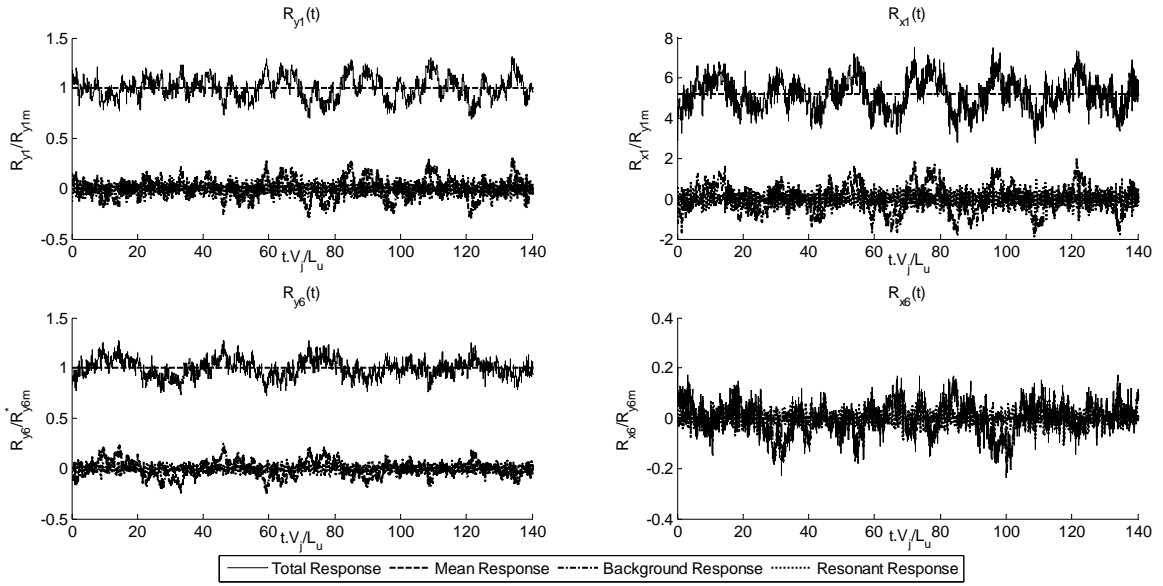


Figure C11 Reaction Responses for Case 11(S_y , $L_x=500$ m, $V_{ref}= 40$ m/s)

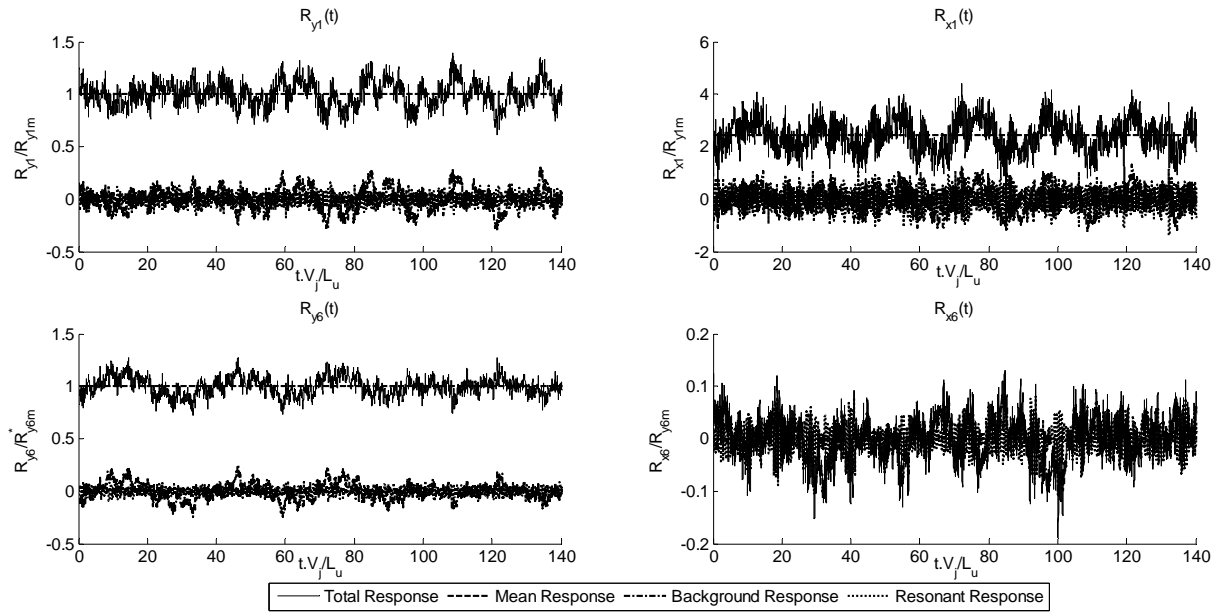


Figure C12 Reaction Responses for Case 12 (S_y , $L_x=500$ m, $V_{ref}= 20$ m/s)

Appendix D: Results of the Dynamic Analyses under Various Terrain Exposures

Samples of the reaction responses

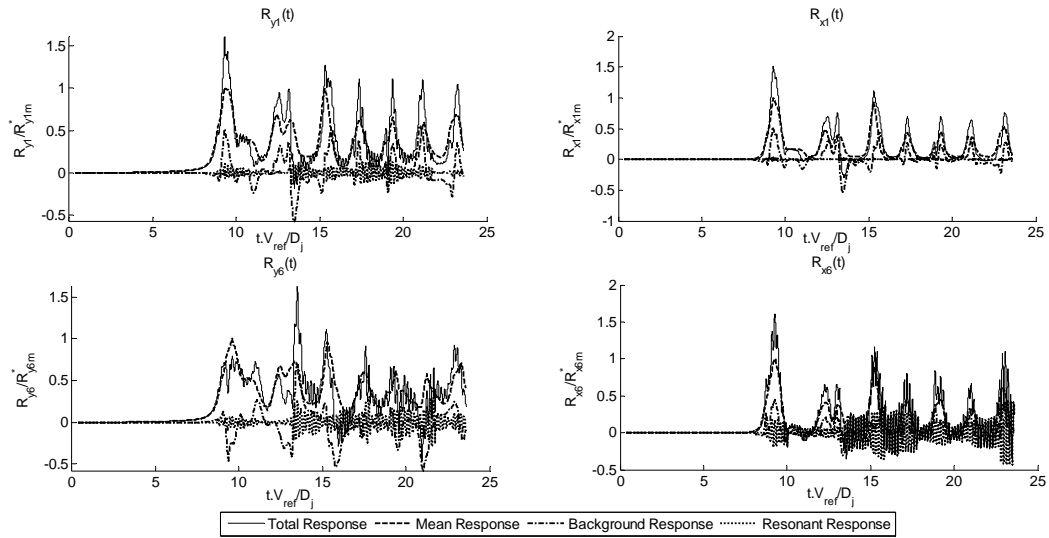


Figure D13 Reaction Responses for Case 1 ($Db_x, L_x=300$ m, $V_{ref}=40$ m/s) for open terrain exposure

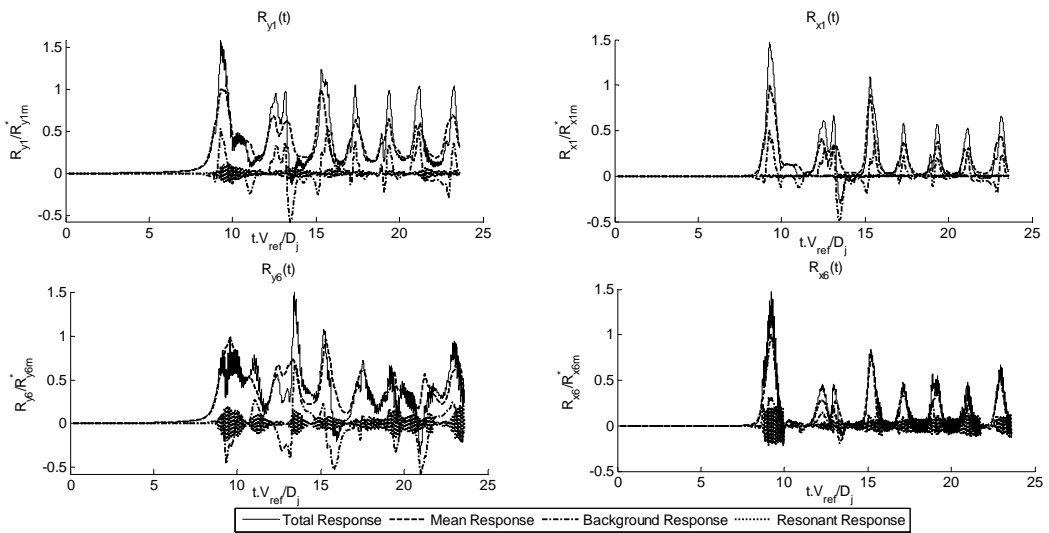


Figure D14 Reaction Responses for Case 1 ($Db_x, L_x=300$ m, $V_{ref}=40$ m/s) for countryside terrain exposure

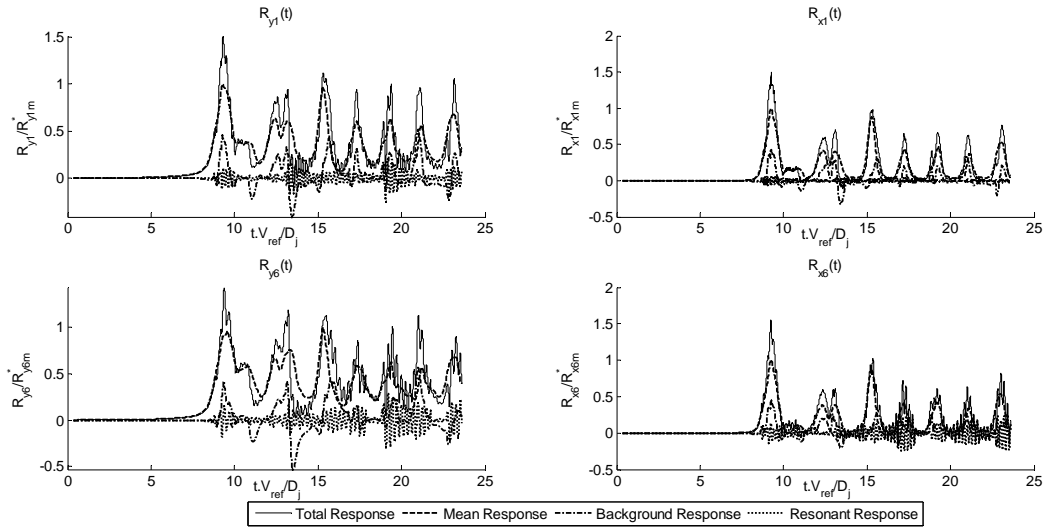


Figure D15 Reaction Responses for Case 1 (Db_x , $L_x=300$ m, $V_{ref}= 40$ m/s) for suburban terrain exposure

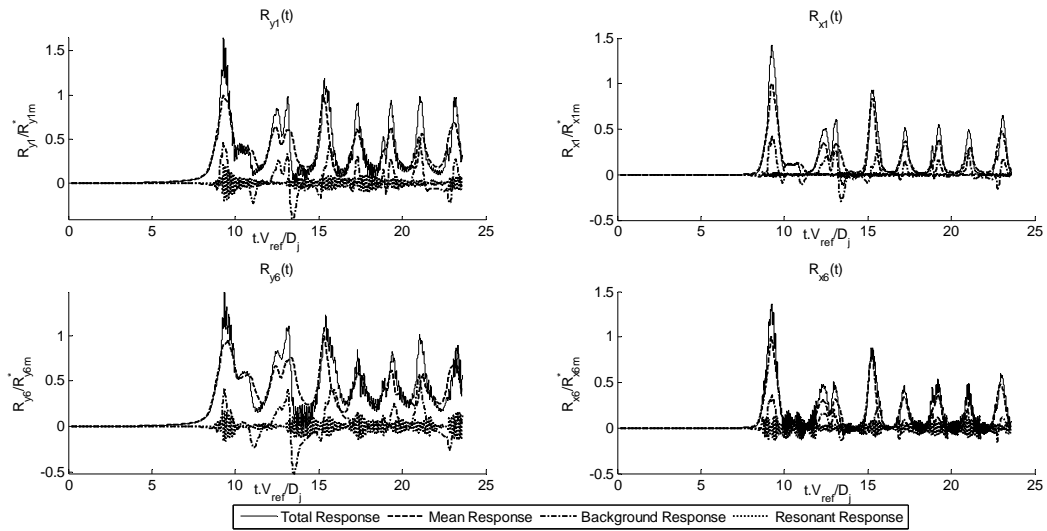


Figure D16 Reaction Responses for Case 1 (Db_x , $L_x=300$ m, $V_{ref}= 40$ m/s) for urban terrain exposure

Table D1 Gust Factors for terrain roughness $z_0=0.03$ m

Resp. Type	Case	Downburst-(Peak R_x)			Case	Downburst-(Peak R_y)		
		GF_{Dy}	GF_{QS}	Cont _R %		GF_{Dy}	GF_{QS}	Diff _{QS} %
R_{y1}	1: L300 V 40	1.62	1.52	6.20	5: L300 V 40	1.12	1.12	0.47
R_{x1}		1.52	1.49	1.68		1.17	1.16	0.10
R_{y6}		1.63	1.39	15.00		1.16	1.14	1.98
R_{x6}		1.61	1.45	10.03		**	**	13.35
R_{y1}	2: L300 V 20	1.59	1.52	4.34	6: L300 V 20	1.14	1.12	2.17
R_{x1}		1.47	1.47	0.27		1.21	1.20	0.60
R_{y6}		1.51	1.40	7.36		1.17	1.13	3.24
R_{x6}		1.48	1.28	13.28		**	**	20.87
R_{y1}	3: L500 V 40	1.52	1.45	4.48	7: L500 V 40	1.18	1.14	3.82
R_{x1}		1.51	1.43	5.31		1.11	1.10	1.27
R_{y6}		1.49	1.37	7.84		1.19	1.15	3.29
R_{x6}		1.56	1.44	7.44		**	**	23.14
R_{y1}	4: L500 V 40	1.64	1.45	11.72	8: L500 V 40	1.20	1.14	5.21
R_{x1}		1.43	1.42	0.48		1.08	1.07	0.36
R_{y6}		1.55	1.38	10.91		1.20	1.15	3.86
R_{x6}		1.36	1.32	3.14		**	**	15.21

** indicated that the mean response is equal to zero

Table D2 Gust Factors for terrain roughness $z_0=0.1$ m

Resp. Type	Case	Downburst-(Peak R_x)			Case	Downburst-(Peak R_y)		
		GF_{Dy}	GF_{QS}	Cont $_R$ %		GF_{Dy}	GF_{QS}	Diff $_{QS}$ %
R_{y1}	1: L300 V 40	1.63	1.53	6.16	5: L300 V 40	1.29	1.25	3.09
R_{x1}		1.71	1.67	2.40		1.33	1.32	0.77
R_{y6}		1.55	1.45	6.04		1.36	1.28	5.42
R_{x6}		1.67	1.50	10.10		**	**	61.01
R_{y1}	2: L300 V 20	1.62	1.53	5.48	6: L300 V 20	1.28	1.24	2.56
R_{x1}		1.74	1.67	4.17		1.30	1.29	0.58
R_{y6}		1.51	1.44	4.86		1.30	1.28	1.87
R_{x6}		1.76	1.38	21.34		**	**	45.47
R_{y1}	3: L500 V 40	1.55	1.47	5.20	7: L500 V 40	1.45	1.32	8.57
R_{x1}		1.53	1.47	3.72		1.31	1.27	2.81
R_{y6}		1.49	1.42	4.17		1.43	1.33	6.79
R_{x6}		1.62	1.43	11.68		**	**	53.72
R_{y1}	4: L500 V 40	1.49	1.48	1.09	8: L500 V 40	1.40	1.32	5.55
R_{x1}		1.60	1.46	8.76		1.15	1.14	0.42
R_{y6}		1.48	1.41	4.63		1.41	1.33	5.57
R_{x6}		1.75	1.43	18.29		**	**	23.12

** indicated that the mean response is equal to zero

Table D3 Gust Factors for terrain roughness $z_0=0.3$ m

Resp. Type	Case	Downburst-(Peak R_x)			Case	Downburst-(Peak R_y)		
		GF_{Dy}	GF_{QS}	$Cont_R\%$		GF_{Dy}	GF_{QS}	$Diff_{QS}\%$
R_{y1}	1: L300 V 40	1.97	1.80	8.24	5: L300 V 40	1.75	1.61	7.97
R_{x1}		2.07	2.07	0.18		1.62	1.61	0.62
R_{y6}		2.17	1.99	8.23		1.71	1.64	3.58
R_{x6}		1.86	1.63	12.33		**	**	49.39
R_{y1}	2: L300 V 20	1.90	1.81	4.83	6: L300 V 20	1.68	1.59	5.13
R_{x1}		2.10	2.09	0.68		1.51	1.48	1.78
R_{y6}		2.01	1.98	1.67		1.81	1.62	10.05
R_{x6}		1.78	1.59	10.96		**	**	6.09
R_{y1}	3: L500 V 40	1.79	1.72	4.34	7: L500 V 40	1.64	1.64	0.15
R_{x1}		1.85	1.83	0.89		1.68	1.62	3.41
R_{y6}		1.93	1.83	5.40		1.68	1.66	1.25
R_{x6}		1.73	1.65	4.43		**	**	26.18
R_{y1}	4: L500 V 20	1.78	1.72	3.48	8: L500 V 20	1.89	1.64	13.23
R_{x1}		1.87	1.85	1.01		1.53	1.51	1.53
R_{y6}		1.91	1.82	4.60		1.84	1.67	9.05
R_{x6}		1.71	1.64	3.94		**	**	16.10

** indicated that the mean response is equal to zero

Table D4 Gust Factors for terrain roughness $z_0=0.7$ m

Resp. Type	Case	Downburst-(Peak R_x)			Case	Downburst-(Peak R_y)		
		GF_{Dy}	GF_{QS}	Cont $_R$ %		GF_{Dy}	GF_{QS}	Diff $_{QS}$ %
R_{y1}	1: L300 V 40	1.83	1.60	12.83	5: L300 V 40	1.61	1.29	20.19
R_{x1}		2.30	2.28	0.59		1.47	1.37	6.93
R_{y6}		1.39	1.16	16.23		1.62	1.34	17.17
R_{x6}		1.65	1.39	15.97		**	**	61.52
R_{y1}	2: L300 V 20	1.74	1.59	8.80	6: L300 V 20	1.56	1.31	15.77
R_{x1}		2.34	2.34	0.29		1.48	1.40	4.81
R_{y6}		1.26	1.17	7.05		2.20	1.35	38.50
R_{x6}		1.46	1.37	6.47		**	**	30.67
R_{y1}	3: L500 V 40	1.97	1.85	6.02	7: L500 V 40	1.72	1.52	11.84
R_{x1}		2.26	2.22	1.42		1.58	1.49	5.75
R_{y6}		1.44	1.31	9.05		1.69	1.45	14.19
R_{x6}		2.19	2.05	6.44		**	**	42.82
R_{y1}	4: L500 V 20	1.93	1.85	3.84	8: L500 V 20	1.83	1.56	15.09
R_{x1}		2.28	2.27	0.51		1.45	1.45	0.51
R_{y6}		1.32	1.32	0.35		1.83	1.48	19.27
R_{x6}		2.04	2.01	1.59		**	**	33.59

** indicated that the mean response is equal to zero

Curriculum Vitae

Name: Haitham Aboshosha
Post-secondary Education and Degrees: Alexandria University
 Alexandria, Egypt
 2001-2006 B.A.

Alexandria University
 Alexandria, Egypt
 2006-2010 M.A.

The University of Western Ontario
 London, Ontario, Canada
 2010-2014 Ph.D.

Honours and Awards: National Science and Engineering Research Centre (NSERC)
 Industrial Post Graduate Scholarship
 2011-2014

Alan G. Davenport Award of Excellence
 2013

Related Work Experience Teaching Assistant
 The University of Western Ontario
 2011-2014

Publications:

Aboshosha, H., El Damatty, A. 2014a. Effective Technique to Analyze Transmission Line Conductors under High Intensity Winds. *Wind and Structures an International Journal* 18(3), 235-252.

Aboshosha, H., El Damatty, A. 2014b. Span Reduction Factor of Transmission Line Conductors under Downburst Winds. *Journal of Wind and Engineering* 11(1), 13-22